2022

Wire Arc Additive Manufacturing of Ni-based Hastelloy C276 Alloy and Ameliorated Processes

Zhijun Qiu

UNIVERSITY OF WOLLONGONG AUSTRALIA

Wire Arc Additive Manufacturing of Ni-based Hastelloy C276 Alloy and Ameliorated Processes

by

Zhijun Qiu

This thesis is presented as part of the requirement
for the conferral of the degree:

Doctor of Philosophy

Supervisors: David Wexler and Stephen van Duin

University of Wollongong
Faculty of Engineering Information Sciences (EIS)
School of Mechanical, Materials, Mechatronic & Biomedical Engineering (MMMB)

August/2022

Certification

I, Zhijun Qiu, declare that this thesis submitted in fulfilment of the requirements for the conferral of the degree Doctor of Philosophy, from the University of Wollongong, is wholly my own work unless otherwise referenced or acknowledged. This document has not been submitted for qualifications at any other academic institution.

_____

Zhijun Qiu

31st August 2022

Acknowledgements

I would like to express my sincere gratitude to my supervisors Dr. David Wexler and A/Prof. Stephen van Duin, and group leader Prof. Huijun Li for the provision of opportunity and scholarship to conduct my PhD research at the University of Wollongong (UOW). I am highly grateful for their supervision, well-directed academic guidance, knowledge acquirement, valuable support, constant encouragement, and warm friendship. I gratefully acknowledge UOW for providing financial support throughout my PhD research and technical training.

I am deeply grateful to Prof. Hanliang Zhu and Prof. Ondrej Muránsky in the Australia Nuclear Science and Technology Organization (ANSTO) in Australia for their promotion of the project and their assistance in the experiment and data analysis. Special thanks are extended to Dr. Zhiyang Wang in ANSTO for his kindly assistance in experiment applications, data analysis, software learning and publication preparation.

I acknowledge Dr. Kristin Carpenter, and Dr. Bintao Wu in the faculty of Engineering Information Sciences (EIS) at UOW for their tremendous assistance in knowledge acquirement, sample fabrication, experiment design, publication preparation and warm friendship.

I highly appreciate the beamtime provided by ANSTO enabling the measurements by neutron diffraction and synchrotron X-ray diffraction, and the staff who assisted in processing my experiment data. Especially I am grateful to Prof. Anna Paradowska and Dr. Mark Reid for residual stress measurements using neutron diffraction (Proposal ID P9914) and for data analysis, Dr. Ulf Garbe from ANSTO for tomography and radiography test using neutron diffraction and for software learning, Dr. Andrew Studer

from ANSTO for the bulk texture test using neutron diffraction (proposal ID P9829) and for data processing, and Dr. Qinfen Gu from Australian Synchrotron for the conduction of synchrotron X-ray diffraction (proposal ID M14469).

I would like to convey my sincere appreciation to the technical staff Mr. Matthew Franklin, Dr. Hoang Tran, Mr. Duncan Best, Mr. Nick Mackie, Dr. Dominic Phelan, and Dr. Suk Chun Moon in the lab of EIS faculty at UOW for their assistance in the experiment and technical training. Greatly thanks to Dr. Azdiar Adil Gazder, Dr. Mitchell Nacarrow, Dr. Gilberto Casillas-Garcia and Mr. Tony Remo in the Australian Institute for Innovative Materials (AIIM) centre for their training in using microscopy and assistance in data analysis. I am grateful to the technical staff Mr. Stuart Rodd, Mr. Michael Grantham, and Mr. Nathan Hodges in the workshop of EIS faculty at UOW for their assistance in the sample preparation.

I appreciate and convey my thanks to all members of EIS faculty of UOW, especially to professors, fellows and colleagues in my research group who cooperated with me and provided their assistance in my experiment conduction, sample preparation, data analysis and warm friendship.

Words cannot express the love and gratitude that I feel for my family. Last but not least, I would like to thank my beloved family members for their continuous love during my period of study abroad. Especially, to my grandma and parents, thanks are given for their love and support.

Abstract

Hastelloy C276 alloy, a typical Ni-based solid solution strengthened trademark superalloy, possesses excellent practical performance under severe environmental conditions and elevated temperatures. Hence, Hastelloy C276 has been investigated as a candidate for structural material for nuclear reactors, chemical processing and aerospace, particularly as aero-engine components. Wire arc additive manufacturing (WAAM), with its relatively high deposition efficiencies and cost-effectiveness, is revolutionising the 3D fabrication of advanced alloy components. However, the effectiveness of WAAM, for fabricating Ni-based alloys, is not fully understood.

This thesis explores Hastelloy C276 structures deposited by the WAAM process, aiming to provide an insightful understanding of this process in the fabrication of Hastelloy C276 alloy and to assess and optimise different processing approaches, permitting a systematical investigation of process-microstructure-property interrelationships in WAAM fabricated Hastelloy C276.

The feasibility of WAAM fabricated Hastelloy C276 was addressed using the gas tungsten arc welding-based WAAM (GT-WAAM) process. Microstructures are non-uniform and responsible for the occurrence of anisotropy and heterogeneity in the observed mechanical properties at ambient temperatures and preliminary creep properties.

The mechanical properties of fabricated structures were optimised through post-processing and in-situ operations. First, stress relieving and solid solution post-heat treatments (PHTs) were applied at selected temperatures of 871 °C and 1177 °C, respectively, in order to refine the microstructures of samples with PHT. The post heat

treated samples at 1177 °C possessed a more homogenised elemental distribution and decreased intermetallics, providing the best mechanical properties. Next, in-situ magnetic arc oscillation (MAO) was added to the GT-WAAM system at three different frequencies of 5 Hz, 10 Hz and 20 Hz to control arc density. The lowest frequency (5 Hz) promoted mechanical properties at a micro and nano scale through manipulated dendrites and elemental distribution. The refined microstructure and mechanical properties were further optimised and stabilised when combining active interlayer cooling and a cold metal transfer (CMT)-based WAAM system, with CMT creating lower heat input, compared with GT-WAAM. The results indicated analogous mechanical properties of three heat input samples. However, lower heat input is more favourable for achieving slightly refined microstructure and decreased mechanical anisotropy.

Finally, this work studied cladding Hastelloy C276 alloy on P91 steel using GT-WAAM process for the potential application in nuclear reactors in a more cost-effective manner. The microstructure was first investigated in an as-cladded condition, and then optimised through a tempering operation, by which an enhanced homogeneity in the microstructure and hardness was obtained.

Based on the outcome of this research, it can be concluded that the fabrication of Hastelloy C276 components via WAAM process is feasible, with a large operational window. A preliminary creep test indicated that the performance of WAAM fabricated components is highly dependent on the texture, which can be utilised based on the stress distribution of the components. Cladding Hastelloy C276 on creep-resistant steel appears to be a cost-effective approach to producing bimetallic components used at elevated temperatures.

List of Publications

1. **Zhijun Qiu,** Bintao Wu, Hanliang Zhu, Zhiyang Wang, A. Hellier, Yan Ma, Huijun Li, Ondrej. Muransky, David. Wexler (2020), Microstructure and mechanical properties of wire arc additively manufactured Hastelloy C276 alloy, *Materials & Design*. [**IF: 9.417**]

2. **Zhijun Qiu**, Bosheng Dong, Bintao Wu, Zhiyang Wang, Kristin Carpenter, Tao Wu, Jianrui Zhang, David Wexler, Hanliang Zhu, Huijun Li (2021). Tailoring the surface finish, dendritic microstructure and mechanical properties of wire arc additively manufactured Hastelloy C276 alloy by magnetic arc oscillation, *Additive Manufacturing*. [**IF:11.632**]

3. **Zhijun Qiu,** Bintao Wu, Zhiyang Wang, David Wexler, Kristin Carpenter, Hanliang Zhu, Ondrej Muránsky, Jianrui. Zhang, Huijun Li (2021). Effects of post heat treatment on the microstructure and mechanical properties of wire arc additively manufactured Hastelloy C276 alloy, *Materials Characterization*. [**IF:4.537**]

4. **Zhijun Qiu***, Zhiyang Wang, Stephen van Duin, Bintao Wu, Hanliang Zhu, David Wexler, Zengxi Pan, Huijun Li (2022), A review of challenges and optimization processing during additive manufacturing of trademarked Ni-Cr-based alloys, Book chapter of *Modern Manufacturing Processes for Aircraft Materials*. (Accepted)

5. **Zhijun Qiu**, Zhiyang Wang, Azdiar Adil. Gazder, Stephen van Duin, Bintao Wu, Hanliang Zhu, Andrew Studer, Ulf Garbe, David Wexler, Huijun Li, Stabilised mechanical properties in Ni-based Hastelloy C276 alloy by additive manufacturing under different heat inputs incorporated with active interlayer temperature control (2022), *Material Science and Engineering A*. (Under review) [**IF: 6.044**]

6. Bintao Wu, **Zhijun Qiu***, Bosheng Dong, Ondrej Muránsky, Hanliang Zhu, Zhiyang

Wang, Zengxi Pan, Huijun Li (2022), The microstructural evolution and microhardness of wire arc cladding Hastelloy C276 alloy on P91 steel, *Journal of materials research and technology*. [**IF: 6.267**]

7. Chengxun Zhang, **Zhijun Qiu***, Hanliang Zhu, Zhiyang Wang, Ondrej Muránsky, Mihail Ionescu, Zengxi Pan, Jiangtao Xi, Huijun Li (2022). On the Effect of Heat Input and Interpass Temperature on the Performance of Inconel 625 Alloy Deposited Using Wire Arc Additive Manufacturing-Cold Metal Transfer Process. *Metals*. [**IF:2.695**]

8. Bintao Wu, **Zhijun Qiu***, Bosheng Dong, David Wexler, Zengxi Pan, Kristin Carpenter, Diego Raimundi Corradi, Huijun Li (2022). Effects of Synchronized Magnetic Arc Oscillation on Microstructure, Texture, Grain Boundary and Mechanical Properties of Wire Arc Additively Manufactured Ti6Al4V Alloy. *Additive Manufacturing*. [**IF: 11.632**]

9. Bosheng Dong, Zhiyang Wang, Hanliang Zhu, Ondrej Muránsky, **Zhijun Qiu**, Chen Shen, Zengxi Pan, Huijun Li (2022). Low neutron cross-section FeCrVTiNi based high-entropy alloys: design, additive manufacturing and characterization. *Microstructures*.

10. Bo Qian, Hongri Fan, Jianrui Zhang, Tengfei Li, Jiangtao Xi, **Zhijun Qiu** (2021) Study on laser powder bed fusion of nickel-base alloy of G-surface structure: scanning strategy, properties and compression properties. *Scientific report.* [**IF:4.996**]

11. Jianrui Zhang, Ge Song, **Zhijun Qiu**, Huijun Li (2020) Thermal analysis and effects study of evaporator exit vapor quality in a separate heat pipe. *Applied Thermal Engineering.* [**IF: 6.465**]

12. Donghong Ding, Bintao Wu, Zengxi Pan**, Zhijun Qiu**, Huijun Li (2020). Wire arc additive manufacturing of Ti6AL4V using active interpass cooling. *Materials and*

Manufacturing Processes. [**IF:5.069**]

13. Bintao Wu, **Zhijun Qiu**, Zengxi Pan, Kristin Carpenter, Tong Wang, Donghong Ding, Stephen Van Duin, HuijunLi (2020). Enhanced interface strength in steel-nickel bimetallic component fabricated using wire arc additive manufacturing with interweaving deposition strategy. *Journal of Materials Science & Technology*. [**IF: 10.319**]

14. Jianrui Zhang, Min Chi, BoQian, **Zhijun Qiu** (2020), Periodic Lattice Porous Structure Produced by Selective Laser Melting: Process, Experiment and Numerical Simulation Analysis, *Computer Modeling in Engineering & Sciences.* [**IF:2.07**]

* *Corresponding author*

List of Abbreviations and symbols

1. Abbreviations

AM	additive manufacturing
A	annealing
AD	as deposit
BEI	backscattered electron image
BF	barrel finishing
CAD	computer-aided design
CALPHAD	calculation of phase diagrams
CAM	computer-aided manufacturing
CCG	creep crack growth
CGHAZ	coarse-grained heat-affected zone
CMT	cold metal transfer
CO_2	carbon dioxide
DA	double aging
DAS	dendrite arm spacing
DED	directed energy deposition
DLF	Directed Light Fabrication
DOF	degrees of freedom
DMD	direct metal deposition
DMLS	Direct Metal Laser Sintering
EBSD	electron backscatter diffraction
EBW	electron beam welding

EDM	electrical discharge machining
EDS	energy dispersive X-ray spectroscopy
Er	Young’s modulus
FCC	face-centred-cubic
FGHAZ	fine-grained heat-affected zone
FSEM	field emission scanning electron microscope
GTAW	gas tungsten arc welding
GT-WAAM	gas tungsten arc welding based wire arc additive manufacturing
GMAW	gas metal arc welding
GM-WAAM	gas metal arc welding based wire arc additive manufacturing
H	horizontal
HAGB	high-angle grain boundary
HAZ	heat-affected zone
HCP	hexagonal close packed
HIP	hot isostatic press
HV	Vickers hardness
IPF	Inverse pole figure
IMC	intermetallic compound
KAM	Kernel average misorientation
LAGB	Low-angle grain boundary
LBW	laser beam welding
LENS	laser engineered net shaping
LPBF	laser powder-bed fusion

LMD	laser metal deposition
LW	laser welding
MAO	magnetic arc oscillation
MGB	migrated grain boundary
MSR	molten salt reactor
MZ	molten zone
ODF	orientation distribution function
OM	optical microscopy
PAW	plasma arc welding
PBF	powder bed fusion
PDAS	primary dendritic arm spacing
PF	pole figure
PHT	post-heat treatment
RSW	resistance spot welding
RT	room temperature
SA	solution annealing
SAC	strain-age-cracking
SAD	selected area electron diffraction
SDAS	secondary dendritic arm spacing
SEM	scanning electron microscope
SFE	stacking fault energy
SLM	selective laser melting
SRHT	stress relief heat treatment
SCC	stress crevice cracking
SP	shot peening

SSHT	solid solution heat treatment
SMAW	shielded metal arc welding
SWCR	supercritical water-cooled reactor
TE	total elongation
TCP	topologically close packed
TEM	transmission electron microscope
TIG	tungsten innert gas
TWW	total wall width
TWH	total wall height
WAAM	wire arc additive manufacturing
W-H	Williamson-Hall
WFS	wire feed speed
WZ	weld zone
V	vertical
VED	volumetric energy density
UIT	ultrasonic impact treatment
USP	ultrasonic shot peening
UTS	ultimate tensile strength
XRD	X-ray diffraction
YS	yield strength
CrC	carbide
Cr_3C_2	carbide
Cr_7C_3	carbide
Ni_4Mo	β phase in Hastelloy B
$(Ni, Cr, Fe)_2(Nb, Mo, Ti)$	Laves phase, intermetallic phase

Ni_3Nb	metastable intermetallic phase
Ni_3(Al, Ti)	intermetallic phase
Ni_3(Al, X)	intermetallic phase, X can be Ti, Mn, Cu, or Si
M_6C	carbide
M_2C	carbide
MC	carbide
$M_{23}C_6$	carbide
TiC	carbide
HCl	hydrogen chloride
H_3PO_4	phosphoric acid
H_2SO_4	sulfuric acid
Fe	iron
Co	cobalt
Ti	titanium
Nb	niobium
Mo	molybdenum
Al	aluminium
C	carbon
N	nitrogen
Ni	nickel
Cu	copper
W	tungsten
Si	silicon
Cr	chromium
Mg	Magnesium

3D	three dimension

2. Symbols

γ	gamma phase, face centre cubic structure in Ni-based alloys
γ'	gamma prime phase
γ''	gamma double prime phase, metastable phase
δ	delta phase, stable intermetallic phase
σ	metastable phase
P	*P* phase Intermetallic phase
μ	μ phase, Intermetallic phase
Å	angstrom
a	lattice parameter of an unit cell (a-axis)
b	lattice parameter of an unit cell (b-axis)
c	lattice parameter of an unit cell (c-axis)
wt.%	weight percentage
k	partition coefficient
R	solidification rate
L	liquid
°C	degree Celsius
°F	degree Fahrenheit
nA	nano-ampere
mm	millimetre
μm	micro-meter
°	degree sign

W	watt
θ	incident angle
x-axis	welding direction
y-axis	transverse direction
z-axis	building direction
kg	kilogram
kN	kilo newton
h	hour
L	litre
g	gram
cm	centimetre
Cs	concentration of solute at solidified metal
Co	concentration of solute in alloy
MPa	mega Pascal
λ	dendrite arm spacing
G	thermal gradient
R	cooling rate
J	joule
$\vec{F}$	magnetic force
$\vec{I}$	current
$\vec{B}$	magnetic field
$\vec{x}$	traveling direction
$\vec{y}$	transverse direction
V	voltage

L_p	distance of the dendrite core
L_s	secondary dendrite arm spacing
Ut	mechanical work
U_e	elastic indentation energy
U_p	plastic indentation energy
H	nanohardness

List of Tables

List of Figures

Table of Contents

1 Introduction

1.1 General

Ni-based alloys, being one of the most important series of engineering materials, have Ni as the principal element, often alloyed with a significant proportion (7 - 30 wt.%) of Cr, and/or additional metallic elements to strengthen performance, such as Fe, Nb, W, Mo, Ti and Co. With rational alloy design, Ni-based alloys present outstanding resistance to corrosion and oxidation, high strength at both ambient and elevated temperatures, relatively low coefficient of expansion, and excellent resistance to creep and fatigue [1]. Hence, they offer a wide range of applications in various environments, including the industries aligned with chemical, aerospace, nuclear, marine, electric, and medical sectors [2-4]. Due to the accelerated advancement of these fields, research and development of these alloy systems are ongoing.

Traditional manufacturing processes for Ni-based alloys depend on hot working and cold working for the production of bulk alloys, followed by processes such as rolling or extrusion, with subsequent subtractive machining processes to arrive at the required geometries. These complex processes can result in a long cycle period and low work efficiencies, which inevitably affect cost-effectiveness. High costs are also associated with a large amount of capital investment in required specific machines, large work areas required for casting or forging operations, and significant quantities of raw material wastage from the subtractive manufacturing process. Furthermore, due to the continuous work hardening of Ni-based alloys, in particular for strengthened alloys, it can also be difficult to fabricate some Ni-based alloy components by traditional machining processes, which in turn, may cause degradation of machining tools and

associated reductions in their usable lifetimes [5, 6].

Additive manufacturing (AM) processes can produce a near-net shape structure of Ni-based alloys based on a pre-designed 3D model via a layer-by-layer deposition strategy, with relatively high accuracy and flexibility [7]. AM has emerged as a highly digital-based manufacturing approach, covering the model design to the end fabrication via computer-aided design/manufacturing (CAD/CAM), which achieves significant resource savings compared to conventional manufacturing methods [8]. A large amount of leading time-saving and less capital investment on the fixed assets can offset the cost of post-finish refinement required for AM [9, 10]. The effectiveness of AM is also attributed to the maximisation of material utilisation, reducing the buy-to-fly ratio in the prototyping or the manufacture of central components, such as aerospace components [11]. Despite their cost benefits and performance efficiencies, current AM methods are associated with some inherent drawbacks, such as residual stresses [12, 13], and a dendritic/columnar microstructure, resulting in anisotropies in mechanical properties and even defects in some cases [14-16]. The series of drawbacks of AM call for an insightful understanding of the relationship in process-microstructure-properties of alloys to enhance the effectiveness of AM process.

Wire arc additive manufacturing (WAAM) is one type of wire-based AM process in which an electrical arc is adopted as a heat source to melt welding wire for fabrication of 3D components in a layer-by-layer deposition strategy [17]. The WAAM approach is advantageous for the production of large metallic components of complex geometry, due to its high deposition rate in comparison to the other AM approaches using laser or electron beams as heating sources. Furthermore, it requires relatively low apparatus investment and enables the fabrication of alloys with high density. These characteristics

enable a significant reduction in capital cost and efficient usage of raw materials [8]. WAAM can be further classified into three types: Gas Metal Arc Welding (GMAW)-based, Plasma Arc Welding (PAW)-based, Gas Tungsten Arc Welding (GTAW)-based.

Hastelloy trademark alloy is a typical family of Ni-based alloys, and research on Hastelloy series alloys has both scientific and industrial significance. In the current study, WAAM processes were utilised to produce Ni-based Hastelloy C276 samples, including GTAW-based WAAM (GT-WAAM) and gas metal arc welding-based WAAM (GM-WAAM) processes, with optimised in-situ and post-processing procedures. Hastelloy C276 is a Ni-Cr-Mo-based superalloy, offers preferable competence in corrosion and creep resistance, hence being applied in extreme acid environments, and has recently been evaluated as one candidate structural material in Generation IV nuclear reactors [18]. Numerous investigations have been conducted on microstructural evolutions, mechanical properties, machinability, and corrosion resistance of Hastelloy C276 [19-21]. So far, component fabrication techniques are still mainly concentrated on welding and traditional subtractive technologies, and only limited research [22] has been reported on AM of Hastelloy C276 alloy; this makes an attempt to apply the AM process timely.

1.2 Objective of current research

This research aims to give an insightful understanding of a novel WAAM of Hastelloy C276 alloy, establish optimal processing parameters and evaluate the mechanical properties of the fabricated material. Furthermore, this thesis also provides a preliminary understanding of a dissimilar metal cladding of Hastelloy C276 alloy on low-alloyed P91 steel. The issues connected to this research include the feasibility of fabrication, fabrication parameters, porosity, deformation, cracking, microstructure

evolution, solidification behaviour, and effects of optimised parameters. Specifically, the objectives of this work are as follows:

(1) To explore the feasibility of fabrication of Hastelloy C276 alloy using GT-WAAM, to determine manufacturing process parameters and identify the operation windows through the study of related microstructures and properties. In this case, the challenges in the as-built component manufactured by GT-WAAM, including cracking, deformation, anisotropy, and non-homogenisation are investigated.

(2) To investigate alternative post-heat treatment processing, in-situ lower heat input arc processes, as well as in-situ interlayer operation routes to optimise material performance characteristics, in comparison with the as-deposited condition.

(3) To develop a dissimilar metal cladding of Hastelloy C276 alloy on low-alloyed P91 steel using GT-WAAM; Moreover, to explore the effects of post-heat treatment (PHT) on the fabricated cladding structure.

1.3 Major contributions of current research

There are limited recorded investigations of WAAM fabricated Hastelloy C276 alloy, so this research is benchmarked with conventionally produced Hastelloy components. The outcome of this research is of particular importance in understanding the WAAM processing-microstructure-properties for the Ni-based Hastelloy C276 alloys, exclusively providing valuable information for process optimisation and improvement in the resultant properties.

This thesis systematically studied WAAM of Hastelloy C276, via interlayer management, heat input control, magnetic arc oscillation and PHT, which is unique for the academic study of this alloy by AM processes. During manufacturing and post

processes, temperature evolution, welding pool behaviour, dendrite and columnar grain pattern, bulk texture, elemental segregation and secondary phases were investigated by the thermodynamic calculation and experimental approaches. These studies will initiatively contribute to the in-depth understanding of the microstructural evolution of Hastelloy C276 alloy in the WAAM process. Of particular importance, this thesis explores mechanical properties at micro and nano scales under various processes, providing WAAM fabricated Hastelloy C276 structures with comparable mechanical properties for practical industrial applications. Through these explorations, this thesis provides reproducible process parameters for the fabrication of full density and property reliable Hastelloy C276 by WAAM.

Due to the intrinsic advantages of WAAM, the synthesis of Hastelloy C276 alloy by the WAAM processes enables an alternative industrial approach to produce structures cost-effectively with complex geometries, and on a large scale in comparison with traditional processes. Furthermore, this thesis also studied the cladding of Hastelloy C276 on steel which is of a comparatively lower cost than a direct synthesis of the single composition superalloy components. This was done in order to enhance cost-effectiveness of this alloy's application. Hence, the high benefits to both industry and academia will be readily offered through the outcome of this thesis work.

1.4 Outline of this thesis

To achieve these aims mentioned above, this thesis is organised in nine chapters as follows:

Chapter 1 introduces the background, studied alloy and processes in conjunction with the objectives and contribution of this research.

Chapter 2 provides a comprehensive review conducted in this chapter to understand Ni and its alloys and, particularly, the Ni-based Hastelloy alloys are introduced in their conventional manufacturing and joining processes. The common defects and challenges of the conventional fabrication processes are summarised. Subsequently, AM as an alternative process is discussed in the fabrication of Ni-based alloys. Finally, Hastelloy C276, as the investigated material in this research, is introduced particularly, at the end section of this chapter.

Chapter 3 introduces the methodology, characterisation techniques, and related instruments required for the realisation of current research.

Chapter 4 studies the feasibility of a fabrication of Hastelloy C276 thin-wall structures by GT-WAAM. The microstructure, primary dendrite arm spacing, dislocation density, second-phase precipitates, ambient temperature mechanical properties and preliminary creep property at elevated temperature of the as-deposited structure are evaluated in detail using specimens extracted from different orientations and locations along the deposition direction.

Chapter 5 explores the influence of PHTs at 871 °C and 1177 °C on the microstructure and mechanical properties of the Hastelloy C276 alloy prepared using the GT-WAAM process. The elemental distribution and intermetallics which are different from those formed under traditional processing conditions are particularly studied in this chapter.

Chapter 6 describes an investigation of the effects of magnetic arc oscillation (MAO) at three different frequencies (5 Hz, 10 Hz and 20 Hz) applied during GT-WAAM deposition of Hastelloy C276. The processing, microstructure, surface finish and mechanical properties on micro and nano scales of the alloy fabricated with MAO are investigated and compared in-depth with the counterpart without the application of

MAO.

Chapter 7 continues to investigate in-situ processing to improve mechanical properties and decrease the anisotropy, in which the cold metal transfer (CMT) process parameters with different associated heat inputs (276 J/mm, 368 J/mm and 553 J/mm), and active interlayer cooling, is applied.

Chapter 8 explores application of a further cost cutting measure, that of cladding of Hastelloy C276 on P91 steel by WAAM. This chapter studies the microstructure of as-cladded alloy with and without tempering treatment. Related effects on hardness are compared.

Chapter 9 summarises the work in this thesis and provides some recommendations for future work on Hastelloy C276 alloy by WAAM.

2 Literature review

2.1 Ni-based alloys

2.1.1 Ni and its alloys

Solid Ni generally retains its face-centred cubic (FCC) crystal structure throughout its temperature range up to the melting point. It presents an inactive chemical property that is difficult to involve in reaction to acid solutions or oxidizing conditions, instead, it can form a protective corrosion resistance or an oxidizing film under exposure to corrosive or oxidizing environments [23]. These properties are sourced as an excellent opportunity for its application in corrosion resistance under high temperatures. Ni is marketed in various forms that are available to widely meet industrial demand, such as Ni powder, salt, pallet, ferronickel, etc. In common with other metals, pure Ni exhibits unstable mechanical properties which are significantly influenced by impurities, temperature, and machining history [24]. Compared with Ni-based alloys, pure Ni possesses lower mechanical properties, especially than those of age-hardening alloys.

Ni-based alloys as one of the most important series of engineering materials have Ni as the balancing element alloyed with some metal materials to strengthen performance. They can offer improved properties, or additional properties that the other alloy families cannot offer. For example, metallurgy and weldability issues for Ni-based alloys are considered to be much simpler than iron-base materials. Inconel 625 can be the material for surface modification of oil and gas components, especially those made of stainless steel because of the high corrosion resistance and ductility [25]. The family of Ni-Cr-Mo welding products is ever applied to weld 9% Ni steel to obtain high mechanical properties and impact toughness under liquid nitrogen temperatures [26]. The new

development of superalloys is in an extremely high requirement for the ultra-efficient power generation system, such as gas turbines designed for electricity generation, which will be doubled due to the rapid development of the economy worldwide [27]. Hence, Ni-based alloys play an important role in the development of the modern world in alignment with the industries of nuclear, chemical, aerospace, etc, which even become the strategy supplies of one country.

2.1.2 Role of alloying elements in Ni-based alloys

The addition of elements contributes to the solid solution strengthening, the formation of precipitation strengthening and hardening in some cases. In addition, based on the content and types of these elements, corrosion resistance is also enhanced.

Ni is an excellent base to design alloys as this element itself can moderately resist corrosion and can be provided as a matrix to maintain the ductile FCC structure with alloying elements. It is outstandingly resistant to alkalies both in hot and cold temperatures and reacts slowly to dilute nonoxidizing inorganic and organic acids [28]. Ni can be cathodically protected by making itself as a cathode of the electrochemical cell, but other easily corroded elements as an anode. Many elements are added to obtain enhancement the properties in mechanical properties and corrosion resistance in various extreme environments.

Mo, as one of the most important refractory elements of Ni-based alloys, is provided for mechanical strengthening and enhances corrosion resistance of the alloy. Mo has larger atomic radii than Ni, and it can impede dislocation and relative solubility, working as solid solution strengthening. The addition of Mo can improve the strength under elevated temperatures and creep strength, but the upper application is limited due to its tendency of severe oxidation over 1150 °C (2100 °F) [26]. Besides, Mo reduces

chlorination resistance for high-temperature applications, yet it can improve chloride stress crevice cracking (SCC) in an aqueous environment. In particular, Mo can resist reducing corrosive media and increase localised corrosion resistance [28].

Cr essentially improves oxidation resistance both at high temperatures and aqueous environment and strengthens mechanical strength. Besides, it enhances the sulfidation and carburization resistance but lowers the resistance to nitriding and fluorination [23, 28]. However, it also has a high risk of forming the intermetallic phase and leads to brittleness if the content is too high [29].

Fe can improve the cost-effectiveness of Ni-based alloys, but it does not optimise the corrosion resistance. It can enhance the high-temperature carburization resistance as it increases the solubility of C in the Ni matrix [23].

W has a larger atomic radius than Ni. W as a refractory element and solid solution strengthening element can improve the high-temperature strength of the alloys [23, 30]. Besides, it also can improve pitting and crevice corrosion.

C is the element of the carbide former. The refined primary M_6C carbide can be the strengthening phase, and it will be the main factor to increase the mechanical properties [31]. The content of C has to be controlled within 0.02 wt%, because C is relatively active over 315 °C (600 °F) in the matrix, resulting in the brittleness of the alloys due to the formation of graphite particles [26].

Co provides solid solution strengthening and increases strength under high temperatures of the alloy. It reduces the rate of sulphur diffusion and increases the solubility of carbon, so it can increase resistance to sulfidation and carburization [28].

Si is added to Ni-based alloys in a minor amount to improve the oxidization and

carburization resistance [23]. It plays an important role in the formation, stabilization, and distribution of primary carbide which might be the strengthening phase in Ni-based superalloys [32].

Other compositions enable to increase the strength under high temperatures through the formation of precipitations. For example, the addition of Ti and Al can be solid solution strengtheners, but they are mainly used to form the γ' phase [Ni_3(Al, Ti)] which can act as precipitation strengthening of the FCC matrix [26]. Ta and Nb are refractory elements and can be used as precipitation hardening. Mg is added to increase the mechanical properties and the resistance to oxidation [24].

In general, the elements in Ni-based alloys, including Ni, Mo, Cr, Fe, Co, participate the austenitic γ and strengthen the matrix with the different atomic radii from Ni. Mo, Cr and Si are strong former of carbide, which can be a strengthening phase. However, the processing technology of these alloys has to be controlled firmly in case of harmful brittle intermetallic phases [33].

2.1.3 Classification of Ni-based alloys

Ni-based alloys have no systematic classification but are usually known by the numbers or trade names signed by the producers of the alloys, such as Inconel® 625, Hastelloy® X, and Monel® 400. Comparing these alloys, the content can witness some differences. Based on the composition, these alloys are classified into commercially pure Ni alloys, solid-solution strengthened Ni-based alloys, precipitation-strengthened Ni-based alloys, and speciality alloys, as listed in Fig. 2.1 [26].

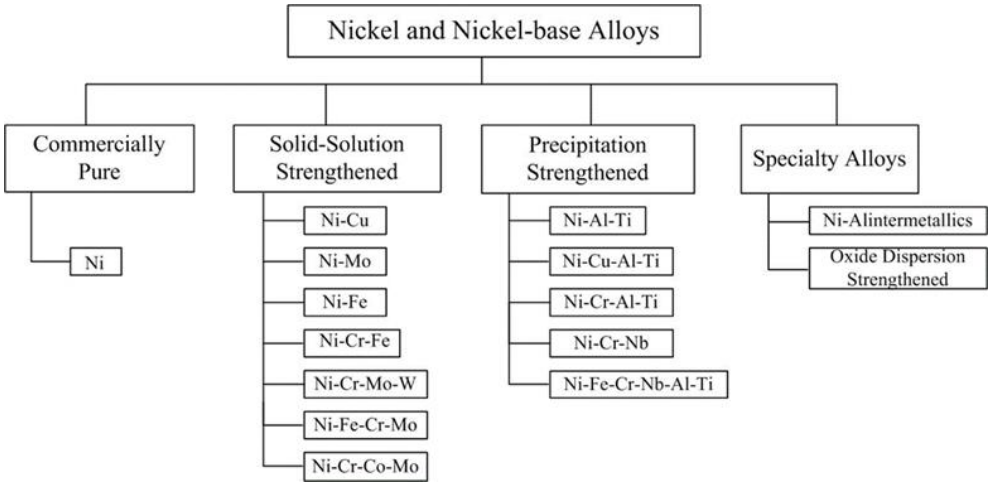

Fig. 2.1 Classification of Ni and Ni-based Alloys [26].

Commercially pure Ni alloys are alloys that contain over 99% Ni, usually with relatively low strength and hardness [34]. These pure Ni alloys are primarily applied due to their corrosion resistance in a severe environment, and they are also selected in electrical or magnetostrictive limited applications.

Solid-solution strengthened Ni-based alloys are those that are strengthened by the added substantial alloying elements to the matrix including Cr, Fe, Mo, W, and Cu, and also Co, Nb, and Ta in some cases, but Nb and Ta are usually used for precipitation strengthening. Due to these substations with different atomic parameters, the local matrix is distorted along with a lowered stacking fault energy. Hence, local dislocation can be formed, resulting in difficulty in further cross slip. Solid solution alloys can remain in an austenitic (FCC) matrix from the start of solidification to absolute zero, hence it can be used from cryogenic temperatures up to 1200 °C (2190 °F) [26]. The versatility of the solid-solution strengthened Ni-based alloys is offered by the combination of the additions of elements. For instance, Cr is added for the high resistance to oxidization, while Mo is for the resistance to corrosion [35]. Given the types of elements and their content, the alloys are applied for their different performance. In general, these alloys are usually used in applications where moderate

strength and excellent corrosion resistance are required at a high temperature [36]. The representative of solid-solution strengthened Ni-based alloys can be found to be Inconel 625, Hastelloy N, or Hastelloy C276.

Precipitation strengthened Ni-based alloys are realised through additions of Ti, Al, and/or Nb, and form strengthening precipitation after heat treatment. The matrix can be strained due to the appearance of these precipitations and thus increase the strength of the alloys remarkably. Being the same as solid-solution strengthened Ni-based alloys, the precipitation strengthened alloys also consist of austenite matrix and secondary phases. The differentiation is that the added elements can be precipitated as a strengthening phase under appropriate heat treatment. The most common phases are gamma prime [γ'-Ni_3Al, Ni_3Ti, and Ni_3 (Ti, Al)] and gamma double prime (γ''-Ni_3Nb), which are effectively coherent with the matrix in most cases [37]. Precipitation strengthened alloys possess the combination of outstanding corrosion resistance and high strength at elevated temperature, which is unique in metal alloys, hence being generally called “superalloys” based on their extremely high strength and corrosion resistance. The wide popular presentative of the precipitation strengthened Ni-based alloys can be found to be Inconel 718.

The other types of Ni-based alloys can also be classified as superalloys due to their high creep strength under high temperatures. For example, the MA 6000 which is an oxide dispersion strengthened alloy exhibits high creep strength through the precipitation strengthening and dispersion strengthening. The hardening of the alloy is created by dispersion particles which can be stable under high temperatures.

2.1.4 Examples of Ni-based alloy manufacturers and their representative alloys

2.1.4.1 Inconel

Inconel 718 contains 50 - 55 (wt) % of Ni, 17 - 21% of Cr, 4.8 - 5.5% of Nb, 2.8 - 3% of Mo, 0.65 - 1.15% of Ti, 1% of Co, small additions of Al (0.2 – 0.8%), and Fe (balance). Inconel 718 is precipitation strengthened Ni-based alloy, which is primarily hardened by γ'- Ni_3(Al, Ti) and metastable γ''-Ni_3Nb phases in an austenite γ matrix, and remains stable under 720 ℃. δ-Ni_3Nb phase and Laves phase transformation can occur if the alloy is exposed to temperatures higher than 720 ℃. Being incoherent with the matrix, carbides and nitrides are also reported to exist in this alloy [38]. Inconel 718 exhibits excellent mechanical properties and corrosion resistance, and superior tensile strength at elevated temperatures up to 700 ℃ [39]. Inconel 718 possesses good weldability because of its relatively low precipitation kinetics. However, this alloy is difficult to shape at room temperature by conventional machining processes, owing to low material removal rates and high shear strength [40, 41]. Inconel 718 has a wide range of applications as components used in harsh environments, such as high-pressure piping, supporting structures, and nuclear reactor applications.

Inconel 625 contains Ni as balance, 20 - 23 (wt)% of Cr, 5% of Fe, 3.15 - 4.25% of Nb, 8 - 10% of Mo, 0.5% Mn, and a small amount of Al (0.4) and Si (0.5%). Inconel 625 is a solid-solution strengthened Ni-based alloy, which is achieved by refractory metallic elements, Nb and Mo, in a Ni-Cr matrix. Due to the occurrence of fine metastable γ''-Ni_3Nb phases after long exposure at a temperature range of 550 to 850 ℃, Inconel 625 can be further precipitation hardened [42]. Laves phase can be formed due to segregation during fabrications, and carbides can also precipitate out in various phases (MC, M_6C, and $M_{23}C_6$), depending on the exposed ageing temperatures and time.

Inconel 625 possesses excellent properties, including high yield strength, creep resistance, fatigue strength, and oxidation and corrosion resistance under severe environments. The alloy can be used extensively, from cryogenic environment to ultra-high temperatures (over ~ 700 ℃ with high tensile strength and ~1000 ℃ for corrosion protection) [43]. With a good balance of weldability, fabricability, corrosion resistance, and mechanical properties, Inconel 625 is widely used as turbine blades and engine components in the fields of petrochemical, power, aerospace, and marine applications [44].

2.1.4.2 Monel

Monel K500 contains Ni (minimum 63%), 27 - 33% of Cu, 2.3 - 3.15% of Al, 0.35 - 0.85% of Ti, and a small amount of Fe, Si, and Mn. Monel K500 is a precipitation-hardened alloy which possesses high mechanical properties, fracture toughness and corrosion resistance in a wide range of corrosion media [45]. The increased strength is obtained by the precipitation of the γ'- Ni_3(Al, X) phase in the matrix under the aging process, in which X can be Ti, Mn, Cu or Si. The incoherent TiC phase which exhibits different morphology with aging can distribute heterogeneously in the matrix [46]. Despite some instances of failures, such as hydrogen embrittlement and stress corrosion cracking (SCC), it shows extraordinary corrosion resistance, on the whole, under the marine environment and sour oil [47]. Monel K500 is widely used in electronic, oil and gas productions, as well as marine industry, such as submarine propeller shafts.

2.1.4.3 Hastelloy

Hastelloy X contains Ni as the balanced composition, and 20.5 - 23 (wt) % of Cr, 17 - 20% of Fe, 8 - 10% of Mo, 05 - 2.5% of Co, 0.2 - 1.0 % of W, and little amount of Al (0.5%) and Mn (1.0 %). Hastelloy X, as a solid solution strengthening alloy containing

Mo, Co, and W, is designed for high-temperature applications. It combines extraordinary oxidation resistance with high-temperature strength over temperatures ranging from 540 to 1000 ℃ [48]. The high-temperature mechanical properties of Hastelloy X are sensitive to microstructural variations, in particular, the Mo-rich carbides (M_6C, $M_{23}C_6$), σ, and μ phase, as reported in this alloy [49-51]. Given the good formability due to its high ductility and weldability, Hastelloy X is widely applied in gas turbines as combustors, transition ducts, spray bars and flame holders, and exhaust components [51].

2.2 Hastelloy® alloys

2.2.1 Hastelloy family

Table. 2.1 Chemical composition of corrosion resistance Hastelloy alloys.

Alloy	Ni[a]	Co	Fe	Cr	Mo	W	Mn	Si	Nb	V	Al	Ti	C	Cu	Others
B-3®	65[b]	3*	1.5	1.5	28.5	3*	3*	0.1*	0.2*	0.2*	0.5*	0.2*	0.01*	0.2*	Ta-0.2*, Zr-0.01*
C-4	65	2*	3*	16	16	-	1	0.08*	-	-	-	0.7*	0.01*	0.5*	-
C-22®	56	2.5*	3	22	13	3	0.5*	0.08*	-	0.35*	-	-	0.01*	0.5*	-
C-22 HS®	61	1*	2*	21	17	1*	0.8*	0.08*	-	-	0.5*	-	0.01*	0.5*	-
C-276	57	2.5*	5	16	16	4	1*	0.08*	-	0.35*	-	-	0.01*	0.5*	-
C-2000®	59	2*	3*	23	16	-	0.5*	0.08*	-	-	0.5*	-	0.01*	1.6	-
G-30®	43	5*	15	30	5.5	2.5	1.5*	0.8*	0.8	-	-	-	0.03*	2	-
G-35®	58	1*	2*	33.2	8.1	0.6*	0.5*	0.6*	[c]	-	0.4*	-	0.05*	0.3*	-
HYBRID-BC1®	62	1*	2*	15	22	-	0.25	0.08*	-	-	0.5*	-	0.01*	-	-
N	71	0.2*	4*	7	16	0.5*	0.8*	1*	-	0.5*	-	-	0.06	0.35*	(Al+Ti)-0.5*

[a]As balance [b]Minimum [c]Cb+Ta *Maximum

Table 2.1 shows the chemical composition of Hastelloy® alloys which are the corrosion resistant alloys of Haynes International Corporation. Based on their composition, they are also numbered by UNS in America. Comparing the chemical element in Hastelloy alloys, it can be found that the corrosion resistance of Hastelloy alloys are mainly Ni-

Cr-Mo alloys except for Hastelloy G-30 alloy as Ni-Cr-Fe alloys. Ni metal is the major ingredient in the most effective manner of Hastelloy alloys, and some other elements with various percentages are added to form the different types of Hastelloy grades. These alloys provide unique properties, composed of a series of Hastelloy B, Hastelloy C, Hastelloy G, Hastelloy N, and Hybrid-BC1. Due to the extraordinary performance, Hastelloy alloys are specially chosen for the applications of corrosion, which is widely applied in chemical industries. The reliable quality leads to their market growth in energy, nuclear power plant, health, environmental, oil and gas industry, pharmaceutical and flue gas desulfurization industries [52]. Their high performance in extreme manners could be attributed to high resistance to outstanding localized corrosion resistance, reliable weldability and fabrication, corrosion cracking resistance [53]. The standard product forms include sheet and plate, wire and welding consumers, pipe and tubing, bar and bullet, fitting, and flangs. In this section, the Hastelloy alloys family will be introduced with details.

Hastelloy family alloys exhibit various corrosion resistance in various corrosion media based on their chemical compositions. With the technique development, the alloys are promoted in weldability, mechanical properties, and corrosion resistance. At present, the fabrication of Hastelloy alloys is mainly the traditional working process.

2.2.2 Fabrication processes of Hastelloy alloys

2.2.2.1 Hot working and cold working

The hot working of Hastelloy alloys includes hot forging, hot rolling, hot upset, hot extruding, and hot forming. Before and during the process of heating, most of the Hastelloy alloy's surface is required to be kept clean and far away from the pollutions, such as sulfur, phosphorus, lead, or other metals with a lower melting point.

During the hot working process, it is important to clarify the alloy's work hardening effects and the softening mechanism, such as dynamic recrystallization, to obtain a defect-free alloy [54]. The Hastelloy alloys have an austenitic matrix and have a high potential of working hardening rapidly. The prime softening mechanism is the dynamic recrystallization phenomenon, which is sensitive to temperature, strain rate, and stain [55]. Higher temperatures can lead to a higher rate of recrystallization, which could suppress the work hardening rate [56]. However, the temperature for hot working to Hastelloy alloys is quite narrow. It is recommended that the start temperature of hot forging is from 1204 ℃ (2200 °F) for Hastelloy G and N, and C-4 or 1232 ℃ (2250 °F) for other Hastelloy C and HYBRID-BC1, and the finish temperature is 954℃ (1750 °F), as they are sensitive to strain rate and strain. In order to optimise the working result, frequent re-heating has to be applied [57], which will highly increase the fabrication cost.

The cold working for Hastelloy alloys includes cold forming, spinning, drop hammering, punching, and shearing. Hastelloy alloys are stiffer than some of the other alloys, such as austenitic stainless steel, therefore, more power is required for cold working. Besides, Hastelloy alloys have higher deformation resistance, the cold working efficiency is correlated with the alloy's microstructure [56]. For example, after cold rolling, the uniform microstructure is expected to lead a good ductility which is better for the next step forming of the alloys, such as extruding. Therefore, some of the Hastelloy alloys require several steps for cold working, and annealing has to be applied before cold working along with intermediate annealing to obtain a refined microstructure. Cold working usually does not affect the general corrosion resistance of Hastelloy alloys, but it can lower the resistance to stress corrosion cracking. Hence, re-annealing to recover corrosion resistance is important. After cold working, the alloys

are required for re-annealing if the working process causes an elongation of 7% or more [57].

As can be seen in the traditional hot working and cold working process, the products will have exceptional mechanical properties and corrosion resistance due to the uniform microstructure, although the procedures are quite complex. The process will be productive and has to work on a large scale if the cost of each piece is controlled to be relatively low, while if the order or requirement of the products is not as many enough, the cost will rise. There are several reasons: First is the high capital investment which can be attributed to the cost of special operating equipment for the hot working and cold working process. Then the equipment will also occupy a large area so a large working plant is required (Fig. 2.2). Again, the hot forging system includes a preheated workpiece, lubricant, and a forging tool, such as the hammer, which is used to deform the workpiece. The working tool will be subjected to repetitive thermal exposure and mechanical loading, resulting in damage to the working tool because of mechanical fatigue, erosion, and deformation [58]. The damaged tool increases the possibility of failures of the workpiece, such as different geometries, or even scrapping of the workpiece.

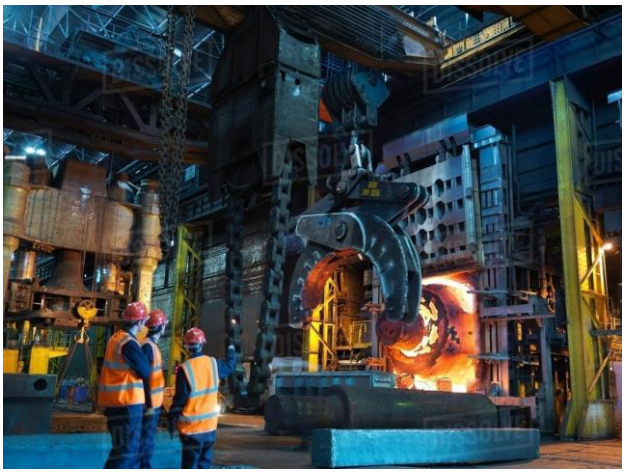

Fig. 2.2 Illustration of materials in a hot forging machine

2.2.2.2 Heat treatment

Given the different composition, forming requirements, and intended service, there are six principle types of heat treatment, including annealing, solution annealing, stress relieving, stress equalizing, solution treatment, and age hardening. Different types of heat treatment are performed either to soften the alloys, such as annealing the work-hardened alloys, or to enhance the mechanical properties, such as age hardening the alloys by precipitation in the matrix [23].

During the cold and hot working process of Hastelloy alloys, intermediate heat treatment is required for the workpieces. When the alloys reach the service size, the final heat treatment has to be given again to restore optimum properties in corrosion resistance and high mechanical properties, especially the ductility. Generally, solution annealing is recommended for Hastelloy alloys, no matter during or after forming work before the following applications. Water quenching (WQ) or rapid air cool (RAC) is required to follow the heating process to keep the single-phase presented under the high temperature of the alloys without the precipitation of the secondary phase in the microstructure, particularly at grain boundaries. These precipitations tend to impair the hot ductility that can fracture before the grain boundary sliding and recrystallization [59].

The solution annealing temperatures for various grades of Hastelloy alloys are provided in Table. 2.2 [57], which can effectively dissolve most of the other phases but keep within the range of grain size to impart optimum mechanical properties. Rapid cooling is essential to the solution annealing in preventing deleterious microstructure changes. The time should be started immediately when the whole material reaches the recommended temperature and controlled between 10-30 minutes depending on the

thickness of the workpieces.

Table. 2.2 Solution-annealing Temperatures of the Hastelloy (corrosion-resistant) Alloys

Alloy	Solution-annealing Temperature*		Type of Quench
	°F	°C	-
B-3®	1950	1066	WQ or RAC
C-4	1950	1066	WQ or RAC
C-22®	2050	1121	WQ or RAC
C-22HS®	1975	1079	WQ or RAC
C-276	2050	1121	WQ or RAC
C-2000®	2100	1149	WQ or RAC
G-30®	2150	1177	WQ or RAC
G-35®	2050	1121	WQ or RAC
HYBRID-BC1®	2100	1149	WQ or RAC

*Plus or Minus 25°F (14°C)

2.2.2.3 Machining and surface finishing

There are three important elements to influence the machining of alloys: workpiece, cutting tool, and machining parameters. The selection of tools and the cutting regime parameters are limited by the machinability of the alloys, while the machining parameters and the alloys can influence the tool's life.

Ni-based Hastelloy alloys are difficult to machine because of their high strength and hardness, and abrasive chips under high elevated temperatures [60, 61]. The metal cutting process can be explained by plastic deformation theory, as the cutting process itself is the process of metal's plastic deformation [62]. However, the high pressure generated between the cutting tools and alloys during the cutting process can lead to a stressed layer on the deformed surface of the workpiece. This deformation stimulates a hardening effect of the cutting layer, which further affects the mechanical properties of the workpiece and causes distortion of the small-sized workpiece.

The choice of the cutting tool must be considered based on the specific content of Hastelloy alloys and their previous operation processes. To achieve better surface

roughness and machinability, the coated insert was ever applied [62]. Another choice is ceramic tools because of their chemical stability and extreme hardness [63]. Being different from the conventional cutting process, electrical discharge machining (EDM) can be an alternative to machining the workpiece. EDM applies controlled and repetitive sparkles produced by a DC pulse generator to erode the material of the workpiece. This process presents advantages in precision and low limitation on the geometry in comparison with the conventional cutting machines, especially it is more economical at the time of machining the superalloys [64]. During the machining process, the tool's life and productivity can be decreased due to the outstanding mechanical properties of Hastelloy alloys. Machining at a high speed can accelerate the element diffusion of the alloys due to the generation of extremely high temperatures. The Ni-Cr-Fe base workpiece might have the possibility to react with the tool materials, such as silicon, and aluminium [61]. These elements diffuse into the tool matrix, resulting in a decrease in the tool's strength. The tool failure modes, such as flank wear, chipping and cracking, can result in the occurrence of notching or cracking on the alloy's surface, and cause a distinguished machining failure. The consumption of cutting tools and, in turn, contributed to the unsatisfied dimensional accuracy and surface integrity was always regarded as the increased cost of the conventional machining process.

Machining parameters include cutting force, cutting speed, feed force, lubricants and coolants, etc. The most important parameter is cutting speed which can significantly influence surface roughness, and the surface roughness can be improved by the increase of cutting depth [63]. Hastelloy alloys can be worked hardening rapidly, so it is recommended to use low cutting speed and high cutting depth. The cutting surface temperature is increased because of extreme friction between the tools and workpieces

under high cutting speed [65]. The lubricants or coolants have to be chosen based on the primary consideration being cooling or lubrication during cutting processes. Soluble water-base fluids are used to essentially remove heat, while ceramic tools are not recommended to use oils due to high risk of ignition. To the EDM, Choudhary, et al. [66] reported that the pulse on time, tool electrode, and current are the most influential parameters to affect the performance and the surface finish. Hastelloy alloys can be sensitive to oxidation and pollution on the surface, so it is important to grind with fine grinding wheels. There are different types of recommended grindings to refine the workpiece surface. The cylinder grinding is used to remove the sharp corner, and the internal grinding is applied for the hole removing, while the thin components or bevels have to use surface grinding. Comparing the grinding by polishing wheels, electrochemical mechanical polishing is also suitable for all types of Hastelloy alloys, and its mechanism is to passivation the alloy and form a passive film. Its high advantages are attributed to high efficiency, low surface scratching, low raw material removes, and particularly it has high quality for work-hardened alloys [67].

Basically, the machining processes of Hastelloy alloys have overcome the drawbacks of the alloy properties that are caused during the working processes. However, conventional machining is a subtractive process, which will cause a significant waste of raw materials. It was reported that about 83% of titanium turned out to be the discarded machining chips during the Ti alloy airframe fabrication process of Boeing 787 aircraft [68]. Hence, no matter how well the parameters are controlled, the machining process can translate the components to high-cost fabrication. To the complicated shape, the component requires careful machining, but sometimes it still cannot be fabricated by conventional machining from a single billet, instead, the welding and joining process is necessary.

2.2.2.4 Welding and joining

Ni-based alloys with high weldability can contribute to the high quality of the welded components. Hastelloy alloys, as one of Ni-based alloys, also exhibit good weldability, which is defined as a high ability to be welded and perform effectively during service. They can be successfully welded by arc welding, laser welding, and electron beam welding. The most common arc welding processes include GTAW, GMAW, and shielded metal arc welding (SMAW) processes. In addition, there are plasma arc welding (PAW), resistance spot welding (RSW), laser beam welding (LBW), and electron beam welding (EBW). Some other joining techniques, such as brazing, are also tried by academic researchers [69]. To achieve high-quality welding of Hastelloy alloys, lower heat input is recommended, by employing the low current and quick travel speed [57].

GTAW is a fusion welding process that is performed by a stable electric arc between the tungsten electrode and the workpiece under an inert environment. It's a wide-use process for Hastelloy alloy welding due to its high work efficiency and flexible operation. Manikandan et. al. studied the weldments of Hastelloy alloy manufactured by continuous and pulsed current GTAW techniques [70]. The results showed that the component by continuous GTAW exhibited less effectiveness than that by pulsed current GTAW. The unwanted brittle intermetallic phase was not precipitated in the weldment using pulsed current, resulting from the lower heat input and controlled solidification. The increased strength was found in the welded joint due to the refined microstructure. However, the normal GTAW technology has a high risk to cause elemental segregation, hot cracking, and non-equilibrium solidification due to high heat input, and lower heat input is critical in arc welding [21].

EBW is fusion welding in which the joints are produced by the fusion of base metal using high power density. It is carried out in a vacuum environment, which can avoid oxidation of the welding. Besides, this process has an extremely high cooling rate and high penetration depth, so there will be a very small heat-affected zone (HAZ). Hence, the EBW is integrated with low risk in the distortion of the workpiece and high working speed [71]. Hastelloy alloy has been welded by an electron beam, and the experiment obtained a fine lamellar structure, without detrimental intermetallic compounds in the welded molten zone (MZ), such as μ phase [72]. By EBW, an enhanced hardness in the MZ is achieved due to refined microstructure, but the defect, for instance, voids or hot cracking is remarkably decreased. The input process parameters, such as beam current, accelerating voltage, and welding speed, can significantly affect the beam width and beam penetration [73], and the welding speed is prior to current and voltage in affecting welding geometry [74]. Yet, a strict working environment is required for EBW, and the component size is also the limitation for a widespread application for this welding process.

Laser welding (LW) is a fusion welding process as another excellent alternative to weld Hastelloy alloys. It can provide benefits in precision, rapid processing capability, high energy density, and narrow heat input [75], hence there will be less distortion and residue stress compared with arc welding with higher heat input. The weldment of Hastelloy alloy was tested by Nd: YAG laser welding in an argon (80%) and CO_2 (20%) environment [21]. It was found that there is no significant HAZ due to narrow heat input, and the microsegregation in the welded zone is limited because of rapid solidification. The refined microstructure led to higher hardness and increased tensile strength in the welded zone. However, similar to EBM, the working environment also limits the work efficiency of LW.

Brazing is used to bond the material through melting and flowing a filler that usually has a lower melting point than the base metal into the joint. For Ni-based alloys, the fillers are Ni-Si, Ni-Cr-P, Ni-Cr-Si, Ni-Cr-Si-B alloys in the form of powder, paste, and amorphous foil [76]. Due to its vacuum operating environment, there will be a low risk of oxidation in the joint. The brazed Hastelloy N has ever been researched by He et al., using Ti foil with different soaking times [77]. The results showed the intermetallic phases Ni_3Ti, NiTi, and Ti_2Ni occurred in the joint, among which Ni_3Ti is adjacent to Hastelloy N and Ti_2Ni is close to Ti foil. The microstructure of the joint varied with the different soaking time and heating temperatures. The joint bond strength was critically governed by the microstructure of the brazed joint. Besides, Ma et al. [78] also reported that the brazing joint potentially becomes the weakest point under extreme environment. Hence, the performance of the joint can significantly determine the overall properties of the workpiece.

There are various types of welding technology that can be applied based on the size of the workpiece, and the working environment. The matrix of the weld joint usually presents a dendrite morphology, along with various amounts of precipitations. Compared to arc welding, laser and electron beam welding can have a better microstructure, nevertheless, they have limitations in workpiece size and work effectiveness. The refined microstructure can be controlled through lower heat input if arc welding is applied. To obtain a well-fabricated component, it is critical to understand its microstructure and the corresponding properties.

2.2.3 Microstructure of Hastelloy alloys

2.2.3.1 Matrix

The matrix of solid solution strengthening Hastelloy alloys is FCC austenite γ-Ni.

Hastelloy alloys usually require solution annealing in the final machining process, hence the grains in the matrix are mainly equiaxed cells with a large number of annealed twins, as is shown in Fig. 2.3 [79-81]. It can be found the grain size varies widely, being about 80 μm on average. Under the solution annealing process, most of the phases in Hastelloy alloys, other than the gamma phase can be dissolved except for some primary carbides. For instance, Hastelloy C-4 witnesses primary MC (TiC) carbide due to the presence of titanium [57]. Wang et al. [79] found that the Hastelloy N sheet can witness a significant amount of carbides inside of the grains and at grain boundaries, with a size of 0.5 - 8 μm. Grain size can affect the distribution of carbides at grain boundaries, which might be formed during solidification in Hastelloy alloys. The coarse grains have less grain boundary area, hence the carbides will become more continuous and have higher density, resulting in impairing the mechanical properties [23].

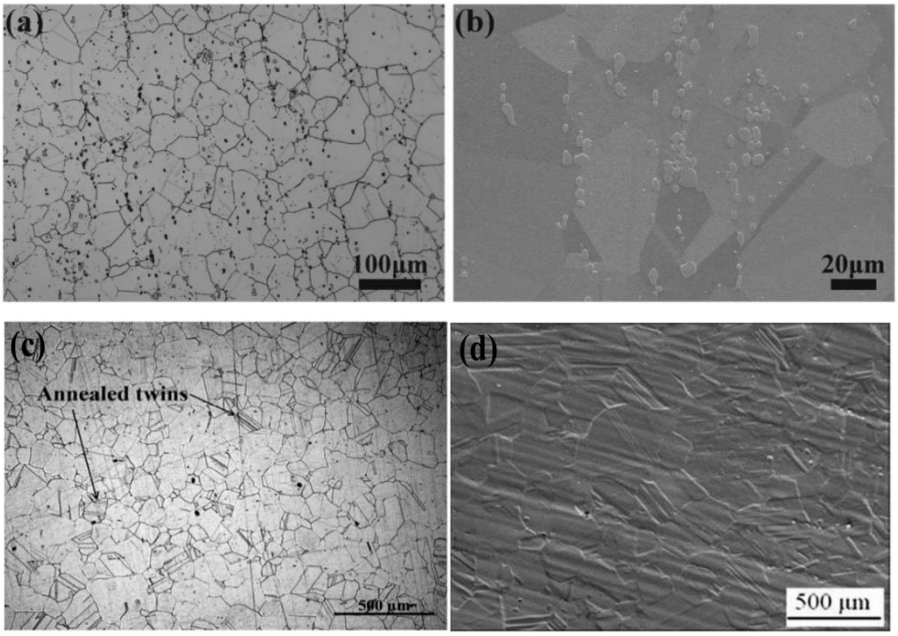

Fig. 2.3 Microstructure of Hastelloy alloys: (a-b) Hastelloy N ; (c) Hastelloy C276; (d) Hastelloy C2000

The distribution of chemical composition in the matrix is an important microstructure parameter to affect the properties of alloys, which can be alternated by the later working

process, such as welding or heat treatment. Ahmad et al. [72] found that the W, Cr, and Ni are higher in the solid solution matrix of Hastelloy C276, which can act as a solid solution hardening. Bal et al. [82] illustrated that the weld zone (WZ) of Hastelloy C276 owned higher corrosion resistance due to lower concentration of Mo and Cr in the dendrite core and higher concentration of Mo in the per unit length within the WZ.

The element and thermomechanical processing can initiate the microstructure and texture, which can influence the anisotropy of mechanical properties. Mehta et al. [83] explored the as-cast Hastelloy C276 alloy and found that the texture showed the dendrite features with high intensity of [200] and [111], while the hot rolled and annealed alloys had annealing twins within equiaxed grains with a moderate intensity of [111]. The presence of twins in the recrystallization microstructure is attributed to the relatively low stacking fault energy (SFE) of the FCC microstructure. Huang et al. [84] observed the hot-rolled following with mill annealed Hastelloy C22HS alloy and found no observed texture, while the measurement by neutrons found a moderate intensity of [111].

2.2.3.2 Intermetallic precipitates

Hastelloy alloys are a complex series of alloy family. Except for Hastelloy G-30 with more content of iron, the Ni-Cr-Mo system forms the basis of corrosion resistance Hastelloy alloys. The liquidus and isothermal sections from 1250 ℃ to 600 ℃ are shown in Fig. 2.4 [26], and the content of Cr (10 - 30 wt%) and Mo (0 - 20 wt%) in the boxes can be found in most of the Hastelloy alloys. As shown in Fig. 2.4, the solidification of these alloys initiates from γ austenite. Mo can segregate aggressively to the liquid during solidification, which has a wide range to promote the formation of intermetallic phases, such as *P*, σ (FeCr) phases [85]. Delta (δ) phase is found in the

low temperature, which is the equilibrium phase corresponding to the metastable γ″ phase [86]. This phase was reported to nucleate at austenite grain boundaries and coherent and incoherent twin boundaries at a lower temperature. However, the solidification in the welding process is usually a non-equilibrium process [72]. The intermetallic phases *P* phase, σ phases, and μ phase will be introduced briefly as follows.

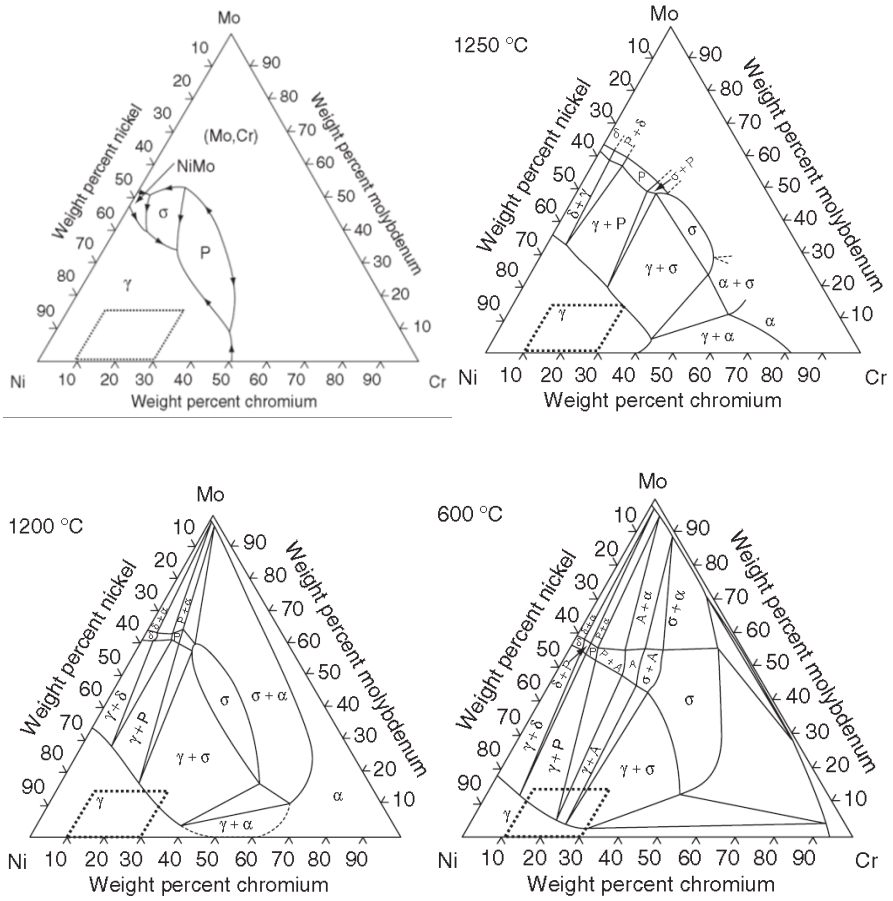

Fig. 2.4 Liquidus and isothermal sections of Ni-Cr-Mo system

P phase ($Cr_9Mo_{21}Ni_{20}$) is reported to be a low melting topological closed packed (TCP) phase by Bal et al. [87]. They investigated laser beam welded Hastelloy C276 with post-weld heat treatment at 1170 ± 1°C, and found a significant increase in hardness and formation of *P* phase in the weld zone after PHT. Leonard reported that the formation time of the *P* phase in Hastelloy C276 is 5 min or more from 650 °C to 1100 °C [88].

Cieslak et al. reported that the intermetallic *P* phase is responsible for the hot cracking during welding [89]. Due to the existence of the brittle intermetallic *P* phase, the strength of the welded structure can be lowered, and the *P* phase can lead to the appearance of failure if the structure is subjected to loading [87].

μ phase (Ni_7Mo_6) is another intermetallic phase in Hastelloy alloys, which is also the TCP phase. Both of them might exist in the Hastelloy C series, such as C276 and C22 [85, 90]. Cieslak et al. found *P* and μ phases in Hastelloy C276 during arc welding [89]. μ phase is known to be hard and brittle [91], and it can be formed from the decomposition of the *P* phase after a long-term thermal exposure. Ahmad et al. [72] found the appearance of the μ phase in Hastelloy C276 after subjecting to a tempering treatment at 950 °C for 3 h and air-cooled. The chemical compositions of the *P* phase and μ phase are similar, but their structures are orthorhombic and hexagonal respectively [85].

σ (sigma) phase as TCP phase is found in Hastelloy C22 and C2000 alloys, with tetragonal structure, and the reported average size is about 150 nm [26, 92]. Being different from *P* and μ phases with a higher content of Mo, the σ phase is higher in Cr, hence the lower content of Cr in C276 alloy lead lower possibility to form a σ phase. The appearance of the *P* phase in C22 alloy occurs by a solid-state transformation from the decomposition of the sigma phase, stabilized by Cr and Fe [26]. The σ phase in C2000 is a metastable phase, formed due to the increase of both defects' density and heterogeneity of alloying elements during plastic deformation [92]. This hard and brittle phase can hinder dislocation and hence increase strength [93].

Both Mo and W are reported to stabilize the TCP phases which are harmful to the weldability and mechanical properties with a large amount in the alloys. These

intermetallic phases can extend the solidification temperature range and increase solidification cracking. They are brittle and can lower ductility. In addition, due to the occupation of Mo and Cr from the matrix, the corrosion resistance of Hastelloy alloys can be decreased. Therefore, controlling and eliminating these intermetallic phases are quite important for the end applications of Hastelloy alloys. According to the Scheil–Gulliver simulations performed by Turchi et al. [94], the results clearly showed that the alloys can be properly annealed in a relatively wide range of temperatures and quenched in order to obtain a single FCC phase.

2.2.3.3 Carbide

The precipitation of carbide can enhance the hardness and strength of the alloys, acting as a dispersion strengthening, but the precipitation of carbide can also reduce the alloy corrosion resistance [95]. This is because the addition of carbon preferentially reacts with Cr and Mo which are used to improve the corrosion resistance in alloys. The precipitation carbides such as M_6C and $M_{23}C_6$ will lead to the accumulation of Mo and Cr in the carbides and depletion in the matrix [96]. Hence, the content of carbon in Hastelloy alloys is limited.

The M_6C carbide is widely reported to exist in Hastelloy alloys, (seeing an image illustration in Fig. 2.3b), such as Hastelloy N, Hastelloy B, and C series alloys [97, 98]. The primary M_6C carbide in Hastelloy N is in the form of Ni_3Mo_3C with FCC structure (11.2 Å), and Ni_2Mo_4C can be precipitated at grain boundaries after the alloy is exposure in the 500 -1000 °C [99]. The primary M_6C can be transformed into undesirable eutectic MoC type (M_6C) carbide in HAZ at grain boundaries after the thermal cycle during the welding process. These eutectic carbides can lead to hot cracking and worsen the performance of the welded component [100, 101]. However,

the eutectic carbide can be spheroidised by heat treatment and benefit to the performance of the welding joint [102]. Primary carbide can be dissolved from 1177 ℃ to 1300 ℃ and relieve Mo and C into the matrix, with reduced lattice parameters, but it can precipitate to the grain boundary again during cooling [79].

The M_2C carbide has a hexagonal close packed (HCP) structure with nano-size at the grain boundaries of Hastelloy alloys. It is a metastable phase precipitated in intermediate temperature from the solid matrix during the cooling in the welding process [31]. Hence, the M_2C carbide is unstable and can be dissolved by heat treatment. This fine carbide can act as dispersion strengthening in the weld component to enhance the hardness and strength [103].

Because Cr has a high tendency to form carbides, there are also some other CrC type carbides, such as Cr_3C_2 and Cr_7C_3, and they are found in laser beam welded Hastelloy C276 [87].

2.2.4 Strengthening mechanisms of Hastelloy alloys

Based on the dislocation theory, the strengthening of mechanical properties is controlled by the density and mobility of dislocations in the microstructure of the alloys. The increase of resistance again the movement of dislocation can be the way to strengthen the alloys, which can be achieved by microstructure refinement, solid solution strengthening, precipitation strengthening, dispersion, or deformation strengthening [104].

2.2.4.1 Grain size strengthening

Grain size, as an important microstructure parameter, can significantly influence the mechanical properties and corrosion resistance. Generally, the fine grain size can

provide better properties under room temperatures, such as strength, or fatigue resistance, while the coarse grain might provide better creep resistance at elevated temperatures [105]. The strengthening by fine grain size can be attributed to the existence of grain boundaries which are the source of dislocations and the barriers of blocking the movement of deformation [106]. Bal. et al. [87] found that the presence of more grain boundaries can provide higher resistance to the dislocation movement, which can increase the tensile strength. Cold working or hot working with the subsequent annealing for Hastelloy alloy are used to realise the grain boundary engineering to form twinning that can retain strain and break up the random grain boundary [107]. It has been proven that the final grain size significantly depends on the degree of deformation during the hot rolling of Hastelloy C276. That is, the greater the deformation, the smaller the recrystallization of grain size [56].

2.2.4.2 Solid solution strengthening

Solid solution strengthening is supplied due to the strengthening through the substantial element, using the solid solution heat treatment and rapid cooling as a way to keep the single phase in the matrix. The alloying additions are assured to be dissolved in the FCC matrix through solution annealing and the alloys are free of embrittle phases, resulting in a local dislocation. As is mentioned during the fabrication process of Hastelloy alloys, the temperature and annealing time are used to control the grain size which should be within the range of most effective temperatures. Rapid cooling is required to prevent the formation of carbide and intermetallic phase during the cooling process, while not necessary if the material is used under elevated temperature [26]. Wang et al. [31] reported that the grain boundary primary carbide is difficult to be dissolved into the matrix with solution heat treatment, but heat treatment can lead to the reduction of lattice parameters of carbide and spheroidisation of the eutectic carbide precipitated

during welding, which is good for the mechanical properties.

2.2.4.3 Precipitation strengthening

Precipitation strengthening is also called ageing hardening or particle hardening. The produced fine particles impede the movement of dislocations or defect the crystal's lattice to increase the strength of alloys. With the coarsening of precipitations, particle shearing and loops from precipitation become possible. The hardening results from the coherence between particles and matrix, the shear modulus, the occurrence of the difference of surface energy, or the change of bond energy after ordered structure. Akhter et al. explored the ageing temperature of Hastelloy C276 at 650 ℃ and 850 ℃ up to 240 hours respectively [108]. The results presented that there was no hardening phase after ageing at 650 ℃ up to 240 hours, but 850 ℃ was effective to harden the alloy while lowering ductility due to the formation of the Mo-rich μ phase. The hardness was also reported to remain after ageing at 850 ℃ for 96 hours. Brooks and Wang [109] studied the aged Hastelloy B from 500 ℃ to 850 ℃ for 1200 hours. The alloy strength and hardness were increased markedly due to the form of Ni_4Mo (β phase), which is the strengthening and embrittle phase in the FCC matrix. However, the ductility was reduced significantly, from 80% under solution annealing conditions to <5% under ageing condition. During the implementation of precipitation hardening for Hastelloy alloy, the temperature and time are critical to avoid the occurrence of over ageing. Due to the lowered ductility, the balance of the increase of strength, and accompanied by the loss of ductility and toughness, have to be considered.

2.2.4.4 Work hardening

As mentioned before, Hastelloy alloys have a moderate to high work hardening rate. Work hardening is alloy strengthening by plastic deformation. The plastic deformation

can lead to the appearance of defects, such as deformation-induced dislocation and deformation twins [110]. Because of the increased energy and heterogeneity of the composition elements of alloys, these defects can be the nucleation location of the second phase [111]. The metastable σ-FeCr phase was found in the cold-rolled Hastelloy C2000, along with an abundance of dislocations in a mutual entanglement pattern around the deformed twins. This led to an increase in hardness, yield, and tensile strengths of the researched alloy [92]. Work hardening can be desirable for the shape change of the alloys to intentionally perform the cold working process, while it might be undesirable under work hardening, such as cutting process, which can damage the cutter surface and increase the machining cost.

2.2.5 Mechanical properties of Hastelloy alloys

2.2.5.1 Tensile properties and hardness

As shown in Table. 2.3 [57], it can be found that the tensile strength of Hastelloy alloys is over 750 MPa, yield strength is over 300 MPa, and elongation is over 50% under room temperature (RT). Hastelloy alloys have excellent tensile properties and hardness, and the properties will be lowered if applicated under high temperatures. It is widely accepted that the mechanical properties are controlled by the microstructure which is determined by chemical composition, fabrication parameters, and post-heat treatment.

First of all, in the single grade of alloy, the properties are influenced by the fabrication processes. For example, from the properties of Hastelloy N under different conditions, it can be found that the aged alloy witnesses a bit higher mechanical properties than those under the solid solution heat treatment (SSHT) condition but induces a decreased ductility, as is shown in Table 2.3. This should be attributed to different strengthening mechanisms which cause the change in the microstructure. Hastelloy alloys are also

strengthened by hot working or cold working, which will present different higher mechanical properties as well. Hastelloy 2000 was reported to be strengthened under cold rolling due to the formation of the FeCr phase which hinders the dislocation movement hence increasing the strength [92].

Table. 2.3 Mechanical properties of Hastelloy alloys.

Form and condition	Temperature °C	Tensile strength MPa	Yield strength Mpa	Elongation %	Hardness HRB (RT)
Sheet					
B-3	RT-649	862-717	421-317	53-56	-
C-4	RT-427	768-656	416-250	52-68	90-92
C-22	RT-760	800-524	407-241	57-63	93
C-276	RT-538	792-613	356-233	61-60	90
C-2000	RT-1200	752-531	359-207	64-62	-
G-30	RT	689	324-352	56	-
G-35	RT-1200	738-517	345-179	60-68	-
Hybrid-BC1	RT-427	841-778	405-280	61.6-75.3	-
N (1177 °C SSHT)	RT-927	794-234	314-179	50.7-30.0	-
N (Aged)	RT-760	827-449	301-340 (RT)	50-20	-
Plate					
B-3	RT-649	883-738	400-290	58-65	-
C-4	RT-538	767-635	336-205	58-71	-
C22	RT-760	786-524	372-214	62-68	95 (RT)
C-276	204-427	682-654	263-210	61-61	87
C-2000	RT-1200	758-524	345-193	68-78	-
G-30	RT-538	676-524	310-200	55-62	-
G-35	RT-1200	689-469	317-165	72-74	-
Hybrid-BC1	RT-427	809-683	362-225	70.5-76.3	-
N	-	-	-	-	-
Bar					
B-3	-	-	-	-	-
C-4	-	-	-	-	-
C22	RT-760	765-496	359-200	70-77	-
C-276	-	-	-	-	-
C-2000	RT-1200	758-531	359-179	67-77	-
G-30	RT-538	689-524	317-200	60-62	-
G-35	RT-1200	710-476	317-159	66-71	-
Hybrid-BC1	RT-427	832-705	385-256	63-71.4	-
N	-	-	-	-	-

The welded Hastelloy applied different processes that have been investigated in past academic research. Luo et al. [112] reported the brazed Hastelloy C276 with BNi2 filler alloy, and the obtained tensile strength under room temperature was 398 MPa. In comparison with the sheet or plate alloy, irrespective of the type of welding process applied, the tensile strength of the welded alloys is lower than the sheet or plate alloys as a whole [80]. Luo et al. [112] presented that the diffusion zone is hardened and the filler zone is softened due to the element diffusion in brazing. Therefore, the weld joint is generally treated as the weakest part of the manufactured component due to microstructure diversity, which is an unavoidable aspect leading to the occurrence of defects or variations in mechanical properties [113].

2.2.4.2 High temperature creep performance

Creep is the permanent deformation caused through long-term exposure to high stress below the yield strength, under a more severe environment subjected to heat for a long period. As some series of the Hastelloy alloys can be applied under high temperature and high pressure, such as Hastelloy N alloy, creep properties and operation under high temperatures have to be ensured. Creep resistance is previously decided by the chemical compositions and the microstructure of the applied alloys. Mao et al. [114] found Hastelloy C276 owns excellent high temperature creep resistance. They compared the Hastelloy C276 with Inconel 800 and Inconel 690 and showed that the Hastelloy C276 alloy can endure higher stress than Inconel alloys under the same rupture time, as is shown in Fig. 2.5 [115]. Kawashima et al. [116] predicted creep strength by stress-strain magnification factors and stress analysis based on the equivalent-homogeneous-solid model. Creep damage is significantly influenced by the applied stress, stress ratio, and average stress [117].

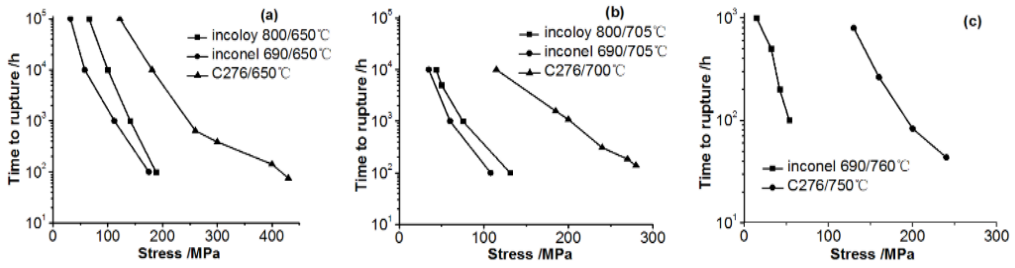

Fig. 2.5 Comparison of creep property between C276, Incoloy 800 and Inconel 690

Chen et al. [118] explored the creep crack growth (CCG) behaviour of the welded joint and found that the harder surrounding materials can increase the CCG rate and decrease the rupture life because of the higher constraint. As aforementioned the weld joint is found to be hardened, it can be induced that the weld joint might have lower creep resistance. This is proved by Luo et al. [119] who studied the notch effect on the BNi2 brazed joint of Hastelloy C276. The results showed that the creep damage initiates from the filler metal because the notch can induce high-stress concentration and alter the uniaxial stress state to a multiaxial one. Besides, they compared the notch of the creep samples with different shapes, as V-type notch, C-type notch, and U-type notch, and found V-type notch as a sharp notch was prone to lead to creep failure.

2.2.6 Corrosion and oxidation resistance of Hastelloy alloys

Corrosion can gradually distract the alloys by the chemical or electrochemical reaction in their application environment, such as acid, alkali, oxidation, and seawater. Corrosion can happen uniformly on the surface of the alloys or occurs in a localised area. General corrosion is the most widespread type, while localised corrosion has several forms: pitting, crevice, and intergranular corrosion.

2.2.6.1 Corrosion resistance of Hastelloy in various media

Table 2.4 presents the SCC comparison of Hastelloy alloys with some representative

alloys. The cracking time is assessed under boiling 45 wt.% magnesium chloride and the testing is performed for 1008 hours (6 weeks). From the results, it can be found Hastelloy alloys exhibit excellent SCC resistance. In accordance with the standard of ASTM 48, the assessment of alloy resistance to pitting and crevice cracking is performed under 6 wt.% ferric chloride. From the comparison provided in Table 2.5 [57], it can be found the Hastelloy alloy presents a high resistance to chloride-induced pitting and crevice attack.

Table. 2.4 SCC comparison of Hastelloy alloys with other alloys

Alloy	Time to Cracking
C-4	No cracking in 1,008 h
C-22	No cracking in 1,008 h
C-276	No cracking in 1,008 h
C-2000	No cracking in 1,008 h
G-30	168h
G-35	No cracking in 1,008 h
HYBRID-BC1	No cracking in 1,008 h
316L	2 h
254SMO	24 h
625	No cracking in 1,008 h

Table. 2.5 Pitting and Crevice comparison of Hastelloy alloys with other alloys

Alloy	Critical Pitting Temperature in Acidified 6% $FeCl_3$		Critical Crevice Temperature in Acidified 6% $FeCl_3$	
	°F	°C	°F	°C
C-4	212	100	122	50
C-22	>302	>150	176	60
C-276	>302	>150	131	55
G-30	131	55	77	25
G-35	203	95	113	45
316L	59	15	32	0
254SMO	140	60	86	30
625	212	100	104	40

Corrosion resistance is controlled by the alloy's chemical stability, arrangement, compactness, thermal expansion coefficient in the corrosion media, etc. [120]. In subject to the different element compositions, the different grades of Hastelloy alloys

are applied under various corrosion media, which exhibit excellent corrosion resistance.

The first application of Hastelloy alloys is in the acids, such as HCl, H_3PO_4, and H_2SO_4, Hastelloy B-3 presents exceptional resistance under HCl, and H_2SO_4, undergoing corrosion rate within the range 0.01 – 0.29 mm/y and 0.01 – 0.11 mm/y respectively, depending on the test temperature and solution concentration [57]. Other Hastelloy alloys can also be resistant to HCl and H_2SO_4, such as C-4, but with a bit lower than B-3, while they might be enhanced in weldability or versatility. For instance, C-22 has a high content of Cr, which provides higher resistance to oxidizing media. The high content of Cr also contributes to its application under high temperatures for its resistance to carburization, sulfidation, and halides attack [121]. The formation of a stable and dense oxide layer, such as Cr_2O_3 or Al_2O_3, is believed to protect the alloys from continuous corrosion by avoiding further corrosive media contact [122]. In contrast, the formation of the intermetallic phase, such as the TCP phase at 593 °C or above for a long exposure, might lower the corrosion resistance and the mechanical properties [108].

In the fluoride salt system, metallic fluorides are unstable in the salt, and the passive layer is excluded. The corrosion depends on the element thermodynamical driven dissolution whose Gibs Free energy of fluoride formation is low [123]. The tendency of reaction to form fluorides increases in the order: W, Mo, Ni, Fe, Cr, Al, Na [124]. Hence, the Hastelloy N alloy with low Cr and no Al is specially designed and considered to be the most successful structural material which is used for the molten salt reactor (MSR) [4, 113, 125]. Ye et al. [126] explored the corrosion behaviour of Hastelloy N in molten fluoride salt at 850 °C. The results show that the corrosion process is mainly controlled by the redox reaction between Fe ion and Cr, and Mo and

Cr depleted at the surface of the alloy. Zhu et al. [123] reported that both the corroded-only and irradiated and corroded samples of corrosion in the eutectic LiF–NaF–KF molten salt are mainly intergranular corrosion at 750 ℃.

The oxide film formed at the surface possibly reduces the diffusion of the alloys. However, the passive film might consume the element of alloys, which will significantly affect or deteriorate the corrosion resistance of the alloys. Hence, understanding the oxidation of Hastelloy alloys is quite necessary. The oxidation kinetics of Hastelloy C276 at 300-800°C in atmospheres followed a parabolic rate law [127]. The oxidation kinetics of the oxidation of Hastelloy C2000 studied at 800 °C and 1000 °C for 100h in the atmosphere also followed a parabolic rate law [81]. The annealing twins lowered the oxidation resistance of the alloys, as the defect structure increased the diffusion rate of alloying elements and oxygen atoms, while the $Cr_{1.3}Fe_{0.7}O_6$ and Fe_2O_3 oxides increased the corrosion resistance of the alloy.

2.2.6.2 Effects of welding on corrosion resistance

Aiming to work in a severe environment, the welding method is essential to ensure the overall service life of the component. Generally, if the welded component is to be exposed to a high acid environment, the corrosion resistance of the welding should be similar to or over the wrought base metal, and the filler should have an over matching composition with higher corrosion resistance if applied [128]. Ma et al. [129] investigated the electrochemistry corrosion properties of Hastelloy C-276 by the pulsed laser welding in the acid, alkali, and neutral solutions. The weldment was found to have a weaker tendency of being corroded in the acid and neutral solution but higher in alkali, and the corrosion rate is slower than the base metal in all solutions. Chai et al. [20] explored the laser-welded cavitation erosion of Hastelloy C276 and found that the weld

metal had higher resistance because of low angle boundaries. The highest damage intensity is in the centre-line of welding due to the largest grain misorientation.

Although Hastelloy alloys possess exceptional corrosion resistance, the weldment still can witness some limitations that can defect the corrosion properties of the alloys. Dupont et al. reported that the weld zone (WZ) usually had lower corrosion resistance than the base metal due to the element concentration gradients between two structures in the WZ [85]. The sensitization of grain boundary in the HAZ and interdendritic attack in the WZ led the weld joint to the most critical zone because of heat input, and a higher corrosion rate and pitting potential were found here [130]. The matching filler wire has been a critical issue, concerned about its quality, cost, and availability. The corrosion resistance and mechanical properties might both be defected by the filler. It has been revealed that the filler wire pits intensely under an aggressive oxidizing chloride situation after welding in Hastelloy C276 base metal [128].

2.3 AM processes

Compared with traditional manufacturing approaches, additive manufacturing (AM) is a promising alternative process, where single-component structures can be built-up layer by layer in various designed shapes, including complex geometries, at much lower costs [8]. In this part, AM process will be discussed in detail.

2.3.1 Classification of additive manufacturing

Based on the forms of feedstocks, commonly used AM approaches for metallic materials can be classified into powder- and wire-based processes. The application of wire-feed AM can achieve a higher deposition rate, while the powder-based AM process can achieve more accurate component geometries, but is often practically

limited for the production of small to medium-sized structures due to relatively low deposition rates [8]. For Ni-based alloys, laser- and electron-beam-based AM processes are generally associated with powder feed/bed techniques, while plasma arc-based AM processes mainly utilize wire-feed. There are many different names to describe the AM processes, as shown in Table 2.6. Based on power sources used for Ni-based alloys, the names of AM processes in this thesis are separated into laser-based Selective Laser Melting (SLM) and Laser Metal Deposition (LMD), electron beam-based EBM, and arc for the case of WAAM. General characteristics of different AM processes applicable for manufacturing Ni-based alloys are summarised in Table 2.6, among which laser-based processes were the most selected operations in Ni-based alloys by AM.

Table. 2.6 A summary of the laser-, electron beam- and arc-based AM processes

Power source	Category & Synonyms		Feedstock	Common Feature	Ref.
Laser-based	SLM	Laser Beam Melting (LBM) Direct Metal Laser Sintering (DMLS) Laser Cusing Laser Powder Bed Fusion (LPBF) Laser Metal Fusion (LMF)	Powder	powder bed-based; layer thickness: 20 - 100 µm; work area: 50 mm x 50 mm - 800 mm x 400 mm; scan speed:15 mm/s; spot size: 50 - 180 µm; laser power: 20 W - 1 kW; surface roughness: 8.5 - 10 µm; operates in an inert gas (nitrogen or argon) environment	[40, 131-134]
	LMD	Direct Metal Deposition (DMD) Laser Engineered Net Shaping (LENS) Direct Energy Deposition (DED) Laser Cladding (LC) Laser Solid Forming (LSF) Directed Light Fabrication (DLF)	Powder	blown powder; layer thickness : 40 µm - 1 mm; Feed rates: 4 - 30 g/min; Scan speed: 150 mm/min - 1.5 m/min; Spot size: 0.3 - 3 mm; surface roughness: 20 µm; operates in an inert gas (nitrogen or argon) environment	[134-138]

		Laser Deposition Welding (LDW)			
Electron beam-based		EBM	Powder	powder bed-based; layer thickness: 50 - 200 µm; work area: 200 mm x 200 mm in x-y-direction or 350 mm in diameter; beam current: 30 mA; scan speed: 10^4 mm/s; Spot size: 200 - 1000 µm; operates in vacuum $<10^{-2}$ Pa, feeding helium during deposition to increase pressure to 1 Pa	[134, 139-143]
Arc based	WAAM	GMAW-based Plasma Arc Welding (PAW)-based GTAW-based	Wire	wire-based; layer thickness: ~ 2 mm; wire feed speed: 1.2 m/min, welding speed: 150 - 300 mm/min; deposition rate: 12 g/min; surface roughness: 200 µm; current: 130 A; operates in an inert gas (nitrogen or argon) environment	[9, 13, 134, 144]

Both SLM and LMD (see Table 2.6) fall into the category of powder-based laser processes, nevertheless, the modes of powder feeding in these processes are different. Generally, both of these laser-based processes involve rapid solidification, and enable the provision of good surface accuracy of produced components, attributed to the small laser spot size and fine powders used. Yet, LMD is less precise in the control of produced component geometries, especially for thin-wall parts, than SLM, which is due to belated in-flight particle sintering on the surface, and the relatively high heat input during LMD. Similar to SLM and LMD processes, EBM also enables low surface roughness (see Table 2.6), contributing to the high geometrical accuracy of produced components [139-142]. EBM is performed in a vacuum environment which allows the fabrication of high purity components due to an absence of oxidation. Moreover, it

lowers entrapment of porosity resulting from gas flow during deposition processes [76]. However, the requirement of operation in a vacuum limits its cost-competitiveness and widespread adoption. Furthermore, the substrate in the AM process is often required to be preheated to a high temperature to facilitate process stability and alleviate residual stress. This preheating operation also influences the produced microstructure, especially grain size and precipitates, of subsequent depositions [145]. Being distinctive from the powder feed/bed-based processes of SLM, LMD and EBM, arc-based additive manufacturing for Ni-based alloys usually uses wires as feedstock. The deposition rate of WAAM (see Table 2.6) is significantly higher than laser- or electron beam-based processes. The wire feedstock is adaptable in a more friendly operation environment, due to its lower surface-to-volume ratio compared to more reactive powder particles [8]. Furthermore, higher volume deposition rates are achievable during wire deposition, and the deposition process using wire-based AM is generally more stable than that of powder-based processes. Hence, WAAM enables the fabrication of large-sized components economically and in a much shorter time. However, a drawback of WAAM is associated with larger volumes of material deposited in each layer, higher heat input, and higher resulting component surface roughness, compared with laser- and electron beam-based processes [13].

Due to the similar main elemental content and strengthening mechanism of Hastelloy alloy, the following section focuses on the AM of three common trademarked Ni-Cr-based superalloys, including Inconel 718, Inconel 625, and Hastelloy X. These alloys possess different elemental contents and constitution phases, represented as typical examples of Ni-Cr-based alloys for a broad range of applications. Inconel 718 is the most popularly studied alloy among these three alloys in academic research, which is considered by the authors due to its excellent properties and potential wide applications

in the future industry field.

2.3.2 Microstructure of additively manufactured Ni-based alloys

2.3.2.1 Solidification and texture under the as-deposited condition

During the AM processes, the deposited alloys are subjected to complex thermal cycles. Numerous re-heating and re-cooling processes continue until the completion of deposition for designed components, hence the microstructure of deposited parts vary, particularly with respect to each individually deposited layer. Fig. 2.6 shows the typical OM and EBSD orientation maps of AM-fabricated Ni-based alloys [146-148]. Irrespective of the Ni-based alloy deposited, the microstructure is dominantly composed of γ-matrix (FCC) grains in the form of an array of columnar dendrites, which tend to grow preferentially inline to the building direction (z) (see Fig. 2.6a - 2.6e). A strong crystallographic texture is usually induced, as a result of the preferential growth of columnar γ-matrix grains generally along the <001> direction, as shown in Figs. 2.6f and Fig. 2.6g [148], corresponding to the maximum temperature gradient direction [145, 149-151]. The crystallographic texture of Ni-based alloys is reported to have a close relationship with their corrosion resistance and mechanical properties. For instance, the corrosion resistance of different crystallographic planes decreases in the order of (001) > (111) > (011), due to the higher equivalent atomic packing density and more compact corrosion products (oxides) on the (001) FCC plane [152]. With regard to mechanical properties, Sanchez-Mata et al. [153] reported the highest tensile strengths along the <111> crystallographic orientation and the lowest of the <110> orientation in the SLM- fabricated Hastelloy X. Consistent with this, a strong texture developed in additively manufactured Ni-based alloys can lead to the anisotropies in corrosion resistance and mechanical properties at both ambient and elevated

temperatures [154, 155]. Several in-situ and ex-situ operations have been applied to limit texture, including post heat treatment [149] and hot isostatic pressing (HIP)[156], nevertheless resulting in potential grain coarsening [157].

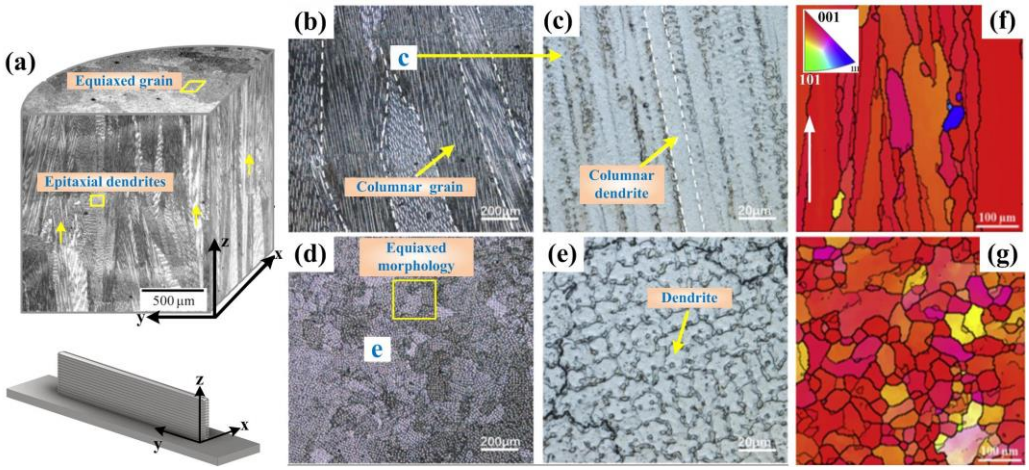

Fig. 2.6 Typical microstructures of as-deposited Ni-based alloys by AM: (a) 3D optical micrographs of the Inconel 718 manufactured by LMD. Reproduced with permission from Elsevier [147]; (b-e) Microstructure of the LMD fabricated Hastelloy X showing the dendritic microstructure on (b, c) the vertical section (d, e) the horizontal section. Reproduced with permission from Elsevier [146]; EBSD orientation maps of Inconel 718 by EBM along (f) the vertical direction (indicated by the arrow) and (g) the horizontal section. The maps in (f) and (g) are shown in inverse pole figure colouring scheme with respect to the building direction and the corresponding colour code is provided as an inset in (f). Reproduced with permission from Elsevier [148].

The microstructural characteristics of AM-fabricated Ni-based alloys, such as grain size (width), primary dendrite arm spacing (PDAS), and secondary dendrite arm spacing (SDAS) are closely correlated with AM processes. For laser and electron beam-based processes, the resultant columnar grains can be less than 15 μm in width [158, 159], and each grain contains very fine dendrites. Alternatively, the resulting microstructure can be cellular, i.e. comprising well-developed primary dendrites with no secondary dendrite arms. For example, a PDAS at ~ 0.5 μm was observed in SLM-produced Hastelloy X in Ref. [153]. Shaji Karapuzha et al. [145] reported about two times coarser grains of the Hastelloy X alloy produced by EBM, compared with that of the SLM-

produced counterpart, and this was attributed to the slower cooling rate in EBM. The dendrite morphology is influenced by the volumetric energy density (VED) of AM [132], i.e. the increased VED can lead to a low cooling rate and a large molten pool, hence contributing to the development of coarser dendrites as well as the strong texture. In contrast to laser and electron beam-based processes, the grains are much coarser in Ni-based alloys produced by WAAM, and the PDAS can be over 40 μm [160]. Although large columnar grains enable higher competition capability for creep resistance, lower strength under ambient conditions is usually yielded. Therefore, the VED and processes should be controlled and modified depending on the required in-service conditions of alloys. Regardless of what type of AM process is applied, dendrites are usually coarser at the top layers due to lower temperature gradients, compared with those produced in the earlier stages of AM layer formation [154, 158, 161].

2.3.3 Precipitation under the as-deposited condition

The rapid cooling rate associated with AM processes relative to traditional casting process contributes to the non-equilibrium compositions of the resultant microstructure. During the solidification, positive segregation elements, such as Mo and Nb, are prone to be rejected into the interdendritic residual liquid, resulting from the small partition coefficient (k) associated with these positive segregation elements ($k < 1$) [162]. As a result, inhomogeneous elemental distributions become a concern, primarily because they can induce the formation of intermetallic phases and precipitates, which are observed to be concentrated in the interdendritic areas.

Kindermann et al. [163] investigated the solidification sequence of the non-equilibrium phases of Inconel 718, showing that the exact temperatures of the precipitation in this

alloy are kinetically dependent on the solidification conditions and alloy compositions. Accordingly, TiN nitride precipitates from the liquid firstly, as its precipitation temperature is above the liquidus, then NbC carbide precipitates at 1265 - 1280 °C, and subsequently Laves phase forms at a lower temperature range from 1075 - 1160 °C. Furthermore, γ″ precipitates form in the range of 700 - 900 °C and γ' in the range of 600 - 700 °C, with δ phase in the range of 870 - 1010 °C.

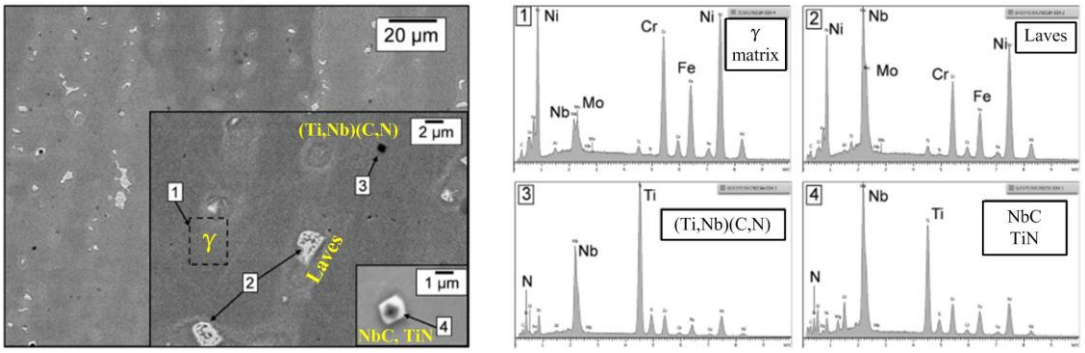

Fig. 2.7 Microstructure of as-deposited WAAM Inconel 718 observed by backscatter electron SEM; and the corresponding Energy Dispersive X-ray Spectroscopy (EDS) analysis of different phase constitutions [149]

The MC carbide precipitation is commonly observed in all AM fabricated Inconel 718, due to rapid solidification process. Fig. 2.7 shows the common precipitates present in the WAAM-produced Inconel 718 under backscattered electron scanning electron microscopy (SEM) observation [149]. The MC precipitates usually include the Nb rich MC carbide, in a cubic shape, showing the bright contrast for heavy elements in Fig. 2.7. As TiN precipitates first when the N content is over 40 ppm, these particles can act as the nucleation site for NbC carbide precipitation, with a dark colour in Fig. 2.7. The NbC carbides can be distributed intragranularly or at the grain boundaries. Their sizes are reported to be below 100 nm in SLM-produced alloy, but can reach up to ~ 1 μm in WAAM-produced alloy due to high heat input and in EBM-produced counterpart applying the substrate preheating and a high power density [149, 164, 165]. The NbC

particles distributed in the interdendritic regions probably result in weakly anisotropic tensile properties [149].

Additionally, Laves phase has a similar light colour with the NbC carbide, as seen in the backscattered image in Fig. 2.7, but it possesses a eutectic script-like morphology, and is distributed at the interdendritic regions and cellular boundaries [14]. Due to the brittle nature of the Laves phase, it often causes the deterioration in strength and ductility of the material, with a composition of $(Ni,Fe,Cr)_2(Nb,Ti,Mo)$. Seow et al. [149] reported that the formation of the Laves phase is driven by Nb elemental segregation, and the relatively high heat input and low cooling rate during WAAM leads to the precipitation of coarse Laves phase particles, whereas the fine Laves phase generally forms in laser and electron-based AM processes. Moreover, Wang et al. [160] found that the sizes of Laves phase regions show a significant variation at different areas of the WAAM deposited Inconel 718 thin-wall component, with the largest precipitates of an average size of ~ 9.43 μm observed in the middle areas, where the alloy experiences a more complex thermal cycling. Kindermann et al. [163] reported that the most refined Laves phase regions occur under the low heat input condition using a relatively high travelling speed during the Cold Metal Transfer (CMT) based WAAM, which is a type of GMAW-based WAAM. This finding was obtained through the microstructural inspection of alloys prepared at four travelling speeds from 0.2 to 0.8 m/min, as shown in Fig. 2.8. Hence, the AM processing applying low heat input and increased cooling rate is considered to be a promising strategy to refine the Laves phase. This is consistent with results obtained using laser-based processes, where the size of the Laves phase regions varies in the range of approximately 100 - 300 nm [164, 166], much smaller than that formed in WAAM. Goel et al. [148] reported that there was no Laves phase present in Inconel 718 alloy produced by EBM under as-deposited conditions involving

pre-heating of the substrate to 1025 °C. However, this operation led to the formation of the δ phase.

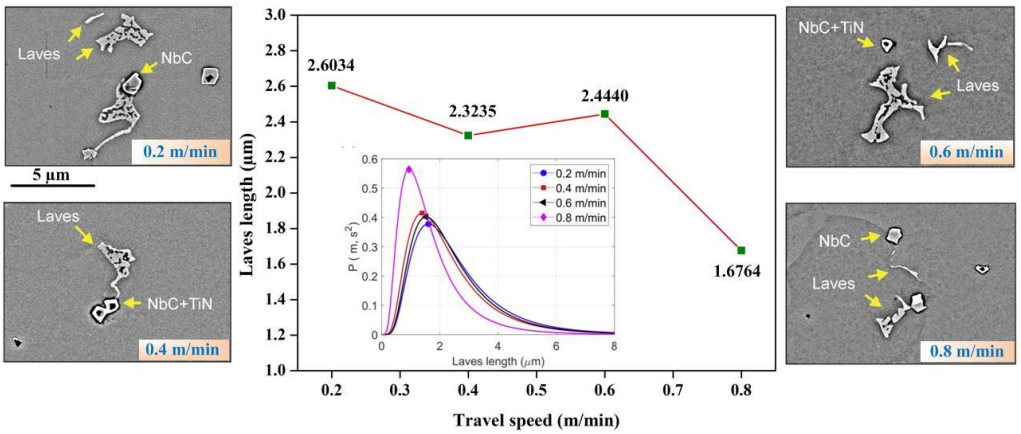

Fig. 2.8 Microstructural response of Laves phase in Inconel 718 by CMT-based WAAM, with increasing travelling speed from 0.2m/min, 0.4 m/min, 0.6 m/min to 0.8 m/min [163].

Note that the δ phase is usually undesirable due to its adverse influence on the mechanical properties [167, 168]. However, the effects of intermetallic δ phase on mechanical properties are strongly dependent on its size and amount in the alloys. For example, Deng et al. [165] reported that there appears to be no direct connection between the reduction of ductility and δ phase formation in the as-deposited Inconel 718 alloy by EBM. Nevertheless, the effect of δ phase on the mechanical properties was possibly overemphasized, as the amount was reported to be very little in that work. The needle-like δ-Ni_3(Nb, Ti) phase is usually observed under a heat treatment condition involving the dissolution of the Laves phase, or transformation of metastable γ″ to thermodynamically stable δ phase. Alternatively, δ phase forms through heterogeneous nucleation at the grain boundaries [148]. It was also reported the δ phase formed at the grain boundaries in the as-deposited alloys produced by either laser or electron beam-based AM processes [165, 167]. However, it is noticeable that in both studies reported in Ref. [165, 167], the substrate was preheated to over 1000 °C, and the formation of δ

phase is attributed to the elongated heat exposure involving multiple thermal cycles during manufacturing. δ phase can be enlarged from less than 100 nm under the as-deposited condition to 500 nm with low-temperature solution heat treatment, or be completely removed by high-temperature solution heat treatment [165].

Sui et al. [169] reported that the nanosized γ'' phase is the main strengthening phase of Inconel 718, which is generally accepted as comprising Ni_3Nb. Therefore, Nb content in the alloy highly influences the size and distribution of the γ'' phase in the as-deposited condition. Similarly, Al and Ti contents affect the content and the size of γ', usually confirmed as Ni_3(Al, Ti), which is regarded as an assistant strengthening phase, often in the nanoscale between 10 to 40 nm in the as-deposited state. The relatively rapid solidification and thermal cycling during the single bead AM processes are generally insufficient for the precipitation of γ'' and γ' [163]. Similar conditions for the formation of δ phase, γ'' and γ' occur under PHT of interdendritic areas with high elemental segregation, nevertheless these precipitates were also found in the pre-heated substrate condition in the work of Deng et al. [165].

The solidification of Inconel 625 starts from the primary liquid → γ- matrix transformation, which is often associated with the segregation of Nb, Mo, C and Ti elements in the interdendritic regions and at the grain boundaries. Then the subsequent liquid → γ + NbC eutectic reaction occurs in the remaining liquid to consume the carbon until the initiation of other transformations of L → γ + Laves → γ + Laves+ δ [170]. MC carbides (including NbC and TiC), δ-Ni_3Nb and Laves phase are widely found in AM-fabricated Inconel 625, which is linked to microsegregation, across the interdendritic and grain boundary areas [13, 44, 171]. Fig. 2.9 shows the typical microstructural response to Laves phase, MC carbide, and δ-Ni_3Nb of WAAM

fabricated Inconel 625 by different observing techniques [170]. It is worth mentioning that, being different from Inconel 718, δ-Ni_3Nb phase was found in the as-deposited Inconel 625 alloy without preheating the substrate in WAAM [170]. The needle-like δ phase was reported to grow along the edge of Laves phase in layers interface regions of the as-deposited component, and a significant quantity of δ phase interconnected with Laves phase at the top part, whereas no δ phase at the bottom part (See Fig. 2.9). In contrast, δ were rarely observed in the as-deposited Inconel 625 manufactured by laser- or electron beam-based AM processes. In particular, the formation of δ phase requires a relatively slow cooling rate, high heat input and heat accumulation as in WAAM [168, 172]. The high cooling rates associated with the laser-based processes limit the segregation of solute elements, hence hindering the formation of the δ phase.

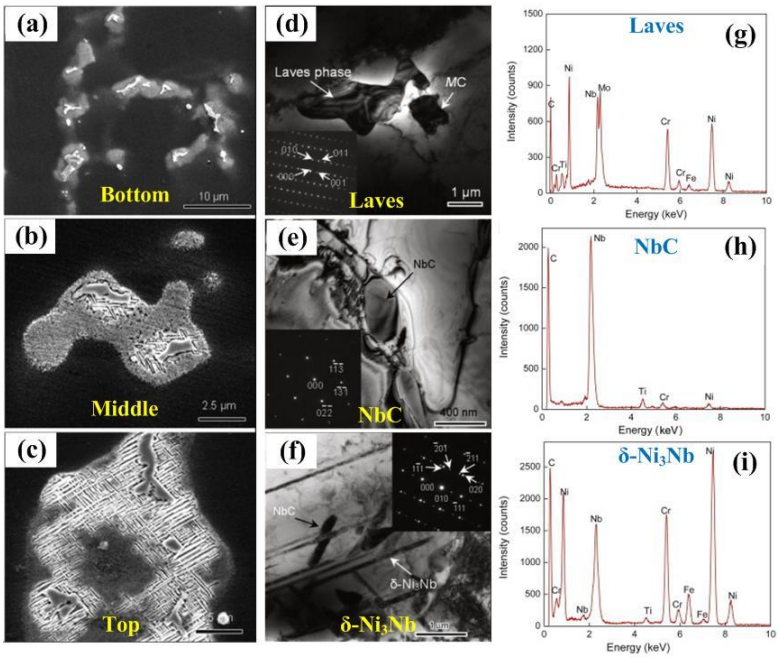

Fig. 2.9. Microstructural response of precipitates of Inconel 625 by WAAM: (a-c) Optical micrograph showing precipitates in (a) bottom; (b) layers interface; (c) top region; and (d-i) Bright field (BF) images of precipitates Laves, NbC, and δ-Ni_3Nb and their corresponding selected area diffraction (SAD) pattern (a), and the EDS spectrum: (d) and (g) Laves phase; (e) and (h) NbC; (f) and (i) δ-Ni_3Nb. Reproduced with permission from Elsevier [170].

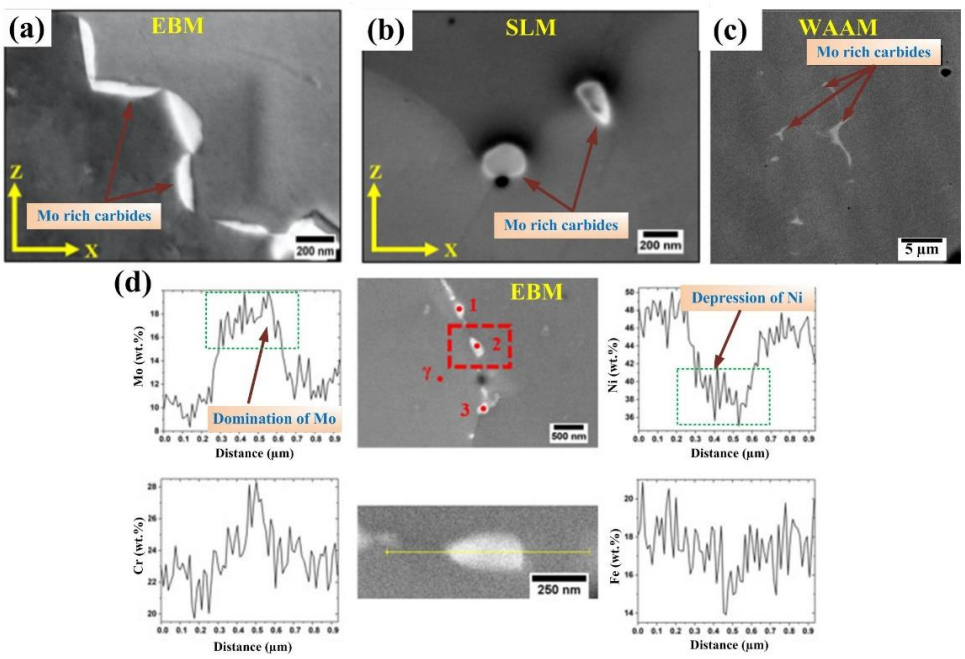

Fig. 2.10 SEM micrographs of carbides in the as-deposited Hastelloy X manufactured by: (a) EBM; (b) SLM. Reproduced with permission from Elsevier [145]; and (c)WAAM. Reproduced with permission from Elsevier [173]. (d) EDS line scan results showing variation in the concentrations of Mo, Cr, Ni and Fe elements across a precipitate (indicated by a red box) in the grain boundary of the as-deposited Hastelloy X sample using EBM. Reproduced with permission from Elsevier [145].

Hastelloy X is a solid solution strengthened alloy with modest strength, which has no γ' or γ'' precipitation [174]. Although the possible secondary phases, including the carbides (M_6C, $M_{23}C_6$), σ, and μ phases, may form in Hastelloy X, carbides are the only precipitates in the γ matrix of this alloy by AM without a long time of ageing, as shown in Fig. 2.10. Despite their strengthening effect, these carbide precipitates adversely lower the ductility of this alloy [51, 175]. Kong et al. [176] found the precipitation of a large amount of nano-sized Mo-rich M_6C carbides in the subgrain boundaries in the SLM-produced Hastelloy X, which is facilitated by the segregation during the repetitive thermal cycling in the AM. These nano-sized carbides enable strengthening via the pinning effect to keep grain boundaries from sliding. These M_6C carbides in the alloy by SLM are much smaller than those in the LMD-produced counterpart [146]. Karapuzha et al. found the Mo-rich M_6C and Cr-rich $M_{23}C_6$ carbides in the EBM

fabricated alloy with preheating of the substrate to 750 °C [145]. Dinovitzer et al. [173] observed Mo-rich carbides (Fig. 2.10c) in the form of intragranular precipitates in WAAM fabricated Hastelloy X. The carbides could be enlarged compared to the initially formed ones, in response to the thermal cycling during AM, resulting in a slow cooling rate for the carbide growth.

2.3.4 Microstructural evolution under post-heat treatment (PHT) conditions

PHTs are common approaches to improve the performance of AM-fabricated Ni-based alloys, which can be classified into stress relieving, solution annealing, homogenisation annealing, and/or ageing for particular purposes [166]. A solution annealing treatment at 980 °C usually accelerates initial recrystallisation of Ni-based alloys, while complete recrystallisation normally occurs under high-temperature (over 1000 °C) homogenisation annealing treatments [177]. Moreover, these over 1000 °C high-temperature annealing enables the elimination of dendrites in laser-fabricated alloys, but the texture, grain size, and grain morphology in these alloys witnessed no significant variation by this treatment [174, 175]. The formation of dendrites under the as-deposited condition is associated with elemental segregation [178]. However, more research efforts are recommended for a complete understanding of the chemical segregation behaviour in the previous research in response to homogenisation annealing.

PHT for Inconel 718 is usually performed to homogenise microsegregation and dissolve undesirable Laves and δ phases, further forming strengthening γ' and γ'' phases during subsequent aging. Solution annealing at 980 °C followed by double ageing at 720 °C for 8 h + 620 °C for 8 h was used to dissolve the Laves phase in wrought Inconel 718 [179]. However, Tucho et al. [164] reported that annealing under 1100 °C for 1 h was

not enough to dissolve the Laves phase and other precipitates formed in SLM-produced Inconel 718. Solution annealing at 980 °C of this alloy often leads to the local enrichment of Nb elements and promotes the formation of δ phase if not performing additional homogenisation heat treatment. Gallmeyer et al. [166] found the PHT at above 1100 °C would lead to recrystallisation and coarsening of γ-matrix grains and carbides. Hence, they applied solution annealing at 1020 °C for 15 min to dissolve the undesired Laves phase in Inconel 718 by SLM and then ageing at 720 °C for 24 h to eliminate Laves and δ phases. When the homogenisation and solution annealing are performed first, elemental segregation can be minimized and subsequent ageing are normally conducted to form strengthening γ' and γ" phases. Note that following annealing treatments, the samples should be quickly cooled down to below 720 °C to minimize the δ phase formation. However, Seow et al. [149] found the aforementioned PHT approaches still could cause the formation of δ phase at the grain boundaries in WAAM fabricated alloy, and they suggested the homogenisation temperature and time up to 1186 °C for 40 mins, above the Laves phase eutectic temperature of 1185 °C in the WAAM produced Inconel 718. This was followed by air cooling then double ageing to successfully remove Laves and δ phases. Based on the findings in AM fabricated Inconel 718, PHT methods appliable for Ni-based alloys produced by traditional manufacturing processes might not be effective for AM-fabricated alloys. It is recommened that complete homogenisation followed by fast cooling and aging to optimise performance of the component through formation of finely dispersed γ' and γ" phases and elimination of undesirable intermetallics.

In addition to the solid solution strengthening, the γ″ precipitates formed after proper PHT provide further strengthening of Inconel 625. Fig. 2.11 shows the microstructure of SLM-produced Inconel 625 after solution annealing and ageing treatments.

Marchese et al. [180] reported the increased tensile strength due to the newly formed γ" phase mostly at grain boundaries of SLM-produced Inconel 625 after ageing at 700 °C for 24 h followed by water quenching. The size of these γ" particles was ranging from ~ 10 to 30 nm. In terms of carbides, it is difficult to dissolve them into matrix by annealing below 1200 °C. Marchese et al. [177] reported that the annealing of Inconel 625 by SLM at 1150 °C for 2 h, followed by water quenching produced fine sub-micrometric carbides. Li et al. [181] observed the formation of γ″ phase and coarse carbides in SLM-produced Inconel 625 after solution annealing at 1150 °C for 1 h followed by furnace cooling. This difference in the precipitation can be attributed to the applied PHT conditions, and especially the cooling rate has significant effects on the carbides and γ″phase formation. High temperature annealed (1150 °C) Inconel 625 alloys exhibited a lower strength, attributed to the occurrence of recrystallisation and grain growth. Solution annealing at 980 °C for 1 h with water quenching can also cause the coarsening of carbides in this alloy by SLM, while δ phase can be formed at the grain boundaries and in the interdendritic areas of SLM prepared alloy after the stress-relief annealing at 870 °C for 1 h [177]. In contrast to SLM-processed Inconel 625, δ phase was formed after annealing at 980 °C for 30 min in the WAAM-fabricated alloy, and the size of both carbide and δ phase increased with the increases of PHT time [13]. The above results demonstrate that proper PHT routines need to be defined for the Ni-based alloys produced by various AM processes to induce the desired precipitates and eliminate detrimental ones.

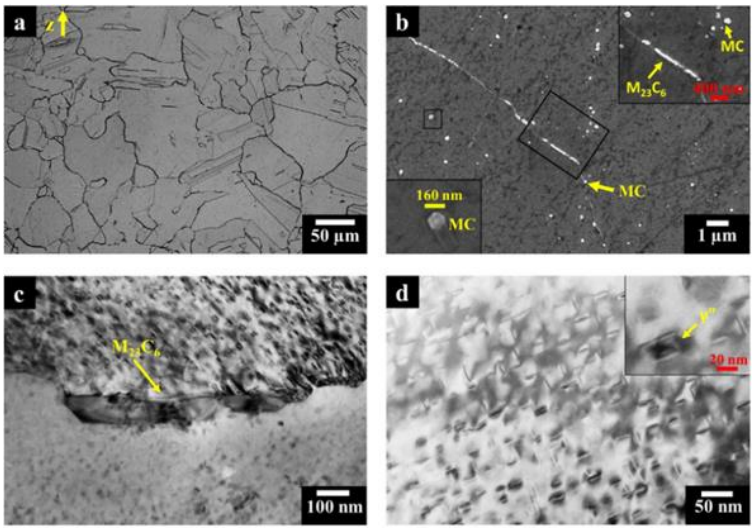

Fig. 2.11 Microstructure of Inconel 625 samples after solution-annealing and ageing treatments: (a) optical micrograph showing equiaxed grains as well as twins and intergranular carbides; (b) SEM image exhibiting fine elongated Cr-rich $M_{23}C_6$ and Nb-rich MC carbides at the grain boundaries and intragranular Nb-rich MC carbides; (c, d) TEM bright-field images showing the precipitation of intergranular Cr-rich $M_{23}C_6$ carbide and γ″ phase, respectively. Reproduced with permission from Elsevier [180].

As the predominant strengthening mechanism of Hastelloy X is associated with the contribution of alloying elements in solid solution, a solution annealing heat treatment is recommended for this alloy to dissolve large precipitates. Zhang et al. [146] reported that carbides still existed in LMD-produced Hastelloy X after the solution annealing at 1177 °C for 1 h followed by water quenching. In contrast, in the report by Montero-Sistiaga et al. [175], the carbides were effectively removed in the SLM-manufactured Hastelloy X after solution annealing at the same temperature for 2 h, then cooled down in an argon atmosphere at a rapid rate of 40 °C/min. Hence, sufficient solution annealing is required to allow the complete dissolution of carbides into the matrix of Hastelloy X. Montero-Sistiaga et al. [175] also studied microstructural response in the SLM-fabricated Hastelloy X after PHT at 800 °C for 2 h with argon cooling at a rate of 40 °C/min. They found $M_{23}C_6$ and M_6C carbides at intergranular and transgranular regions, but no changes were observed in the matrix grain size and morphology. Additionally,

another Mo-rich phase (presumably the intermetallic μ phase) was formed after this PHT. Given that this brittle intermetallic μ precipitate may deteriorate the ductility of the alloy, the PHT at 800 °C for 2 h is not recommended in this review work. However, to the best of the author's knowledge, no research work on the influence of PHTs on the precipitation behaviour in the WAAM-produced Hastelloy X alloy has been reported by the time of this review.

2.3.5 Tensile properties at room temperature and creep resistance

To promote the applications of Ni-based alloys produced by advanced AM, it is important to achieve AM-fabricated components with comparable or superior properties relative to the commercial counterparts produced by traditional manufacturing processes. This section will summarise the mechanical properties, including tensile strengths at room temperature, and high temperature creep resistance of the reviewed alloys.

2.3.5.1 Tensile properties

Tables 2.7 to 2.9 summarise yield strength (YS), ultimate tensile strength (UTS) and total elongation (TE) of the three Ni-based alloys prepared by different AM and conventional manufacturing processes. Results for as-deposited and heat-treated conditions by AM are described from vertical (V) direction and horizontal (H) direction at room temperature. They are compared with the results for these alloys prepared by traditional processes. Fig.2.12 further presents the comparison of the YS of these alloys under different processes. Generally, the tensile properties of AM fabricated Ni-based alloys are comparable with those of alloys prepared by traditional casting processes (see Table 2.7 - 2.9), and the refined microstructures and increased dissolution of solute elements are considered to enable significant increases in mechanical properties

through PHTs. Compared with as-deposited alloys by WAAM, the alloys prepared by laser-based processes generally show higher tensile strengths. This is largely attributed to a refined microstructure of the alloys manufactured using laser-based processing. Furthermore, the EBM offers advantages of in-situ precipitation strengthening and residual stress minimising through effects associated with preheating of the substrate [179].

Anisotropies in the mechanical performance are expected in as-deposited alloys (see Tables 2.7 - 2.9), and these result in higher ductilities and lower strengths of the samples along the vertical deposition direction compared with those along the horizontal direction. The UTS and YS in the vertical direction can be about 60 MPa lower than those in the horizontal direction, while the ductility shows an opposite trend, with the value along the vertical direction being 5% higher than that in the horizontal direction. Overall, such anisotropy can be attributed to the strong <001> texture and columnar grain morphologies produced in the FCC structures matrix of Ni-based alloys [149, 177, 182]. However, the opposite tendency of directional mechanical property is found in some of the laser and electron beam-based processes, such as in Ref. [183], where the horizontal direction is shown to have lower strength. This was attributed to the entrapped stringer porosity that is aligned to the columnar grain boundaries, resulting in the lowering of strength [183]. Salarian et al. [184] reported that the frequency, size, morphology, and orientation of pores are closely related to the UTS in SLM produced Inconel 625, whereas the general bulk porosity level has no direct relationship to the tensile strength. The tensile properties were also studied at different heights along the deposition direction. The strength in the bottom part is usually higher in the SLM, LMD, and WAAM fabricated Ni-based alloys, because of the finer columnar dendrite size, induced by the higher cooling rate from the substrate for the first several layers, and the

increased amount of thermal cycling induced precipitates at the bottom part. However, the EBM process showed a different tendency, with the strength increasing with the increased distance from the bottom. This was attributed to coarsening of strengthening phases, such as the γ″ phase, and the increased amounts of δ phase induced by preheating of the substrate, as discussed above.

The tensile properties of AM fabricated Ni-based alloys are quite sensitive to the cooling rate of the deposition. For instance, Xu et al. [156] reported that the WAAM fabricated Inconel 718 exhibited a higher ductility but lower tensile strength compared with the counterpart produced by laser-based AM processes. This was attributed to the formation of large columnar grains under a slow cooling rate during the WAAM. Compared with the columnar grain size, the typical epitaxial dendrites with/without secondary and tertiary dendrites play a more critical role in affecting the mechanical properties of Ni-based alloys. Marchese et al. [180] reported that the fine dendritic microstructure resulting from fast solidification in SLM process contributed to the high mechanical properties of Inconel 625 alloy. Furthermore, precipitation can significantly define the strength of the manufactured alloys. Karapuzha et al. [145] studied the SLM and EBM fabricated Hastelloy X alloy, respectively. The carbides were reported to be formed along the alloy's grain boundaries by EBM due to the higher bed temperature and slower cooling rate in this process, compared to SLM, which leads to a lower ductility [175]. The cooling rate during deposition processes affects many aspects of microstructural development including the matrix grain size, dendrite formation, solute segregation, texture evolution, amount of precipitates, and size distribution of precipitates, and all of these can influence the mechanical properties of the fabricated alloys by AM.

As shown in Tables 2.7 - 2.9 and Fig. 2.12, the as-deposited alloys have relatively lower tensile strengths, but higher ductilities. Hence, proper PHTs are performed to alter the tensile properties of as-deposited Ni-based alloys. Among all of the PHT conditions, those alloys which are directly aged, usually display dramatically increased UTS and YS, yet suffer from a sacrifice in ductility. An example is the Inconel 625 in Ref. [180], where increases in strength and concurrent decreases in ductility are attributed to the formation of elongated $M_{23}C_6$ precipitates along the grains boundaries and fine γ″ phases. Ageing can result in precipitation strengthening, but not coarsening of the columnar grains. Annealing can lead to solution strengthening, however it can result in recrystallisation of the grains, at the expense of tensile strength. Gallmayer et al. [166] reported the formation of monolithic γ″ (31 ± 8 nm) and γ′ (21 ± 7 nm) but a few, relatively large monolithic γ″ precipitates (210 ± 50 nm) with remaining Laves phase in the directly aged alloy, while dense, homogeneously distributed nanoprecipitation γ″ (29 ± 7 nm) and γ′ (23 ± 4 nm) formed under solution annealing and ageing conditions in SLM fabricated Inconel 718. The latter contributed to an increase of the UTS to over 300 MPa higher than that of the as-deposited condition, with much less loss of ductility than the directly aged alloy. As seen in Tables 2.7 - 2.9, in comparison with the as-deposited condition, the anisotropy in tensile properties is significantly decreased with high-temperature annealing or with interlayer rolling due to the formation of equiaxed grains. However, the effect on anisotopy in tensile properties by the direct ageing and stress relieving conditions appear to be insignificant.

Table. 2.7 Mechanical properties of Inconel 718 under different conditions.

Process	Condition	UTS （MPa）	YS (MPa)	TE (%)	Ref
Forge	-	1275	1030	19.1- 20.6	[185]
Casting	-	909	651	10.3	[185]
Wrought	-	1276	1034	12	[156]
SLM	AD H	938 ± 10 - 1055 ± 5	692 ± 29 - 775 ± 10	16.4 ± 2.3 - 29.5 ± 1.1	[185]

	AD	-	1335	760	21.3	[166]
	AD (pulsed laser)	H	1070.5 ± 11.6	754.3 ± 4.4	20.5 ± 0.8	[38]
	AD (pulsed laser)	V	1018.9 ± 0.8	659.4 ± 19.2	23.9 ± 0.5	[38]
	AD	V	904 ± 22	572 ± 44	19 ± 4	[186]
	AD	H	991 ± 62	643 ± 63	13 ± 6	[186]
	SA	-	1325	620	21.3	[166]
	SA + A	-	1640	1245	16.6	[166]
	A	-	1580	1300	9.6	[166]
	SA	V	1320 ± 6	1074 ± 42	19 ± 2	[186]
	SA	H	1377 ± 66	1159 ± 32	8 ± 6	[186]
DMD	AD	-	847	525	29	[157]
	AD	-	904	552	16.2	[187]
	HIP + SA	-	1301	1120	18	[157]
	SA	-	1221	1007	16	[187]
	A	-	1333	1084	8.4	[187]
	HIP + SA + A	-	1194	949	19.9	[187]
EBM	AD	-	455.4 ± 6.1~ 1300.6 ± 22.5	443.5 ± 16.4 ~1122.3 ± 17.4	4.3 ± 0.2 ~ 31.5 ± 4.3	[140]
	AD	V	1138 ± 24	925 ± 20	15.7 ± 4.3	[183]
	AD	H	1061 ± 83	894 ± 24	11.5 ± 6.9	[183]
	AD	V	1060 ± 26	822 ± 25	22	[188]
	AD	H	929 ± 25	744 ± 44	5.5	[188]
	HIP + SA + A	V	1266 ± 44	1061 ± 16	21.1 ± 1.1	[183]
	HIP + SA + A	H	1240 ± 19	1035 ± 17	21.8 ± 2.4	[183]
WAAM	AD	H	818 ± 13	525 ± 7	33.3 ± 2.5	[15]
	AD	V	756 ± 7	506 ± 2	27.9 ± 1.3	[15]
	AD (Interpass rolling)	H	1082 ± 13	763 ± 8	26.2 ± 2.2	[15]
	AD (Interpass rolling)	V	1072 ± 6	687 ± 1	26.6 ± 1.3	[15]
	AD	H	824 ± 15	514 ± 17	34.0 ± 0	[156]
	AD	V	832	416	30.9	[156]
	AD	H	872 ± 31	563 ± 14	34 ± 3	[160]
	SA + DA	H	1152 ± 28	864 ± 21	23 ± 2	[160]
	SA	H	763 ± 32	384 ± 8	24.4 ± 3.7	[15]
	SA	V	693 ± 0	384 ± 11	32.5 ± 3.0	[15]
	SA + A (Interpass rolling)	H	1348 ± 10	1057 ± 19	15.1 ± 3.3	[15]
	SA + A (Interpass rolling)	V	1356 ± 10	1035 ± 20	17.4 ± 1.1	[15]
	SA + A	H	1110 ± 3	807 ± 1	15.5 ± 0.3	[156]
	SA + A	V	1233 ± 16	889 ± 5	19.4 ± 2.8	[156]

* AD - As-deposit; SA - solution annealing; A - aging; DA - double aging; H - Horizontal; V - vertical

Table. 2.8 Mechanical properties of Inconel 625 under different conditions.

Process	Condition		UTS （MPa）	YS (MPa)	TE (%)	Ref
Casting	-		710	350	48	[170]
Wrought	grade 1		>827	>414	>30	[177]
Wrought	grade 2		>690	>276	>30	[177]
As-rolled	-		827 - 1103	758 - 414	60 - 30	[177]
SLM	AD	V	891 ± 5	618 ± 33	40.7 ± 0.5	[177]
	AD	H	1041 ± 36	783 ± 23	33 ± 1	[180]
	AD	H	925 ± 13	652 ± 10	32 ± 3	[151]
	SA	H	869 ± 7	567 ± 15	38 ± 1	[151]
	SA	H	886 ± 11	409 ± 14	56 ± 5	[151]
	A	H	1222 ± 56	1012 ± 54	23 ± 1	[180]
	SA	H	883 ± 15	396 ± 9	55 ± 1	[180]
	SA + A	H	1116 ± 6	722 ± 7	35 ± 5	[180]
	SR (870 °C, 1 h)	V	900 ± 2	621 ± 7	40.9 ± 1.7	[177]
	SR (870 °C, 1 h)	H	996 ± 3	667 ± 3	35.8 ± 1.8	[177]
	SA (980 °C, 1 h)	V	854 ± 4	579 ± 5	47.6 ± 0.6	[177]
	SA (980 °C, 1 h)	H	948 ± 8	612 ± 5	39.8 ± 0.5	[177]
	SA (1080 °C, 1 h)	V	867 ± 2	430 ± 6	52.8 ± 0.3	[177]
	SA (1080 °C, 1 h)	H	896 ± 1	451 ± 1	50.9 ± 1.5	[177]
	SA (1150 °C, 2 h)	V	851 ± 3	379 ± 9	54.5 ± 1.1	[177]
	SA (1150 °C, 2 h)	H	883 ± 15	396 ± 9	54.9 ± 1.2	[177]
LMD	AD	H	733.7	500.41	29.4	[158]
	AD	H	1000 ± 10	656 ± 14	24 ± 5	[189]
	AD	V	882 ± 7	480 ± 20	36 ± 5	[189]
	AD	H	1073 ± 5	723 ± 23	26 ± 2	[151]
	SA	H	1084 ± 2	654 ± 15	27 ± 2	[151]
	SA	H	991 ± 13	532 ± 22	43 ± 1	[151]
EBM	AD	-	750	410	44	[190]
	HIP	-	770	330	69	[190]
WAAM	AD	H	695 ± 11	384 ± 7	46.4 ± 1	[191]
	AD (+ magnetic field)	H	740 ± 14	436 ± 13	48.7 ± 1.9	[191]
	AD	V	658 ± 4	373 ± 5	56 ± 4	[192]
	SA (980 °C, 0.5 h)	V	669 ± 7	363 ± 10	48 ± 2	[192]
	SA (980 °C, 1 h)	V	672 ± 8	360 ± 11	43 ± 1	[192]
	SA (980 °C, 2 h)	V	688 ± 4	397 ± 15	46 ± 3	[192]
	AD	-	687 MPa	400 MPa	46.5	[161]

Table. 2.9 Mechanical properties of Hastelloy X under different conditions.

Process	Condition		UTS （MPa）	YS (MPa)	TE (%)	Ref
Wrought			760	340	49	[193]
SLM	AD	H	970 ± 14	785 ± 18	14 ± 2	[194]
	AD	V	620 ± 15	480 ± 10	40 ± 1	[195]
	AD	V	826 ± 32	615 ± 4	38%	[145]
	AD	H	876 ± 2	693 ± 8	33 ± 1	[153]
	AD	V	648 ± 13	730 ± 6	49 ± 8	[153]
	AD	-	821	617	54	[193]
	HIP	V	560 ± 9	350 ± 6	41 ± 4	[195]
	SA (1177 °C)	-	793	455	52	[193]
	SA (1066 °C + 1177 °C)	-	765	455	46	[193]
LMD	AD	V	367 ± 6	628 ± 4	66 ± 3	[196]
EBM	AD	V	~ 600	300 ± 16	60%	[145]

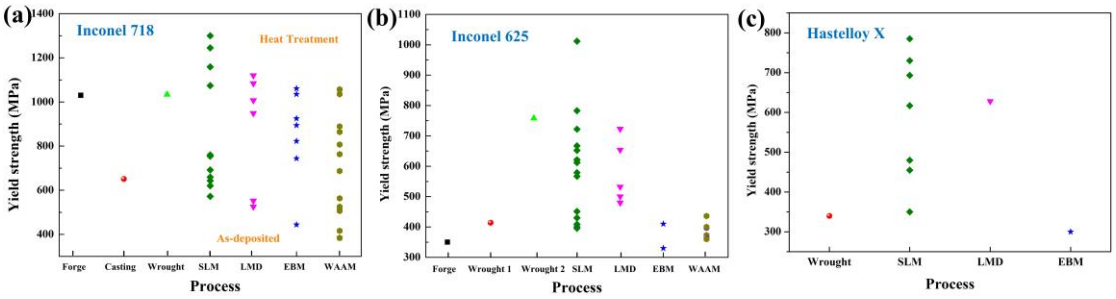

Fig. 2.12 Comparison of yield strength of Inconel 718, Inconel 625 and Hastelloy X under different manufacturing processes based on Table 2.7 - 2.9. The tensile properties were increased after post-heat treatments.

2.3.5.2 Creep properties

The creep resistance of Inconel 625 and Inconel 718 by laser and electron beam-based AM processes were both well explored in the previous studies [197-201]. However, there appears to have been no published research on creep resistance of AM fabricated Hastelloy X. Ni-based alloys usually exhibit good high-temperature creep resistance, and the AM fabricated alloys are widely reported to show comparative or superior creep properties than the cast and wrought alloys; particularly alloys fabricated by AM under a PHT state (see Fig. 2.13 [179, 198]). The specific microstructures induced from the AM processes and the PHT operations contribute to a considerable increase in the creep resistance of these alloys.

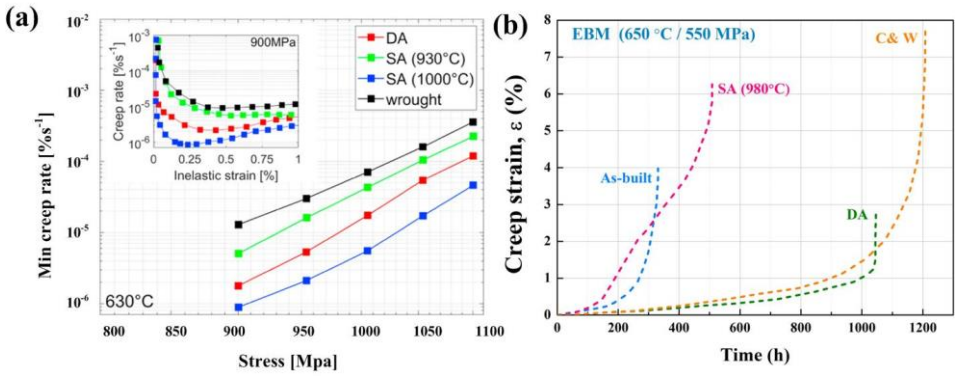

Fig. 2.13 (a) Compressive creep rate for Inconel 718 by SLM at 630 °C under different heat treatment conditions. Reproduced with permission from Elsevier [179]; (b) Creep curves of Inconel 718 by EBM at 650 °C under different heat treatment conditions [198]; (DA: Direct aging, SA: solution annealing + aging)

Pröbstle et al. [199] reported an improved compressive creep strength of as-deposited Inconel 718 prepared by SLM compared with cast and wrought alloy. This was attributed to the formation of a large number of subgrains. Im et al. [200] reported that EBM fabricated Inconel 718 with different focus offsets, exhibited a strong <001> texture under an as-deposited state, and showed a longer creep rupture time than that of conventional forged Inconel 718 subjected to full heat treatment. The strong <001> texture from AM contributes to the enhancement of creep under loading parallel to the building direction, explaining why creep anisotropy can be found in AM fabricated Ni-based alloys [202]. Being different from room temperature tensile properties, the coarse columnar grains with fewer grain boundaries enable the benefit of creep life, as the grain boundary areas can accelerate diffusion and sliding, and generally accumulate damage at high temperatures [179]. Kuo et al. [198] compared the as-deposited Inconel 718 by EBM and SLM, and found the EBM fabricated alloy exhibited higher creep properties due to the relatively larger grain size and lower dislocation density. Moreover, comparing these two processes (EBM and SLM), the involvement of preheating of the substrate in EBM, results in lower residual stresses and conditions which stimulate the formation of strengthening γ" phase. The creep resistance of these

three Ni-based alloys fabricated by WAAM is yet to be explored, as they usually possess large columnar grains, a high possibility of residual stress build-up and the presence of large-sized precipitates.

The creep performance of Ni-based alloys can be enhanced by the PHTs, as the Nb rich δ phase or Laves phase in Inconel 625 and Inconel 718 by AM can be eliminated under PHTs, and the released Nb can act as solution strengthening element or promote the formation of the strengthening γ" and γ' phases to optimise the creep properties [158, 160, 200, 203, 204]. It's worth mentioning the effect of δ phase, as very fine-sized δ phases can enhance creep properties through pinning grain boundaries [205]. However, Probestle et al. [199] reported that a higher creep strength can be obtained with an absence of δ phase in SLM fabricated Inconel 718 after annealing, as δ phase can consume Nb during the formation of strengthening γ", hence reducing the amount of γ" phase. In their experimental results, the higher γ" phase volume fraction in Inconel 718 by SLM was reported to contribute to the superior creep strength after the 1000 °C solution annealing due to the absence of Nb consuming δ and Laves phase particles [199]. This is because that the γ" particles can effectively prevent the motion of dislocations to lead to higher creep resistance. The PHTs, as aforementioned, especially the high-temperature annealing will allow recrystallisation and grain growth, which will also decrease grain boundaries and accommodate more dislocations before creep rupture. In addition to PHTs involving thermal cycling, hot isostatic pressing (HIPing) has also been reported [206]. HIPing of Inconel alloys has been shown to contribute to increased creep properties, via the product with lower porosity, increased strengthening phases, and larger and more uniform grains. Son et al. [206] found increased creep ductility in Inconel 625 produced by LMD and HIPing, and this was attributed to the formation of strengthening γ" phase and less porosity.

However, AM processes have drawbacks which affect creep properties, including porosity and impurity phases. Creep is quite sensitive to the porosity in the tested samples, as the pores will cause premature failure under high temperatures [188]. Moreover, Son et al. [207] reported that the creep ductility of Inconel 625 by SLM under as-deposited conditions is much lower than that by wrought. This was attributed to the high content of impurities in the as-supplied powder with high levels of oxygen and sulphur. Hosseini et al. [179] also mentioned that the powder quality can highly determine the porosity of the fabricated alloys, hence, the creep life can be significantly influenced by the powder quality.

2.3.6 Challenges and defects associated with AM of Ni-based components

Despite the high effectiveness witnessed in AM processes, and the comparative properties of AM fabricated components relative to those prepared via conventional casting processes, there are inherent problems associated with AM of Ni-based alloys which have to be evaluated and addressed. For example, surface finish is an extensive problem that can be controlled by optimising process parameters to a large extent, such as control of overflow and decrease of heat input [208]. However, Liu et al. [209] reported that nearly all components by AM require post-machining to improve their surface accuracy. The following section describes the most common currently-recognised structural defects resulting from the AM of Ni-based alloy components and the associated challenges to achieving AM-produced materials and components of high quality and performance.

Above all, the associated residual stress in the AM-produced components is a critical challenge related to the high temperature gradients and complex thermal histories during the AM processes. These can cause component distortion and often adversely

influences the mechanical properties of AM fabricated Ni-based alloys [179]. The previous deposition layers constrain the free expansion of the next layer, and large compressive plastic deformation results at high temperatures in the newly deposited layer during the solidification. With cooling of the new deposition layer, shrinkage and residual tensile stress in the new deposition will be retained in the layer. Residual stress is significantly influenced by a number of processing parameters, such as heat source power, travelling speed, scan strategy, etc. [144]. Note that although the EBM utilises relatively high power density and induces a high temperature gradient, the pre-heating of the substrate significantly decreases the temperature gradient in the following deposition, hence reducing the residual stress. Goel et al. [210] reported that EBM-produced Inconel 718 had lower residual stress than that by the SLM, as measured by neutron diffraction. A PHT is usually performed to relieve the residual stress, nevertheless, Wang et al. [211] reported that the PHT could modify the microstructure of the alloys and also influence residual strain. One of the most important challenges is that the formation of intermetallics occurs in a shorter time with respect to the wrought alloys with stress-relieving heat treatment for AM fabricated Ni-based alloys due to segregation [177]. However, there is no systematic report on residual stress and its evolution in WAAM fabricated Ni-based alloy, although stress-relieving heat treatments for these alloys have been routinely conducted.

Porosity commonly exists in the microstructure of powder-based AM fabricated Ni-based alloys, and can be promoted by the trapped gas and insufficient melting, resulting in the pore sizes varying from 1 to 100 μm in SLM [209] and LMD [212] produced materials. The alloys fabricated by these powder-based AM commonly show higher porosity than that by wire-based WAAM. Fig. 2.14 a - b shows a typical example of pore defects in Inconel 718 produced by SLM [213]. In Fig. 2.14, spherical pores can

be seen (Fig. 9a), which can be attributed to the trapping of gas from original powder particles in solidified molten pools under high cooling rates. In Fig 2.14b, smaller aspherical pores can be seen, which are presumably caused by insufficient melting. These aspherical pores appear to have formed at the deposited layers and scan tracks, likely because of a lack of fusion under low laser energy power and/or high scanning speeds. The spherical pores are often distributed randomly, while the aspherical pores are typically aligned with the deposition direction. High local stress gradients induced by the peripheries of pores facilitate the nucleation of cracking, hence reducing fatigue life and wear resistance of the components [214]. Increased laser power can decrease the porosity, while the increased laser scan speed may cause a linear increase of porosity [215]. Increasing laser energy density (LED), which is correlated to scan speed and laser power, can be a solution in reducing porosity but should be limited to a critical value to avoid other processing problems. Moreover, Yi et al. [185] attempted to apply various LEDs in the SLM fabrication of Inconel 718, and suggested shifting scanning with a half hatch distance for the consecutive layers if the laser density is low, in order to decrease porosity. Lesyk et al. [213] proposed the processings of barrel finishing (BF), shot peening (SP), ultrasonic shot peening (USP), and ultrasonic impact treatment (UIT) to refine porosity, and found an increased hardness with these post-processings, as shown in Fig. 2.14c and d. In comparison, for wire-feed WAAM with a single bead, almost fully-dense as-deposited Ni-based alloys are readily achievable, due to the relatively high heat inputs involved and the stability of the feed wire. However, overlap distance, depositing path, and heat input applied in the WAAM processes still need to be optimised in order to avoid insufficient melting, and/or to collapse defects, particularly in large bulk depositions by WAAM [216].

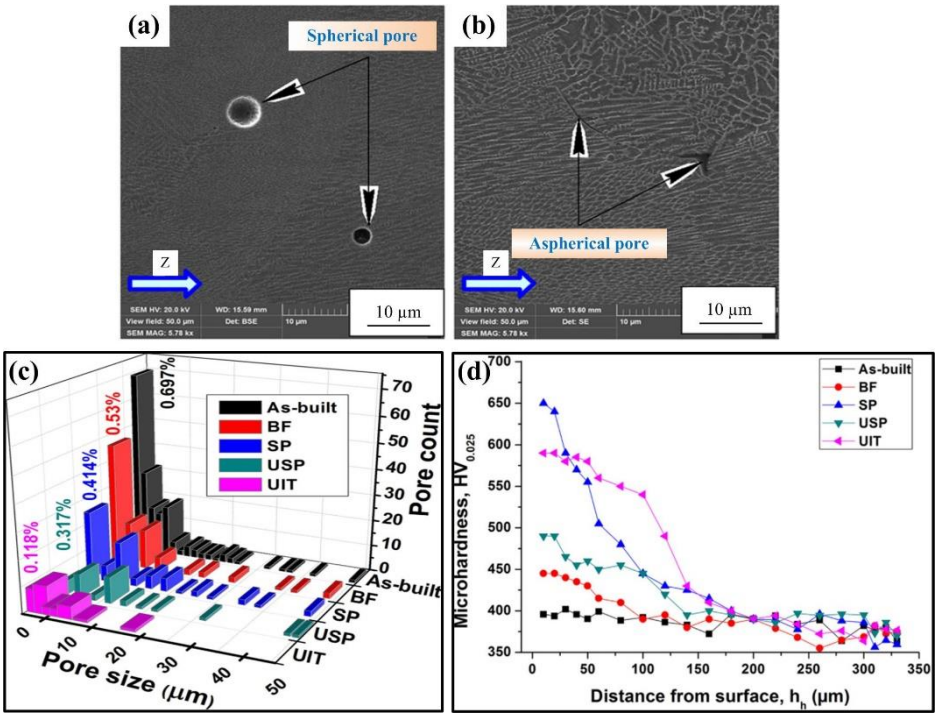

Fig. 2.14 SEM micrographs of residual porosity of the SLM produced Inconel 718 in the deposition direction: (a) Spherical pore; (b) Aspherical pore; (c) Refinement of porosity by BF, SP, USP, and UIT; and (d) Hardness distribution with the refinement of porosity by BE, SP, USP, and UIT post processings. Reproduced with permission from Elsevier [213].

The cracking is another defect found under unfavourable AM conditions, which is attributed to the solidification and liquation cracking related to the presence of intergranular liquid films [217]. Cracking during the solidification is usually found in thick WAAM depositions, resulting from local stresses associated with the layer by layer deposition process, while the liquation cracking is mainly from the lower melting point constituents solidified in the microstructure. Seow et al. [217] found the occurrence of hot cracking in WAAM fabricated Inconel 718 in the centre of the deposition bead, along the high angle grain boundary, and related this to the presence of Laves phase, see Fig. 2.15 a-c. Yuan et al. [212] reported micro-cracking in the LMD-produced Inconel 718 formed in regions containing Laves phase, which is epitaxial with the deposition direction. Hence, intermetallics induced by excessive solute segregation can motivate the formation of hot cracking, although the

intermetallics can be removed by proper annealing. However, annealing cannot eliminate the cracking in the Hastelloy X fabricated by SLM reported by Wang et al. [194]. They also evaluated the solidification process and chemical segregation during solidification using thermodynamic calculation, as shown in Fig. 2.15d - i. It was further reported that the cracking density is higher in the bottom and top regions of as-built thin wall structures (see Fig. 2.15f) than middle region, due to the higher cooling rate and larger thermal contractions in these regions, which induce larger thermal stresses to promote solidification cracking.

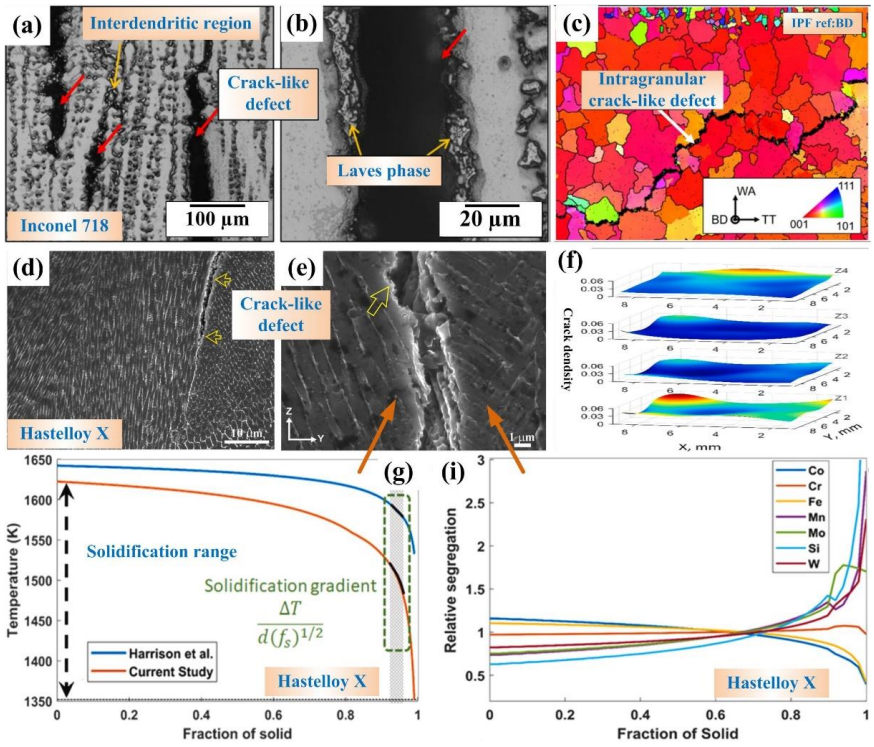

Fig. 2.15 (a-c) Cracking in the as-built sample of Inconel 718 by WAAM. [217]: (a) OM of crack-like defects, indicating their location in the interdendritic area; (b) Laves phase particles lining the edges of the cracking defect; (c) EBSD orientation maps of crack-like defects with inverse pole figure (IPF) reference of the building direction, showing the presence of strong texture and intergranular nature of the defect; (d-i) Solidification cracks in as-built sample of Hastelloy X by SLM. Reproduced with permission from Elsevier [194]: (d) SEM showing solidification cracks in the sample; (e) Micrographs in higher magnification showing retained dendrite structure, indicating cracks occurred in the solidification; (f) Spatial distribution of micro-cracks at different heights of sections (from Z1 to Z4); (g) Scheil-Gulliver solidification curve of the Hastelloy alloy calculated by ThermoCalc software; (h) Relative elemental segregation captured from Scheil-Gulliver solidification simulations.

During the AM processes, the temperature field of the processed component experiences a complex evolution with the heat source movement within one individual molten pool and along depositing path. Fig. 2.16 illustrates the temperature field evolution of a single-pass multi-layer AM deposition. Figs. 2.16a - c are temperature distributions in a component when heat source is at the middle points of the 1st, 5th, and 10th layers, respectively [218], and Figs. 2.16d - e are typical microstructures within one individual molten pool and temperature distribution of Inconel 625 by LMD [219]. Control of thermal history and local thermal profile is recognised as manufacturing challenges, as these are responsible for inhomogeneity of phase formation and elemental distribution. Thermal profiles may vary in response to deposition geometry and thermal cycling, hence influencing the thermal gradient. At the beginning of deposition, heat transfer is mainly via the conduction into the substrate, which can result in higher cooling rates than for later deposition, with residual heat generated in previous layers. Hence, there is decreased heat extraction and increased heat accumulation with built-up, leading to variations of microstructure in the deposition direction. For example, Wang et al. [220] reported Inconel 625 produced by WAAM comprised cellular grains without secondary dendrites at the near-substrate regions, a columnar dendrite structure with secondary dendrites further up, and equiaxed grains at the top region. These results are attributed to variations in a temperature gradient during deposition. The resultant inhomogeneous grain size and morphology can lead to variations of mechanical properties that widely appear from the top to bottom. Additionally, as the aforementioned high elemental segregation can lead to the formation of intermetallic phases and carbides, precipitated in interdendritic areas. Moreover, heat accumulation can result in the deformation of produced components. Consistent state of the deposition is also limited due to inclusion of heat

dissipation from adjacent beads, and heat indulges by repetitive thermal cycles.

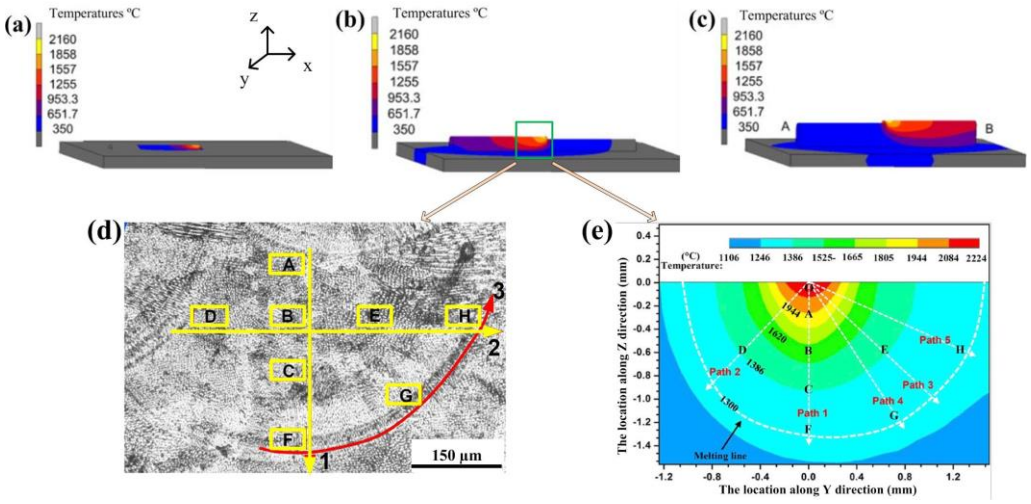

Fig. 2.16 Temperature field evolution in the (a) 1st layer; (b) 5th layer and (c) 10th layer of a thin-wall structure by AM. Reproduced with permission from Elsevier [218]; (d) a typical OM image showing the microstructures of an individual molten pool of Inconel 625 by LMD and (e) related temperature distribution: location A on the surface; location B-E in the upper part; location F in the bottom and location G-H along the boundary. Reproduced with permission from Elsevier [219]

2.4 Feedstock and AM process in the current research

The feedstock in the current research is Hastelloy C276 provided by Haynes International Corporation, which is a solid solution strengthened Ni-based superalloy and possesses exceptional oxidation resistance and corrosion resistance in severe acid environments [221]. In combination with the demonstration of promising mechanical properties at both ambient and elevated temperatures [222], Hastelloy C276 has been investigated as a candidate structural material for Generation IV nuclear reactors, such as supercritical water-cooled reactor (SWCR) [18]. In addition, Hastelloy C276 is utilised extensively in aerospace, particularly as aero-engine components, and for chemical processing applications (e.g. in flue gas desulfurization systems) [90].

Hastelloy C276 alloy components are traditionally manufactured by hot forming or cold working. After such forming procedures, solution annealing is often required to restore

optimum corrosion resistance and mechanical properties [57]. Machining and welding are normally employed to produce the Hastelloy C276 alloy components with complex geometries, adding significantly to processing complexity and the cost. In particular, the welding of Hastelloy C276 components must be carefully controlled to prevent the degradation of mechanical performance. Dupont et al. [1] reported that elemental segregation that occurred during the welding process promoted the precipitation of the detrimental *P* and μ second-phases in Hastelloy C276. The *P* and μ phase precipitates are hard, brittle intermetallics with TCP structures, which are potentially deleterious to mechanical performance and corrosion resistance of the alloy depending on their size, morphology and distribution in the microstructure [223]. The μ phase is transformed from the *P* phase after a long-term exposure, which might be 8 hours or more [88]. As such, research has been carried out using several welding techniques, including continuous and pulsed LBW [21, 129], GTAW [70], and EBW [82]. Cieslak et al. [89] have proved the occurrence of *P* and μ phase by studying the tungsten inert gas (TIG) welding of Hastelloy C276. Ahmad et al. [72] explored the Mo and W rich micro-eutectoids (no separation of *P* and μ phases) in the MZ of welded Hastelloy C276 by the electron beam (EB) method, and found the hardness in the MZ to be higher than that for the as-received alloy due to the fine lamellar microstructure and micro-eutectic phase hardening in this region. The authors further reported the growth of the μ phase after heat treatment.

A major effort has been devoted to having a deep understanding of the intrinsic characterisation in phase transformation, microstructure evolution, and related mechanical property optimisation of Hastelloy C276 alloy by conventional manufacturing processes. However, based on the review above, in terms of the cost consideration for raw materials and capital investment, the conventional processes

might not satisfy the requirement of the model or prototype production of the expensive Hastelloy alloy; hence, the AM is a considerable alternative.

The applied AM process in the current research is WAAM, which uses an electrical arc as a fusion source to melt the wire feedstock and directly build up a component using a layer-by-layer deposition strategy. Despite the outstanding cost-saving and efficient performance, AM as a welding-based process can also witness some drawbacks. Due to the intrinsic characterisations during the WAAM process, the good profound knowledge of the process government can avoid some challenges during fabrication. To promote the development and fabrication of a satisfying Hastelloy C276 component by the WAAM process effectively, it is quite necessary to address the issues related to the microstructure resulting from the processes, and the corresponding properties.

There is limited reported in-depth investigation on the WAAM fabricated Hastelloy C276 components and research on the optimised processes to produce components with competitive properties in comparison with the traditional processes. In the current research, the first-ever study of the manufacturing parameters and related influence on the components by WAAM will be presented. Several effective optimised processes with the in-situ process and ex-situ process will be illustrated based on the problems discussed above. Moreover, recent publications reported the successful application of WAAM in the fabrication of functionally graded material of steel and Hastelloy C276 alloy [224]. However, a detailed exploration of the effects of WAAM parameters on the texture and segregation was not carried out. The current work will study the cladding of Hastelloy C276 and P91 steel using WAAM and tempering treatment, presenting the microstructure in segregation, phase transformation, texture evolution, and the related mechanical properties.

3 Experimental Instruments and Methodologies

In this chapter, the experimental instruments and methodologies will be introduced to prepare the samples and characterise the as-received fabrications. The detailed microstructure was investigated by elemental distribution, phase determination, dendrites and columnar grain morphology and orientation, and texture evolution. These were conducted by optical and electron microscopes, X-ray diffraction (XRD), synchrotron XRD, and a high-intensity powder neutron diffractometer, WOMBAT. The properties are studied using nanoindentation, microhardness, tensile, and creep resistance tests. Above all, elemental contents of the Hastelloy C276 alloy used in this research will be presented, followed by the WAAM system introduction, including the GT-WAAM and CMT-WAAM. Then the corresponding equipment was introduced, and setup parameters to explore the microstructure and mechanical properties are presented in the following chapters to understand how the experiments in this work were conducted.

3.1 Material

Commercially supplied Hastelloy C276 wire with a diameter of 1.2 mm was applied as feedstock in this research, and its chemical composition is listed in Table 3.1. Plain carbon steel was used as a substrate for deposition and preparation of each component.

Table. 3.1 Chemical composition of Hastelloy C276 wire used in this study

Element	Ni	Mo	Cr	Fe	W	C	Mn	P	S	Co	V	Si
wt%	Bal.	16.5	16.0	5.8	4.0	0.01	0.19	0.015	0.01	0.20	0.06	0.08

3.2 Wire Arc Additive Manufacturing System

3.2.1 Gas Tungsten Arc Welding-based Wire Arc Additive Manufacturing (GT-WAAM)

The GT-WAAM system, as shown in Fig. 3.1, used in this study consists of a GTAW welding system with an unconsumable tungsten torch (see Fig. 3.2), a shielding gas unit, a "cold" wire feeder, and a travelling device [11]. High purity argon (99.99%) was utilised for both the TIG welding torch and the trailing shielding gas to limit oxidation of the deposited part during the manufacturing process. Following extinguishment of arc for each layer, additional argon shielding gas continued to flow for about 30 s. To keep stable of the wire, the wire feeder was set at 30° from the substrate. The main processes are listed in Table 3.2. A stainless steel brush was used to remove any spattering or fine particles from welding fume deposition of the welded layer before depositing the next layer.

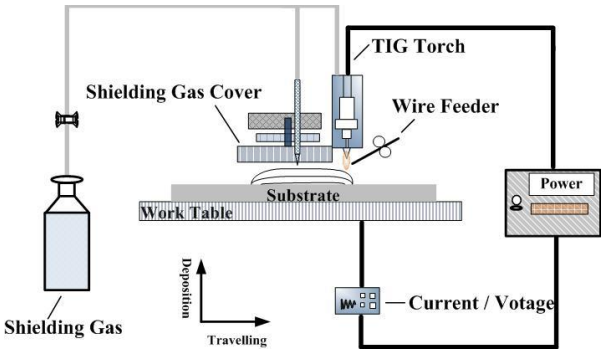

Fig. 3.1 Illustration of WAAM system

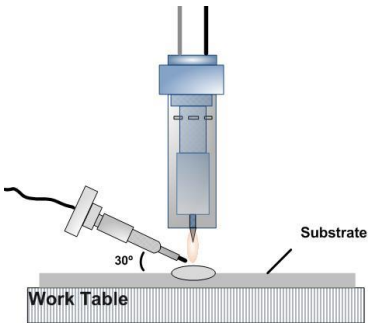

Fig. 3.2 Illustration of GTAW welding system

Table. 3.2 Process parameters for WAAM deposition

Process parameters	Details	
Power	Current	140 A
	Arc voltage	13.0 V
Speed	Torch travel speed	100 mm/min
	Wire feed speed	1000 mm/min
Shielding gas	Welding torch	10 L/min
	Shielding gas cover	15 L/min
Time	Interpass dwell time	60 s
Distance	Electrode to workpiece	3 mm
Angle	Wire feeder and substrate	30°

3.2.2 Cold Metal Transfer (CMT) -based WAAM

The hardware of the WAAM system includes an industrial robot, a welding machine with the feedstock wire as a consumable torch, a laser scanner, a cooling gas gun, a computer and a worktable, as shown in Fig. 3.3. An ABB IRB 2600 robot with six Degrees of Freedom (DOF) was applied to hold and move the welding torch along the preprogrammed robot path. A Fronius CMT Advanced 4000 device with synergic welding programs was selected as the power source and software. Instantaneous welding current and voltage were measured using a National Instruments NI-6008 card and a self-built PCB board with a sampling rate of 2500 Hz. A structured laser scanner with a 300 Hz measurement speed was attached to the welding torch to obtain the bead profile. ABB's Robot Studio was used to program the robot motion and coordinate the weld settings. The distance from the contact tip to the substrate, regarded as the stick-out distance, was kept in a range from 15 - 20 mm. Before the deposition of a new layer, a stainless steel brush was used to remove possible spatter or impurities. The shielding gas was argon (99.99%) with a flow rate of 25 L/min. A FLIR A655sc thermal imaging camera with a measurement range of -40 °C to 2000 °C and a wavelength range of 7.5

μm to 14 μm was used to monitor and record the temperature evolution during the deposition processes. The emissivity was set as 0.45 consistently and used to compare the cooling rate and temperature evolution of the working alloy.

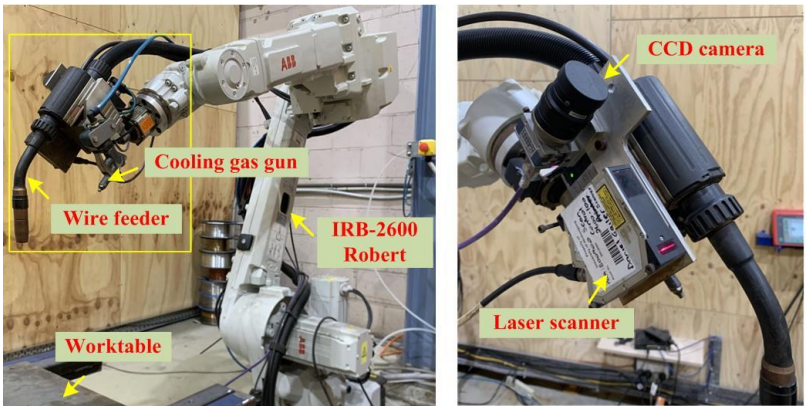

Fig. 3.3 Illustration of CMT-based WAAM system

3.3 Magnetic Arc Oscillation (MAO) system

The MAO system comprising the electromagnetic coils and the oscillation control device is incorporated into the WAAM system. The magnetic force ($\vec{F}$) known as the "Lorentz force" is the vector product of the current ($\vec{I}$) of the welding arc and the external magnetic field ($\vec{B}$), i.e., $\vec{F} = \vec{I} \times \vec{B}$. The external coil defines the directions of $\vec{F}$ and $\vec{B}$, and determines the oscillation pattern. Fig. 3.4 summarises the three types of arrangements for incorporating the electromagnetic coil in the welding system that has been reported [225]. These arrangements lead to three different possible orientations of applied magnetic fields: (1) $\vec{B}$ parallel to the traveling direction ($\vec{x}$) applying a single electromagnetic coil to induce the transverse oscillation of arc (Fig. 3.4a), (2) $\vec{B}$ parallel to the transverse direction ($\vec{y}$) with a single electromagnetic coil causing the longitudinal oscillation of arc (Fig. 3.4b) and (3) $\overrightarrow{B_1} \parallel \vec{x}$ and $\overrightarrow{B_2} \parallel \vec{y}$, with two electromagnetic coils inducing a circular oscillation of the arc (Fig. 3.4c). Circular arc oscillation mode was chosen in this research.

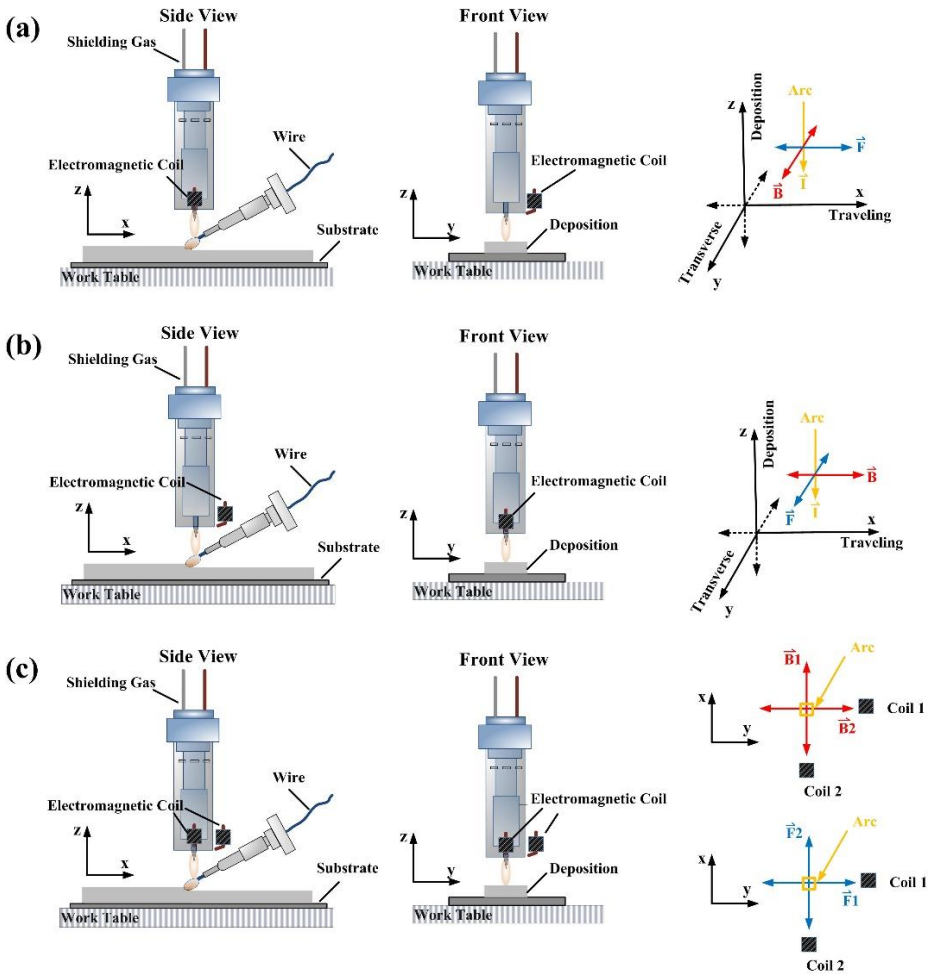

Fig. 3.4 The positions of the electromagnetic coil for (a) longitudinal oscillation, (b) transverse oscillation, and (c) circular oscillation.

3.4 Sample preparation for metallography

After the deposition of the samples under different manufacturing parameters, the samples for microstructure and mechanical studies were sectioned into appropriate sizes in the regions of interest using a computer-controlled wire-cut EDM process. The sample sectioned position and size will be illustrated in each chapter. The metallography samples were prepared with hot mounting by a CitoPress-20 Hot mounting press equipment, as shown in Fig. 3.5, to mount the metallography samples in the conductive Polyfast resin. The mounted samples were then ground and polished by a Struers Tegrapol-21 automatic grinder-polisher shown in Fig. 3.6, with detailed

polish procedures for optical microscopy (OM) and electron backscatter diffraction (EBSD) samples, shown in Table. 3.3, respectively. Afterwards, the OM samples were electro-etched in a mixed solution containing 5 mg oxalic acid and 15 mL hydrochloric acid with 6 V direct current for 2 s at room temperature.

Fig. 3.5 Struers CitoPress-20 Hot mounting press equipment

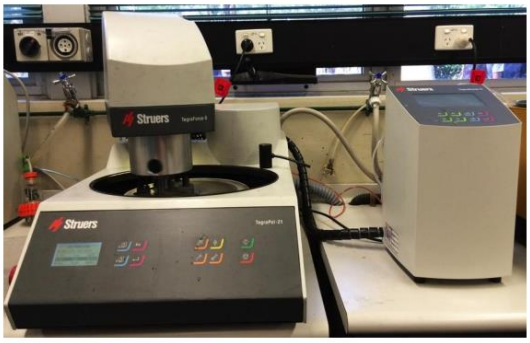

Fig. 3.6 Struers Tegrapol-21 automatic grinder-polisher

Table. 3.3 Procedures for metallographic sample preparation

For OM samples

Process	Surface (Disk/cloth)	Rotation (rpm) (Disk/Holder)	Force per sample (N)	Time (mins)	Suspension
Grinding	220 grit Diamond disk	300/150, comp	30	2-5	Water
Polishing	MD Largo disk	150/150, comp	30	4-6	Water-based 9 µm Diamond
	MD DAC cloth	150/150, comp	30	4-5	Water-based 3 µm Diamond
	MD Chem cloth	150/150, contra	15	2	0.05 µm colloidal silica (50% OP-S)

For EBSD samples

Process	Surface (Disk/cloth)	Rotation (rpm) (Disk/Holder)	Force per sample (N)	Time (mins)	Suspension
Grinding	220 grit Diamond disk	300/150, comp	30	2-5	Water
Polishing	MD Largo disk	150/150, comp	30	5	Water-based 9 µm Diamond
	MD DAC cloth	150/150, comp	30	5	Water-based 3 µm Diamond
	MD DAC cloth	150/150, comp	30	12	Water-based 1 µm Diamond
	MD Chem cloth	150/150, contra	15	15	0.05 µm colloidal silica (5% OP-S)

3.5 Microstructure characterisation

3.5.1 Optical microscope

The overall microstructures of the etched samples, including dendrites, precipitations, and columnar grains were captured using Leica Optiphot OM, as shown in Fig. 3.7. The low magnification (5×) microstructures were combined into a macrostructure of the cross-section of received samples. ImageJ software [226] was used to calculate the dendrite arm spacing (DAS) in all cases.

Fig. 3.7 Leica Optiphot optical microscopy

3.5.2 X-ray diffraction (XRD) and Synchrotron XRD

X-ray diffraction (XRD) with a Cu Kα radiation source (λ=1.5418Å) was performed to identify the phase constituents by a GBC MMA X-ray diffractometer (see Fig. 3.8). The

accelerating voltage and tube current were set at 35 kV and 28.6 mA, respectively. The synchrotron X-ray diffraction, as shown in Fig. 3.9, was conducted within the Australian Synchrotron, Melbourn, Australia. A monochromatic X-ray beam of 18 keV (wavelength ~0.68933 Å) and the MYTHEN detector was used in the measurements in flat-plate reflection geometry. The data was analysed using the Topas software (V4.2) [227] and Pseudo-Voigt functions.

Fig. 3.8 GBC MMA X-ray diffractometer

Fig. 3.9 Australia Synchrotron and illustration of beamline

3.5.3 Scanning Electron Microscopy (SEM)

The detailed observation of the matrix microstructure, precipitation, fracture mode, and chemical composition was preliminarily performed using a JEOL JSM-6490LA Scanning Electron Microscope (SEM) equipped with Oxford Instruments X-Max Energy Dispersive X-ray Spectroscopy (EDS) detector, as shown in Fig. 3.10, operating at 20 kV and working distance as 15 mm.

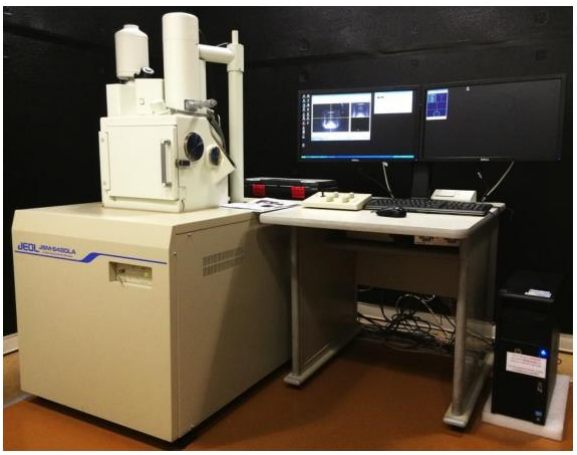

Fig. 3.10 JEOL JSM-6490LA SEM

Due to the relatively lower resolution of JEOL JSM-6490LA, the microstructures, which consist of grain boundary observation and fined particles, were characterised by the JEOL JSM-7001F Field Emission SEM (FSEM), as shown in Fig. 3.11. The working distance was 10 mm at 15 kV. In addition, the current equipment also worked on the grain size, texture and grain angle misorientation distribution by EBSD equipped with Oxford Instruments Nordlys II(S) high resolution EBSD camera. Channel 5 software integrated Aztec software was used to process the EBSD results. The EBSD maps were collected at 15 kV accelerating voltage, 24 mm working distance, and 3 μm step size.

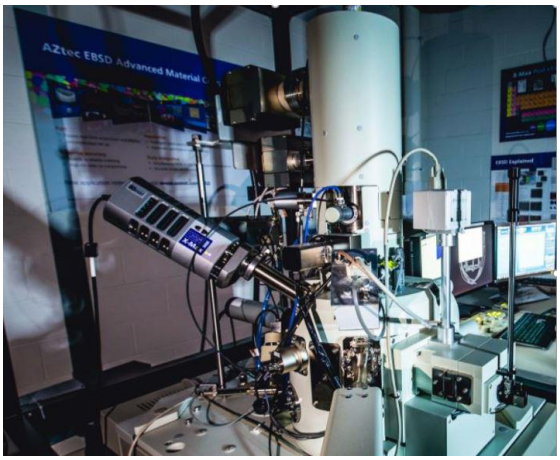

Fig. 3.11 JEOL JSM-7001F Scanning Electron Microscope

3.5.4 Transmission electron microscope (TEM)

In order to further understand the precipitation that could not be recognised by the EDS and XRD, transmission electron microscope (TEM) analyses were carried out on the JEOL JEM-ARM 200F instrument (see Fig. 3.12). The interested samples were finely polished, followed by which 15 μm wide, ⩽ 50 nm thick lamellae were prepared for the TEM sample by an FEI Helios Nanolab G3 CX FIB-SEM (Fig. 3.13). The precipitates were identified by selected area electron diffraction (SAD) and processed by Gantan software.

Fig. 3.12 JEOL JEM-ARM 200F instrument

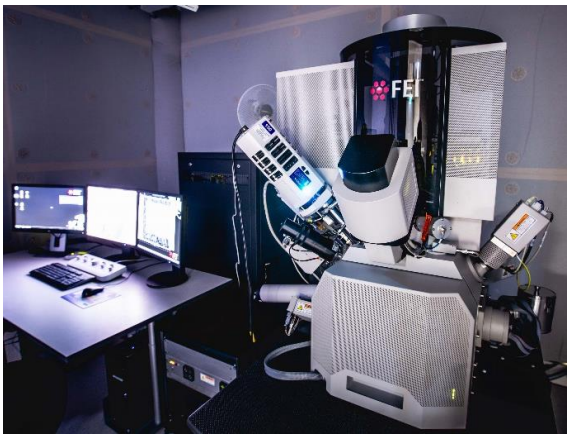

Fig. 3.13 FEI Helios Nanolab G3 CX FIB-SEM

3.5.5 Neutron diffraction

WOMBAT, which is a high-intensity and high-speed powder diffractometer in the Australian Nuclear Science and Technology Organisation (ANSTO) was used to undertake the neutron diffraction experiments for the texture characterisation of the CMT-based WAAM samples. Before the neutron diffraction experiment, the sample with the same orientation was fixed by Al foil, as shown in Fig. 3.14. A neutron beam of wavelength 1.54 Å and a position sensitive area detector were used to collect the diffraction data from square bar samples mounted on an Eulerian cradle. For complete pole figure measurements, the samples were tilted (χ = 0 - 90°) and rotated (φ = 0 - 360°) in equal-distance steps of $\Delta\chi$ = 15° and $\Delta\varphi$ = 3°. The neutron diffraction data were analysed to obtain the pole figure data using 2DiffCalc [228] software package and recalculate the pole figures from the orientation distribution function (ODF) using the MTEX program [229].

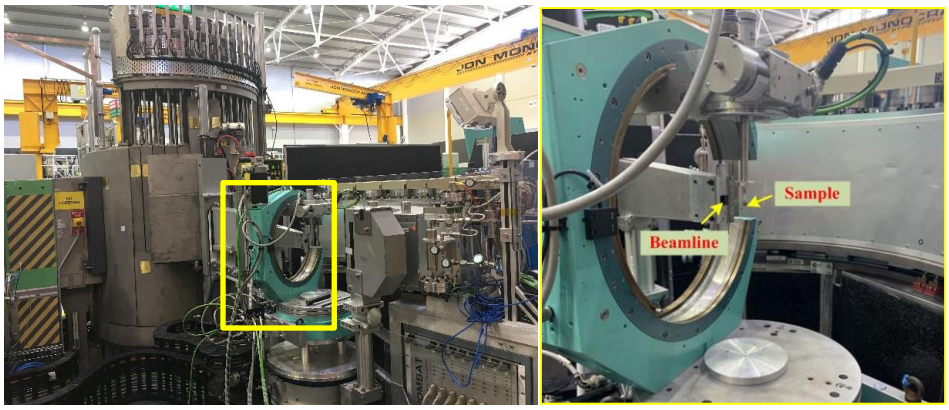

Fig. 3.14 Sample tested by Wombat high-flux neutron diffractometer in ANSTO

3.6 Mechanical testing

3.6.1 Vickers hardness and nanoindentation

Vickers microhardness was measured on the same metallographic specimens. The tests were carried out by a Matsuzawa Via-F automatic Vickers tester, as shown in Fig. 3.15,

at a load of 500 g, with a spacing of 0.5 mm between each step, and an indentation duration of 15 s for each test. The nanoindentation was performed at the same metallographic specimens, as well, at both interdendritic and dendrite core areas in the middle region of specimens to obtain the nanohardness (*H*) and Young's modulus (Er) on a Hysitron TI 950 Triboindenter, as shown in Fig. 3.16. An indentation load of 7 mN and a step size of 7 μm were used in nanoindentation tests.

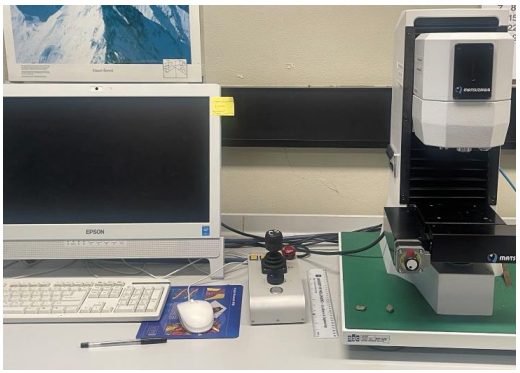

Fig. 3.15 Matsuzawa Via-F automatic Vickers tester

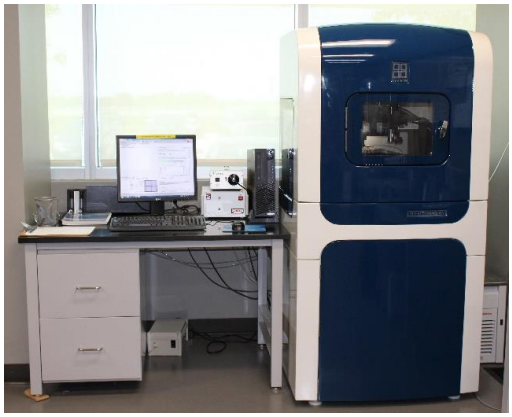

Fig. 3.16 Hysitron TI 950 Triboindenter

3.6.2 Tensile test

Flat dog-bone-type samples with the dimensions in Fig. 3.17 were prepared for all the tensile tests. The tensile tests were carried out at a constant crosshead displacement rate of 1 mm/min by an Instron 3367 tensile test machine with a maximum load capacity of

30 kN (Fig. 3.17) at the ambient temperature. A video extensometer was used to measure the displacement during tension loading.

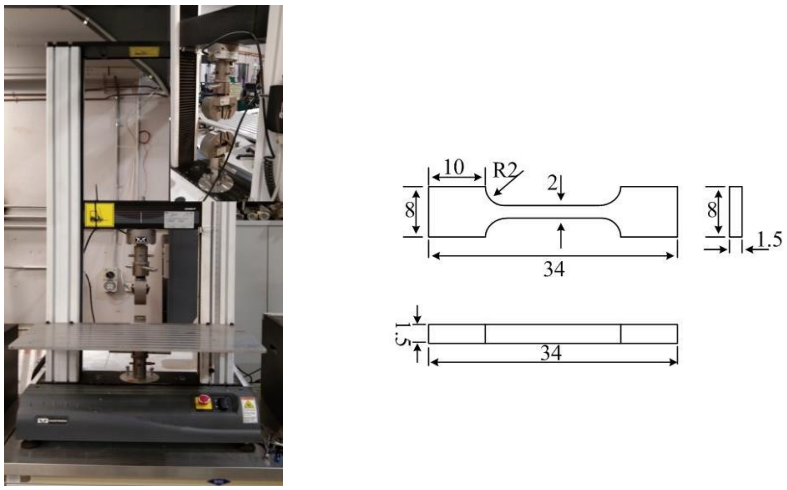

Fig. 3.17 Tensile testing using MTS Landmark servohydraulic testing machine and dimension of the tensile test sample

3.6.3 Creep test

An iso-thermal creep test was operated at constant stresses in the Australian Nuclear Science and Technology Organisation (ANSTO), as shown in Fig. 3.18. The dimensions of miniature samples are shown in Fig. 3.18, and were manually measured to assure accurate sizes before the tests. To limit oxidation of samples, the creep test was operated in a vacuum atmosphere (10^{-5} torr).

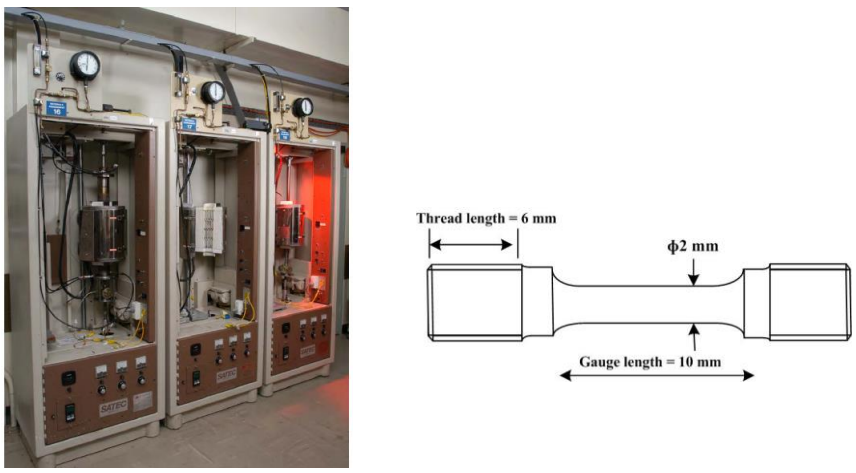

Fig. 3.18 Creep testing machine and dimension of the creep test sample

4 Microstructure and mechanical properties of wire arc additively manufactured Hastelloy C276 alloy

4.1 Introduction

There has been an increased focus from the academic community and manufacturing industry on the area of additive manufacturing (AM), owing to its ascendency in component fabrication over the past few decades. The WAAM approach is advantageous for the production of large metallic components of complex geometry, due to its high deposition rate in comparison to the other AM approaches using laser or electron beams as heating sources, plus it requires relatively low apparatus investment. These characteristics enable a significant reduction in capital cost and efficient usage of raw materials [8]. Currently, various metallic materials, such as titanium alloys, aluminium, Ni-based superalloys, and titanium aluminide intermetallics have been successfully utilized in the WAAM process [230-232].

Hastelloy is normally supplied in forged, rolled, and extruded states, and welding has been widely used for fabricating Hastelloy components. Hastelloy is readily weldable, and it can be welded with GTAW [70], electron beam welding (EBW) [233], and laser welding (LW) [20]. However, a welded joint is generally treated as the weakest part of the manufactured component due to microstructure diversity, which is an unavoidable aspect leading to the occurrence of defects or variations in mechanical properties [79, 113]. Moreover, the high temperature and stressed working conditions for Hastelloy alloys will result in creep deformation and restrict the attainable in-service life of the alloy. Especially for that produced by traditional cast processes, the resulted equiaxed grains will lead to poor performance under elevated temperatures due to nucleation and propagation of micro-crackings in the grain boundary areas. In recent years, additive

manufacturing (AM) techniques have been used to fabricate the components by one grade of Hastelloy alloy, named Hastelloy X, by laser powder-bed fusion (LPBF) [234, 235] and selective laser melting (SLM) [236]. LPBF and SLM, as metal powder-based AM technologies, are often associated with the concerns that the metal powder raw material does not show the same competitive efficiency with regard to cost and availability as the metal wire, in addition to the challenges concerning the properties of manufactured components caused by the potential defect of porosity [8, 236]. In contrast, WAAM, as a wire-based AM technology, is a potentially cost-effective alternative to fabricate defect-free components, albeit that the post-machining of the WAAM processed components is often required due to their low geometric accuracies [237].

So far, the component fabrication techniques are still mainly concentrated on welding and traditional subtractive technologies, and only limited research [22] has been reported on additive manufacturing of Hastelloy C276 alloy; this makes an attempt to apply the AM process timely. It has been widely accepted that various additive manufactured components would possibly exhibit heterogeneity with respect to both microstructure and mechanical properties from the bottom to the top part of the fabricated components, resulting from the line-by-line and layer-by-layer manufacturing strategy [220, 238].

In this study, the GT-WAAM process was utilised to produce Hastelloy C267 samples. The microstructure (columnar dendrites and precipitates) and mechanical performance (tensile properties, hardness and preliminary creep resistance) were investigated through comprehensive comparison and evaluation in different regions and orientations of the component after deposition. These results show that Hastelloy C276 components

with high-quality performance can be efficiently fabricated using the GT-WAAM process.

4.2 Experimental procedures

4.2.1 Experiment setup

The WAAM system and experiment setup were presented in Section 3.2.1. WAAM system was used to deposit a Hastelloy C276 thin-wall structure with dimensions of 10 × 100 × 45 mm (width × length × height) on a plain carbon steel substrate, and the process parameters for the experiment are listed in Table 3.2. Fifty layers were deposited on a single thin-wall structure, and no adjacent layer was built. Following the extinguishment of the arc for each layer, additional argon shielding gas continued to flow for about 30 s, and complemented friction by a stainless steel brush was utilised. Hence, the dwell time of interpass is about 60 s without an interpass temperature control in this research.

4.2.2 Material characterisation

Mechanical testing and metallographic specimens were extracted from the middle of an as-deposited Hastelloy C276 wall sample, as shown in Fig. 4.1, which also shows the travelling direction and deposition direction, and defines the selection of reference planes, y-z, x-y, and x-z. To avoid element dilution from the substrate, the test samples were extracted from the regions in the as-deposited materials at least four layers away from the substrate. The metallographic samples were ground and polished following standard procedures, and subsequently electro-etched for 2 s at room temperature. Microstructures were observed using a Leica Optiphot OM. ImageJ software was applied to calculate the size of the dendrites [226]. The Thermo-Calc® software (2019 version) was used for the thermodynamic calculation of the Hastelloy C276 system.

The characteristic fast solidification and cooling rate of the WAAM process relative to the conventional casting process were taken into account in the simulation. The classic Scheil simulation based on the well-known Scheil-Gulliver model [239] which assumes zero diffusion in the solidified material and the TCNi9 thermodynamic database for Ni-based superalloys were used to predict the phases transformation during the solidification process of the investigated Hastelloy C276 with the chemical composition listed in Table 3.1. Detailed observation of the matrix grain structure, precipitation, fracture mode, and chemical composition was performed using a JEOL JSM-6490LA SEM equipped with EDS detector. TEM analyses were carried out, operating at 200 kV. The identification of phase constituents was performed using XRD. The data were collected over a scattering angle (2θ) of 30° to 100° on the samples taken from the longitudinal region in the y-z plane. The sample with a dimension of 5 mm × 5 mm × 10 mm for bulk texture of the fabricated component was taken in the middle area and measured using neutron diffraction on the high-intensity WOMBAT diffractometer (see Fig. 4.1), with parameters shown in section 3.5.5.

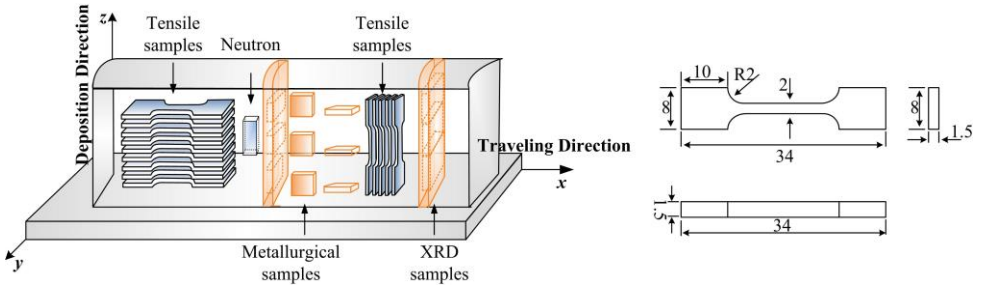

Fig. 4.1 Schematics of sample extraction for metallurgical and mechanical tests

Vickers microhardness samples taken from the y-z plane for vertical (z) and horizontal (y) direction tests were measured. The mechanical samples for tensile testing were extracted from both the deposition direction (y-z plane) and travelling direction (x-y plane). Tensile tests were performed equipped with a digital camera to assure precise

displacement measurement.

Creep tests were conducted in the samples taken from both deposition direction and travelling direction at 973 K (700 °C), using stress of 165 MPa by dead-weight loaded creep machines, as shown in Fig. 3.18. The creep extension for the duration of tests was recorded by a linear variable differential transducer extensometer, mounted onto the pull rod which extends out from the test chamber/furnace assembly. Two K-type thermocouples were in contact with the top and bottom shoulders of the sample to record the tested temperatures which were continuously monitored and maintained at + 0.5 °C between two areas. The samples were creep tested up to failure, then unloaded and furnace cooled to room temperature at the end of the test.

4.3 Results and discussion

4.3.1 Macrostructure

Fig. 4.2 illustrates the overall macro morphology of the as-deposited sample of Hastelloy C276 using the WAAM process. Slight deformation of the substrate is observed, with a corrugated morphology surface on the sample as a result of layer-by-layer deposition. Also, the component is characterized by being free of visual defects or any cracks, the following microscopic observation from numerous sections proved this. It appeared to be a uniform surface finish from the visual appearance after the whole manufacturing process. These results indicate that the applied WAAM process yields the defect-free Hastelloy C276 material in this work.

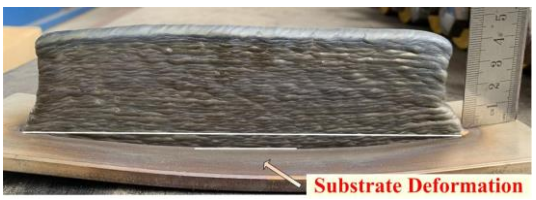

Fig. 4.2 Macro morphology of the fabricated component

4.3.2 Microstructural evolution

4.3.2.1 Typical morphology of as-deposited microstructure

The microstructures and microstructural anisotropies of the as-deposited component were thoroughly investigated from the bottom to top regions. Samples were extracted in the traveling direction and deposition direction from the previously defined y-z, x-y and x-z planes, as shown in Figs. 4.3 - 4.5, respectively. Typical columnar dendrites are clearly observed in the samples in different regions from top to bottom, with additional evidence for the occurrence of precipitates (dark regions in Fig. 4.3f-h).

The longitudinal cross-section (y-z plane), shown in Fig. 4.3, displays a typical dendritic microstructure. The directional arrangement of these dendrites is expected to lead to a strong texture, which is studied in the following part. A large number of elongated dendrites have grown across several deposited layers and are oriented upwards, almost perpendicular to the substrate in the z-direction. These appear homogenous and aligned in the middle region (Fig. 4.3d), but take the form of mixed dendrites, with a cellular-like pattern in local areas of the side regions (Fig. 4.3b) and the first several layers in the bottom region (Fig. 4.3e). Layer boundaries (fusion interfaces between deposited layers) can be readily observed, and are roughly parallel to the traveling direction (x), as is shown in Fig. 4.3d. Formation of the epitaxial columnar dendrites along the deposition direction is attributed to heat transfer from subsequent layers, and growth which follows the highest thermal gradient. During the

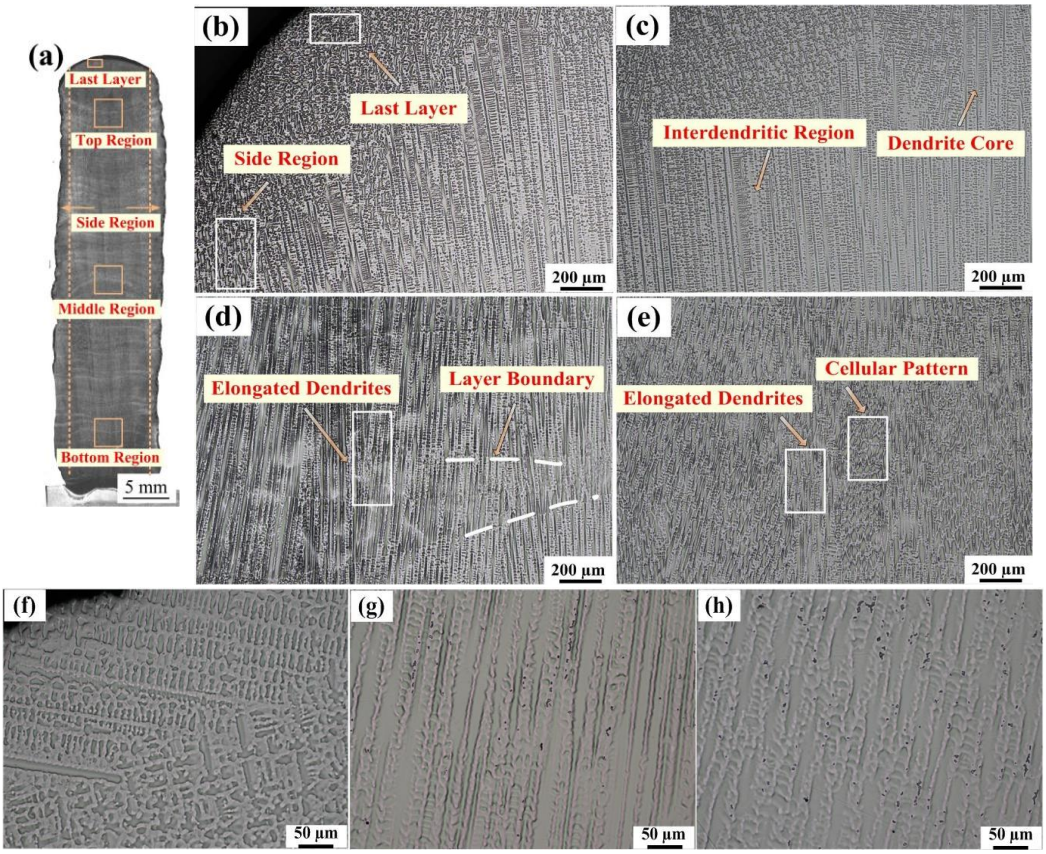

Fig. 4.3 Microstructure morphology in cross-section (y-z plane) of as-fabricated component: (a) whole profile of the part in cross-section (y-z plane), (b-h) are representative microstructures in different areas; (b) the side region and the last layer; (c) the top region; (d) the middle region; (e) the bottom region; (f) higher magnification of the last layer in Fig. 3a; (g) higher magnification of the middle part in Fig. 4.3d; (h) higher magnification of the bottom part in Fig. 4.3e.

WAAM process, the dendrites of preceding deposited layers are partially remelted by the thermal cycling, becoming nucleation regions for the subsequent layer [240]; simultaneously, layer bands are formed (highlighted in Fig. 4.3d) [241]. In contrast, at the commencement of the deposition, due to rapid heat transfer into the cold substrate, the dendrite growth is facilitated during the solidification process. The more rapidly growing dendrites can encroach on space in front of the slower-growing ones, and finally suppress their growth [242]. Dendrites which experience heat accumulation from the deposition of previous layers experience relatively lower thermal dissipation. However, despite this complex thermal history, it is possible that all the dendrites

survive [242, 243]. In accordance with expected heat transfer, the bottom region and side regions display more cellular form without secondary dendrites, whereas the main section displays a well-aligned elongated dendritic structure. The top region in the last deposited layer, as is shown in Fig. 4.3b and Fig. 4.3f, exhibits a transitional microstructure, from directional elongated dendrites to fine equiaxed dendrites. It is attributed to last layer experiencing an accelerated cooling induced by the atmosphere surrounding the sample and the lack of remelting as it occurs during the WAAM process [244]. Similar fine top layer microstructures have been observed in other AM processed materials including, the Ni-based alloy Inconel 625 [220], and NiTi intermetallic [245]

Similarly to the y-z plane, the x-z plane also exhibits a columnar microstructure with epitaxial dendrites growing upwards (z), as is shown in Fig. 4.4. However, there is a slight deviation, compared to the upward dendrite growth orientation in the y-z plane. For the y-z plane, most of the upwardly elongated dendrites occur at an angle of about 80° to the substrate, as shown in Fig. 4.4a. A similar phenomenon has been observed in previous WAAM investigations of Inconel 625 [220]. During the GT-WAAM process, the heat conduction of the molten pool predominantly comes from the substrate for the first few layers and previously deposited layers with buildup (z), and partially from the adjacent solidification along the traveling direction (x). Due to the temperature gradient from these two orientations, the angular grain growth appears in higher layers along the deposition direction instead of being perpendicular to the substrate, which follows the maximum temperature gradient. However, in this research, the angle is slightly different from observation in the previous study, which was about 70° [220]. This is attributed to differences in wire traveling speed and interlayer temperature control for the different studies. Taking into account the close link between the dendrite microstructure and the development of crystallographic texture, this result indicates that the manipulation of

texture is potentially viable during the WAAM of Hastelloy C276, via careful control of processing conditions including the temperature gradients.

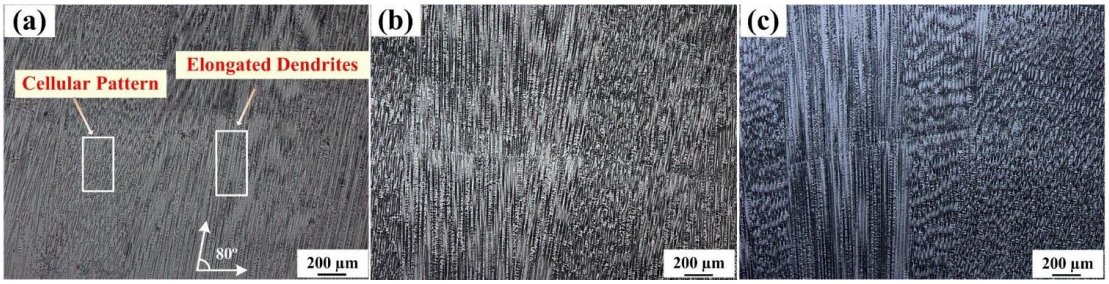

Fig. 4.4 Microstructure morphology in cross-section (x-z plane) of as-fabricated part: (a) the bottom region; (b) the middle region; (c) the top region

The microstructure in the x-y plane is displayed in Fig. 4.5. A typical equiaxed microstructure is observed in this region and is attributed to sectioning of the epitaxial dendrites, which grow upwards along the deposition direction. This cross-section reveals both the primary dendrites, short secondary dendrite arms perpendicular to each other, and tertiary dendrite arms which are visible on a few of the secondary dendrites. Slight differences observed in the sizes of the primary dendrites can be attributed to different growth velocities, especially at the bottom area, as is shown in Fig. 4.5.

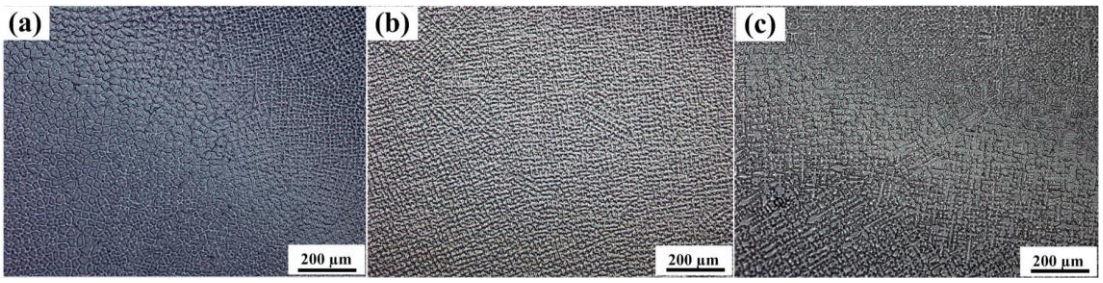

Fig. 4.5 Microstructure morphology in cross-section (x-y plane) of as-fabricated part: (a) the bottom region; (b) the middle region; (c) the top region

4.3.2.2 Primary dendritic arm spacing

Fig. 4.6 shows a statistical analysis of PDAS from different regions of the as-deposited

sample. The PDASs are primarily distributed between 20 µm to 40 µm, except for several large size spacings associated with the top and bottom regions. As previously explained, the cooling rate in the first few layers above the cold substrate is quite high, and during the deposition of subsequent layers, the cooling rate is lower, commensurate with the lowered temperature gradient. However, the cooling rate is accelerated again in the top region. The similar thermal behavior is also studied via the heat transfer numerical simulation by Zhao et al. [218]. Complexities associated with the thermal cycling contribute to slight variations in WAAM Hastelloy C276 microstructures.

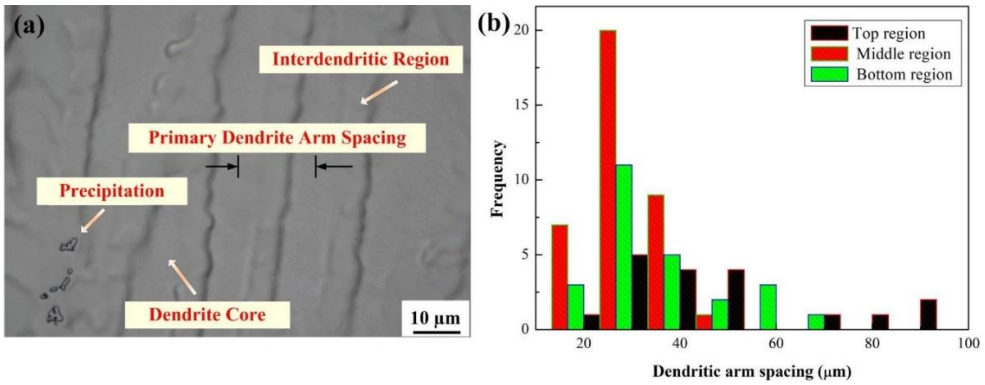

Fig. 4.6 Illustration of PDAS: (a) illustration of dendritic structure; (b) PDAS distribution frequency in different regions

4.3.2.3 Precipitation

Figure. 4.7 shows precipitations found in the as-deposited samples at different locations from bottom to top taken in the y-z plane along the deposition direction. A considerable number of precipitates, of differing sizes, are dispersed at the interdendritic area, many of these aligned with the growth orientation of the primary dendrites. Based on optical microscopy (Fig. 4.7), it appears that a secondary phase predominantly precipitates at the interdendritic area in the vicinity of secondary dendrites, regardless of the sample location.

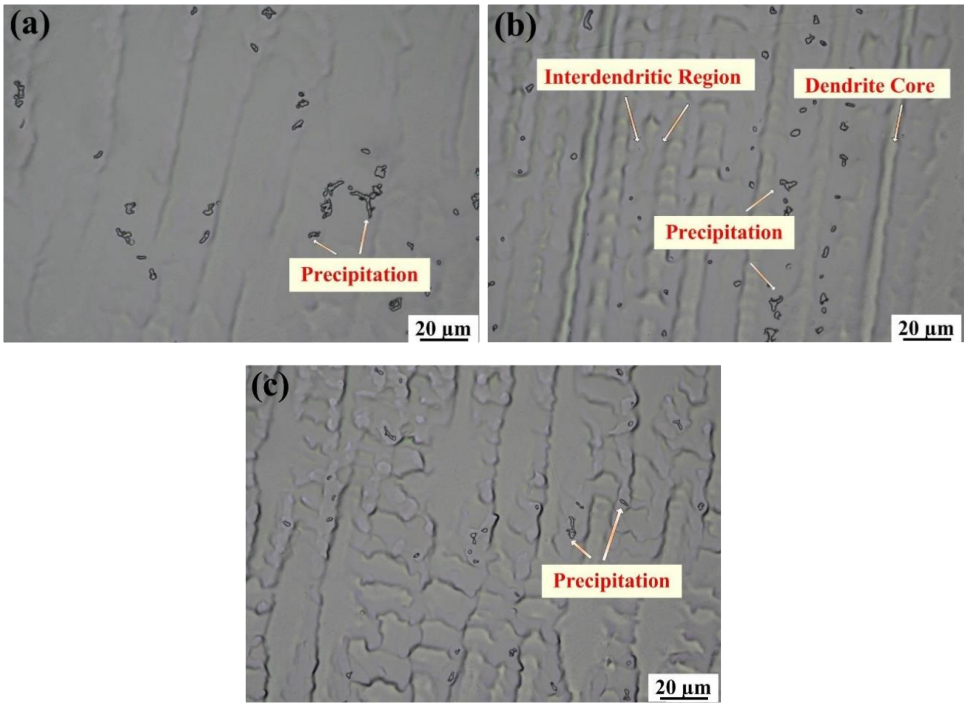

Fig. 4.7 High magnification OM image showing the microstructure of precipitates in different regions: (a) distribution of precipitates in the bottom region; (b) distribution of precipitates in the middle region; (c) distribution of precipitates in the top region

In order to study the microstructure at high magnification and identify the element distribution in dendrites, SEM with EDS analysis was performed. As shown in Fig. 4.8, Mo segregation is evident, indicating Mo is a positive segregation element that tends to be rejected into the interdendritic residual liquid. Elemental analysis in the matrix and precipitations is listed in Table 4.1 and Table 4.2, respectively. It was found that the precipitates are rich in Mo and W. Due to the insensitivity to the C element as well as its extremely low content, the carbon content cannot be measured properly by EDS [102], and thus EDS results in Table 4.1 and Table 4.2 do not include the C element. Fig. 4.9 presents the process of microsegregation during the solidification process predicted by the Scheil-Gulliver model based on the composition content of Hastelloy C276 in this research. In this model, carbon is treated as a fast solute element. Solidification starts from liquid to γ phase, and the σ phase and *P* phase are formed last during the solidification process, so it can be seen that the *P* phase is formed during

solidification by the WAAM process. Obviously, the high deposition efficiency of WAAM will not expose the heat input for so long period. DuPont et al. also presented that the lower content of Cr in Hastelloy C276 pushes the solidification further away from the ternary point with γ, σ, and *P* phases [26]. Hence, based on the composition of the *P* phase cited by Ma et al. (Table 4.2) [246], the precipitates with similar elemental composition in this research were induced as *P* phase. The slight variation in the content of the composition might result from some of the tested *P* phases in a relatively small size. The interaction volume of EDS analysis is normally 1-2 μm, so the accuracy of EDS spot analysis on small particles will be compromised by the surrounding matrix.

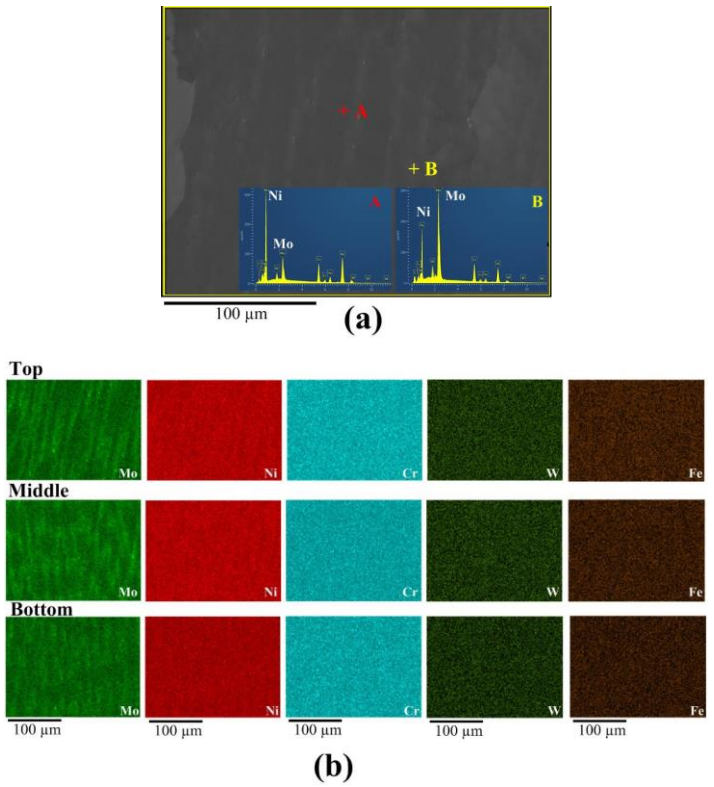

Fig. 4.8 (a) Backscattered electron image (BEI) of the deposited sample from the bottom area in the y-z plane, with the spectrum of the matrix (Location A) and precipitates (Location B); (b) the respective chemical composition distribution maps for Ni, Mo, Cr, Fe and W in the bottom, middle and top

Table. 4.1 EDS semi-quantitative standardless analysis of elements in different regions (wt%)

Area		Ni	Mo	Cr	Fe	W
Matrix	Top	56.6	17.8	15.8	5.9	4.5
	Middle	57.0	17.0	16.3	5.7	4.1
	Bottom	58.5	14.0	15.9	7.2	4.5

Table. 4.2 Comparison of EDS analysis of the precipitations' composition in this research and in the previous research [246]

	Ni	Mo	Cr	Fe	W
Precipitation (Average)	32.6	42.3	14.7	4.0	6.3
P phase [246]	34	40	16	4	7

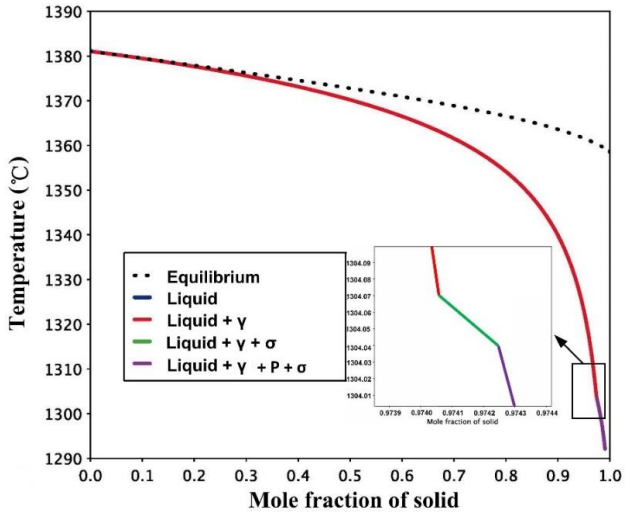

Fig. 4.9 Phase transformation illustrated as mole fraction by Scheil-Gulliver model

Note that in Fig. 4.8 the constitutive elements are not distributed uniformly. Specifically, Mo is more concentrated in the interdendritic area than in the dendritic cores, and a reverse situation is observed for Ni. In addition, compared with the *P* precipitate, the matrix is rich in Fe and deficient in W, from the results given in Table 4.1 and Table 4.2. This solute segregation in the γ-matrix is considered to be attributed to the significant partition of Mo element between the solid and liquid phases during WAAM as well as the low diffusivity of heavier Mo element than other lighter alloying elements such as Ni [85, 89]. During the WAAM process of Hastelloy C267 alloy,

primary dendrites first develop in the initial stage of solidification, and then secondary and tertiary dendrites are formed. In the present case, the partition coefficient (k) for the Mo element in the solid and liquid γ-matrix phases is believed to be lower than 1 [80], where $K = C_s/C_l$ (C_s and C_l are the Mo solute concentrations in the solid and liquid phases, respectively). As a consequence, the interdendritic areas are rich in Mo compared with the dendrite cores (Fig. 4.8b). This also explains the observation that the Mo-rich *P* phase tends to precipitate out in the interdendritic areas (Fig. 4.7), especially in the vicinity of secondary or tertiary dendrites.

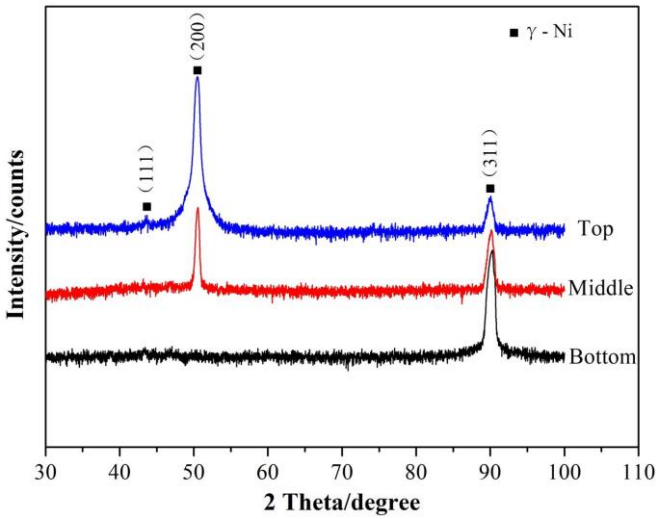

Fig. 4.10 XRD analysis result for the y-z plane of the deposited sample

The XRD analysis of different regions from top to bottom in a perpendicular cross-section (y-z plane) to the travelling direction is presented in Fig. 4.10. It can be confirmed that the matrix is a γ-Ni phase. Secondary phases in the matrix are not detected by XRD due to their low volume fraction. The very high peak reveals an intense columnar dendritic texture growth, and a variation in preferential growth orientation can be observed from bottom to top, which is consistent with the microstructural observations. The diffraction pattern at (311) in the bottom region demonstrates a peak shift towards higher angles, which is from ~ 89.98° in the top

region to ~ 90.13° in the bottom region. A possible explanation of the observed (311) peak shifts is the chemical changes among the bottom, middle and top regions, i.e., the depletion of Mo occurs together with the segregation of Ni and Fe in the matrix at the bottom, which is supported by the EDS results shown in Table 4.1. The atomic radii of Ni and Fe are smaller compared with Mo, hence this chemical difference leads to a decrease of the lattice constant and the resultant peak shift towards a higher angle for the bottom region. Furthermore, the top region sample shows a broader (200) peak with a full-width-at-half-maximum (FWHM) of 0.51° compared with that of the middle region sample (FWHM = 0.40°). This may be because of more dislocations existing in the top region. More discussions will be presented below in conjunction with the TEM results.

The microstructure of the samples in different areas was further investigated by TEM, as shown in Fig. 4.11. It is evident that the matrix of the alloy is γ-Ni, and a larger number of dislocations exist in the top region (Fig. 4.11a and b) than in the other two regions (Fig. 4.11c-f). During manufacturing, the dislocations can move at high temperatures and form arrays of dislocations, i.e. subgrain boundaries with an example shown in Fig. 4.11d. This is in agreement with the XRD results. One set of selected area diffraction (SAD) patterns for the two areas in the middle region further confirms that the boundary between the two areas is a subgrain boundary (Fig. 4.11c), whereas different SAD patterns between the two areas in the bottom region indicate that the boundary is a grain boundary (Fig. 4.11e). Moreover, it can be observed that from the top to the bottom region, the length and density of dislocations within grains decrease, but the amount of subgrain boundaries seems to increase. In addition, arrays of particles are found at the grain boundaries in the bottom part, which is rich in Mo, as shown in Fig. 4.12a, whereas the particle is not found in the middle and top regions in the

examined TEM specimens. The particle in Fig. 4.12b is identified as Ni_2Mo_4C in terms of its cubic structure of a = b = c = 11.2 Å [31], according to the SAD patterns in Fig. 4.12c. The chemical composition of the particles (Fig. 4.12d) further confirms that these particles are carbides. From the exploration of the thermal cycle in 3D rapid prototyping by Zhao et al. [218], the bottom region can experience longer heat immersion after solidification, which acts as heat treatment from the upper layers. This is considered to contribute to the appearance of carbides at the bottom.

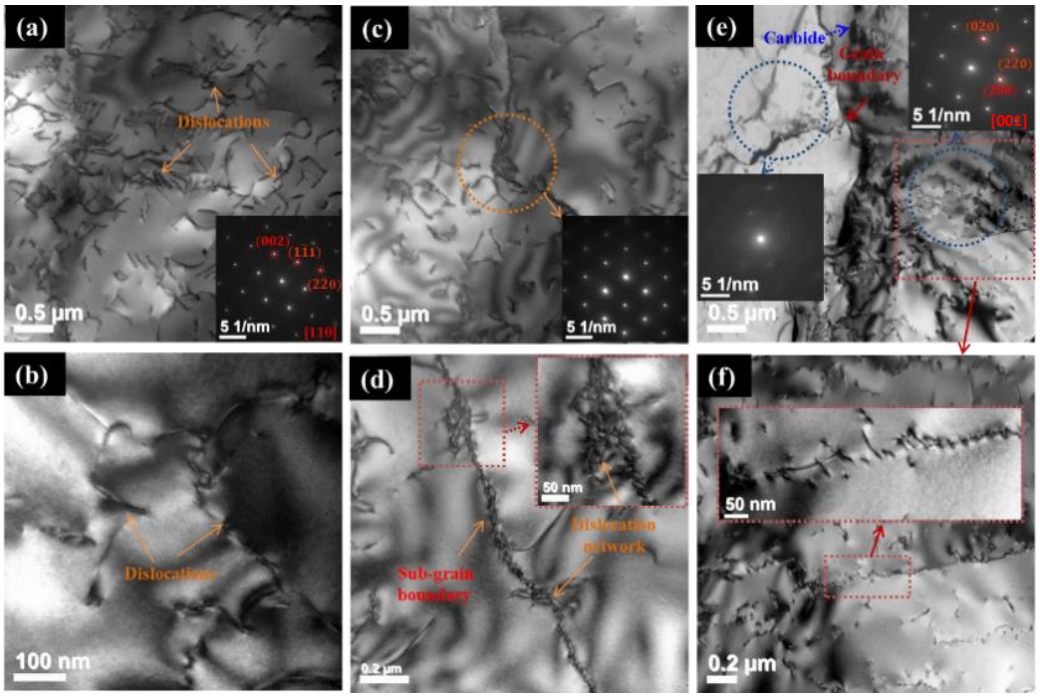

Fig. 4.11 Typical TEM images for the three sections: (a-b) top region; (c-d) middle region; and (e-f) bottom region

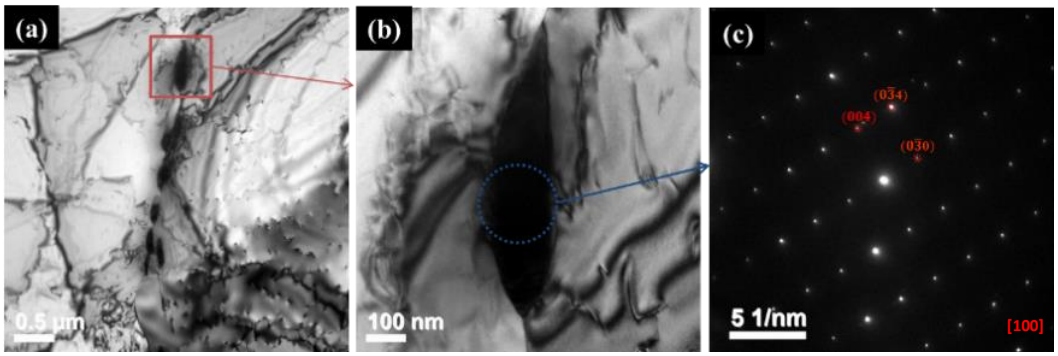

(d)	Composition wt.%
Element	Ave. (10 points)
C	9.94
O	0.23
Si	0.07
Ti	0.26
Cr	11.10
Mn	0.09
Fe	4.07
Ni	29.50
Mo	39.00
W	5.74

Fig. 4.12 TEM, SAD and EDS of carbides in the bottom area of the sample: (a-b) TEM images showing carbides at grain boundaries; (c) SAD pattern indexed according to Ni_2Mo_4C; and (d) EDS composition of carbides

4.3.2.4 Bulk texture

Neutron diffraction was used to study the bulk texture in the as-fabricated Hastelloy C276 alloy. The recalculated (111), (200) and (220) pole figures of the matrix phase from the orientation distribution function (ODF) are presented in Fig. 4.13, and the unit of multiples of random distribution (m.r.d) was used to depict the texture strength scale for each pole. As can be seen, a sharp fibre-type (200) crystallographic bulk texture was observed, which is consistent with the TEM results. As is widely studied, the strong texture along the <001> direction in AM-fabricated Ni-based alloys occurs ascribed to the maximum solidification driving force from the highest temperature gradient which is almost aligned with the deposition direction [177].

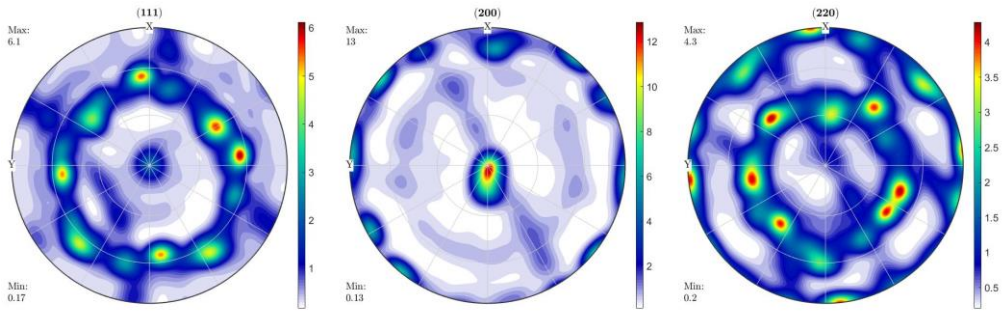

Fig. 4.13 Bulk texture from neutron diffraction and strong fibre-type (200) texture can be found.

4.3.3 Mechanical properties

4.3.3.1 Microhardness

Figure 4.14 shows the microhardness profile of the specimens in the cross-section part (y-z plane) along the lines at the top, middle, and bottom in the horizontal direction (y) and along the centerline in the vertical direction (z). Fig. 4.14a shows the test locations, among which the bottom test line is 5 layers away from the substrate to avoid the influence of dilution. The traverse hardness measurements were performed on both as-deposited layers and re-heated layers. Comparing the microhardness distribution (Fig. 4.14b - c), the values from horizontal (y) and vertical (z) tests display a uniform state and no significant variations of the microhardness values in different regions or directions, fluctuating from 200 to 215 $HV_{0.1}$ in readings. This is considered due to the reasonably homogeneous dendritic structure. The consistent hardness of WAAM Hastelloy C276 is a positive aspect of the mechanical properties.

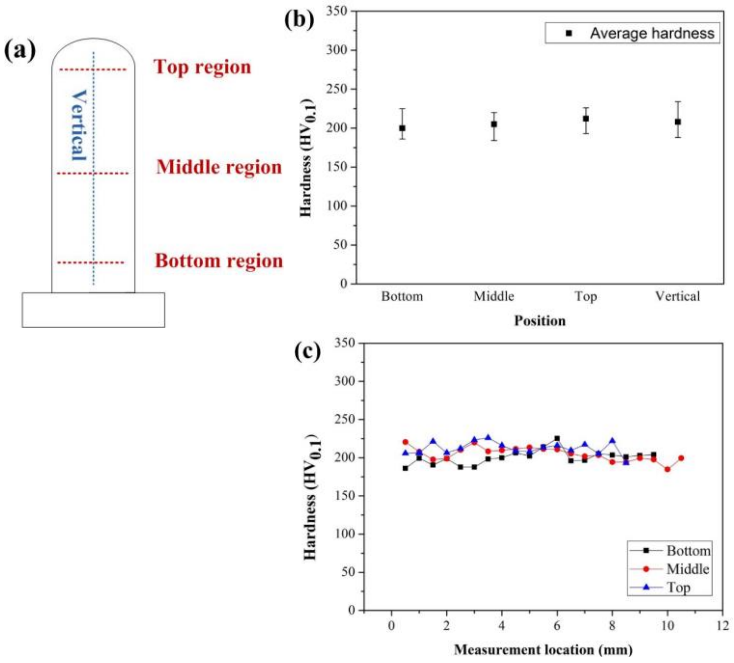

Fig. 4.14 Hardness comparison of the specimen taken from the y-z plane: (a) Illustration of hardness testing position; (b) Comparison of average hardness in different regions and directions; (c) comparison of horizontal (y-direction) hardness from top to bottom

4.3.3.2 Tensile strength

The mechanical properties, including ultimate tensile strength (UTS), yield strength (YS), and elongation of as-fabricated samples in the travelling direction (x-y) and deposition direction (y-z) are shown in Fig. 4.15. As can be seen in Fig. 4.15a, the average values of UTS and YS for the travelling direction samples (469 ± 52 MPa and 287 ± 50 MPa) are larger than those (399 ± 12 MPa and 186 ± 27 MPa) for the deposition direction samples. Both directions have excellent ductility properties, but also display different values. A deterioration in elongation is present in the x-y plane, being 43 ± 6%, but higher ductility is exhibited in the y-z plane, being 55 ± 3%. This anisotropy in mechanical properties can be attributed to microstructure variation. As is seen in Fig. 4.3, the sample has intense upward elongated dendrites. Compared to the vertical samples, the travelling direction samples have more dendritic boundaries or interdendritic areas in the loading direction and, therefore, more dislocations with the increase of loading can be accommodated within the crack nucleation in this area before a fracture occurs [220]. Moreover, the strong texture (see Fig. 4.13) will also induce tensile anisotropy, as reported in the previous study [149, 177, 182].

Figures. 4.15b - c presents the distribution of the sample tensile properties from top to bottom (travelling direction H1-H10) in the x-y plane and three deposition direction samples (V1-V3) in the y-z plane. Generally, the tensile strength and elongation are relatively uniform, but a slightly decreased tensile strength can be found at the top part, as shown in Fig. 4.15b. Conversely, ductility exhibits a roughly contrary tendency, as shown in Fig. 4.15c. The variability in the travelling direction test is generally consistent with the finding of the PDAS, where the top part possesses more larger-sized PDAS while a refined microstructure exists at the lower part. A fine PDAS induces better mechanical properties to a large extent in this research. More dendritic

boundaries possibly resist further dislocation movement, increasing resistance to some extent to plastic deformation, resulting in higher tensile strength. However, due to the significant difference in size and amount of *P* phase, there is no evidence to lead the connection between *P* phase and mechanical properties in this research.

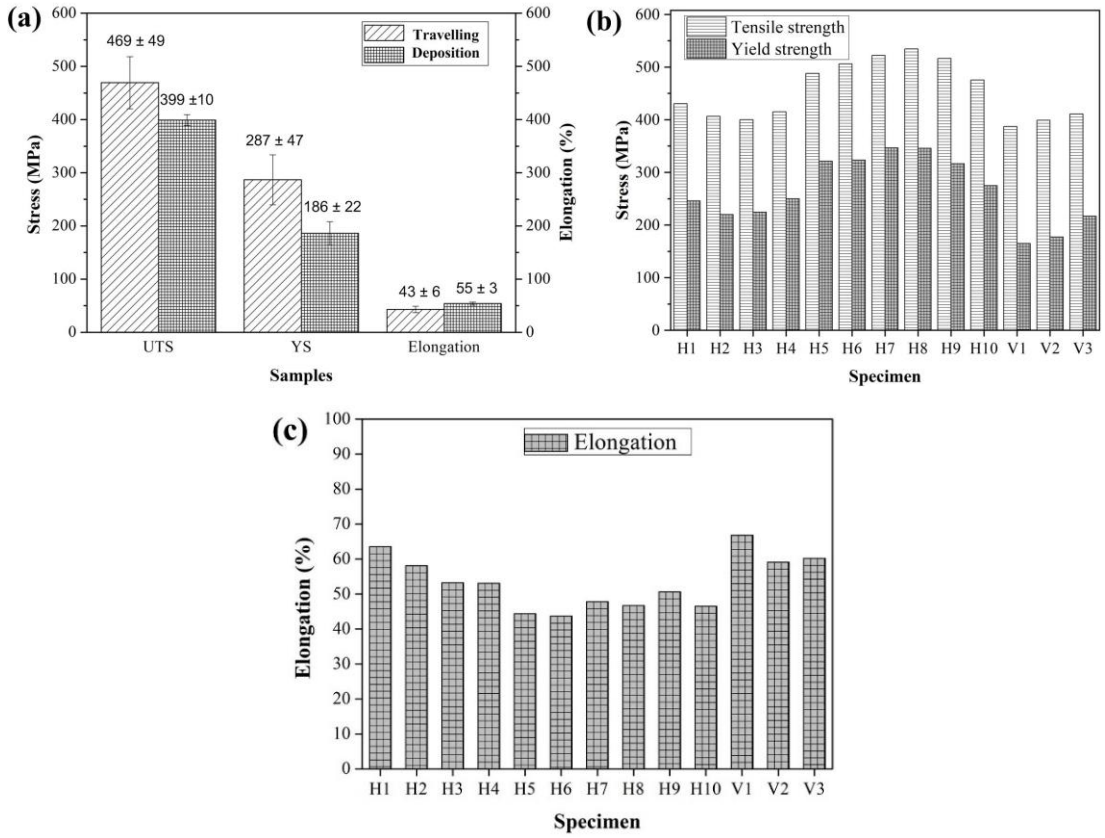

Fig. 4.15 Tensile properties of as-deposited samples taken from travelling (x-y plane) and deposition (y-z plane) directions: (a) comparison of an average value of the specimens from the travelling and deposition directions; (b) stress distribution of different specimens; (c) elongation of different specimens

4.3.3.3 Fracture behaviour

Figure. 4.16 presents the fracture surfaces of the as-received tensile samples. It may be observed from Fig. 4.16a that the tensile specimens were not fully separated when the tensile tests stopped. A large number of dimples scattered throughout the fracture surfaces demonstrate a typical ductile morphology (Fig. 4.16b-d), evidencing favorable ductility properties for the as-deposited WAAM Hastelloy C276. Anisotropy in

mechanical properties may be deduced from the fracture morphology. Comparing the travelling and deposition direction samples, the fracture surface for the travelling direction samples (Fig. 4.16b - c) is quite sharp, implying a lower ductility than the deposition direction ones where there are significant microvoids scattered uniformly throughout (Fig. 4.16d).

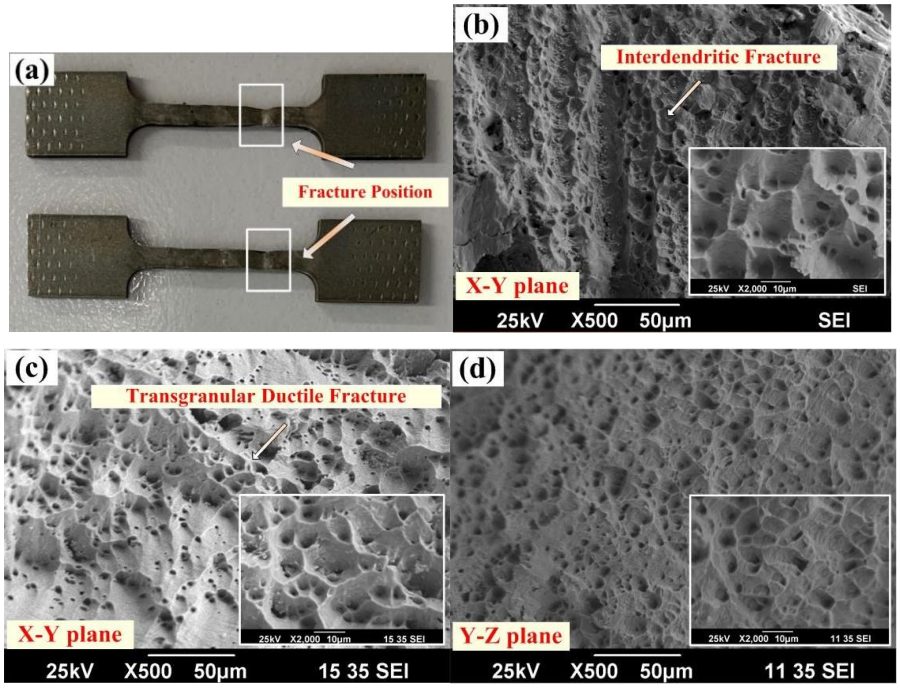

Fig. 4.16 Fracture behavior of deposited metal: (a) fracture position of tested samples, (b-d) SEM microstructure of fracture surface of the sample; (b) the sample in x-y plane with lowest strength value; (c) the sample in x-y plane with highest strength value; (d) the sample in y-z plane

Fig. 4.16b - c presents the fracture morphology of the samples with the lowest (Fig. 4.16b, sample H3 at the top part), and the highest (Fig. 4.16c, sample H8 at lower part) strength values in the travelling direction. From the images under high magnification, there is no significant difference. However, at lower magnification, it was found that the fracture at failure occurs along the dendrite boundaries, showing an interdendritic fracture morphology in Fig. 4.16b, while Fig. 4.16c displays a transgranular fracture. It may be concluded that interdendritic fracture leads to a lower tensile strength than

transgranular fracture. The tensile properties are significantly affected by microstructure where the occurrence of large dimples on the fracture surface results in a low tensile strength [161, 247]. In this research, a finer microstructure existed in lower regions than the top part, which is in agreement with previous findings, as is shown in Fig. 4.6.

4.3.3.4 Preliminary creep testing

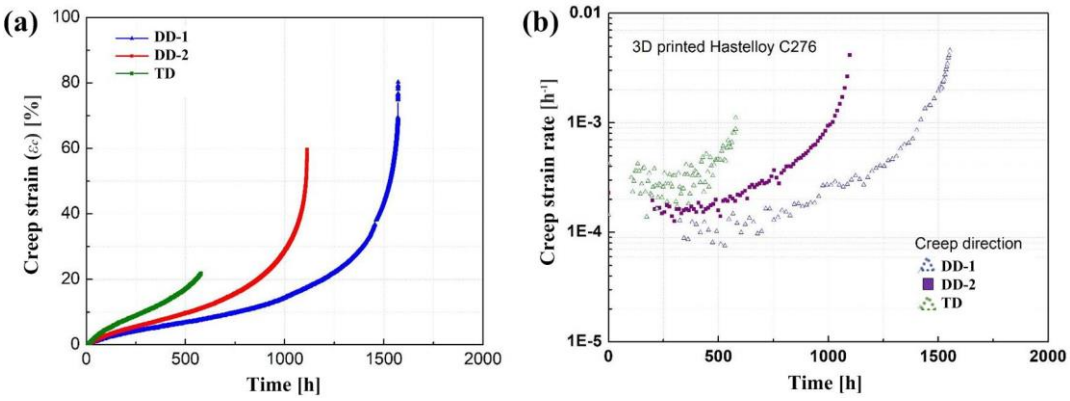

*DD-deposition direction; TD-travelling direction

Fig. 4.17 The creep behaviour of the Hastelloy C276 alloy crept at 973 K (700 °C) and stress condition of 165 MPa. (a) Creep strain vs. time curve, and (b) Creep strain rate vs. time curve

Figure 4.17 shows creep rupture curves and creep rate-strain curves, and travelling direction and deposition direction had high heterogeneous creep behaviour responses to the creep load. The creep rupture curve indicates that the test in the travelling direction sample failed after 579 h (t_c) at 33% strain (ε_c), while two deposition direction samples fractured after remarkably extended creep life and strain of 1572 h and 1113 h at 84% and 62%, respectively. The creep rate ($\dot{\varepsilon}_c$) was decreased from 2.36×10^{-4} h^{-1} in the travelling direction to 1.02×10^{-4} h^{-1} and 1.04×10^{-4} h^{-1} in the deposition direction, respectively. This is well demonstrated that the creep anisotropy existed in the GT-WAAM fabricated Hastelloy C276 alloy. All three samples displayed the first, secondary and tertiary stages of creep curves, and the stable stage was highly increased

in the two deposition direction samples, revealing an elongated t_c compared with the travelling direction sample.

Creep properties can be influenced by different microstructures, such as dislocations, precipitations, textures or grain size and morphology, etc. As shown in the previous part, a strong texture was found in the as-fabricated samples. The columnar boundaries parallel with the loading axis were found to be highly resistant to strain accumulation during creep. In comparison, more grain boundaries existing in the horizontal direction sample will lead to a higher creep rate, ascribed to the dislocation movement and the tendency of dislocations to accumulate and become a fracture point. The anisotropy of creep results from two directions is considered due to the strong texture induced by AM processes, which can be utilised based on the stress distribution of the components. Due to the current work being just a preliminary study for the creep test, and the extremely long testing times required to perform thorough creep tests. More work will be required to confirm the influencing factors on creep anisotropy.

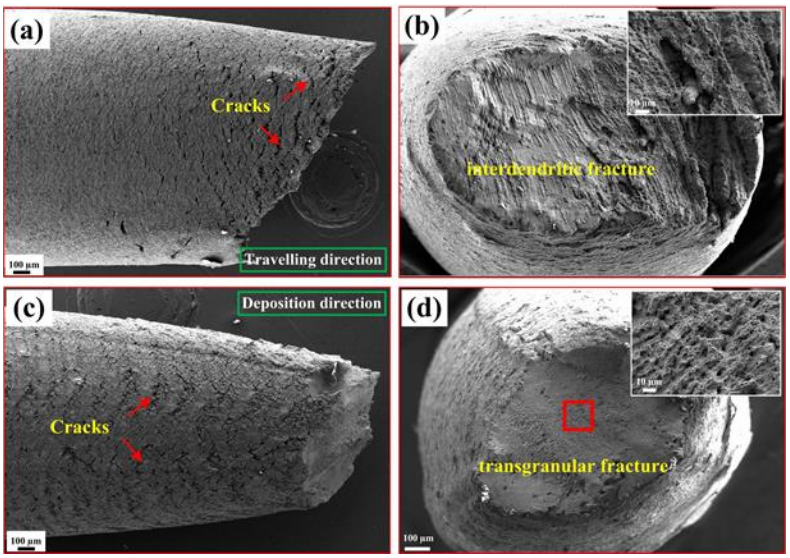

Fig. 4.18 Cracks and fracture surface of the samples from two directions: (a-b) travelling direction;(c-d) deposition direction

The typical fracture surface of the samples from travelling direction and deposition direction after creep test is displayed in Fig. 4.18. In general, a significant amount of cracks were observed on the surface of the samples perpendicular to the loading direction, and a large number of dimples on the fracture surface of two direction samples indicated a ductile creep fracture of GT-WAAM fabricated Hastelloy C276 alloy. It was noted that the amount of surface cracks in the travelling direction is much less than that in the deposition direction, which were highly concentrated in the vicinity of the rupture area, while the cracks in the deposition direction sample were spread throughout the sample's surface. An obvious necking phenomenon was observed in the deposition direction sample. Moreover, cracks on the fracture surface propagated in a sharp interdendritic fracture manner in the travelling direction sample, while the deposition direction sample exhibited a very plane surface in a transgranular fracture.

4.4 Conclusions

Applying the GT-WAAM process to a Hastelloy C276 component is feasible, enabling accurate fabrication without any visible defects. In the current research, the microstructure and related mechanical properties of the WAAM Hastelloy C276 component are explored and evaluated. Anisotropy is found both in microstructure and mechanical properties. Based on the results obtained, the following conclusions may be drawn:

(1) The microstructure of GT-WAAMed Hastelloy C276 has Ni-γ matrix, dominated with directional elongated columnar dendrites and scattered with intermetallic *P* phases in the interdendritic area. Ni_2Mo_4C carbide is found only in the bottom regions, which might be due to a longer period of heat accumulation than upper regions. There are a large number of dislocations which can form subgrain boundaries, and the amount of

subgrain boundaries seems to increase from top to bottom.

(2) The variations in microstructure lead to anisotropy in mechanical properties. The travelling direction samples (x-y plane) exhibit higher tensile strength but lower ductility than the deposition direction samples (y-z plane), which is considered due to the elongated dendrites in the matrix. However, the opposite tendency was observed in high-temperature creep properties. Higher strength and ductility were obtained from deposition direction than from travelling direction samples. This is considered due to the strong fibre-type texture.

(3) The well-distributed microhardness in different locations of the as-deposited specimens can be explained by the strong directional dendrites that dominate with microstructural evolution.

5 Effects of Post Heat Treatment on the Microstructure and Mechanical Properties of Wire Arc Additively Manufactured Hastelloy C276 alloy

5.1 Introduction

Due to the complex rapid thermal-cycling histories experienced during manufacturing, the WAAM-produced components may suffer from high residual stresses, compositional segregation, and anisotropies in the microstructure and mechanical properties, all of which limit the application of the as-deposited components [8, 144]. Approaches that have been employed to improve the quality of fabricated components using WAAM include; interpass cold rolling to control residual stress and distortion [248], and interpass cooling to refine the microstructure and improve hardness and strength [249]. Additionally, PHTs have been used to improve the mechanical properties of the manufactured Ni-based alloy components.

A PHT for Ni-based alloys is usually implemented to relieve residual stress, homogenise the microstructure and composition, and/or dissolve the second-phase precipitates after the manufacturing process [250]. These PHT processes for Ni-based alloys should avoid certain sensitisation temperature ranges to mitigate susceptibility to intergranular corrosion attacks [251]. The recommended stress relief temperature range for the Ni-based alloys is from 650 °C to 870 °C, however, such heat treatment may lead to the formation of secondary phases or precipitation that are detrimental to mechanical properties [252]. The solution annealing of Ni-based alloys is normally performed in a temperature range of 1040 °C to 1200 °C, in order to dissolve all the second phases into the γ-Ni matrix [252].

A suitable PHT is essential for most additively manufactured Ni-based alloys to optimise their microstructure and properties, including creep and corrosion resistance at both ambient and elevated temperatures. The feasibility of the synthesis of Hastelloy C276 by WAAM was investigated in the last section. It was found that crack-free Hastelloy C276 components could be deposited by WAAM, however, the room-temperature strength of the as-deposited alloy was lower compared to the traditionally manufactured counterpart. The focus of the present chapter is to investigate the effects of selected PHTs on the microstructure and the corresponding mechanical properties at room temperature of a Hastelloy C276 component fabricated by WAAM. The results revealed that PHT can be an effective way to improve the performance of the WAAM fabricated Hastelloy C276 alloy.

5.2 Experimental

5.2.1 Experimental setup

A GT-WAAM system [76] was used in this work to deposit a thin wall structure on a plain carbon steel substrate with dimensions of 205 mm × 105 mm × 6 mm. Post flow shielding gas was applied for a duration of about 30 s. A Hastelloy C276 wire with a diameter of 1.2 mm was used, and the compositions are listed in Table 3.1. The main process parameters are summarised in section 3.2.1. The as-deposited component was a single thin-walled structure of fifty deposition layers with dimensions of 10 mm × 100 mm × 45 mm (width × length × height).

5.2.2 Material characterisation

The as-deposited component was sectioned into three groups of samples along a direction parallel to deposition. One group of samples was used for the as-built component examination, and the other two groups were for the PHT component

examinations. One of the applied two PHTs was performed at 871 °C for 6 h in the air, followed by water quenching based on Ref. [102]. Note that this PHT at 871 °C for 6 h has been confirmed to be an effective process for the stress relief treatment of Ni-based alloy weldment components produced by LB welding [102] and GTAW [253]. The other PHT was carried out for the solution annealing at 1177 °C for 30 min in the air, then water quenched following Ref. [254]. The sampling locations and dimensions of the mechanical testing and metallographic analyses are shown in Fig. 5.1. To avoid element dilution from the substrate and a stable microstructure, the test samples were extracted at least four layers away from the substrate and 10 mm away from the side regions in the as-deposited materials.

Metallographic samples were observed on the deposition cross-section (y-z plane). Samples were prepared by mounting, grinding, and polishing followed by electro-etching. Microstructures were first observed using a Nikon Optiphot reflected light OM. SEM equipped with an EDS detector was further utilised for observations of grain structure, precipitation, fracture mode, and composition. Compositions (wt.%) were estimated using internal Oxford EDS standards. ImageJ software was applied to calculate the size of the dendrites [226]. TEM analyses were carried out, operating at 200 kV. Thin lamellae for TEM examination were machined using a FIB, and precipitates were identified by SAD.

Twenty tensile test samples in the travelling direction (x-y plane) and five in the deposition direction (y-z plane) were extracted for testing (Fig. 5.1). Tensile tests and Vickers microhardness were performed at room temperature with parameters shown in section 3.6. XRD was performed for phase identification of the samples taken from the longitudinal region (y-z plane) (Fig. 5.1). A GBC diffractometer equipped with the Cu

Kα radiation and a graphite monochromator was used for the data collection over a 2θ range from 30° to 100°.

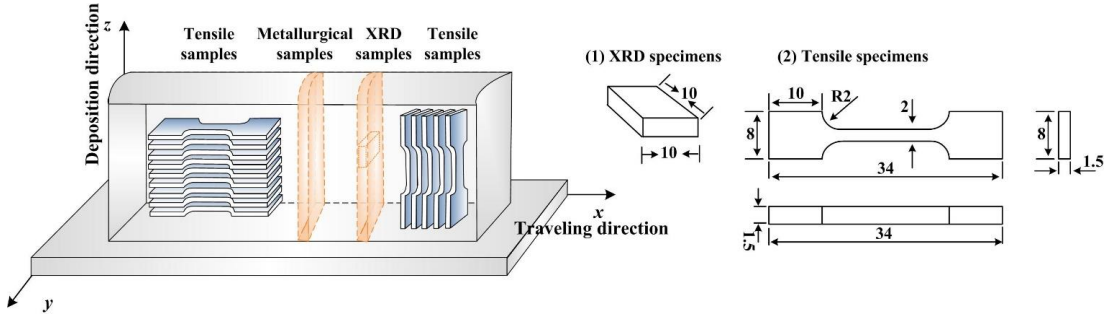

Fig. 5.1 Schematic illustration of sampling location and geometry of each sample

5.3 Results

5.3.1 Microstructural features

Figure 5.2 shows the microstructures of the as-built and heat-treated (871 °C and 1177 °C) samples. For all the three conditions investigated, a columnar dendrite microstructure was observed. As shown in Fig. 5.2a, the as-built sample was dominated by large columnar grains in the microstructure which was composed of aligned dendrites oriented closely along the deposition direction. These aligned dendrites transverse several layers, demonstrating a significant directional growth feature. Some cellular-like grains without any secondary or tertiary dendrites are occasionally observed. Grain boundaries and layer boundaries (fusion interfaces) were visible, as indicated by yellow dotted lines in Fig. 5.2a. The heat-treated sample at 871 °C displayed a similar dendrite microstructure as the as-built sample, showing the well-defined layer boundaries and columnar grain boundaries. However, some of the columnar grain boundaries observed in this sample appeared to have formed migrated grain boundaries (MGBs), consistent with [1], as highlighted in Fig. 5.2b. As shown in Fig. 5.2c, the 1177 °C PHT sample showed a more homogenous microstructure indicated by the uniform etching characteristics, compared with that of the 871 °C PHT

sample (Fig. 5.2b), which resulted from the solution annealing treatment. The layer boundaries and grain boundaries were still perceivable after the 1177 °C PHT.

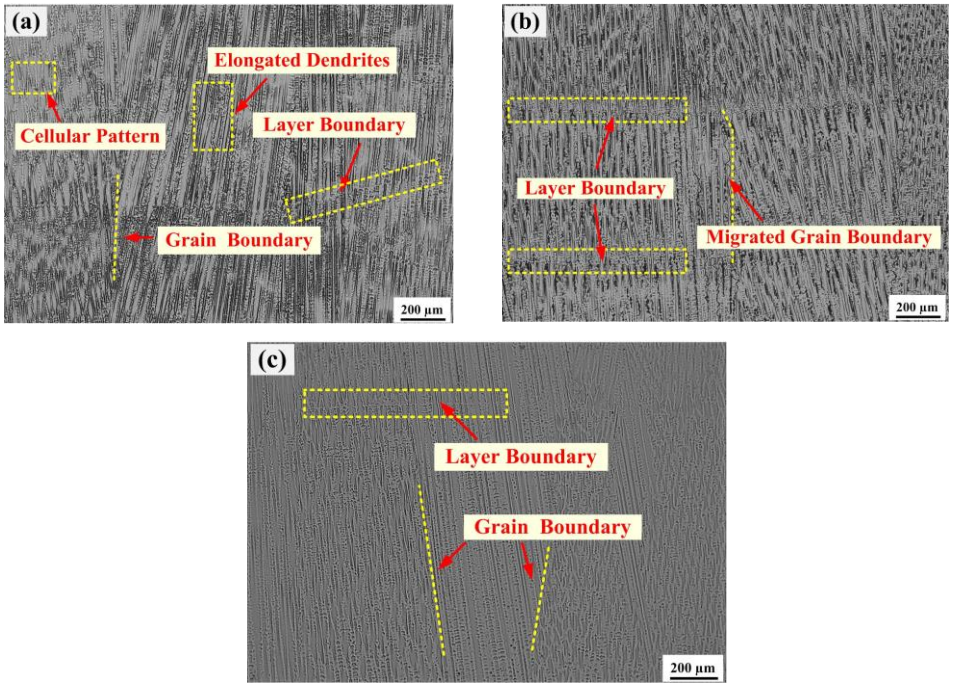

Fig. 5.2 Optical micrographs showing the cross-sectional (y-z plane) microstructure in the middle region of the components under three conditions: (a) as-built, (b) PHT at 871 °C, (c) PHT at 1177 °C

Figure 5.3 presents the dendritic microstructure and the precipitation morphology at higher magnifications for all three conditions. For the as-built sample, Figs. 5.3a-b, precipitates were located in the interdendritic areas. For the heat-treated sample at 871 °C, Figs. 5.3c-d, the clusters of newly formed submicron-sized precipitates were found in the dark interdendritic areas. Moreover, the small-sized particles were observed in the MGBs. For the heat-treated sample at 1177 °C, Figs. 5.3e-f, there was a reduction in both the size and amount of the interdendritic precipitates compared to the other two conditions. The small-sized or submicron-sized particles in the 871 °C PHT sample were not observed for the 1177 °C PHT sample.

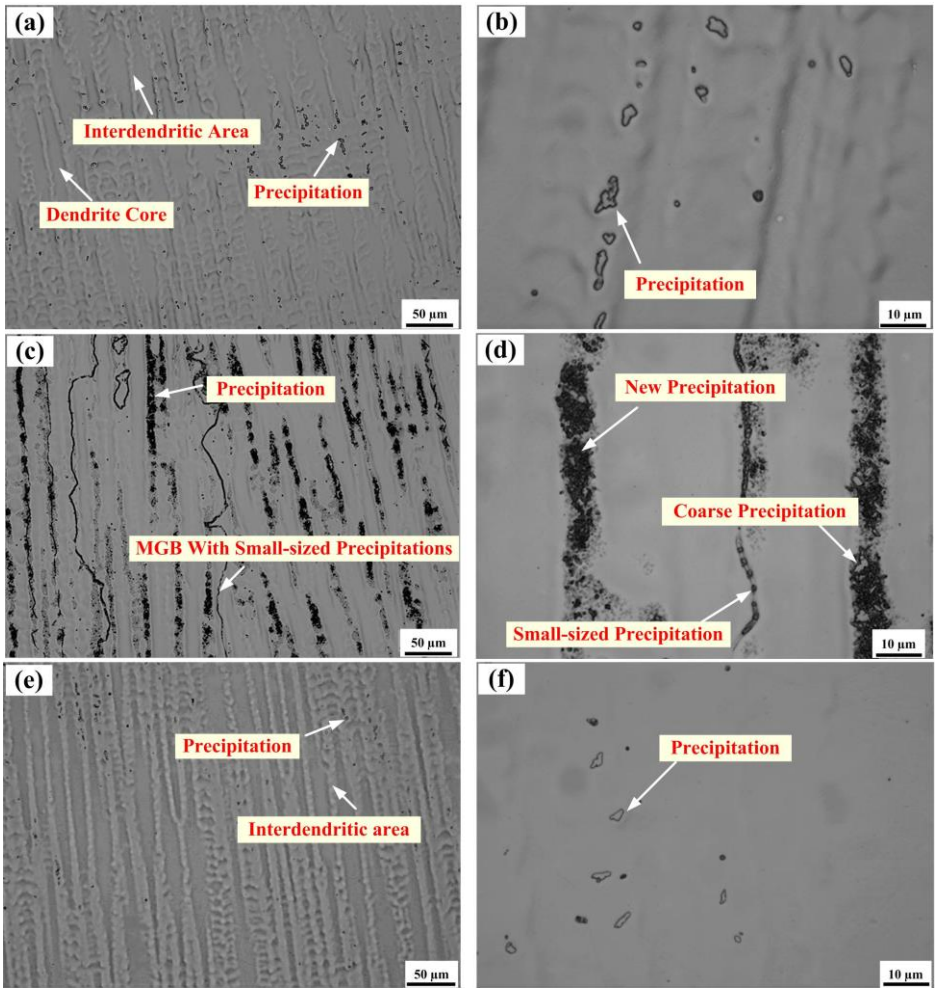

Fig. 5.3 Optical micrographs showing the dendritic microstructure containing precipitation at low and high magnifications in the three conditions investigated: (a-b) as-built, (c-d) PHT at 871 °C, and (e-f) PHT at 1177 °C

Figure 5.4 shows XRD patterns of the as-built and heat-treated samples taken from the y-z sections. The y-z plane is parallel to the deposition direction, in which the columnar grains are orientated. A dominant strong (200) peak was found in all three samples, suggesting the preferred orientation of the columnar grains was along <100> direction. Compared with the as-built sample, columnar grains with different orientations along the deposition direction were developed after PHT, i.e. more grains of <220> orientation along the scattering vector direction in both heat-treated samples and fewer grains of <311> and <111> orientations in the sample with PHT at 1177 °C. A possible cause for this observation is the potential abnormal dendritic grain growth [255]

occurred during PHT, which may induce changes in the preferred orientations of γ-matrix grains. However, the exact microstructural origin for the presumed textural change from the XRD data (Fig. 5.4) cannot be determined conclusively. In addition, no secondary phases of types frequently observed in the Hastelloy C276 matrix (*P*, μ nor carbide phases [1, 178]) were detected by XRD in the as-built and PHT samples. Note that for the PHT sample at 871 °C, some weak peaks were observed in a lower 2θ range of 30° to 50°, however, unambiguous phase identification was not possible presumably due to the fact that the low volume fractions of precipitates in the as-built and PHT conditions were beyond the detection limits of the applied XRD technique [220].

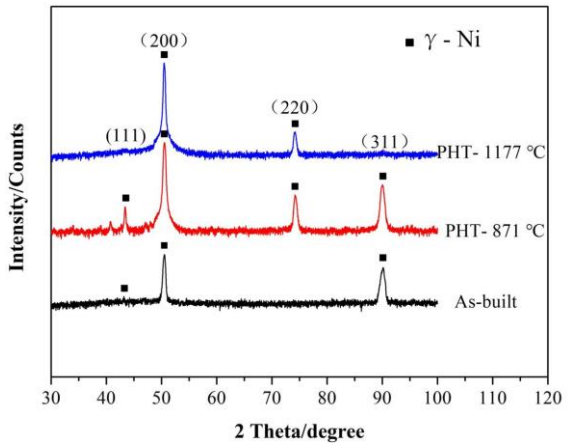

Fig. 5.4 XRD patterns of the samples under three conditions including as-built, PHT at 871 °C, and PHT at 1177 °C.

To further investigate the chemical composition and microstructural evolution (in particular, the precipitation) of as-built and heat-treated samples, SEM and EDS analysis was carried out. The results are shown in Fig. 5.5. For the as-built sample, Fig. 5.5a-b, the interdendritic precipitates (Point A in Fig. 5.5a) were not very distinct (lighter contrast compared to the matrix) and there were a few small-sized precipitates located at the grain boundary (Point B in Fig. 5.5b). For the sample after PHT at 871 °C, Fig. 5.5c-d, coarser precipitates relative to the as-built condition were clearly observed

at interdendritic areas (Point A in Fig. 5.5c). These were classed as coarsened primary precipitates. Moreover, a significant volume fraction of small-sized precipitates in the vicinity of the grain boundaries (Point B in Fig. 5.5d) and additional nano-sized precipitates (Point C in Fig. 5.5d) were observed. The average size of the nano-sized precipitates was 86 nm (width), as calculated using ImageJ software. After PHT at 1177 °C (Fig. 5.5e-f), interdendritic precipitation (Point A in Fig. 5.5e) was still present, but at a lower frequency compared with the 871 °C PHT condition, and the nano-sized precipitates were no longer present as well as the MGBs. As shown in Fig. 5.5f, grain boundary precipitates were not observed.

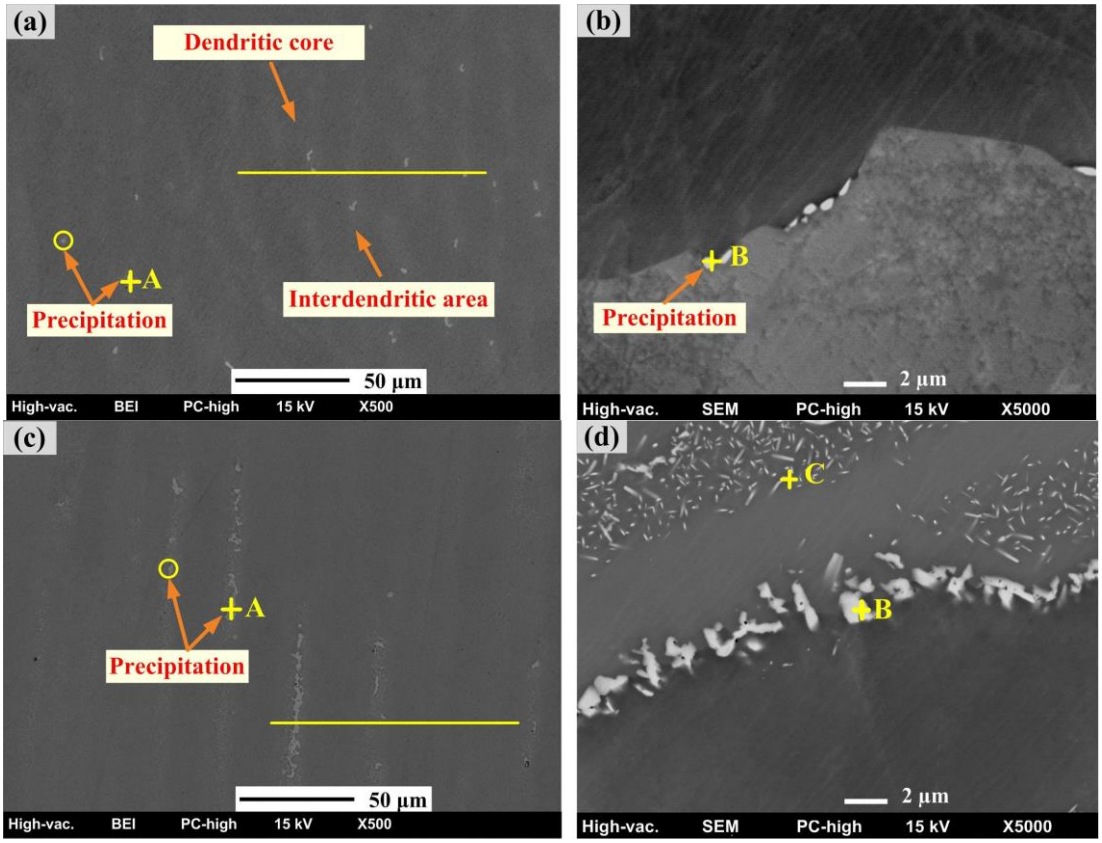

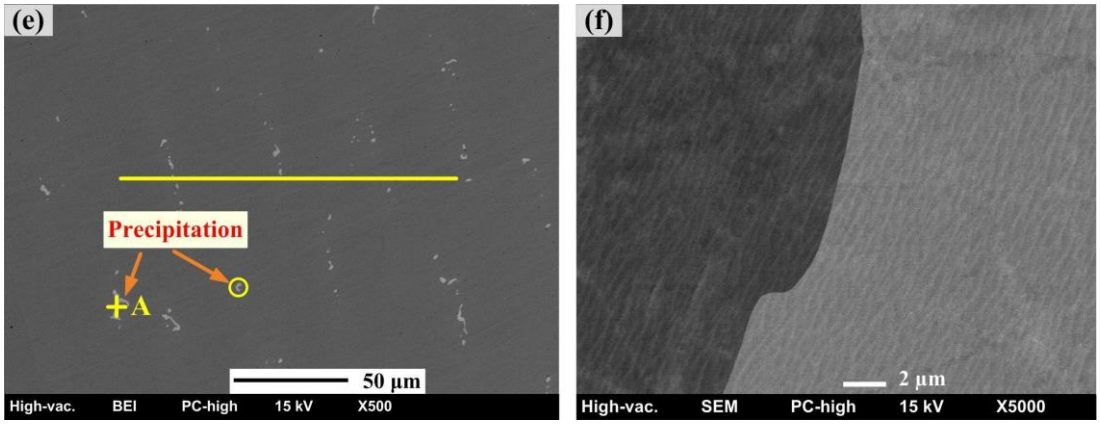

Fig. 5.5 Backscattered electron images of the matrix (left side) and grain boundary locations (right side), of Hastelloy C276 under three conditions: (a-b) as-built; (c-d) PHT at 871 °C; (e-f) PHT at 1177 °C. Note: locations of EDS analysis in Table 3 are marked in yellow.

The compositions of selected precipitates, the dendritic core, and interdendritic areas were analyzed by multiple EDS spot scans, and the estimated compositions, based on in-build EDS machine standards, are listed in Table 5.1. It was found that the precipitates were rich in Mo and W, and deficient in Ni and Fe compared with the matrix. The nano-sized particles at interdendritic locations, under the PHT at 871 °C, show higher Ni and lower Mo contents compared with the larger precipitates. Due to the small size of these particles, only qualitative results could be obtained, and the higher Ni concentrations might be due to increased beam interaction with the matrix. Elemental distributions from the line scans are shown in Fig. 5.6 (see Fig. 5.5 for line scan locations). These line scans showed that the interdendritic areas typically had higher Mo and decreased Ni compared to the dendritic core areas, especially at precipitate locations. The sample under PHT at 1177 °C showed the least variation in Mo and Ni between the interdendritic and dendritic core regions, which corresponds with the more uniform etching behaviour observed for the optical images (see Fig. 5.3).

Table. 5.1 EDS analysis estimates (wt.%) of the dendritic core, interdendritic area and precipitates, where interdendritic particles are 'location A', grain boundary particles are 'location B' and nano-sized particles are 'location C'.

Condition	Site	Ni	Cr	Mo	W	Fe
As-built	Precipitation (A)	32.4	14.8	41.8	6.6	4.4
	Precipitation (B)	37.1	14.5	36.4	7.5	4.5
	Dendritic core	58.3	15.9	14.2	4.5	7.2
	Interdendritic area	52.6	16.2	21.5	4.1	5.7
PHT-871°C	Precipitation (A)	30.1	15.5	45	5.9	3.7
	Precipitation (B)	29.4	15.2	45.2	6.9	3.3
	Precipitation (C)	39.8	15.0	34.3	6.5	4.4
	Dendritic core	59	15.5	14.8	4.4	6.4
	Interdendritic area	55.4	16.5	19.3	4.1	5.6
PHT- 1177 °C	Precipitation (A)	32.6	13.7	40.3	9.8	3.7
	Dendritic core	56.5	15.8	17.2	4.5	5.9
	Interdendritic area	55.3	16.2	18.4	4.1	5.9

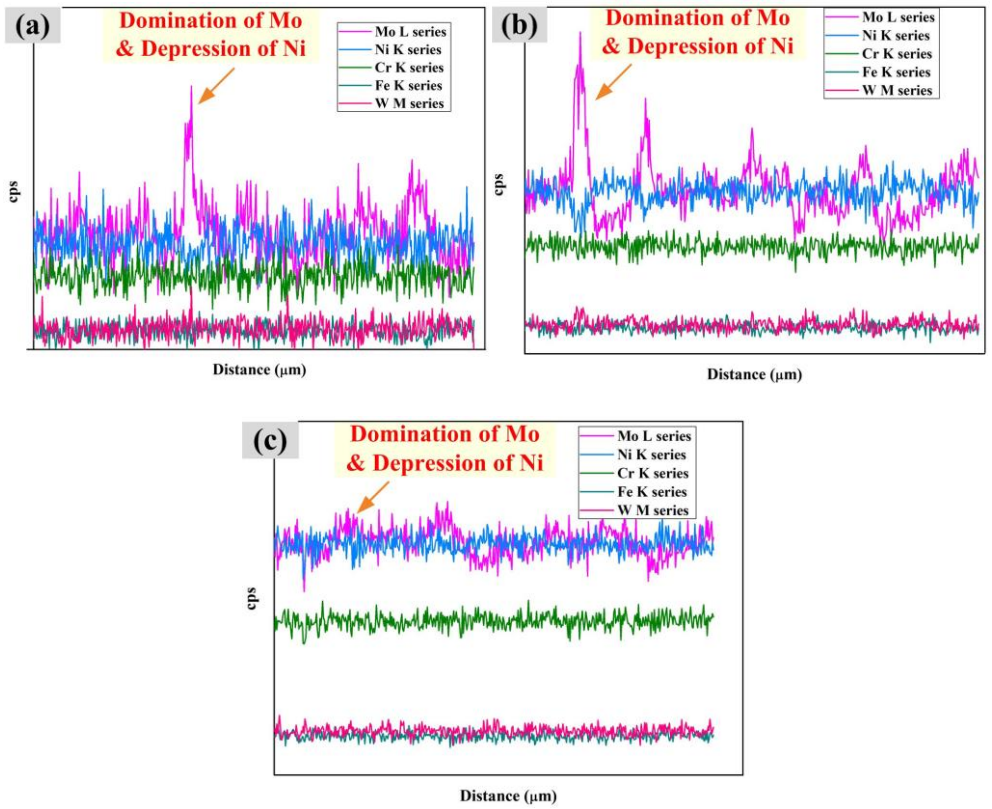

Fig. 5.6 Element distributions of the line scans, as shown in Fig 5, for the three sample conditions; (a) as-built; (b) 871°C PHT; and (c) 1177 °C PHT.

The significance of solid solution heat treatment at 1177 °C is to dissolve the intermetallic *P* phase, and no new phases will be formed under this temperature [256]. As more significant precipitations were observed in the 871 °C heat-treated sample, TEM analysis was further performed to confirm the phases in this sample. In Fig. 5.7a, three types of particles in the γ-Ni matrix (indexed in Fig. 5.7b) were identified; 1) relatively large, blocky, grain boundary particles; 2) primary interdendritic angular particles; and 3) smaller, rod-shaped interdendritic particles. The grain boundary Mo-rich particles are shown in Fig. 5.7c, with the corresponding SAD patterns of the particle in three tilt orientations. The indexed SAD patterns (Fig. 5.7 c) identified the grain boundary phase as the *P* phase in terms of its orthorhombic structure of a = 9.07 Å, b =16.98 Å, and c = 4.752 Å [87]. These precipitates had fine striations indicating planar defects, which were also manifested as light lines between spots in some SAD patterns. These defects are considered to be stacking faults or twins which are in the close-packed layer structure of the *P* phase [257]. Correspondingly, as shown in Figs. 5.7d-e, another examined grain boundary phase and the primary large-sized interdendritic precipitates were also indexed as *P* phase. In comparison, the smaller, rod-shaped Mo-rich interdendritic precipitates could be indexed as μ phase of hexagonal structure with a = b = 4.8 Å and c = 25.6 Å [258], as shown in Fig. 5.7f.

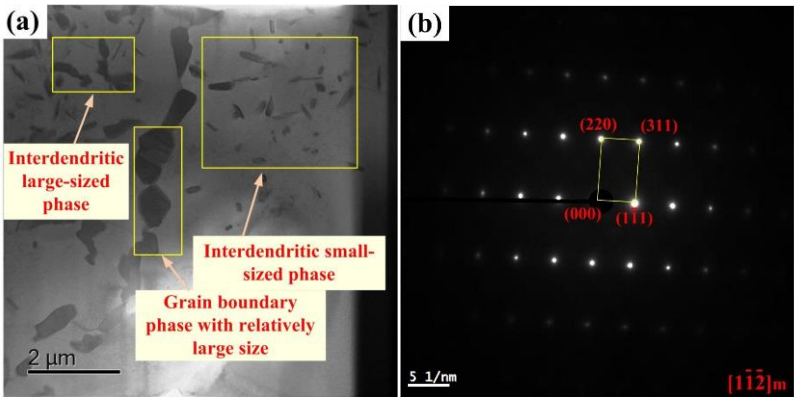

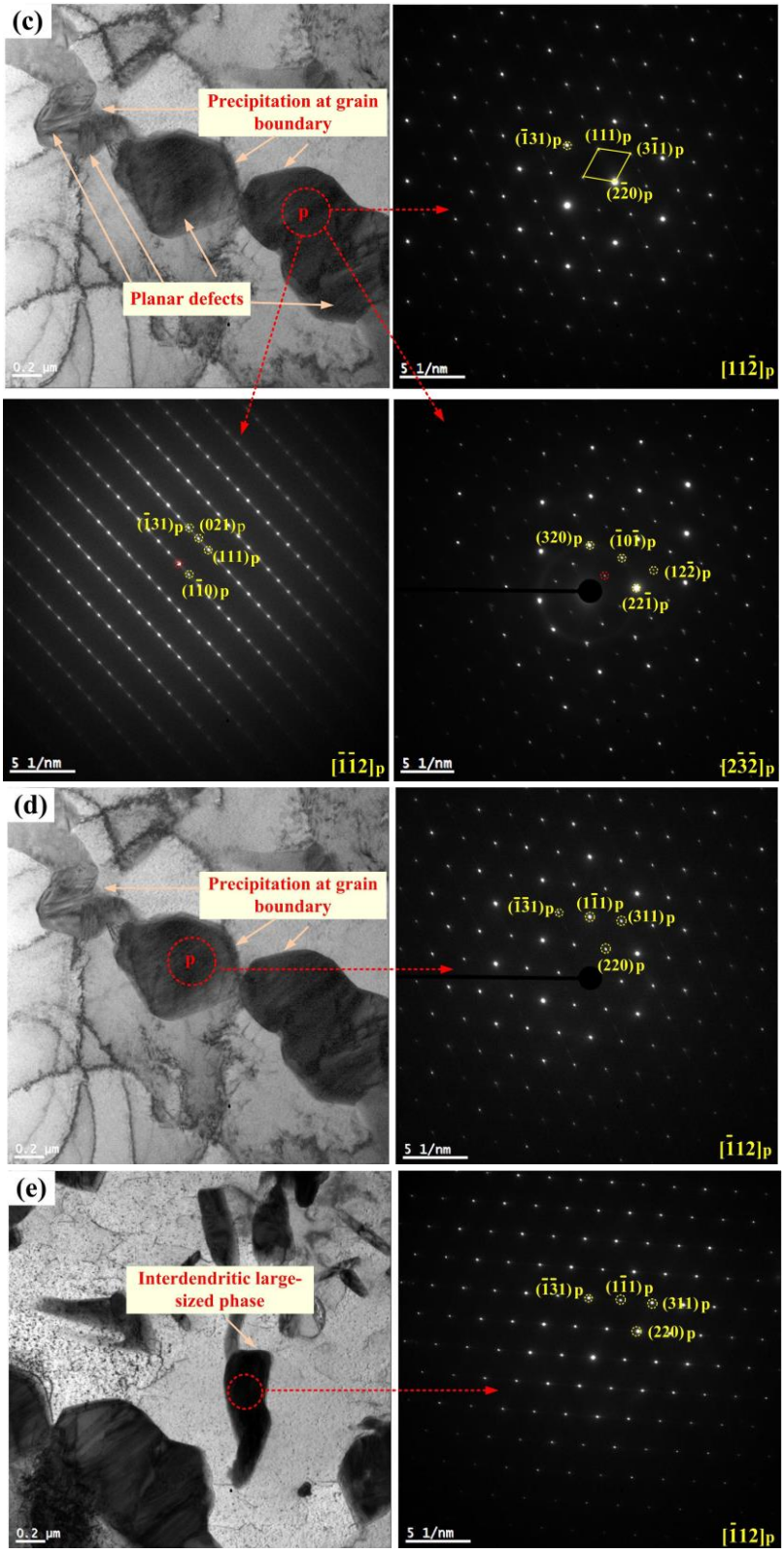
(c)
Precipitation at grain boundary
P
Planar defects
0.2 μm
(1̄31)p
(111)p
(31̄1)p
(220)p
5 1/nm
[11̄2̄]p
(1̄31)p
(02̄1)p
(111)p
(1̄1̄0)p
5 1/nm
[1̄1̄2]p
(320)p
(1̄0̄1)p
(12̄2̄)p
(22̄1̄)p
5 1/nm
[2̄3̄2̄]p
(d)
Precipitation at grain boundary
P
0.2 μm
(1̄31)p
(1̄1̄1)p
(311)p
(220)p
5 1/nm
[1̄12]p
(e)
Interdendritic large-sized phase
0.2 μm
(1̄31)p
(1̄1̄1)p
(311)p
(220)p
5 1/nm
[1̄12]p

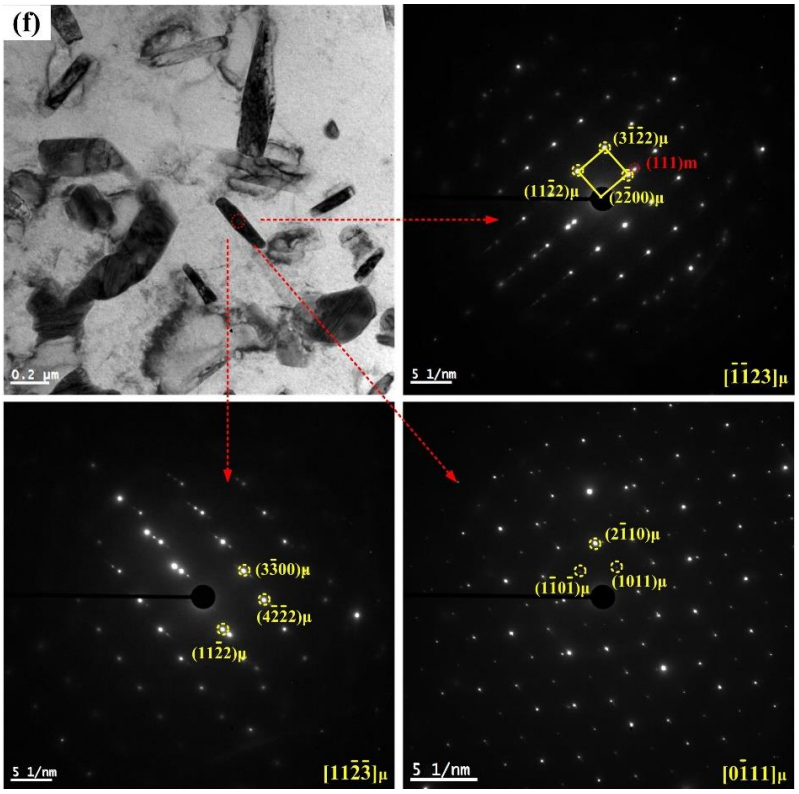

Fig. 5.7 Representative TEM results of the heat-treated sample at 871 °C: (a) a micrograph showing three types of precipitates observed; (b) SAD patterns of γ-Ni matrix; and (c, d) morphologies of the grain boundary *P* phase, (e) the large-sized interdendritic *P* phase, and (f) the small-sized interdendritic μ phase, which were indexed based on the corresponding SAD data.

Note that the SAD data of the precipitation were collected at three sample orientations to facilitate conclusive phase identification.

5.3.2 Mechanical properties

Figure 5.8 shows the microhardness results of the samples before and after PHT. The average microhardness result in Fig. 5.8a showed that the as-built sample exhibited the lowest mean hardness value of 207 ± 10 $HV_{0.1}$, compared to the samples under PHT at 871°C (274 ± 13 $HV_{0.1}$) and 1177 °C (242 ± 7 $HV_{0.1}$). After PHT, the hardness increased by 32% and 17% for 871 °C and 1177 °C PHT conditions, respectively. Fig. 5.8b presents the microhardness distribution on the cross-section in the y-z plane of the samples under three conditions. The microhardness fluctuations were observed from top to bottom in the deposition direction (z), among which the heat-treated sample at 1177 °C exhibited the most homogeneous hardness profile.

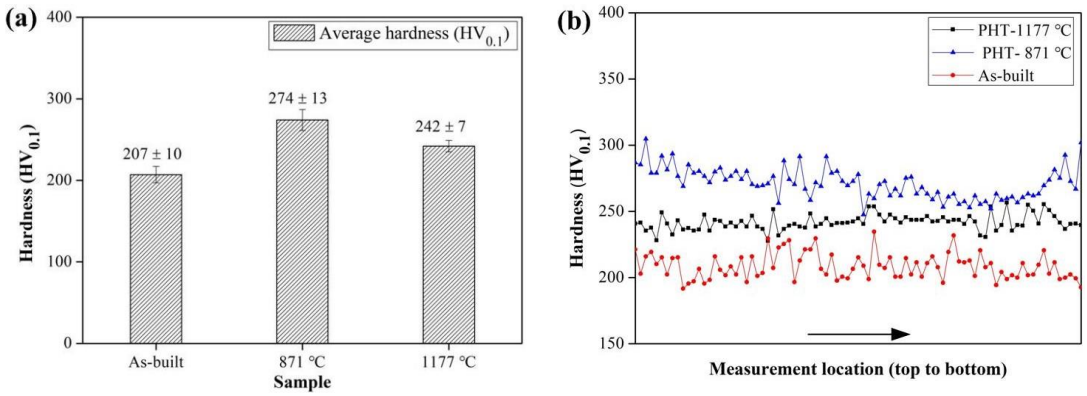

Fig. 5.8 Hardness distribution of the component under three conditions: (a) Comparison of average hardness; (b) Hardness distribution of three samples from top to bottom

The tensile properties in the travelling (x-y plane) and deposition (y-z plane) directions are shown in Fig. 5.9 for the three conditions. The average tensile properties of two testing directions at room temperature of the as-built and PHT specimens are shown in Fig. 5.9a. The increase in tensile strength after PHT aligned well with the hardness results. Compared with the as-built specimen, the heat-treated sample at 871 °C showed the highest increase in strength (strength increased from 453 ± 55 MPa to 743 ± 54 MPa) but the lowest total elongation (TE) (ductility decreased from 46 ± 8% to 38 ± 7%). In comparison, the heat-treated sample at 1177 °C not only showed an increase in strength (600 ± 60 MPa) but also a substantial improvement in TE (59 ± 5%), compared with the as-built sample. Figs. 5.9b-d display the tensile test results at the travelling and deposition directions for the as-built, PHT at 871 °C and 1177 °C, respectively. The as-built sample showed the greatest anisotropy, where strength was higher in the travelling direction than that in the deposition direction, but TE was lower. The heat-treated sample at 871 °C presented similar strengths in both directions, but slightly lower TE in the traveling direction. In comparison, the sample treated at 1177 °C showed only slightly higher tensile strength in the traveling direction, but almost the same YS and TE. Hence, the mechanical anisotropy property was decreased under this condition.

Overall, the component under 1177 °C PHT showed the best combination of strength and ductility.

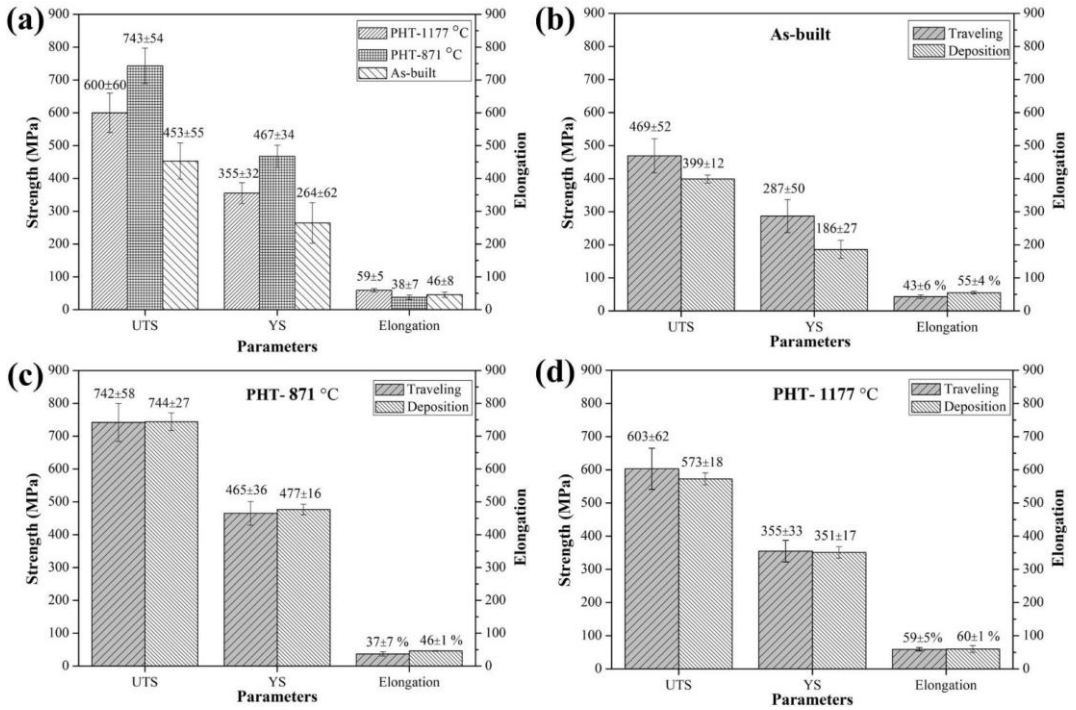

Fig. 5.9 (a) The average ultimate tensile strength (UTS), yield strength (YS), and total elongation of two testing directions (traveling and deposition) for the three conditions; and (b) - (d) the tensile properties measured from the traveling and deposition directions of the as-built, and 871 °C and 1177 °C heat-treated samples, respectively.

Figure 5.10 displays typical fractography of the samples under the three conditions for both the traveling (x-y plane) and deposition (y-z plane) directions after the tensile testing. In Fig. 5.10a-b, the traveling and deposition fracture surfaces were compared for the as-built sample. In the traveling direction, the fracture was predominately interdendritic, showing large microvoids and sharp tear ridges (inset). Whereas in the deposition direction, transgranular ductile fracture occurred, with numerous small-sized, but quite uniform microvoids (inset). This illustrates the anisotropic tensile property of the as-built WAAM Hastelloy C276 alloy. After PHT at 871 °C, as shown in Figs. 5.10c-d, a similar trend to above occurred - only the interdendritic fracture in the travelling direction was more prominent, and voiding in the deposition direction was larger,

corresponding to the lower ductility. From Figs. 5.10e-f, the samples after PHT at 1177 °C exhibited transgranular ductile fracture, regardless of the sample direction. Several deep and small microvoids together with some occasional spherical precipitation were observed, suggesting the improved plasticity of the sample under the condition of PHT at 1177 °C. After PHT at this temperature, the anisotropic nature of the as-built component was significantly decreased.

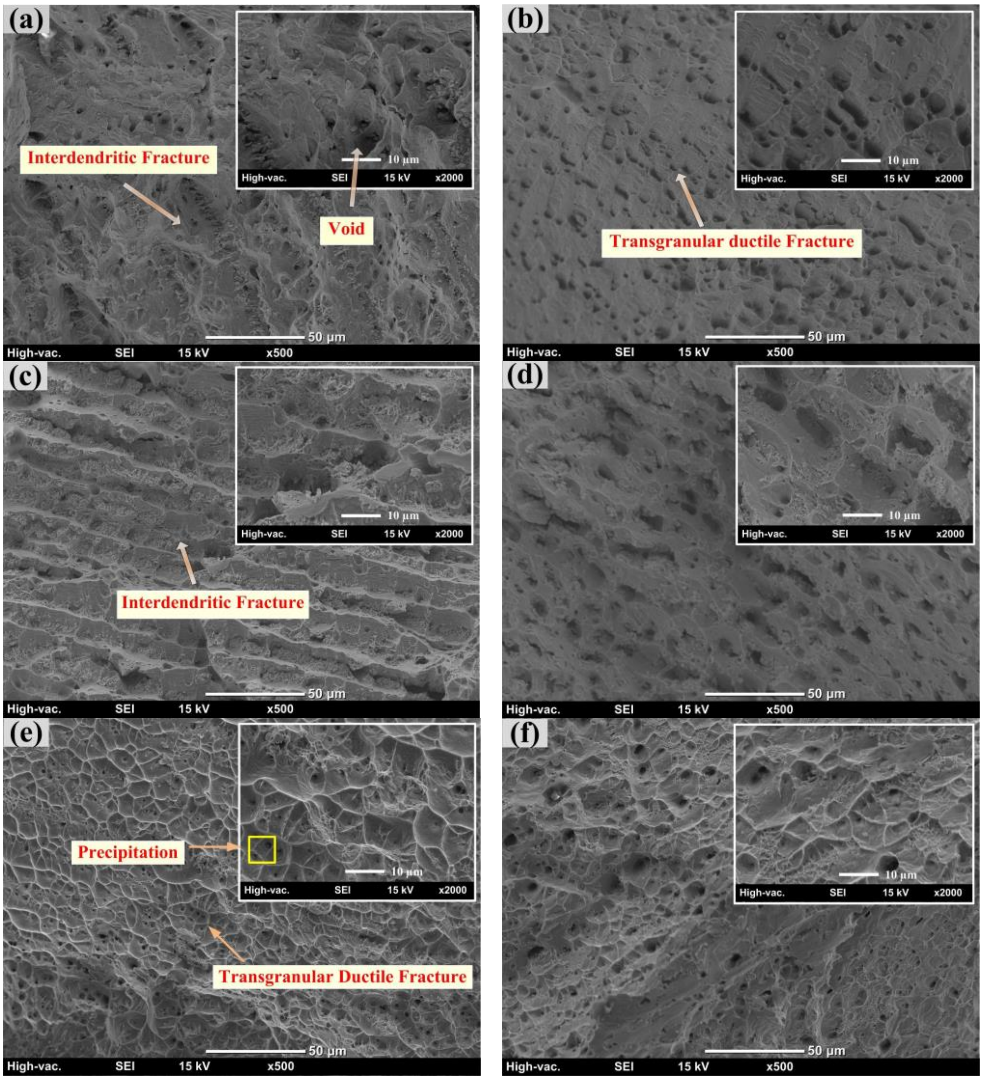

Fig. 5.10 Typical tensile fractography of the samples under three conditions in the traveling (x-y plane) and deposition direction (y-z plane) for (a-b) the as-built, (c-d) PHT at 871 °C and (e-f) PHT at 1177 °C.

5.4 Discussion

5.4.1 Microstructural evolution during deposition and PHT

As was shown in Fig. 5.2, the microstructure of all three components consists of epitaxial columnar dendrites which traversed several weld layers in the deposition direction. This phenomenon is inherent to other additively manufactured alloys and is attributed to the rapid thermal cycling experienced during the layer-by-layer deposition [148, 259, 260]. Due to the heat transfer from the subsequent layers, the previous dendrites can partially re-melt and realign in the preferred growth direction, i.e. the direction of the maximum thermal gradient. As a consequence, the preferential directional growth of the dendrites (i.e. the texture development) leads to the development of anisotropic mechanical properties [176]. It was found that the dendritic microstructure of the as-built alloy retained after PHT at 871 °C and 1177 °C, however, significant changes in the chemical elemental distribution and the precipitation were induced after PHT, as detailed in Section 5.3.1.

Based on the SEM-EDS elemental distribution analysis (Figs. 5.5 and Fig. 5.6, and Table 5.2), the dendritic core was found to be rich in Ni and Fe but depleted in Mo. This was attributed to the different diffusion coefficients of these elements caused by their different atomic radii [1, 31]. With the progression of the solidification which starts at the dendrite core, the heavy Mo element with a relatively large atomic radius will segregate aggressively in the molten pool and produce a steep concentration gradient against the interdendritic area. Thus, the dendrite core is depleted of Mo and the interdendritic regions are rich in Mo, which promotes the precipitation of Mo-rich particles. This is evidenced by the metallographic examination which showed that intermetallics were located in the interdendritic areas (Fig. 5.3).

Cieslak et al. [89] reported the sequence of phase transformation of Hastelloy C276 during solidification, which follows L → L+γ → L + γ + p → γ + p → γ + p + μ (L denotes the liquid phase, γ the austenitic matrix phase of the alloy). Leonard [88] heat-treated Hastelloy C276 in the temperature range of 650 °C to 1100 °C and found that the *P* phase formed after soaking for only 5 minutes, but subsequently transformed to μ phase after long term exposure. The kinetics of μ phase formation was reported to be slow, requiring a long annealing treatment up to hundreds of hours [223] (μ phase did not form after 15 h at 800 °C in ref. [223]). Given the relatively rapid cooling rate during solidification in the WAAM process compared with traditional casting processes, the transformation of *P* to μ phase is not expected to readily occur within the relatively short solidification process, and hence μ phase is less likely to be precipitated out in the as-built sample in the present case. There is also an absence of expected blocky morphology for μ particles, as indicated by microstructural observation under low and high magnifications in Fig. 5.3 or Fig. 5.5.

After PHT at 871 °C for 6 h, the microstructure exhibited coarser precipitates in the interdendritic zones compared to the as build sample, and additional fine particles were formed at the MGBs. The non-equilibrium segregation of Mo in the interdendritic zone was believed to promote the coarsening of these second phases. Due to the segregation of Mo in these intermetallic phases, a decrease of Mo element in the dendritic core areas of the sample after PHT at 871 °C was evident from the SEM-EDS results (see Table. 5.1). As grain boundaries are known to have a high concentration of defects, it is believed that Mo preferentially segregated to the MGBs, which provided a driving force for the formation of these smaller *P* phase particles [1, 261]. Additionally, a significant amount of nano-sized particles were formed in the interdendritic areas during the heat treatment, these being identified as intermetallic μ phase by TEM. These particles had

a similar rod-like morphology to the μ phase observed in the research of Akhter et al. [108].

The precipitation of the secondary μ phase can occur during aging heat treatment or in service at temperatures ranging from 800 to 1140 °C [262]. It should be noted that most aging-related research is for traditionally manufactured Hastelloy C276 that has a homogeneous matrix as the starting point, as the alloys are supplied in the solution annealed condition. The formation of the μ phase after 6 hours at 871 °C in this research may be related to the segregation of Mo to the interdendritic regions during the WAAM process, providing sufficient concentrations of Mo for the intermetallic compound to precipitate at relatively less heat treatment time. The formation of the μ phase can deplete the γ matrix of Mo and W, which can result in the transformation of the γ' phase in the vicinity of the μ phase [263]. However, from the current TEM results (see Fig. 5.7f), this did not occur for the conditions used in this research, and the matrix is still γ-Ni.

For the PHT at 1177 °C sample, as was shown in Figs. 5.3 and 5.5, the *P* phase was partially dissolved at interdendritic areas and fully dissolved at grain boundaries. The significant amount of μ phase throughout in the interdendritic area and *P* phase at grain boundaries observed after the PHT at 871 °C were not found after the 1177 °C PHT. Hence, a stress-relieving PHT is not recommended for these WAAM produced samples, rather a solution annealing PHT is required to dissolve the *P* phase and release Mo atoms back into the solid-solution matrix. The elemental distribution analysis (Fig. 5.6 and Table 5.1) supported this finding, where a higher amount of Mo was measured at the dendritic core area and the element distribution was more uniform. This demonstrates that a PHT at 1177 °C for only half an hour is effective to achieve a

relatively homogeneous microstructure of WAAM produced Hastelloy C276.

5.4.2 Mechanical property evaluation

Compared with the as-built sample, the PHT at 871 °C and 1177 °C resulted in an increase in the microhardness by approximately 57 $HV_{0.1}$ and 25 $HV_{0.1}$, respectively. Hardening or strengthening can be readily achieved through solid solution hardening, microstructure refinement, precipitation, and/or work hardening [72, 104, 264]. The precipitation of the nano-sized μ phase for the heat-treated sample at 871 °C increased hardness via precipitation hardening [258]. The fluctuations in the hardness traverse profile for the PHT at 871 °C component were consistent with the non-uniform distribution of the hard particles affecting the local hardness variation. For the heat-treated sample at 1177 °C, the dissolution of Mo-rich precipitates enabled more Mo to redissolve into the matrix, which leads to solid solution strengthening. As Mo has a relatively large atomic radius it can distort the lattice of the matrix phase and obstruct the movement of dislocations, resulting in the observed modest increase in hardness and strength. The loss of Mo due to Mo-rich precipitation in the as-built specimen led to the reduced hardness and strength.

In agreement with the hardness results, the tensile strength of the PHT components increased commensurately. The component under PHT at 871 °C showed a large increase in the tensile strength, but a sharp decrease in ductility. The nano-sized Mo-rich μ particles can effectively improve the tensile strength by pinning the movement of dislocations. However, both the μ phase and the *P* phase are TCP phases that are brittle intermetallics. As such, these intermetallic phases can fracture during plastic deformation and act as nucleation sites for micro-cracks and microvoids [1]. The fractography results showed that cleavage fracture occurs in this component (Fig. 5.10).

Due to the segregation of Mo in the vicinity of grain boundaries and interdendritic areas, precipitation was concentrated in these regions, accounting for the observed interdendritic fracture and decreased ductility. In contrast, the 1177 °C PHT sample displayed a more uniform compositional distribution and less precipitation of TCP phases, which promoted transgranular ductile failure (Fig. 5.10). The resultant solid solution strengthening led to the improvement of both strength and ductility. As a consequence, the PHT at 1177 °C resulted in the most favourable mechanical properties (both the ductility and the strength) at room temperature among the three conditions for the investigated Hastelloy C276 components.

Commercial Hastelloy C276 alloy sheet is normally provided in a solution annealed condition. According to the manufacturer (Haynes Company [57]), the commercial sheet product of Hastelloy C276 shows a UTS of 792 MPa, a YS of 356 MPa, and a TE of 61%. In comparison with the commercial sheet, the PHT at 871 °C sample had similar tensile strength, but much lower TE, while the PHT at 1177 °C sample had similar YS, but lower TS and TE. It is expected that a longer solution annealing time would dissolve more *P* phase and lead to further improvement of the mechanical properties of WAAM produced components. In conclusion, the WAAM process in conjunction with a solution annealing heat treatment (1177 °C) offers a viable, low-cost production approach for the manufacture of Hastelloy C276 materials with suitable mechanical properties.

5.5 Conclusions

The present work focused on the evaluation of post-heat treatment (PHT) effects on the microstructure and mechanical properties of the Hastelloy C276 alloy fabricated by wire arc additive manufacturing (WAAM). Two different PHTs at 871 °C and 1177 °C

were performed to explore suitable PHT procedures for WAAM produced Hastelloy C276. The following conclusions can be drawn:

(1) The strength and hardness of Hastelloy C276 fabricated by the WAAM process under room temperature can be increased by the application of PHT.

(2) After PHT at 871 °C, extensive Mo rich μ phase precipitates are formed in the interdendritic areas and *P* phase at the grain boundaries. This leads to the sample having the highest hardness and tensile strength among the three conditions investigated, but the lowest ductility. Tensile test coupons displayed brittle, interdendritic failure. Thus, post heat treatment at 871 °C is not recommended for Hastelloy C276 produced by the WAAM process.

(3) For the component under 1177 °C PHT, the Mo rich phase in the as-built sample was partially dissolved, releasing Mo into the matrix, providing solid solution strengthening. Due to a reduction in the amount of brittle *P* phase, excellent ductility was achieved, leading to ductile, transgranular failure of tensile coupons. Compared to the as-built component, the anisotropy in mechanical properties was reduced. Therefore, a solution annealing heat treatment is recommended for the improvement of the mechanical properties of Hastelloy C276 fabricated by WAAM.

6 Tailoring the surface finish, dendritic microstructure and mechanical properties of wire arc additively manufactured Hastelloy C276 alloy by magnetic arc oscillation

6.1 Introduction

As mentioned above, due to the intrinsic characterisation of WAAM processes, like thick deposition layer as well as the complex thermal cycling and relatively high heat input experienced in the manufacturing process, WAAM-produced components possess some common features, including high sample surface roughness, significant compositional segregation, large residual stresses, heterogeneities and anisotropies in microstructure and associated variations in mechanical properties [265]. These characteristics mediate the final properties of the WAAM-produced materials and components, which normally limit their immediate applications in the as-manufactured condition. Therefore, optimisation of the manufacturing and post-manufacturing processes is critical for improving the overall performance of WAAM-produced materials. PHT operation is an effective way, however, increasing the cost of manufacturing processes and in-situ operation might be a preferential alternative.

Solidification of the molten pool during WAAM is largely controlled by the thermal gradient, and the nucleation and growth behaviour of the grains, which in turn have a strong influence on the final microstructure and the performance of the as-deposited materials [9]. The welding arc current and its intrinsic magnetic field lead to an electromagnetic Lorentz force, contributing to a self-induced stirring effect and fluid flow in the welding pool. The application of external magnetic field during WAAM has

been explored in previous studies, which showed that the applied magnetic field would strengthen the Lorentz force and provide enhanced artificial agitation by magnetic arc oscillation (MAO) [266, 267]. Alternating external magnetic fields during the conventional solidification process (casting) have been used for decades to induce electromagnetic stirring (EMS) for grain refinement in the casting processes [268]. In addition, the successful application of MAO during WAAM and traditional arc welding has been reported to achieve improvements in manufacturing quality and grain refinement of various alloys including stainless steels, Al-, Ni- and Ti-alloys [191, 269-272]. For example, Sundaresan and Ram showed that the incorporation of MAO during the GTAW process led to refinement of the fusion zone grains in α-β dual-phase Ti-alloys, resulting from the promoted grain nucleation activities during solidification due to increased stirring and fluid flow in the welding pool [270]. Wang et al. [191] found the refined dendrites and decreased chemical segregation in the WAAM fabricated Inconel 625 with MAO, which contributed to their enhanced mechanical properties. Ram et al. [273] reported the achievement of decreased grain size and enhanced tensile ductility of an Al-alloy weld as a consequence of applying MAO during GTAW. These encouraging results demonstrate that the application of MAO during the solidification process is a promising approach to refining the grains of the weld and weld deposited materials, thereby improving their mechanical properties.

Unlike the common equiaxed microstructure in the materials using the traditional manufacturing processes, additively manufactured alloys normally feature dendritic microstructures accompanying a preferred grain orientation. Other than the grain size, the dendrite morphology, including the DAS and dendrite orientations, and associated solute distribution are important microstructural factors affecting the densification level and mechanical properties of additively manufactured materials [274, 275]. It is shown

in Chapter 4 [178] that Hastelloy C276 alloy manufactured by GT-WAAM is characterised by an elongated dendritic microstructure of the γ-Ni matrix, which is responsible for the resultant anisotropy in the mechanical properties. The results also revealed the formation of brittle intermetallic phases in the interdendritic areas due to the elemental segregation during solidification, which are detrimental to the properties of additively manufactured Hastelloy C276 components. In addition to grain refinement, the application of MAO has been shown to have additional advantages of minimising undesirable micro-segregation and decreasing the possibility of hot cracking, hence improving the mechanical properties of the metallic materials [276]. Despite these recognised advantages, little research has been performed to explore the addition of MAO during WAAM of Ni-base Hastelloy C276 alloy and understand its effects on the microsegregation, the dendritic microstructure and mechanical property developments of the produced components. Towards this end, the present chapter aims to understand the changes in the macrostructure, microstructure and the mechanical properties of the produced Hastelloy C276 alloy induced by the application of MAO during the GT-WAAM.

6.2 Materials and methodologies

6.2.1 Materials manufacturing

The deposition system is built upon an established WAAM system consisting of a GTAW welding system. The MAO system, which was built by the current research group, comprising the electromagnetic coils and the oscillation control device is incorporated into the WAAM system, as shown in Fig. 3. 4 [266].

Table 3.1 lists the chemical composition of the Hastelloy C276 wire (1.2 mm diameter) used in this chapter. Four thin-wall structures with fifteen layers, one without MAO and

the other three with MAO under the oscillation frequencies of 5 Hz, 10 Hz, and 20 Hz, respectively, were deposited on four identical plain carbon steel substrates with the dimensions of 205 mm × 105 mm × 6 mm. The WAAM process parameters for four samples were kept constant, and presented in section 3.2.1. An interval of approximately 60 s between the interlayer deposition was used. No other approaches were applied to control the interlayer temperature. Thermal imaging camera was used to capture the temperature field of the formed part and measure the solidification time. In addition, another welding (Xiris) camera was used to observe the arc and molten pool behaviour during the deposition process. The camera was mounted horizontally at the same level of the welding arc, which is most commonly used and considered the best angle to visualise the arc behaviour.

6.2.2 Material characterisation

The surface finish of the four as-deposited samples was evaluated using a laser surface scanner. The scanned results were processed using MATLAB software. The standard deviation (SD) of the measured surface roughness was calculated and used to quantify the surface finish quality. The metallographic specimens were extracted from the y-z plane of each deposited sample, as shown in Fig. 6.1, and prepared following the standard procedures including mounting, polishing and electro-etching with the solution in chapter 3. The micrographs were taken by a Leica DM6000 OM. The microstructure was further observed by an SEM equipped with an EDS. XRD with a Cu Kα radiation source was performed to identify the phase constituents. Nanoindentation was performed on the same metallographic specimens with the parameters in section 3.6.1. Vickers hardness was measured on the same specimens as well, traversed down top to bottom in the vertical direction and across the width in the horizontal direction (see Fig. 6.1). Seven tensile testing specimens were extracted from

each of four samples in the traveling direction (x-y plane), 15 mm away from the side regions, as shown in Fig. 6.1. Tensile tests were carried out with a video extensometer to measure the displacement during tension loading.

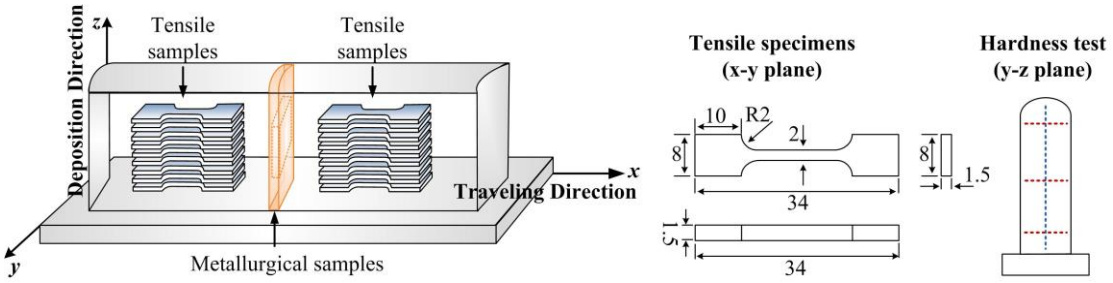

Fig. 6.1 Schematics of specimen extraction for metallurgical and mechanical tests

6.3 Results and discussion

Figure 6.2 shows a series of welding arc profiles captured during the deposition process without MAO and with MAO at different frequencies of 5, 10 and 20 Hz. As seen in Fig. 6.2a, a stable and static arc profile was observed during WAAM without MAO. In contrast, a dynamically oscillated arc was found during the depositions when MAO at different frequencies was applied (Figs. 6.2b-d). Under the currently applied circular oscillation mode, the direction of the plasma arc changed simultaneously when the external magnetic force deflected the welding arc. Therefore, the arc moved in a circular mode and produces extra stirring on the molten metal. There was only a slight change in the deflection angle (~10°) when the frequency increased from 5 Hz to 20 Hz. Subsequently, the arc length was slightly increased with the addition of MAO, for all frequencies. Corradi et al. [266] also found the oscillated arc profile during the WAAM deposition of steel and Ti-alloy materials after applying MAO. These results confirm that the application of MAO did cause arc movement during the WAAM process. Further investigation of the application of MAO during WAAM will be presented in the following sections to discuss its influences on molten pool behaviour, thermal

evolution, macrostructure and microstructure, as well as the mechanical properties of the produced Hastelloy C276.

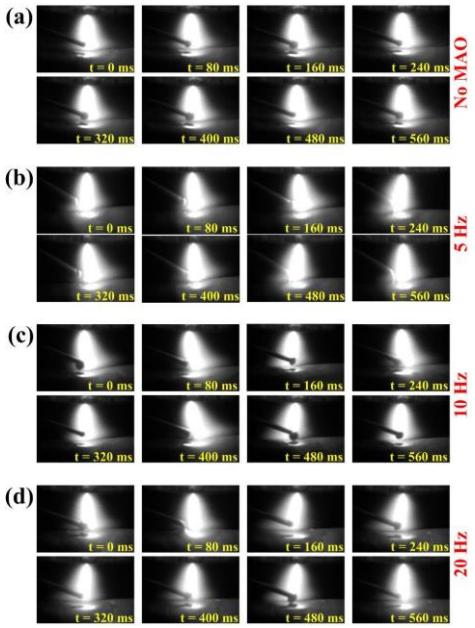

Fig. 6.2 Arc behaviour during the deposition processes: (a) without MAO; and with MAO at (b) 5 Hz; (c) 10 Hz; and (d) 20 Hz.

6.3.1 Molten pool performance

Figure 6.3 presents the typical molten pool behaviour captured during the deposition of the fifth layer (selected to exclude the matrix dilution effect in the first few layers). Among four deposition conditions, the narrowest welding pool was observed from the front view in the sample without MAO, as shown in Fig. 6.3a, being 17.7 ± 0.4 mm in the length measured by ImageJ software [277]. In comparison, the application of MAO induces a longer welding pool, and the values of the welding pool length at the frequency of 5 Hz, 10 Hz, and 20 Hz were 19.2 ± 0.4 mm, 21.1 ± 0.4 mm, and 21.9 ± 0.4 mm, respectively. Furthermore, a consistent arc thermal exposure position and a sunken deformation exactly under the welding arc in the molten pool without MAO were noticed (Fig. 6.3a). However, as the arc exposure position oscillated periodically with the addition of MAO, a larger thermal loading area was induced, hence increasing

the molten pool length. The sunken deformation of the molten pool also shifted with the arc deflection, as can be seen from Figs. 6.3b - d. This swinging behaviour was reported to cause a physical stirring and increased the convective flow in the weld molten pool, contributing to a relatively large overall temperature gradient and a short solidification time [278]. The liquid phase temperature range of Hastelloy C276 is 1323 - 1371 ℃. Based on the observations using the thermal camera, the cooling rate during solidification without MAO was about 160.3 ℃/s, much lower than that of 229.6 ℃/s recorded when applying MAO at 5 Hz. Note that the further increases in the frequency of MAO to 10 Hz and 20 Hz decreased the solidification rates to 177.8 ℃/s and 180.5 ℃/s, respectively. It is worthwhile to mention that with the increase of the MAO frequency, the solidification time also increased instead of the decrease as reported previously [269]. The phenomenon of the increase of frequency (10 and 20 Hz) along with the increased solidification time is considered to be related to a low amplitude of the magnetic field used in the present work. As a consequence, the MAO at the higher frequencies induced a more concentrated and higher density of heat input than that at the lower frequency (5 Hz). At higher frequencies, less time is available for reversing the fluid flow direction during an oscillation cycle, consequently resulting in a lower velocity of agitated liquid in the welding pool, hence reducing the effectiveness of the magnetic field. The application of MAO appeared to have no significant impact on the metal droplet sizes in the current GTAW mode, as shown in Figs. 6.2 and Fig. 6.3, which is considered due to the relatively small arc deflection angle and low magnetic power used.

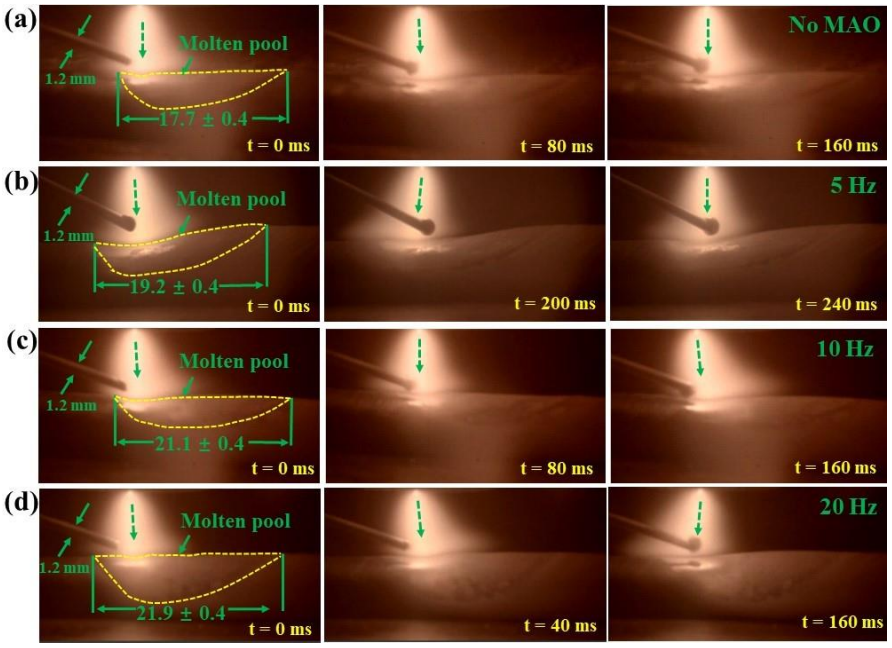

Fig. 6.3 Representative dynamic welding pool morphologies recorded during deposition of the fifth layer: (a) without MAO; and with MAO at (b) 5 Hz; (c) 10 Hz; (d) 20 Hz.

6.3.2 Surface roughness and geometrical measurements

The surface finish of the as-deposited four samples was scanned by a laser sensor. In order to limit detection noises, the scanned areas were chosen at 15 mm away from the starting and toe regions of the deposited layers where their dimensions were unstable because of the initiation and extinguishing of the arc. Surface roughness (R_s) scanning results are shown in Fig. 6.4. It is determined that the SD values of R_s decreased from ~200 µm of the sample without MAO to ~145 to ~160 µm for the MAO samples at three different frequencies. This demonstrates the capability of MAO for the improvement in the surface finish of WAAM-fabricated materials. The surface roughness of as-deposited materials may be affected by a range of processing parameters, including the filler wire, shielding gas, travel speed (TS), wire feed speed (WFS), ratio of WFS to TS (WFS/TS), heat accumulation, and the solidification time [279-281]. As the starting wires and the deposition parameters were consistent for the four samples, the reduction of the molten pool solidification time caused by MAO was

considered to be a contributing factor to the observed decrease in R_s [266]. As mentioned above, the reduced solidification time by MAO promotes the control of the overflow in the molten pool. Moreover, less heat accumulation may benefit the lower surface roughness of the MAO samples. Swinging behavior of the arc and its greater length can lower the input heat density, so the average temperature of the molten pool is likely lowered, thereby lessening heat accumulation with the application of MAO [266, 282]. The shorter solidification time and less heat accumulation could decrease the surface roughness by reducing overflow of the molten pool. On the other side, the surface roughness is also affected by the magnetic stirring effect on the molten pool. The stirring efficiency is dependent on the inertia and viscosity of the molten metal [266]. Overall, the magnetic stirring improved the wall surface finish. Note that the sample deposited at 5 Hz of MAO showed the lowest Rs (~145 µm) among the four studied conditions, and the refinement of the surface roughness however was not linear with the increase of MAO frequency (Fig. 6.4). Further increasing the frequency of magnetic stirring to 10 Hz and 20 Hz appeared to mildly reduce the solidification rate, indicated decreased stirring efficiency (Section 6.3.1), and hence yielded a slightly increased surface roughness. Nevertheless, samples deposited with 10 Hz and 20 Hz still demonstrated lower R_s of ~152 and ~160 µm relative to the sample without MAO. Considering the scale of surface roughness, the difference between the conditions of 10 Hz and 20 Hz is insignificant. The current results illustrate that the application of 5 Hz MAO produced the best surface finish, indicating 5 Hz is the most effective frequency in the present experimental condition to improve the surface finish. The achievement of improved surface accuracy of the deposited layer facilitates the stable deposition and reduces the post-machining, hence the application of MAO is favourable for improving the WAAM processing accuracy and stability and the final component quality.

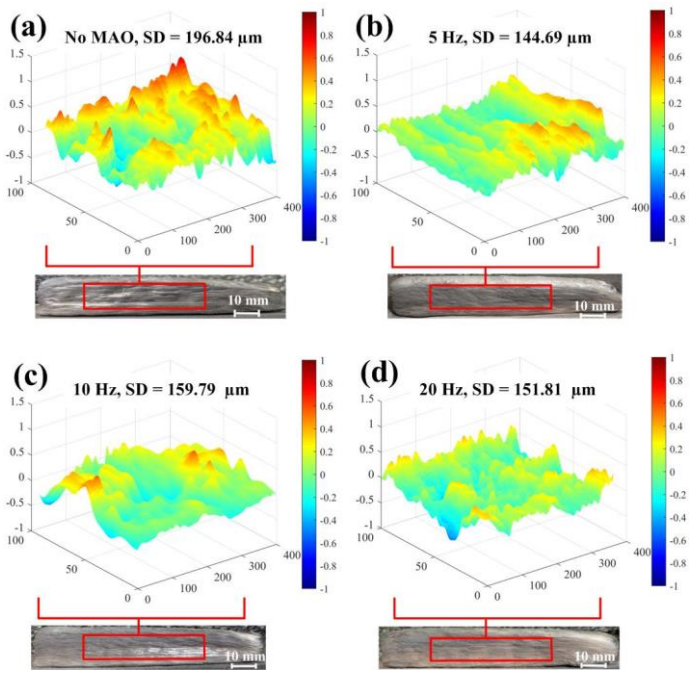

Fig. 6.4 Surface roughness profiles of the as-deposited materials at different conditions: (a) without MAO; and with MAO (b) at 5 Hz; (c) at 10 Hz; and (d) at 20 Hz.

Cross-sectional micrographs of the deposited alloys, under all four conditions, are presented in Fig. 6.5. The total wall width (TWW) and total wall height (TWH) parameters of the deposited materials are determined (Fig. 6.5) and the results are listed in Table 6.1. Compared with the no MAO sample (TWH = 16.5 mm and TWW = 13 mm), an increase in the sample height and a decrease in width were observed for the sample with MAO. Among the three MAO samples, the 5 Hz sample had the largest TWH and lowest TWW, whereas the 20 Hz sample showed the opposite trend of the lowest TWH and the largest TWW. As shown in Fig. 6.5 and reported in Ref. [283], due to the high cooling rate enabled by the heat dissipation from the substrate, the first several deposition layers have a higher or varying layer band spacing, but with the continuation of the deposition, the morphology and height of the layer band become stable. Moreover, except for the first several layers, the sample without MAO (see Fig. 6.5a) showed relatively flat and shallow layer bands; while the MAO samples often had thicker bands. The increased layer band spacing in the MAO samples agrees with the

observed increased TWH.

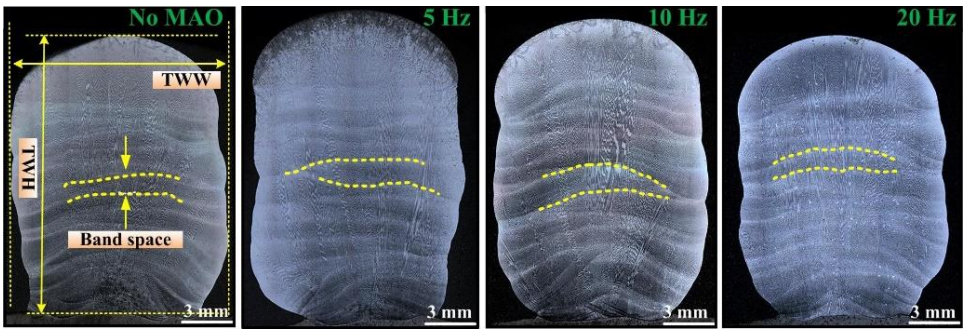

Fig. 6.5 Cross-sectional micrographs showing the geometries of the deposited samples at different conditions. The TWW (total wall width) and TWH (total wall height) are shown. The band spacing between adjacent layer boundaries is also marked.

Table. 6.1 The measured parameters of total wall height (TWH) and total wall width (TWW) of four samples.

Sample	TWH (mm)	TWW (mm)
No MAO	16.5	13.0
5 Hz	17.7	12.5
10 Hz	17.3	12.6
20 Hz	16.7	12.8

6.3.3 Microstructure

Qiu et al. [284] showed that the microstructure of the additively manufactured Hastelloy C276 comprised the precipitation *P* phase and the γ-Ni matrix columnar grains with epitaxial dendrites. XRD was used to identify the phases and the potential preferred grain orientations in the investigated alloys. Fig. 6.6 presents the XRD patterns for the metallographic samples under four conditions in their middle areas. The XRD analysis shows that only the γ-Ni phase of the FCC structure was identified in the investigated samples. The *P* phase was not readily detected in any sample based on the XRD data, likely due to its low volume fraction beyond the detection limit of the applied XRD technique. For the sample without MAO, a strong (311) diffraction peak was observed, indicating the development of the preferred orientation of the {311} grain family at the

observation sample orientation. With the application of MAO at 5 Hz, an additional strong peak (220) developed. At 10 Hz the strongest peak maintained to be (311), whereas at 20 Hz the development of strong (111) and (200) peaks was observed. These observations qualitatively suggest that the application of MAO affects the columnar growth orientation in the solidification microstructure presumably caused by the oscillation stirring effect in the molten pool during WAAM. It was found there is a relatively lower <001> direction peak in the sample without MAO, compared with the as-deposited samples taken from the middle area in Chapters 4 and 5. This should be attributed that samples in the previous two chapters were taken from a highly deposited part with more deposition layers, so they experienced more thermal accumulation and had a stronger texture than the sample in this chapter. Fewer grains in <001> orientation in this chapter are expected to be induced by a high cooling rate and less thermal accumulation than the as-deposited samples in previous chapters.

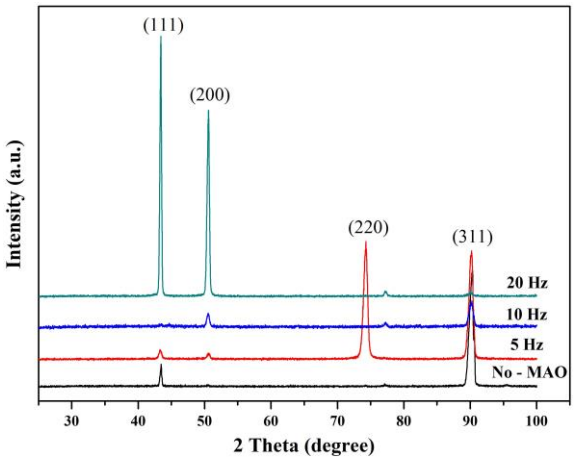

Fig. 6.6 XRD patterns of the samples under four conditions including without MAO, with MAO at 5 Hz, 10 Hz, and 20 Hz.

Figure 6.7 shows the typical optical micrographs of the deposited parts under four conditions taken from the middle area of the same cross-section samples. Observation areas under higher magnifications are highlighted in yellow (Fig. 6.7). Columnar grains in a variety of sizes are prominent in the microstructure of all four samples and such

grain is indicated in red in the images of Fig. 6.7a-d, yet evidence of refinement of the grains was not readily observable in the MAO samples investigated in the present work. This contrasts with previous observations where grain refinement was observed in, stainless steel, Al-based samples with the addition of MAO [271, 285].

Under the higher magnification, the dendrites within the columnar grains show some divergence in their morphologies. First, the sample without MAO is commonly characterized by the upward oriented elongated dendrites from the fusion interface and listed uniformly (Fig. 6.7i). In comparison, the samples with MAO witness noticeably more fragmented or misoriented dendrites, resulting in reduced dendrite lengths or interlocked dendrites (Figs. 6.7j-l). This can be explained as follows: MAO induces a continuous change of the molten pool shape, and swinging behaviour of the arc, as was observed above in Fig. 6.3, leading to the orientation changes of the maximum thermal gradient in the molten pool boundary with time [286]. The growth of dendrites will follow the maximum thermal gradient. As a result, unlike the preferential growth orientation over a long distance under a relatively steady thermal dissipation condition without oscillation, the dendrites with MAO grow in respect to the instantaneous direction of the maximum thermal gradient that is continuously changing over time. Furthermore, Hastelloy C276 alloy has a wide liquid phase temperature range, being about 50 °C. In this case, with a large mushy zone promoted by the long melting and high heat accumulation by the WAAM process, the arc force from the magnetic field can result in the fragmentation of the dendrite tip at the rear end and bottom of the molten pool. These detached tips with lower temperatures can be taken into the new molten pool and subsequently become the nuclei for the formation of new dendrites [287]. They are attributed as the reasons that the MAO samples exhibited more short or misoriented dendrites.

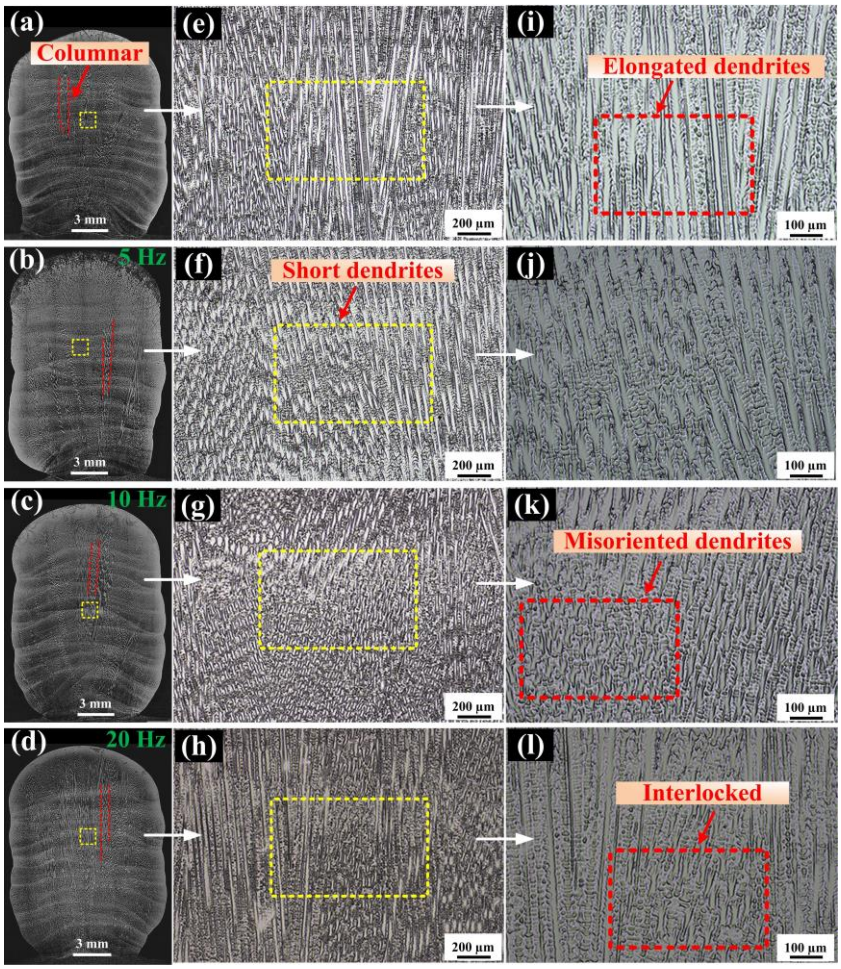

Fig. 6.7 Microstructure of the deposited samples under four conditions: (a) without MAO; (b) with MAO at 5 Hz; (c) 10 Hz; and (d) 20 Hz.

As a common solidification microstructure found in metallic alloys, dendrite has a significant influence on the in-service mechanical properties of the as-produced alloys [288]. Hence, we analysed in detail the DAS, morphology and compositions of the WAAM-produced Hastelloy C276 under four conditions. Fig. 6.8 illustrates the calculation of the primary DAS (Fig. 6.8a) and secondary DAS (Fig. 6.8b), i.e. the center-to-center distance of the dendrite core (L_p), perpendicular to the primary arm for the primary DAS and the secondary DAS follows the equation secondary DAS (L_s) = $\frac{L}{N-1}$, in which L is the center-to-center distance between the secondary arms, parallel to the primary arm, and N is the number of secondary arms that are chosen randomly

[289]. ImageJ® software [277] was used to calculate the DAS, and the results are summarised in Table 6.2. It can be seen that application of MAO decreases the primary DAS and secondary DAS, particularly for the 5 Hz arc oscillation. The DAS is reported to be closely related to the increase in the cooling rate [290]. Therefore, the decrease of DAS further demonstrates that a higher cooling rate was achieved under arc oscillation conditions.

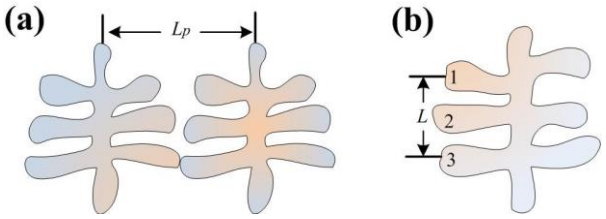

Fig. 6.8 Calculation of (a) primary dendrite arm spacing and (b) secondary dendrite arm spacing.

Table. 6.2 The PDAS and SDAS measured under four conditions.

Distance	No MAO	5 Hz	10 Hz	20 Hz
PDAS (μm)	32.3 ± 5.0	26.3 ± 4.4	29.1± 6.7	28.2 ± 4.2
SDAS (μm)	11.6 ± 3.0	10.5 ± 2.3	11.5 ± 1.9	11.2 ± 1.8

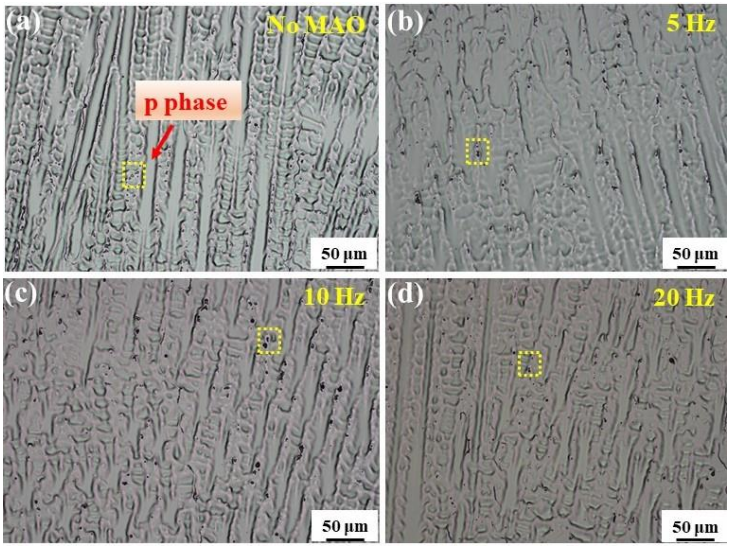

Fig. 6.9 High magnification OM image showing the *P* phase in different conditions: (a) No MAO; with MAO at (b) 5 Hz; (c) 10 Hz; and (d) 20 Hz.

Figure 6.9 shows high-magnification optical micrographs under the four conditions. The dark particles in the optical micrographs spread in the interdendritic area in a wide variety of sizes and amounts (see Fig. 6.9). SEM with EDS analysis was performed to further study the microstructure of the samples. The chemical compositions of particles were analyzed by multiple EDS spot scans, and the estimated compositions, based on in-build EDS machine standards, are indicated as Mo-rich *P* phase with the Ni/Cr/Mo/W/Fe contents of about 32.4/14.8/42.2/6.7/3.9% (wt.%), respectively, similar to those in Ref. [284]. However, there was no clear evidence showing that the *P* phase decreased in size or amount through application of MAO. To further understand if any compositional segregation occurred within the dendrites for the four conditions, the concentrations of major elements in the dendrite core and interdendritic regions were determined by EDS, and the line scan and multiple spot scan are shown in Fig. 6.10 and Table 6.3. The high-melting-point heavy Mo element was found to segregate in the interdendritic regions of all the samples, consistent with the previous observation [284]. The Mo segregation level in the dendrite core (Mo_c) and interdendritic region (Mo_i) was estimated based on the corresponding concentration ratio of Mo_c/Mo_i, which is 0.70 for the sample without MAO. With MAO, Mo_c/Mo_i increased to similar values at different frequencies, being 0.78, 0.79, and 0.77 for 5 Hz, 10 Hz, and 20 Hz, respectively. This result indicates that with the addition of MAO, compositional micro-segregation can be reduced to a certain extent, which is attributed to the higher solidification rates and cooling rates associated with MAO, as described in Section 6.3.1.

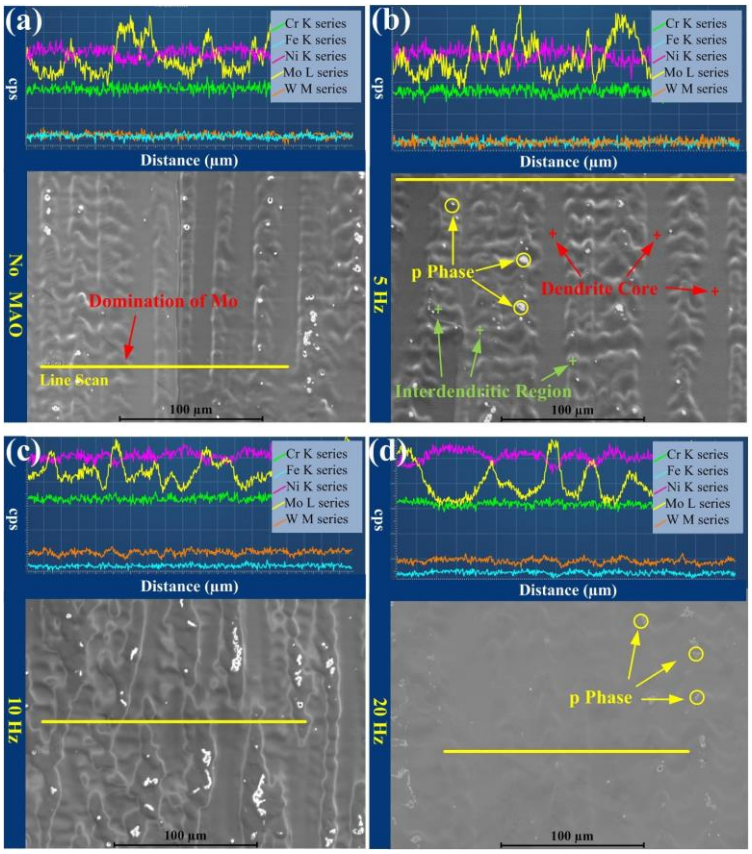

Fig. 6.10 SEM images and element distributions of the line scans for the four conditions; (a) without MAO; (b) 5 Hz; (c) 10 Hz; and (d) 20 Hz.

Table. 6.3 Concentrations of major elements (wt.%) in the interdendritic regions and dendrite core areas under four conditions.

Conditions		Ni	Mo	Cr	Fe	W
No MAO	Interdendritic region	54.0 ± 1.6	19.7 ± 1.7	16.3 ± 0.1	5.9 ± 0.2	4.2 ± 0.2
	Dendrite core	59.5 ± 0.3	13.8 ± 0.2	15.6 ± 0.1	6.5 ± 0.1	4.6 ± 0.1
5 Hz	Interdendritic region	55.0 ± 1.4	18.1 ± 1.6	16.2 ± 0.1	6.5 ± 0.2	4.2 ± 0.2
	Dendrite core	58.8 ± 0.8	14.1 ± 0.7	15.6 ± 0.3	7.0 ± 0.2	4.6 ± 0.2
10 Hz	Interdendritic region	54.9 ± 1.2	18.4 ± 1.3	16.0 ± 0.2	6.3 ± 0.3	4.5 ± 0.1
	Dendrite core	58.6 ± 0.2	14.6 ± 0.2	15.5 ± 0.2	6.4 ± 0.1	4.8 ± 0.2
20 Hz	Interdendritic region	55.4 ± 1.3	18.0 ± 1.6	16.2 ± 0.3	6.1 ± 0.5	4.2 ± 0.4
	Dendrite core	59.7 ± 0.8	13.8 ± 0.6	15.7 ± 0.2	6.4 ± 0.3	4.8 ± 0.2

6.3.4 Mechanical properties

6.3.4.1 Nanohardness and Vickers hardness

Figure 6.11 presents the results of nanoindentation tests. Nanoindentation is widely treated as a rapid and non-destructive way to estimate and evaluate the mechanical

properties of metals without special size or shape. In this research, an indentation mapping was made in six areas of the dendrite core and interdendritic regions, respectively. The imprints avoided the *P* phase and were discarded in the data analysis if they landed in the boundary of the dendrite core and interdendritic area, as shown in Fig. 6.11a. The average values of nano-hardness (*H*) and the reduced elastic modulus (*Er*) of each condition are shown in Figs. 6.11b and 6.11c, respectively. As seen from Fig. 6.11b, the nano-hardness of the interdendritic regions was slightly higher than that of the dendrite core areas under all four conditions. This is attributed to the local Mo segregation to the interdendritic areas, as determined from EDS observations (Table 6.3), which provide localised solid solution hardening. On the basis of the classical theory, this solid solution hardening occurs because dislocation movement is inhibited by distortion of the atomic lattice, due to the misfit of the atomic radius [291]. According to Fig. 6.11c, the reduced elastic modulus for interdendritic regions of each sample is similar to that acquired from the dendrite core areas. The average nano-hardness value of the sample without MAO is 3.65 ± 0.13 GPa, and the reduced elastic modulus is 134.03 ± 2.31 GPa. By the application of MAO, the average nano-hardness was considerably increased to the highest value of 5.28 ± 0.21 GPa for the 5 Hz sample, and then slightly decreased for the 10 Hz (H = 3.77 ± 0.11 GPa), and the 20 Hz (H = 4.05 ± 0.13 GPa) samples. The same tendency was noticed in the reduced elastic modulus, with Er = 210.48 ± 4.11 GPa at 5 Hz, 156.74 ± 2.96 GPa at 10 Hz and 172.86 ± 3.50 GPa at 20 Hz. It emerged that with the increasing frequency of oscillation, these parameter values did not increase correspondingly, rather the highest one was found at the lowest MAO frequency of 5 Hz. The increased *Er* value of 5 Hz is considered to be attributed to refined microstructures in segregation and dendrite morphology, as shown in Table 6.2 and Table 6.3, which resist the dislocation movement.

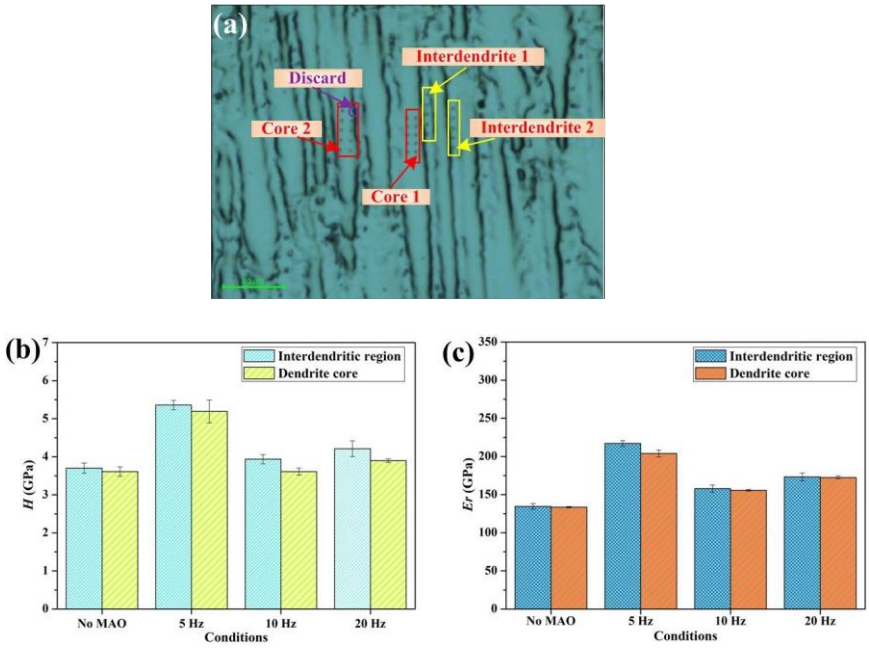

Fig. 6.11 The nanoindentation illustration: (a) Imprint illustration of interdendritic regions and dendrite core areas; (b) average values of the hardness (*H*); and (c) reduced elastic modulus (*Er*) in the interdendritic regions and dendrite core areas.

In addition to the hardness and elastic modulus, other parameters measured by nanoindentation can be used to assess the mechanical properties of materials by the calculation of *H* and *Er* ratios. A key parameter, described as H^3/E_r^2 (as referred to as yield pressure), is to evaluate plastic deformation [292]. Theoretically, a higher H^3/E_r^2 ratio indicates a higher resistance to plastic deformation [293, 294]. Fig. 6.12a displays the H^3/E_r^2 ratio of the samples under four conditions in the interdendritic regions and dendrite core. It was found that the 5 Hz sample had the highest H^3/E_r^2 ratio among the four conditions. Average H^3/E_r^2 ratios increased to about 0.0033 ± 0.00035 with application of MAO at 5 Hz in comparison to no MAO (0.0027 ± 0.00025), however, both MAO samples prepared at higher frequencies (10 Hz and 20 Hz) had slightly decreased H^3/E_r^2 of about 0.0022 (0.0022 ± 0.00032 for 20 Hz and 0.0022 ± 0.00029 for 10 Hz). Hence, the 5 Hz MAO sample was predicted to have higher yield strength than those of the other conditions. Friction caused by the gradual material removal is

dependent on the plastic deformation, so the resistance to plastic deformation can also be used to gauge the anti-wear capability of the materials [295]. In this case, the addition of MAO at 5 Hz during the manufacturing process is expected to result in improvements in wear resistance, which can be investigated in future research.

Another parameter, the mechanical work, U_t, imparted by the indenter during loading is the sum of elastic indentation energy, U_e, and plastic indentation energy, U_p. The plasticity index, U_p/U_t, is also treated as an important parameter to determine the mechanical properties of the alloys, which corresponds to the intrinsic plasticity of the materials [294]. A lower plasticity index indicates good workability and high ductility at room temperature [292]. Based on the previous simulation and experimental results, the U_p/U_t (Where $U_p = U_t - U_e$) is a unique function of *H/Er* as follows [292, 296]:

$$\frac{U_t - U_e}{U_t} \approx 1 - x\left(\frac{H}{E_r}\right) \qquad (1)$$

Where *x* is a constant, about 7 for the metallic materials [297]. The U_p/U_t was estimated from the *H/Er* ratio. From the depicted graphs shown in Fig. 6.12b of the tendency of the U_p/U_t ratio, it can be seen that the plasticity index increased slightly, corresponding to the addition of MAO, which suggests a slightly lower room temperature ductility and less workability of the samples fabricated with the addition of MAO.

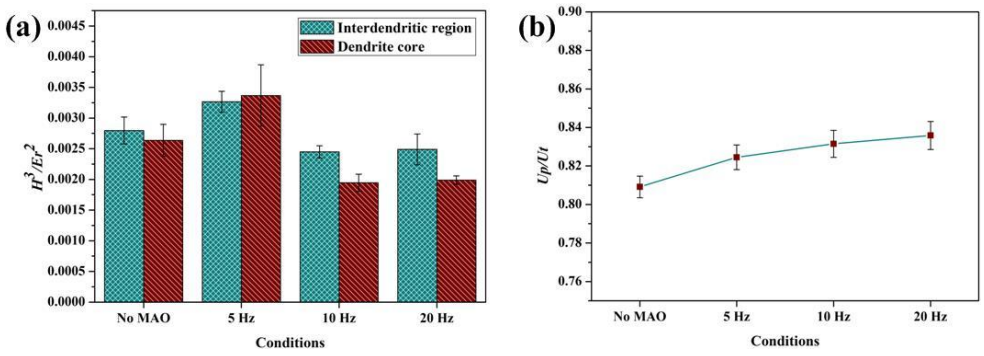

Fig. 6.12 (a) H^3/E_r^2 ratio in the interdendritic regions and dendrite core areas; (b) the average values of U_p/U_t of four conditions.

Note that nanoindentation reveals local mechanical properties, and does not necessarily reveal overall bulk mechanical properties of the materials. To further check the hardness of the deposited samples, Vickers hardness testing was performed on all four samples was performed and compared in the horizontal and vertical directions from the top to bottom in the y-z plane. It was found that the average hardness of the sample without MAO is 201 ± 10 $HV_{0.1}$, and it increased after the addition of MAO, reading 225 ± 13 $HV_{0.1}$ (5 Hz), 204 ± 7 $HV_{0.1}$ (10 Hz), 218 ± 12 $HV_{0.1}$ (20 Hz), respectively. Fig. 6.13 further shows the hardness distribution along the vertical (deposition) direction of four samples. It is observed that the hardness does not vary significantly from the top to the bottom under four conditions investigated. Moreover, with the same tendency as for the nanoindentation results, the 5 Hz MAO sample exhibited the highest average microhardness. The increased hardness value with increased refinement of the DAS induced by the arc oscillation, as described earlier, appears to have similarities with the Hall-Petch relationship, where a materials' grain size is inversely proportional to its hardness [298]. In the case of dendrites, there is a structure with discrete interdendritic regions and relatively soft dendrite cores. When this structure is refined, it exhibits higher hardness. The arc oscillation, despite preserving the columnar grains, permitted an increase in hardness, apparently, owing to the decrease of the DAS and complex dendrite network.

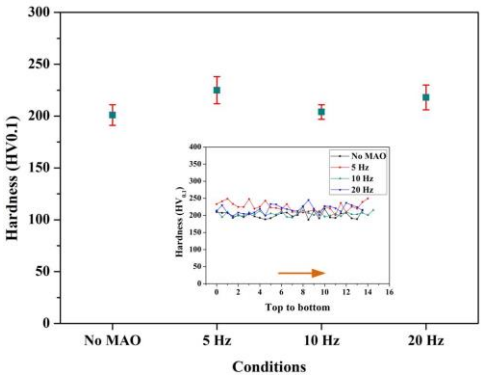

Fig. 6.13 Vickers hardness distribution of four samples from the top to bottom.

6.3.4.2 Tensile and fracture

Figure 6.14 shows the tensile results (averaged over seven locations from the top to bottom of the wall) of the deposited samples for the four conditions. The average ultimate tensile strength (UTS) of the samples without MAO is 661 ± 39 MPa, and the yield strength (YS) is 356 ± 25 MPa, and total elongation is 58 ± 7%. With the application of MAO, the UTS appears to have moderately increased, to 688 ± 36 MPa, at 5 Hz, although this result is still within the bounds of experimental error for the no MAO case. For 10 Hz and 20 Hz, the UTS were 648 ± 27 MPa and 673 ± 39 MPa, respectively. The average YS appears to increase slightly with the addition of MAO for all cases, where the highest was 369 ± 30 MPa at 5 Hz. The total elongation of the samples with MAO at 5 and 20 Hz, 58 ± 6% and 59 ± 2%, respectively, which was similar to that without MAO, but for 10 Hz it was lower, only 53 ± 4%.

Although the range of mechanical properties overlaps due to the scattering of tensile test data, the sample of 5 Hz showed the overall highest average UTS, YS, and almost the same ductility as the sample without MAO, while with further increase of the frequency, the effect of MAO on tensile properties becomes less efficient. This outcome is consistent with the result estimated by the nanoindentation H^3/E_r^2 ratio that the sample with MAO will increase YS at 5 Hz, as is described in Fig. 6.14. From the U_p/U_t ratio, the ductility might be decreased by the addition of MAO. However, there was no significant decrease in ductility, which is preferable in practical utilization. The higher strength of the 5 Hz sample is in line with its increase in hardness [299]. As reported by Campbell [300], the interdendritic area can be, on average, cleaner and sounder, with the decreased DAS, leading to enhanced mechanical properties. Furthermore, the decreased DAS and complex dendrite matrix morphology induced by the MAO act like interconnected fibres and network, so can better resist localized deformation and

dislocation movement, hence increasing the strength of the samples [290]. In comparison with the tensile strength in Chapters 4 and 5, the strength of the as-deposited sample in this chapter without MAO is much higher. It is because of higher heights of samples in the previous two chapters without interlayer temperature control during deposition. That means the previous two chapter samples experience more thermal cycling and heat accumulation, which will lead to coarse grains and more precipitations during thermal exposure. Hence, the previous two tensile results are lower than the current one.

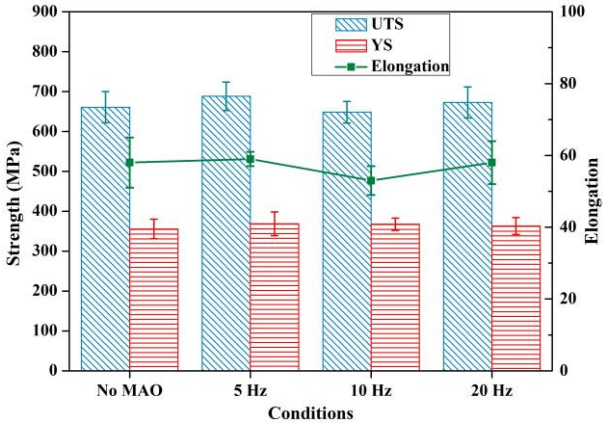

Fig. 6.14 Tensile strength and elongation of the samples under the four conditions.

Figure 6.15 displays the typical fractography of the tensile samples under the four conditions. A large number of dimples on the fracture surface clearly illustrates the nature of ductile fracture. Comparing the four conditions, the sample without MAO showed a more pronounced feature for interdendritic fracture, while the arc oscillation specimens showed an increased amount of transgranular ductile fracture. The effect of the MAO on decreasing the length and size of the dendrite arm spacing is believed to be responsible for the change in fracture appearance.

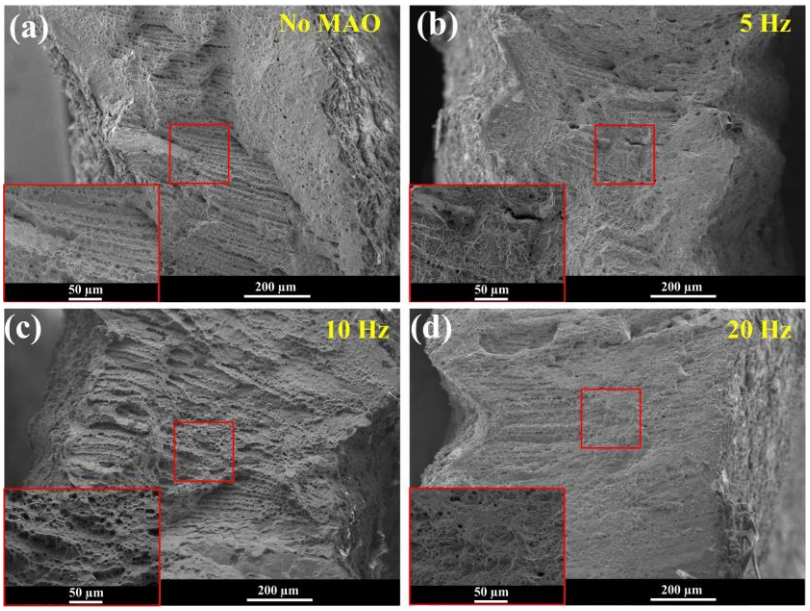

Fig. 6.15 Fractographs of tensile specimens under the four conditions: (a) without MAO; (b) 5 Hz; (c)10 Hz; (d) 20 Hz.

6.4 Conclusion

The present work shows that magnetic arc oscillation (MAO) can be used as an effective in-situ process incorporated during the manufacturing of the Hastelloy C276 samples by the GT-WAAM. This is confirmed by the analysis of four Hastelloy C276 wall-structures deposited under four different conditions, i.e. without MAO, with MAO at three frequencies of 5 Hz, 10 Hz, and 20 Hz, respectively. The manufacturing process and the surface roughness, macrostructure, microstructure, and mechanical properties of the manufactured samples without and with MAO were explored and evaluated. The following conclusions can be drawn:

(1) Application of MAO causes a dynamic moving of the arc, lowers the heat density, and results in a decreased solidification time. In this case, the addition of MAO during the WAAM process contributed to a slight refinement of the surface roughness, an increase in total wall height, and a decrease in total wall width, providing an incremental improvement in the deposition efficiency.

(2) Application of MAO leads to a lower Mo segregation in the interdendritic location, a fragmented dendrite structure and the misorientation of the dendrites. The DAS decreases with MAO, particularly at 5 Hz. However, bulk grain refinement and a decrease in *P* phase precipitation were not evident. The lower heat density resulting from the MAO, leads to an increase in the solidification rate which is considered to be responsible for the observed decrease in DAS.

(3) Compared to the no MAO sample, MAO at 5 Hz results in increases in nano-hardness, yield strength (YS), ultimate tensile strength (UTS), reduced elastic modulus and increased resistance to plastic deformation. Effects of MAO on mechanical properties for higher oscillation frequencies (10 Hz and 20 Hz) were less pronounced. The increased mechanical properties are attributed to the decrease of DAS.

Overall, the best combination of the dendrite refinement and improvements in the surface accuracy and mechanical properties were achieved using the lower frequency, 5 Hz, of MAO at the present conditions.

7 Stabilised mechanical properties in Ni-based Hastelloy C276 alloy by additive manufacturing under different heat inputs incorporated with active interlayer temperature control

7.1 Introduction

WAAM offers high deposition rates, contributing to significantly decreased cycle time [9]. The possibility of WAAM-related defects, including porosity, distortion, and surface defects requiring surface finish machining, is readily offset by the optimised process efficiency, as mentioned in the last chapter. Cold metal transfer (CMT)-based WAAM is a controlled dip transfer variant of the GMAW-based WAAM process, which primarily enables lower heat input coupled with a high deposition rate and a negligible amount of spatter [144]. Thin-wall Hastelloy C276 structures have been fabricated using the GT-WAAM process [162], where relatively coarse columnar grains with epitaxial dendrites grew along the deposition. Mo segregation occurred at interdendritic areas, resulting in anisotropy in mechanical properties, and a large amount of intermetallic *P* phase throughout the matrix. Since large-scale elemental segregation and intermetallic precipitation usually degrade mechanical properties, hence curtailing the applicability of WAAM-fabricated Hastelloy C276 alloy.

To obtain desired properties for WAAM fabricated Ni-based alloy components, it is important to understand the process-microstructure-property correlation. The microstructure is controlled by the (a) liquid-solid and (b) solid-solid phase transformations in the alloy system under thermal or thermo-mechanical treatment regimes. For example, an increase in mechanical properties under ambient temperature can be achieved by reducing the transformation time from liquid to solid, thereby

eliminating large-sized columnar grains [87]. The columnar dendritic microstructure was refined in AM fabricated Inconel 718 by increasing the cooling rate via laser diameter management and decreasing offering the heat input per unit during AM [301]. Complementary studies have also been performed to limit the precipitation and refine DAS, including primary and secondary DAS in additive manufactured Ni-based alloys [302]. Reducing heat input and applying magnetic arc oscillation during the WAAM of Ni-based alloys were effective in producing fine DAS due to enhanced heat dissipation [208, 303]. However, crystallographic texture along with the MAO and heat inputs was not thoroughly studied.

Crystallographic texture and density of crystalline defects during fabrication also influence the final mechanical properties of the alloy. Ni-based alloys fabricated by WAAM are characterised by relatively large grain sizes [15, 304]. Optical and electron microscopy-based investigations of these large grain structures are useful but tend to be destructive and do not usually give enough sampling statistics. Deeper knowledge of the microstructural development and how the WAAM process might be further optimised calls for additional neutron and/or synchrotron X-ray diffraction. Compared to micro-texture studies, neutron or synchrotron X-ray diffraction probes comparatively large sample volumes and return statistical data on bulk texture and detailed insights into phase determination, lattice distortion, and dislocation density.

Ma et al. [305] studied the bulk texture of laser-based directed energy deposited Inconel 625 alloys using neutron diffraction, and found that <100> grains grew along the laser-scanning direction. However, arc-based processes with more heat input, which potentially induces different textures, were not studied. Wang et al. [161] studied different heat inputs in fabrication of Inconel 625 using interlayer temperature control,

while the variation of heat inputs was limited to a small range (only ~ 50 J/mm fluctuations). Zhang et al. [306] found an effective interlayer temperature control under different heat inputs in the fabrication of Ni-based alloy by CMT-based WAAM, but there was no systematic study into related microstructure study, such as texture evolution. Especially, little research devoted to CMT-based WAAM process evaluation for Ni-based Hastelloy C276 alloy, particularly on the tailored, bulk texture and microstructure evolution associated with different heat inputs and interlayer operation during processing.

This work is part of our ongoing studies to facilitate the process optimisation of CMT-based WAAM for future large-scale manufacturing and practical applications of Ni-based Hastelloy C276 alloy. Here CMT-based WAAM was evaluated by depositing three thin-wall Hastelloy C276 structures using different heat inputs with active interlayer cooling and interlayer temperature control. The novelty and significance of this work are to provide insight into understanding the effects of active interlayer control in the stabilisation of mechanical properties in manufacturing Hastelloy C276 alloy, and the systematic investigation into the reasons and related microstructure evolutions. These include dendrite and grain morphology, segregation through interlayers, geometrically necessary dislocation (GND) density, and especially the bulk texture and total dislocation density (TDD) evolution in a large study scale using Neutron and Synchrotron X-ray diffraction, respectively.

7.2 Materials and methodologies

7.2.1 Materials manufacturing

A CMT-based WAAM, as shown in Fig. 3.3, was used in this chapter to deposit three thin wall structures on three substrate plates of plain carbon steel with dimensions of

150 mm × 300 mm × 6 mm. The feedstock was the Hastelloy C276 wire with a 1.2 mm diameter, and the chemical composition is listed in Table 3.1. To limit the deformation induced by heat accumulation, a zig-zag (forward and backward) deposition direction was used in material manufacturing. To enhance the cooling rate and optimise deposition geometry, compressed air was blown to the surface of depositions after each layer's deposition and the interpass temperature was controlled to below 50 °C. Three single bead thin-wall components were deposited in this work with a height of 40 mm and a length of 120 mm.

7.2.2 Determination of heat input conditions

In this study, bead-on-plate tests were conducted using various welding conditions to investigate the bead geometry under different heat inputs. The wire feed speed (WFS) varied from 4 - 6.5 m/min with a step size of 0.5 m/min and the torch travel speed (TS) was 2 - 10 m/min with a step size of 2 m/min. The recorded arc voltage *U (V)* and arc current *I (A)* were analysed after deposition to obtain the average arc power and linear heat input per unit length. The average arc power *P (W)* was calculated according to

$$P = \frac{1}{n} \times \sum_{t=0}^{n} U_t I_t \, , n = \frac{t_{weld}}{sampling\ rate} \qquad (1)$$

where t_{weld} is the total deposition time, and *I* and *U* are the instantaneous welding current and voltage, respectively. The linear heat input *E* (J/mm) was calculated according to

$$E = \frac{60}{1000} \times \frac{P}{V} \qquad (2)$$

where *V* is the travel speed (m/min). Note that heat conduction, convection and radiation to the environment and substrate were not considered in this equation.

Fig. 7.1 shows the bead geometries under various linear heat input *E*. The results of these preliminary bead-on-plate tests show that insufficient heat input conditions occurred for $E \leqslant 197$ J/mm (bead no. 1). Such inadequate heat input resulted in poor heat penetration and incomplete melting, leading to a twisted bead and consequently unacceptable for the successive deposition of the next layers. The bead width increased with increasing the heat inputs and a stable bead of ~6 mm width was reached when the heat input was increased to E = 276 J/mm (bead no. 9) under the present testing conditions (Fig. 7.1). Narrow bead will induce more bead deposition and overlapping of adjacent layers in the deposited component, which may result in macroscopic defects, such as voids between the overlaps, and reduced deposition efficiency. However, the too high heat inputs of E > 552 J/mm (bead no. 10) can lead to other drawbacks, counteracting the characteristics of CMT-induced low heat input. These include deposition collapse, increased overflow of welding pool, rough surface finish, and enlargement of columnar dendrite width, all of which result from high heat accumulation [185, 306]. Therefore, with combined consideration of work efficiency and favourable properties, three heat inputs of 276 J/mm, 368 J/mm, and 552 J/mm were selected in this research to evaluate the process and operation window in the fabrication of Ni-based Hastelloy C276 by CMT-based WAAM. Table 7.1 presents the applied WAAM processing parameters under different heat inputs.

Fig. 7.1 Bead-on-plate tests to determine the heat input parameters.

Table. 7.1 WAAM process parameters of three samples.

Sample	WFS/(m/min)	TS/(mm/min)	Current/(A)	Voltage/(V)	Heat input/(J/mm)
1	6.5	600	157	17.6	276
2	6.5	450	157	17.6	368
3	6.5	300	157	17.6	553

7.2.3 Material characterisation

All specimens for the same functional observations were taken from equivalent positions on each of the three walls. As shown in Fig. 7.2, the macrostructure and layer morphology were observed from the cross-section of the deposition direction (y - z plane). For all microstructure characterisation work, metallographic specimens were extracted from the middle of the travelling direction (x - z plane) of each deposited sample, with a dimension of 10 mm × 10 mm × 2 mm. They were then prepared using standard metallographic sample preparation procedures including mounting, polishing and final electro-etching at room temperature. Optical micrographs were obtained using a Leica DM6000 OM, and the layer height and DAS were calculated using ImageJ software [277]. The microstructure was further studied by SEM operating at 20 kV with an EDS detector. For preliminary observation of grain size, micro-texture and misorientation distribution analysis, samples were studied by EBSD and Aztec software suite. Post-processing of EBSD data was undertaken using the OI HKL-Channel 5 software suite.

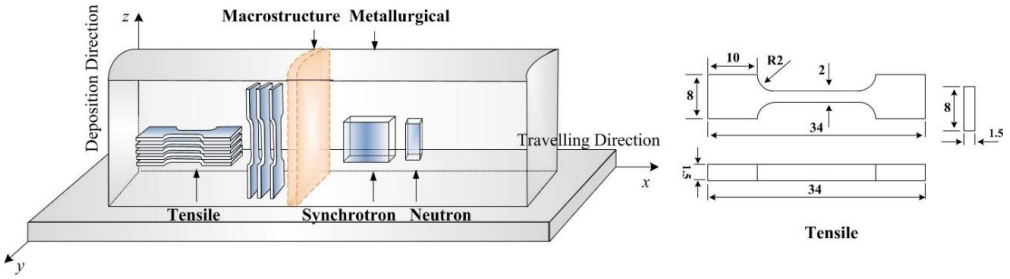

Fig. 7.2 Schematic illustration of sampling location and the sample geometries

The EBSD samples were also measured by synchrotron X-ray diffraction with the setup parameters in section 3.5.2 and data was analysed using Topas software (V4.2) [227]. To evaluate if any peak broadening occurs under different heat inputs, the measured diffraction peak profiles were fit using split Pseudo-Voigt functions with the instrumental broadening effect on the peak profiles corrected using the data measured from the NIST-certified Standard Reference Material 660b of LaB_6 powder. The bulk texture was measured using neutron diffraction on the high-intensity WOMBAT diffractometer. The setup parameters and data analysis are presented in section 3.5.5.

Five tensile testing specimens were extracted from the middle of each sample in the travelling direction (x - y plane), 15 mm away from the side regions, and three from the deposition direction (y - z plane). Tensile tests were carried out, with an installed video extensometer used to measure the displacement during tension loading.

7.3 Results and discussion

7.3.1 Microstructure

7.3.1.1 Dendrite evolution

Figure 7.3 shows the macrostructure in the y - z plane and microstructure in the x - z plane of cross-sections of etched samples under three conditions. From the macrostructure shown in Fig. 7.3a - c, considering the dilution from the substrate and instability of the first few deposition layers, the height of each layer was measured from the fifth layer, with average values of 1.7 ± 0.5 mm, 2.2 ± 0.8 mm, and 2.5 ± 1.1 mm for the heat input of 276 J/mm, 368 J/mm, 553 J/mm, respectively. Additionally, as shown in Fig. 7.3c, the highest fluctuation in the layer width was observed in the 553 J/mm sample. Therefore, the best surface quality is expected to be achieved in the

lowest heat input sample, due to lower layer height, layer width fluctuation and less overflow.

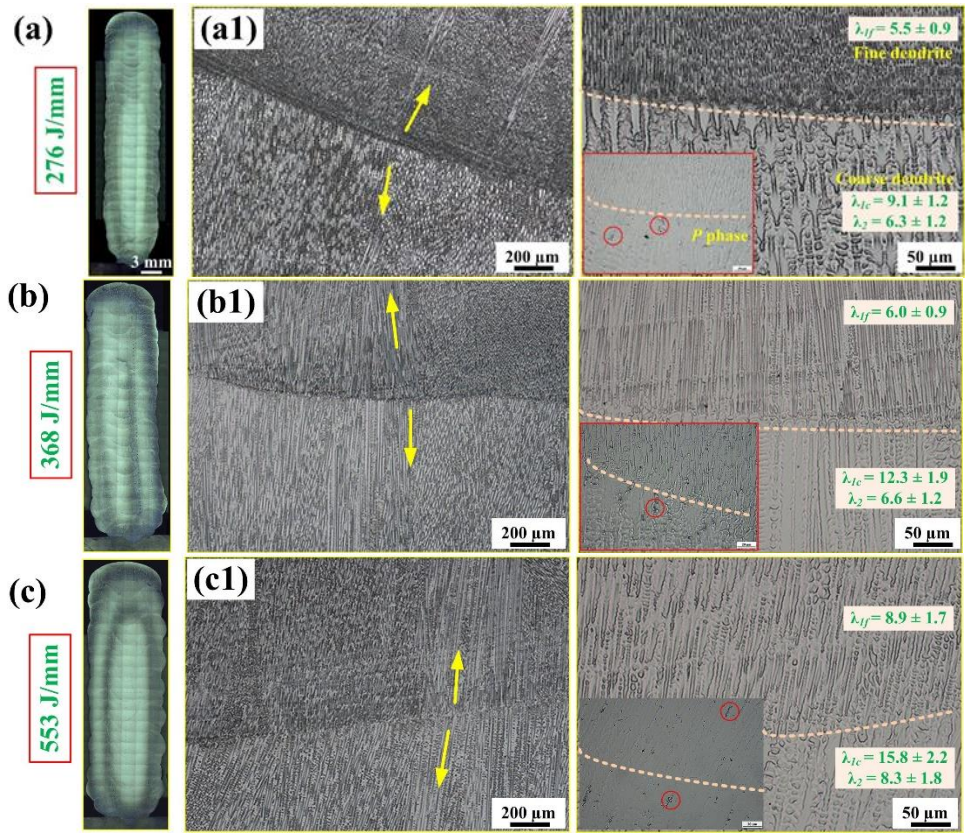

Fig. 7.3 (a - c) Macrostructure (from y - z plane) and (a1- c1) microstructure (from x - z plane) of three heat input conditions: (a) 276 J/mm; (top panel); (b) 368 J/mm (middle panel); and (c) 553 J/mm (bottom panel); (a1- c1) Microstructure of three samples with a comparison of DAS: (a1) 276 J/mm; (b1) 368 J/mm; (c1) 553 J/mm. The DASs are indicated in the micrographs.

Figures 7.3a1-c1 show the microstructures observed from travelling direction (x - z plane). As can be seen, the matrix presents columnar grains with epitaxial dendritic microstructure growing along the deposition direction over successive layers, meaning the newly dendrite orientation maintained the same as previously solidified structures from the molten pool underneath. Although a backward and forward (zig-zag) deposition path was adopted in the current work, there is only a slightly alternative angle to their growing orientation with respect to that in the previous layer, which has been found previously to be much higher (~ 45°) in laser-based AM fabricated alloys

[307, 308]. Solidification of columnar dendrites during AM occurs through nucleation and/or grain growth, while the driving force for growth is much smaller than the nucleation, hence dendrites grow epitaxially in the matrix following the heat flow. However, compared to the laser-based AM process, the solidification rate by CMT is much lower [9, 134]. Hence, the dendrites grow epitaxially, but only a slight variation of growing orientation was found due to the zig-zag deposition path with forward and backward heat flow directions, and the angle is more obvious in the sample prepared with the faster travelling speed (lower heat input).

Examination of Fig. 7.3a1- c1 reveals that all dendrites under three heat inputs exhibit a refined morphology at the very beginning of a single layer, adjacent to the previous layer surface, and subsequently the dendrites were coarsened with growth. *P* phase, which was confirmed by authors' previous studies [162], was found to be spread throughout coarsening interdendritic areas especially, and less in refined interdendritic areas. During cooling after deposition, solute Mo and W elements were rejected by each dendrite to liquid and formed the interdendritic areas, where microsegregation of alloying elements occurs. The coarsening interdendritic areas are rich in solute element segregations, including Mo as strong *P* phase-stabilising elements, which was confirmed by EDS in the following section. Mo is reported to be favour the precipitation and growth of intermetallic *P* phases [170].

The average DAS (λ) at the start and end of a single layer along deposition direction under three conditions were presented and compared in Fig. 7.3. It can be found that with increasing heat input, the DAS (λ) also coarsens. The primary DAS (λ_1) within the coarsened dendrite areas (λ_{1c}) for the 276 J/mm heat input sample was ~ 73.5 % lower than for the 553 J/mm sample, and ~ 61.4 % lower at the refined dendrite area

(λ_{1f}). The secondary DAS (λ_2) at regions containing coarsened dendrites under the three conditions exhibited the same tendency, being ~ 31.7% lower for 276 J/mm heat input than for 553 J/mm heat input. Additionally, the obtained DAS (λ) of Hastelloy C276 by CMT in the current work was dramatically lower than that of this alloy produced by the GTAM-based WAAM processes [178, 208]. Ascribed to the same material studied here, factors including: Gibbs-Thomson coefficient, diffusion coefficient or non-equilibrium solidification range, should have negligible effects on the variety of DAS (λ), but predominantly affected by temperature gradient [309]. As the interpass temperature is being controlled to be relatively low, it is important to understand theheat flow effect on the dendrite growth within one single layer. At one moment the heat exchange in the molten pool at some height can be described by heat accumulation, heat input and heat loss, as $\Delta h_{cum} = \Delta h_{input} - \Delta h_{loss}$, *where* heat loss is dependent on heat conduction, convection and radiation, as $\Delta h_{loss} = \Delta h_{cond} + \Delta h_{conv} + \Delta h_{rad}$. The predominant direction of heat flow is given by [309]:

$$\nabla \mathrm{T} = \frac{\partial T}{\partial x} i + \frac{\partial T}{\partial y} j + \frac{\partial T}{\partial z} k \qquad (3)$$

where T is the temperature and i, j and k are unit vectors in the scanning (x), width (y) and vertical (z) directions, respectively. The temperature gradient, G, is:

The temperature gradient, G, is described as:

$$\mathrm{G} = \|\nabla \mathrm{T}\| = \sqrt{\left(\frac{\partial T}{\partial x}\right)^2 + \left(\frac{\partial T}{\partial y}\right)^2 + \left(\frac{\partial T}{\partial z}\right)^2} \qquad (4)$$

which $\|\nabla \mathrm{T}\|$ is the magnitude of ∇T. It is assumed that no temperature gradient exists along the y-direction at any point on the longitudinal mid-section symmetry plane at y = 0.

As aforementioned, the sample with higher heat input possesses a higher layer height. Owing to the interpass temperature control to below 50 °C, the new deposition on the colder surface of the previous layer than the welding pool is associated with favourable heat diffusion conditions via effective thermal conduction and radiation to the relatively cold surface, while with lower conduction rate with the increase of height [218]. With the increase of a welding pool height, the heat diffusion condition becomes worse, and heat loss (Δh_{loss}) decreases gradually, leading to the decrease of $\frac{\partial T}{\partial x}$ and $\frac{\partial T}{\partial z}$. Hence, a better heat diffusion condition leads to a high temperature gradient (G). This will leave less time for solute element redistribution, hence the dendrites are refined at the beginning but coarsened with growth, and wherefore lower heat input contributes to lower DAS as well. On the other hand, the sample with higher heat input experiences more heat accumulation (Δh_{cum}). Therefore, the higher heat input also results in a higher dwelling time for the following layer deposition, which can stimulate crystalline evolutions. For Ni-based alloys, the dendrite growing orientation and spacing are of particular importance for mechanical performance, and their influence might persist in the following applications [310].

7.3.1.2 Columnar microstructure

To evaluate the heat input effects on the grain size, morphology and orientation of CMT fabricated Hastelloy C276 alloy, EBSD mapping was performed on samples taken from travelling direction (x - z plane), and the results are shown in Fig. 7.4. The obtained inverse pole figure (IPF) orientation maps show the grain crystallographic orientations along deposition direction.

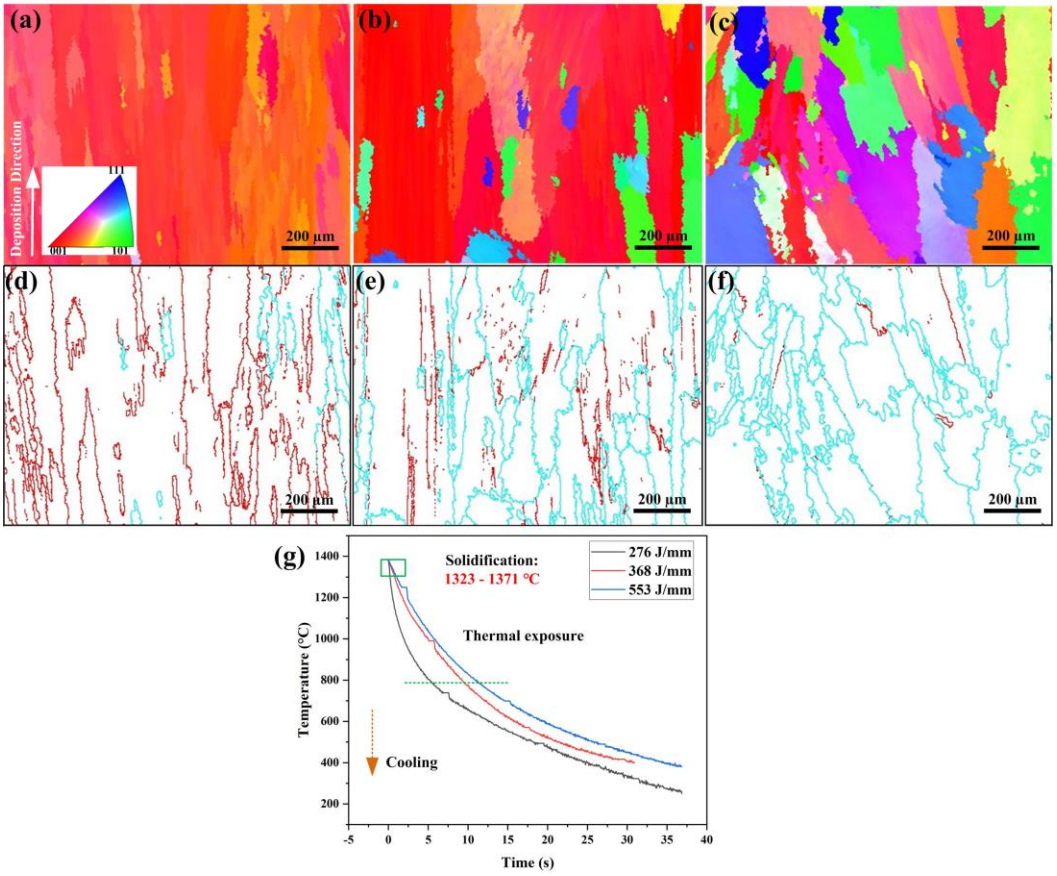

Fig. 7.4 EBSD orientation maps of the CMT-processed Hastelloy C276 samples fabricated under (a) 276 J/mm, (b) 368 J/mm, and (c) 553 J/mm heat inputs. (d), (e), and (f) show the corresponding grain boundary maps of the above-mentioned three heat input conditions, with the LAGBs (misorientation 2°-10°) and HAGBs (misorientation >10°) coloured in red and blue, respectively. (g) Temperature evolution during cooling of three samples

As can be seen from Figs. 7.4a - c, the as-fabricated samples exhibited coarse columnar grain morphology observed along the deposition direction, with various sizes throughout the matrix. The higher heat input appeared to lead to more grain nucleation, hence inducing some small grains of varying orientation. It should be mentioned that the grain-scale EBSD mapping on the relatively large grain size of Ni-based alloy by WAAM has significant limitations on the grain sampling statistics. Additionally, it was found that all the investigated samples exhibited a strong (200) fiber texture along the deposition direction. For *FCC* metals, <0 0 1> is the preferential grain growth direction, and the growth velocity along this direction is faster than in other directions due to the

maximum solidification driving force from the direction of the highest temperature gradient [311]. In the solidification process, the growth of grains of the <0 0 1> orientation closely aligned with the temperature gradient direction will prevail over other grain orientations [310]. The bulk texture results from neutron diffraction will be also discussed in Section 7.3.1.4.

The grain boundary maps with three different heat inputs are further shown in Fig. 4d - f. The low- and high-angle grain boundaries (LAGBs: misorientation in the range of 2°-10°, HAGBs: >10°) were present in red and blue, respectively. As can be seen, more HAGBs developed with increasing heat input. Due to the thermal cycling experienced in the CMT-based WAAM process, reheating and partially/completely remelting occurred, leading to the recrystallisation and development of HAGBs [312]. The deeper level of remelting and longer thermal exposure from the increased heat input will promote the recrystallisation, resulting in a high fraction of HAGBs, while the lower heat input from raised travelling speed postpones the immigration and integration of sub-grains and reduces HAGBs. In order to look into the temperature evolution during deposition, a thermal camera was used to observe the cooling rate under different heat inputs, and a typical temperature profile taken during the cooling stage of the tenth layer was present in Fig. 4g. It is found the higher solidification rates and cooling rates were associated with the lower heat input, which is ascribed to the better heat diffusion conditions [218]. The relatively large cooling rate in lower heat input samples by CMT may produce a steep temperature gradient as aforementioned. This inhibits the recrystallisation, hence retaining more LAGBs than the high heater input samples. Therefore, the sample with lower heat input and a higher solidification rate possessed more LAGBs, which leads to higher geometrically necessary dislocation (GND) density [313].

7.3.1.3 Synchrotron X-ray analysis

To further evaluate the microstructure in terms of phase constitution and dislocations in studied samples, high-resolution synchrotron X-ray diffraction was performed at room temperature. Fig. 7.5 shows the measured diffraction patterns in a 2θ range of 5° to 85°. Under three heat input conditions, in addition to the dominant matrix γ-Ni phase, a minor intermetallic *P* phase was indexed based on its characteristic weak diffraction peaks present at low 2θ angles of approximately 16° and 19.5°. Moreover, significant variations in the intensities of the same reflections of the γ-Ni phase in three samples were observed, which is likely due to the crystallographic texture typically developed in the AM samples. It was noticed that strong (h00) reflections including (200) and (400) appeared in the measured sample orientations for three conditions. Further analysis of the γ-Ni matrix crystallographic texture with neutron diffraction will be presented in the following sections.

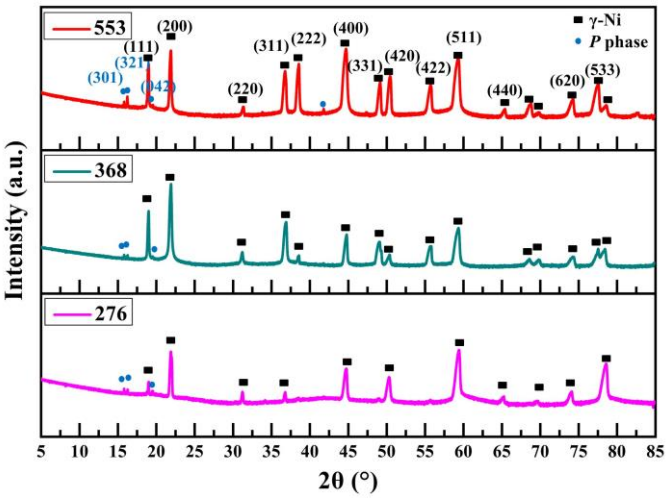

Fig. 7.5 Synchrotron results of three samples with the heat inputs of 276 J/mm, 368 J/mm and 553 J/mm.

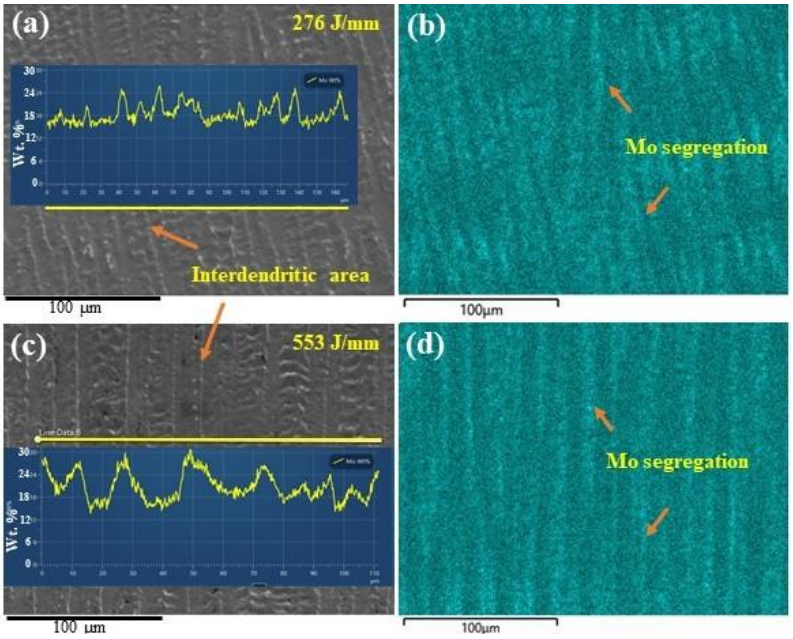

Fig. 7.6 SEM-EDS analysis of Mo element distributions in typical heat input conditions of (a) and (b) 276 J/mm, and (c) and (d) 553 J/mm. Reduced Mo segregation was observed in the 276 J/mm sample.

The lattice parameter (*a*) of the matrix γ-Ni phase was obtained from full-pattern Pawley refinement. The result shows that the γ-Ni lattice parameter tends to slightly decrease with increasing the heat input, with a = 3.60246 Å at 276 J/mm, a = 3.59915 Å at 368 J /mm and a = 3.59664 Å at 553 J/mm. This lattice parameter variation may be related to the Mo segregation in the alloys under different conditions [178]. To find out Mo distribution in the microstructure, SEM-EDS analysis at similar layer areas was conducted for 276 J/mm and 553 J/mm in which obvious differences in Mo segregation were found, as shown in Fig. 7.6. It was found that Mo was segregated in the interdendritic areas under two conditions, due to its low partition coefficient [80, 178]. Lower Mo segregation (see Mo compositional line scan profiles in Fig. 7.6a and 7.6c) was observed in the 276 J/mm heat input sample, which may correlate with the increase of lattice parameter in this sample. Higher heat input reduced cooling rate and postponed the solidification to a certain degree, promoting more Mo segregation and possibly leading to more precipitates [306]. As Mo has a larger atomic radius than base

element Ni, the less Mo segregation as in the lower heat input leads to the resultant slight increase of lattice parameters of the matrix phase.

Additionally, a high-resolution synchrotron X-ray peak broadening analysis was used to evaluate the crystalline sizes and lattice strain by the modified Williamson-Hall (W-H) analysis, as shown in Fig. 7.7. The synchrotron X-ray diffraction data showed that no significant difference in peak widths of the same reflections was observable among three heat input conditions. The modified W-H analysis enables the separation of the size-strain diffraction broadening contributions following the formula [314, 315]:

$$\Delta K \cong \frac{0.9}{D} + \left(\frac{\pi M^2 b^2}{2}\right)\rho^{\frac{1}{2}}K\bar{C}^{\frac{1}{2}} + O(K^2\bar{C}) \qquad (5)$$

where D is the crystalline size, M is a constant, ρ and b are the average density and the magnitude of the Burgers vectors of dislocations, respectively. $\Delta K=2\cos\theta[\Delta(2\theta)]/\lambda$, where $\Delta(2\theta)$ is the FWHM of a diffraction peak, $\bar{C}$ is the average dislocation contrast factor that can be determined following [316], and $O(K^2\bar{C})$ denotes the high order in $K^2\bar{C}$. In the modified W-H plots (Fig. 7.7), the slopes of linear fits are quite close for three samples. This evidence qualitatively suggests that no significant change in the average total density of dislocations (a source of the diffraction peak broadening) of three conditions was identifiable from the obtained synchrotron X-ray data. This finding appears to suggest that the heat input controlled by travelling speed is not a determining factor for the thermally induced plasticity and the micro-strain development associated with the dislocation accumulation in the studied conditions, although it does alter the thermal history, ascribed to active cooling and interlayer temperature control. Such behaviour is believed to be beneficial for the present CMT-based manufacturing of Hastelloy C276 over a broad processing window, under which no additional dislocation

hardening occurs during AM and hence lowers the thermal cracking susceptibility in the processing.

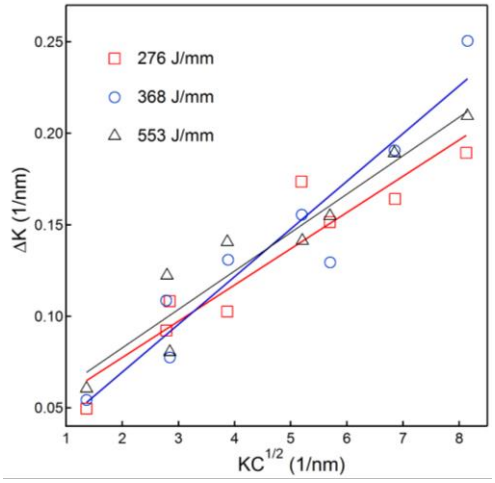

Fig. 7.7 The modified Williamson-Hall plots of three samples manufactured under various heat inputs.

7.3.1.4 Bulk texture

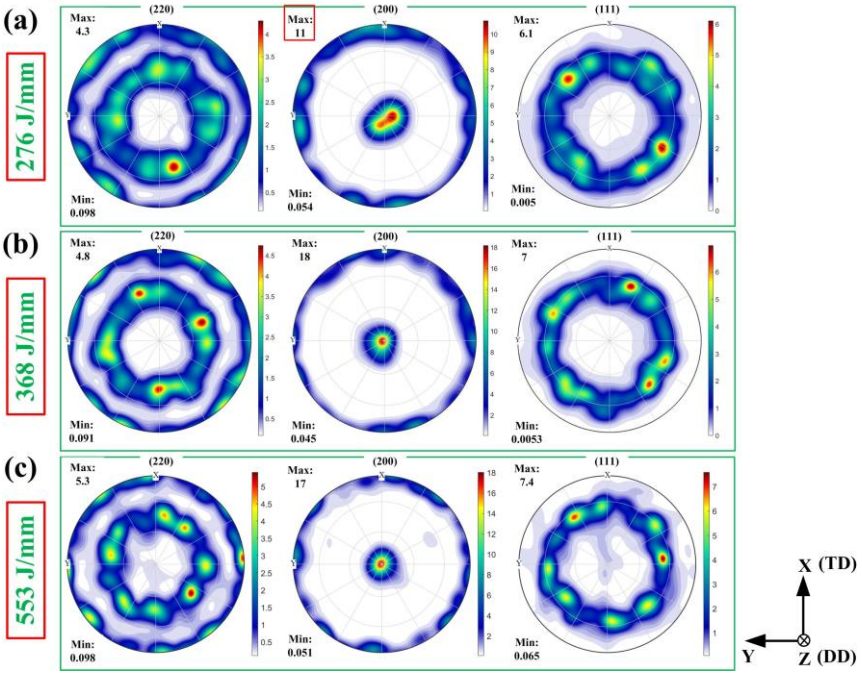

Fig. 7.8 Neutron diffraction bulk texture results of γ-Ni phase represented by (220), (200) and (111) pole figures for three samples: manufactured at (a) 276 J/mm, (b) 368 J/mm, and (c) 553 J/mm. TD and DD denote the travelling direction and deposition direction, respectively.

Crystallographic anisotropy is another important factor that influences the properties of deposited materials. This motivated the bulk texture analysis by neutron diffraction on the as-fabricated Hastelloy C276 under different heat inputs. The recalculated (220), (200) and (111) pole figures of the matrix phase from the ODF are depicted in Fig. 7.8. Note that individual texture strength scales in the unit of multiples of random distribution (m.r.d) were used for each pole.

As can be seen, a sharp fibre-type (200) crystallographic bulk texture with pole densities concentrated along the deposition direction was found in three samples, which is typical in AM fabricated Ni-based alloys [15, 149]. There are also (200) pole densities distributed perpendicular to the deposition direction. This result is consistent with the local observation by EBSD which shows various grain orientations as typically seen in higher heat input conditions (Fig. 7.4c). Moreover, the (200) texture strength of 276 J/mm heat input sample was measured to be 11 m.r.d., which increased to 18 and 17 m.r.d. for higher heat inputs of 368 J/mm and 553 J/mm, respectively. Hence, the higher heat input tends to induce a relatively stronger (220) texture. Additionally, it is noted that the (200) poles along the deposition direction were split in the 276 J/mm heat input sample, and in combination with (220) and (111) pole figures, such splitting was considered to be the reason for the decreased (200) texture strength in the 276 J/mm sample. At the higher heat input samples, the (200) pole distribution presents an ellipse shape without split. The ellipse shape or split is possibly due to the deviation of the (200) grain growth directions from the preferred deposition direction caused by the zig-zag deposition path, and the split occurs under a lower heat input with a higher solidification rate and faster travelling speed. Primary dendrites of the later-deposited layer are slightly misaligned with that in the previous layer, which leads to the misorientation of columnar grains, while the solidification texture still follows heat flow

and the highest gradient, hence developing the split (200) pole distribution following the zig-zag heat flow direction [307]. Therefore, it can be inferred that the solidification texture of AM fabricated Ni-based alloy is likely manipulatable through proper heat transfer and deposition path adjusting strategies.

7.3.2 Mechanical properties

Figure 7.9 displays the tensile strength of the samples taken from the deposition direction and travelling direction to illustrate the variations of strength under different heat inputs and mechanical anisotropy. Generally, under current processing conditions, all three heat input process parameters showed similar strength. A slightly lower tensile strength was found in the deposition direction than that from travelling direction of every fabrication condition. This is possibly correlated with the columnar microstructure with strong texture produced in the Ni-based alloys by WAAM. Solidification texture depends on the local heat flow directions and competitive grain growth in one of the six <1 0 0> preferred growth directions in FCC alloys. Such texture will result in a relatively lower strength along the solidification direction, as the (111) plane aligns close to maximum shear stress orientation [153]. This makes it easier to activate the dislocation slip system, hence lowering the strength in the deposition direction.

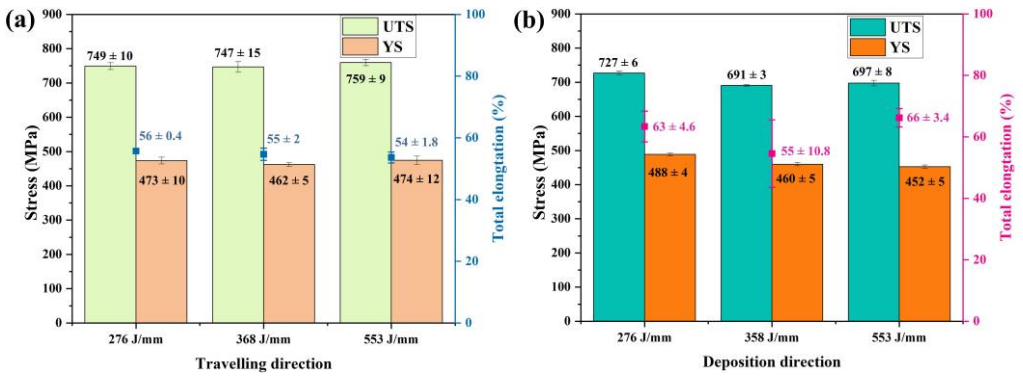

Fig. 7.9 Mechanical properties of three samples from different directions: (a) travelling direction (x-y plane), (b) deposition direction (y-z plane)

As can be seen from Fig. 7.9a, there is no significant difference in average ultimate tensile strength (UTS) of three heat input samples along the travelling direction of the deposition, which fluctuated only slightly from 747 ± 15 MPa to 759 ± 9 MPa. Similar trends with the heat inputs were observed for 0.2% yield strength (YS) varying from 462 ± 5 MPa to 474 ± 12 MPa, and for total elongation (TE) from 54 ± 2% ~ 56 ± 0.4%. This is considered due to the well-controlled interlayer temperature, which decreased the heat accumulation and minimised the repetitive thermal exposure [306]. Under effective interlayer temperature control, the coarse grains of similar sizes are maintained at various heat inputs (Fig. 7.4), thus no variation in the grain boundary strengthening under these conditions. In addition, although the samples of the lowest heat input were demonstrated to have more LAGBs and higher GND density, the contribution of dislocation strengthening in the alloys under three heat inputs is considered to be similar. This is consistent with the similar average total density of dislocations, including GND and statistically stored dislocation (SSD) developed in the as-fabricated microstructure under various heat inputs.

In comparison, a larger fluctuation in UTS was found from 691 ± 3.1 MPa to 727 ± 6 MPa along deposition direction, with the highest average UTS achieved in 276 J/mm sample, especially the YS increased to 488 ± 4 MPa. The lowest heat input sample possessed a decreased mechanical anisotropy, which is favourable for the application of AM Ni-based alloys. In the deposition direction, effects of crystallographic evolution of samples under three fabrication conditions are more visible in the related mechanical properties. It was found that texture and Mo elemental segregation of 276 J/mm samples were both slightly lower than the other two heat input samples, as seen in Fig. 7.8. This promotes reduced mechanical anisotropy [149]. Moreover, the dendrites in the columnar microstructure of 276 J/mm sample are refined, which is considered to

enhance the strengthening contribution, having similarities with the Hall-Petch relationship. [298]. Although the current work suggests no significant thermally induced plasticity in CMT-based WAAM fabricated Hastelloy C276 with active temperature controls, further work is still required to understand the effect of initial as-fabricated microstructure on the strengthening behaviour of the manufactured alloys.

7.4 Conclusion

The present work evaluated the CMT-based WAAM process in the fabrication of Ni-based Hastelloy C76 alloy under different heat inputs with active cooling and interlayer temperature control. The manufacturing process, microstructure, and mechanical properties of the manufactured samples under three heat input conditions were explored and evaluated. The main conclusions are summarised in the following:

(1) Incorporating active interlayer temperature control in the CMT-based WAAM process is effective to stabilise the mechanical properties of Hastelloy C276 over broad heat input conditions from 276 J/mm to 553 J/mm. Analogous mechanical properties of the manufactured alloys were achieved under the investigated processing conditions.

(2) Sharp fibre-type (200) crystallographic bulk texture was found in the fabricated samples. However, the texture was slightly weakened at the lowest heat input, which is related to the deviation of the (200) grain growth orientation induced by the zig-zag deposition path under the highest solidification rate.

(3) More GNDs were observed in the lowest heat input condition, however, the average total dislocation density in the as-fabricated microstructure appeared to be similar under various heat inputs. This suggests that no significant thermally induced plasticity accumulated in the prepared alloys.

(4) Decreased mechanical anisotropy and favourable microstructure in terms of refined dendrites and reduced chemical segregation were obtained in the lowest heat input of 276 J/mm.

8 Microstructural characterisation and hardness assessment of wire arc cladded Hastelloy C276 on creep resistant steel P91

8.1 Introduction

Dissimilar metals have been widely applied in industrial sectors, such as defence, energy, transportation and aerospace [317, 318]. At present, one of the main impediments to dissimilar metal design is the atomic dilution of metals in interfacial regions, leading to the potential formation of detrimental brittle intermetallic compounds (IMCs) [319]. Extensive studies have been undertaken to develop manufacturing processes or approaches that are capable of producing advanced bimetallic materials with desired functionalities. Additive manufacturing (AM) techniques, where materials are introduced to parts sequentially, provide exciting opportunities for producing high-quality dissimilar metal components with discrete properties in an integrated manner. This can be achieved by tailoring local chemical composition distribution in components to eliminate detrimental IMCs formation via manipulating local feedstocks during AM.

Hastelloy C276 alloy is a solid solution strengthened Ni-based superalloy and it has superior high-temperature stability, high-temperature oxidation resistance and corrosion resistance [320, 321]. These properties enable this alloy for a wide range of applications in nuclear and chemical industries under high temperature or harsh environmental conditions, such as SWCR and flue gas desulfurization systems [18]. This alloy consists of high content of Mo and Cr alloying elements that are usually coherent with topologically closed packed (TCP) intermetallic precipitates of *P* phases under as-fabricated conditions [322]. In general, Hastelloy C276 is observed to be

readily weldable, however, due to the rapid precipitation of hard and brittle intermetallics during the welding process, the weldment is possible to have cracking or deteriorated properties. Hence, there requires a critical control for the welding of Hastelloy C276 components to impede *P* phase precipitation.

P91 steel is a type of 9Cr-1Mo steel with deliberate addition of V and Nb elements, and it has outstanding heat resistance and creep strength while suffering from relatively low corrosion resistance. This alloy is primarily used for the superheater and reheater in power plant boiler construction, and heating furnace piping in the petrochemical industry, with a steam temperature of around 650 °C and pressure of 30 MPa [323]. P91 steel has a typical tempered martensitic structure, which may be further decomposed during long-term service at elevated temperatures. Meanwhile, it often faces the challenge of property degradation [324]. To maintain required mechanical properties at high temperatures, several attempts have been directed towards modifying P91 steel through the addition of N or carbonitride elements, which promote the precipitation of carbonitride particles or fine carbides in material [325]. However, the use of P91 steel is limited at a temperature above 650 °C due to its limitation in oxidation resistance.

Although Hastelloy C276 alloy and P91 steel are both suitable for a high-temperature application, Hastelloy alloy exhibits much better corrosion and oxidation resistance but suffers from higher production costs compared to P91 steel. Cladding Hastelloy C276 on P91 steels has great potential to produce a component with both excellent high-temperature mechanical properties and oxidation/corrosion resistance in a cost-effective manner, which presents attractive nuclear application significance under elevated temperatures. The operational strategy involves a new hierarchically-heterogenous Ni-based alloy-steel structure that offers specific properties to severe

environments. Since both Hastelloy C276 alloy and P91 steel exhibit good weldability, these two materials are potential candidate materials that can be further joined using WAAM method to create a structural part. Here the WAAM technique offers flexibility for producing cladding materials at specific locations of a component and modifying the interfacial microstructure to achieve good bonding. Sridar et.al [326] reported P91 steel - Inconel 740H bimetallic structure fabricated using WAAM, while they found the crack is susceptible to being generated in gradient regions. The cracking susceptibility represents a major challenge for achieving reliable applications of these promoted P91 steel and nickel-based alloy parts during fabrication.

To explore the fabrication of more reliable structural materials, this study focuses on the development of a new dissimilar metal structure where Hastelloy C276 is cladded on P91 steel for nuclear application. Here a sound metallurgical bonding between two structural materials was achieved, and the material characterization was explored under both as-cladded and heat-treated conditions. The challenges potentially occurring in dissimilar structures, especially cracking and unhomogenized microstructures, have been addressed. This work provides insights into the development of dissimilar metal cladding with in-site specific properties.

8.2 Materials and methods

The P91 steel was in normalized and tempered condition, and it was cut to a substrate plate with a dimension of 100 mm ×50 mm ×6mm. The Hastelloy C276 welding wire, with a diameter of 1.2 mm, was used as the feedstocks and it was cladded on steel substrate using a GT- WAAM system. The chemical compositions of studied materials are listed in Table 8.1. The process parameters used for cladding were kept constant, with the same parameters in section 3.2.1. The interval time between each cladding

layer was maintained at approximately 30 seconds. After the cladded part was produced, specimens were extracted from the cladded plate mid-section for tempering treatment, which was carried out at 760 ℃ for 2 h in a vacuum furnace, followed by air cooling.

Table. 8.1 Chemical compositions of materials (wt.%).

Composition	Ni	Mo	Cr	Fe	W	C	Mn	Co	V	P	Si
Wire (Hastelloy)	Bal.	16.5	16.0	5.8	4.0	0.01	0.19	0.20	0.06	0.015	0.08
Substrate (P91)	0.17	0.9	8.65	Bal.	-	0.1	0.9	-	0.21	0.009	0.28

The metallographic specimens were hot mounted, ground and polished according to the standard procedures. After that, the specimens were etched in Villela's reagent (95 ml ethanol, 5 ml hydrochloric acid and 1 g picric acid) for steel microstructure observation, and then electro-etched in a mixed solution (5 mg oxalic acid and 15 ml hydrochloric acid) with 6 V direct current for 2 s at room temperature to reveal Hastelloy microstructure features. The microstructure was examined using a Leica M205A deep field stereoscopic microscope and a JEOL JSM-7001 SEM equipped with EDS detector. EBSD analyses were performed using a Zeiss® Ultra Plus SEM. The collected EBSD data were analyzed using the MTEX package [327]. Vickers hardness was measured on the same metallographic specimens, at a test load of 1 kg, an indentation dwelling time of 15s, and a step size of 0.5 mm, in accordance with the ASTM E384 standard. A hardness map was further drawn to depict hardness distributions from cladded Hastellloy layer to steel substrate.

8.3 Results and discussion

8.3.1 Metallographic observations

Fig. 8.1 shows cross-sectional macrographs and high-magnification micrographs at the

representative locations in as-cladded and heat-treated conditions. As can be seen, no macro-scale defects, including pores, cracks, or insufficient fusion, were observable on macrographs, which is favourable for practical application.

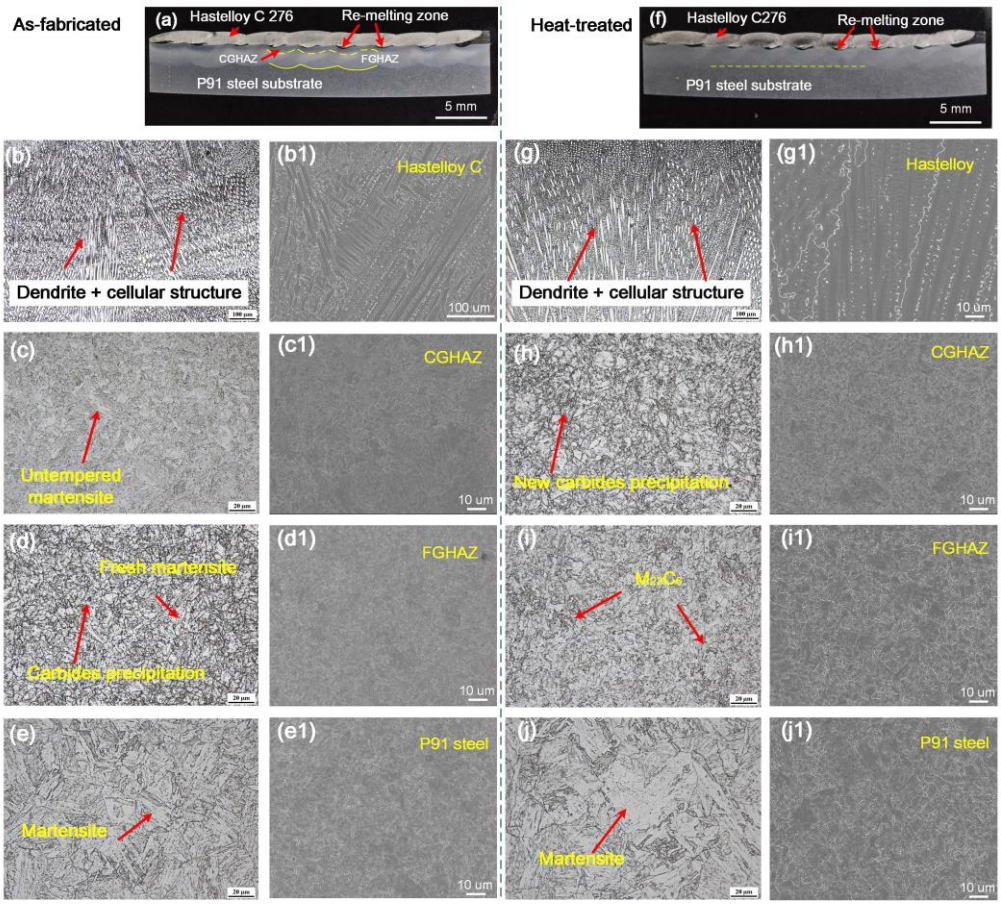

Fig. 8.1 The cross-sectional macrographs of the specimens: (a) as-cladded; (f) heat-treated, and optical micrographs and SEM images of selected locations for the studied specimens: (b), (c), (d) and (e) as-cladded condition for Hastelloy C, CGHZZ, FGHAZ, substrate; (g), (h), (i) and (j) heat-treated condition for the corresponding regions as mentioned above.

The coating layers (Hastelloy C276) exhibit a typical weld-like microstructure, comprising columnar dendrites with epitaxial or cellular morphologies, as shown in Fig. 8.1b. These columnar grains are recognized as the γ-Ni matrix, and it has been reported that dendrite generation in Hastelloy γ-Ni matrix is often associated with solute element segregation during rapid solidification conditions [178]. Hence, the intermetallic *P* phase can be found in the interdendritic area, as shown in Fig. 8.2.

The HAZ exhibits two distinct regions in as-cladded and heat-treated conditions: (i) coarse-grained HAZ (CGHAZ, Figs. 8.1c/h), and fine-grained HAZ (FGHAZ, Figs. 8.1d/i). The CGHAZ (T_p>>A_{c3}) and FGHAZ (T_p>A_{c3}) regions are formed due to the thermal cycling experienced during WAAM [328]. Here, T_p is the peak temperature experienced during deposition, and the temperature of A_{c3} for P91 steel is in the range of 890 - 940 ℃ [329]. The CGHAZ (Fig. 8.1c) regions are mainly composed of a typical lath martensitic microstructure with negligible precipitates. This region is close to the interface and experiences a temperature well above A_{c3} transformation temperature. As the T_p is much higher than the A_{c3} temperature in the CGHAZ region, the dissolution of the precipitates located along the prior martensite grain boundaries was promoted, leading to the grain boundary migration and resultant coarsening of prior grains during deposition [330]. It is evident that the CGHAZ often features the highest hardness of the HAZ [331], and this will be further presented in the following section. Moreover, the remelting from the subsequent thermal cycle also contributes to grains growth at the CGHAZ due to re-heating in this region. In contrast, The FGHAZ (Fig. 8.1d) experienced a peak temperature slightly higher or equal to the A_{c3} temperature, which leads to a complete phase transformation of austenite without significant grain growth, following the formation of fresh martensite during cooling, and then causing fine martensitic structure [331]. The substrate (P91 steel) shows highly tempered lath martensite together with a large amount of carbide precipitates located at both martensitic lath boundaries and prior austenite grain boundaries (Fig. 8.1e).

After heat treatment, grains appeared to be coarsened in all regions (Figs. 8.1g to 8.1j), including the cladding layer, CGHAZ, FGHAZ, and substrate, compared with that of as-cladded condition. On the Hastelloy side, more *P* phase precipitates in the interdendritic area, as shown in Fig. 8.2. The *P* phase can strengthen the alloy at ambient

temperature, but it has some adverse effects on corrosion resistance and hot cracking susceptibility [15]. On the steel side, tempering may result in the formation of new carbides and carbonitride precipitates at CGHAZ, and the main precipitates are widely reported to be Cr-enriched $M_{23}C_6$ and (Nb, V) enriched MX [328]. P91 steel has a narrow solidification temperature window to allow the material to solidify to the point that carbides become thermodynamically stable. Hence, these precipitates have a non-uniform distribution, and altered amounts or volume fractions, as shown in Fig. 8.1.

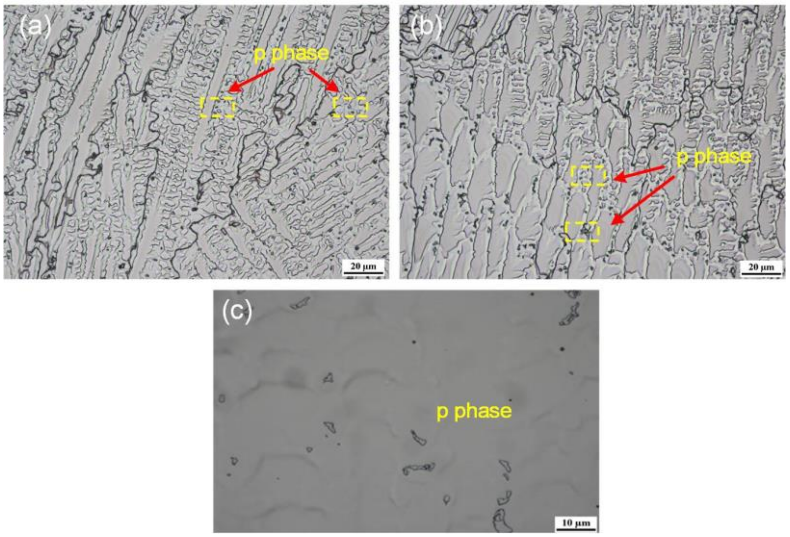

Fig. 8.2 The *P* phase appearing in the interdendritic area of Hastelloy cladding: (a) as-fabricated state; (b) heat-treated state; (c) high-magnification optical micrograph.

Fig. 8.3 shows a close observation of interfacial bounding regions for two specimens. As can be seen, Hastelloy coating presents obvious elemental segregation, especially Mo and W that congests along interdendritic boundaries. From EDS mapping, there is no discernible diffusion of main constitution elements (Ni, Fe, Cr, Mo, W) between two materials, but inhomogeneous pervasion of minor alloying elements W, Si, Mn and Co appeared during the deposition process. The dispersion of W element contributed more carbide precipitations to substrate, which could further impede grain in heat-affected zones [332]. Meanwhile, this behaviour benefits improving the oxidation and

carburization resistance of the cladding via the stabilization of primary carbides which are the strengthening phases in Ni-based alloys [333]. It is noticed that the Mn element has a significant dispersion into the Hastelloy side, especially after heat treatment. This behaviour is likely to improve the mechanical properties and oxidation resistance of the material [334].

On P91 steel side, as shown in Fig. 8.3, some δ-ferrite formed in CGHAZs in the vicinity of fusion line, which may be attributed to the carbon partitioning to Hastelloy C276 at high temperature and relatively high cooling rate after cladding [316]. It is observed that the mixing zones or remelting zones were generated near the interface (Fig. 8.3c). These mixing zones were promoted by the formation of a stagnant molten layer of the cladded material. As the overlapped path was used during WAAM, there will generate a mixing between the new layer and the adjacent deposited layer. It is well recognised that the melt pool of newly deposited layer has a temperature much higher than the solidification temperature. However, at the overlapped layer, the melting temperature remains close to the solidification temperature. Owning to such a temperature gradient near the interface, the portion of non-mixing deposition flowed to melt pool, and was quickly concreted prior to mixing with fresh melt pool, which finally result in the formation of mixing zones or remelting zone. Fig. 8.3c further shows EDS line scanning results across the remelting zone of bimetallic structure. As can be seen, there exists a sharp compositional gradient for the Ni, Fe, Cr, Mo elements. Such elemental variation across the interface is believed to contribute to the heterogeneous distribution of microhardness in a narrow region, which will be discussed in the following section.

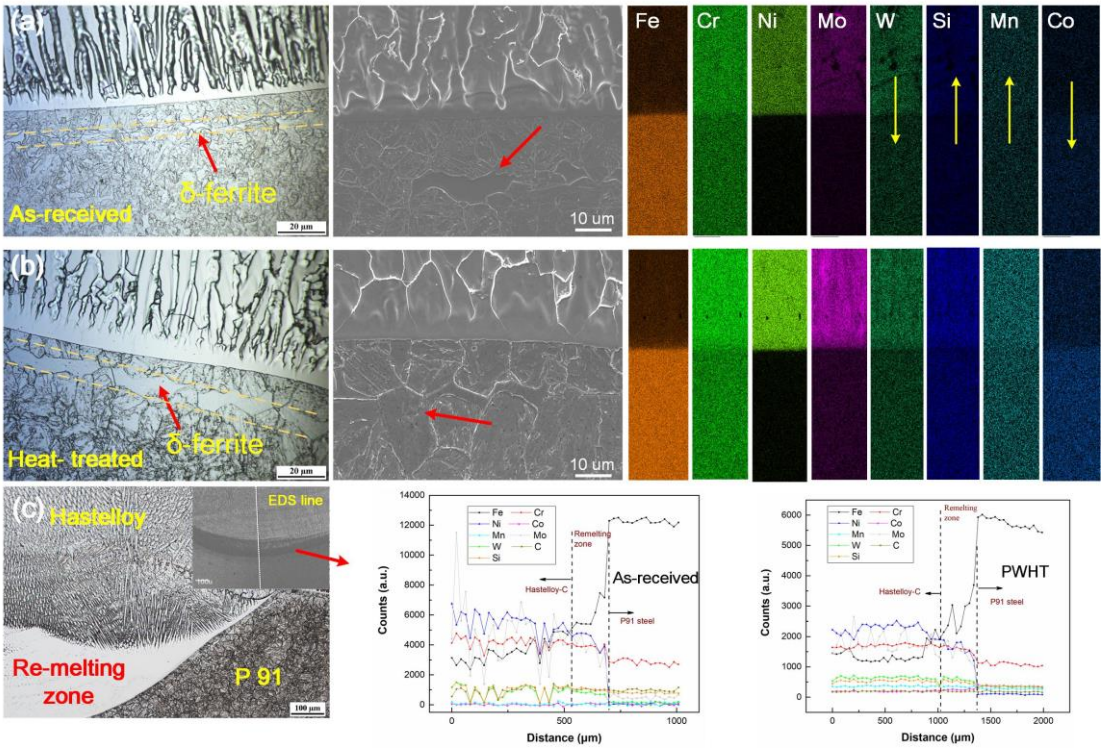

Fig. 8.3 Interfacial features and elemental diffusion behaviour of: (a) as-cladded and (b) heat-treated specimens. (c) the re-melting zone shown in Fig. 8.1a.

Fig. 8.4 further presents a quantitative analysis of the grains and elements segregation in interfacial regions. As shown in Fig. 8.4a, it is displayed that Hastelloy C276 exhibits columnar grains of various sizes, and element Mo is segregated to the interdendritic areas. The P91 steel is characterized by tempered martensite. There is negligible change in its grain morphology, but the partial recrystallization that occurred during cladding thermal excursion led to grains growth. After heat treatment (Fig. 8.4b), the grains at both alloy sides are confirmed to be coarsened, and chemical segregations were homogenized in the microstructure. In the heat-treated state, the less pronounced segregation and coarse grains are beneficial for creep strength and corrosion resistance.

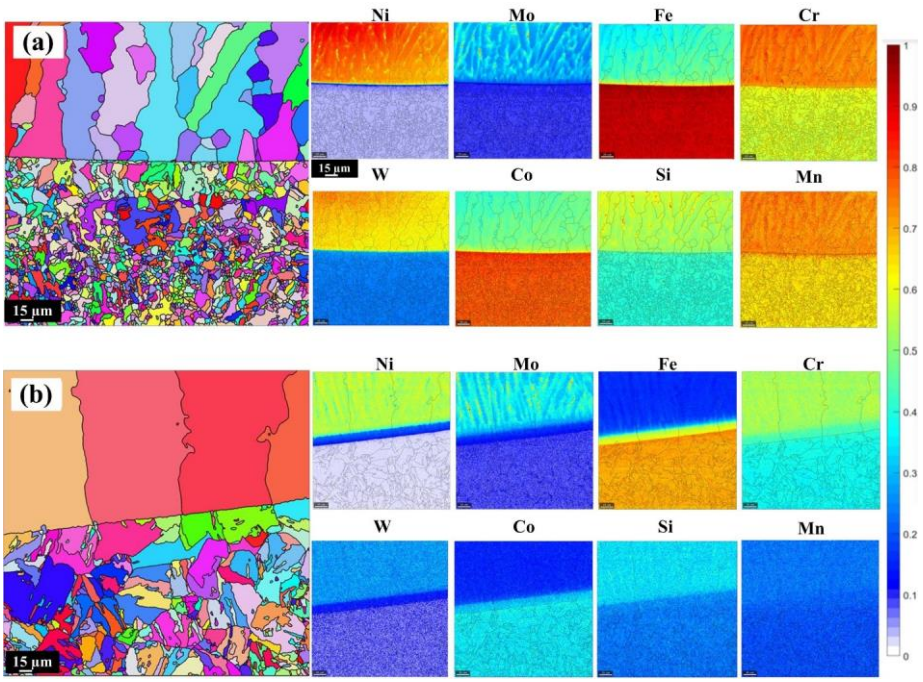

Fig. 8.4 EBSD maps for interfacial elements distribution of: (a) as-cladded state and (b) heat-treated state.

8.3.2 Grain orientation and misorientation

Figure 8.5 presents EBSD orientation maps of two specimens at different conditions. In Fig. 8.5a and b, the <1 0 0> direction, as shown in arrows in the heat flow direction, determines the competitive grain growth [335]. It is well known that if the angle between heat flow and preferred crystallographic orientation is small, the favourably oriented grains grow faster, while other less-favourably oriented grains fall behind and will be suppressed. In the as-cladded condition, the coating grains (Hastelloy side) have great variation in their crystallographic orientation. However, there are occasional clusters of grains with orientations <1 1 1> in the deposition direction (Fig. 8.5c), which is associated with the fluctuations in thermal condition during cladding, instead of due to the cooling rate locally. For Hastelloy C276, the generation of <1 1 1> is relative to the symmetric twist boundaries during production, which strongly affects the extent of oxide film formation in the air environment [336]. This demonstrated the cladded surface would be slightly prone to oxidize due to the grains aligned with <1 1 1> along

the deposition direction. In the case of heat-treated state, there is a greater tendency for coating grains to be columnar and to assume the preferred solidification growth direction of <0 0 1> aligned with deposition direction (Fig. 8.5d). Typically, the orientation <0 0 1> is the fast-growing dendritic orientation in Ni-based alloy and its growth is consistent with the anisotropy of solid-liquid interfacial energy [337]. Under stable thermal conditions, modified heat treatment could be desirable to promote the formation and coarsening of γ-Ni phases, while recrystallising as-cladded grains into the sequenced structure with <0 0 1> along the deposition direction. After heat treatment, the microstructure of substrate steel kept equiaxed grains, but also highly coarsened. It is well accepted that the microstructure has been significantly modified via PHT.

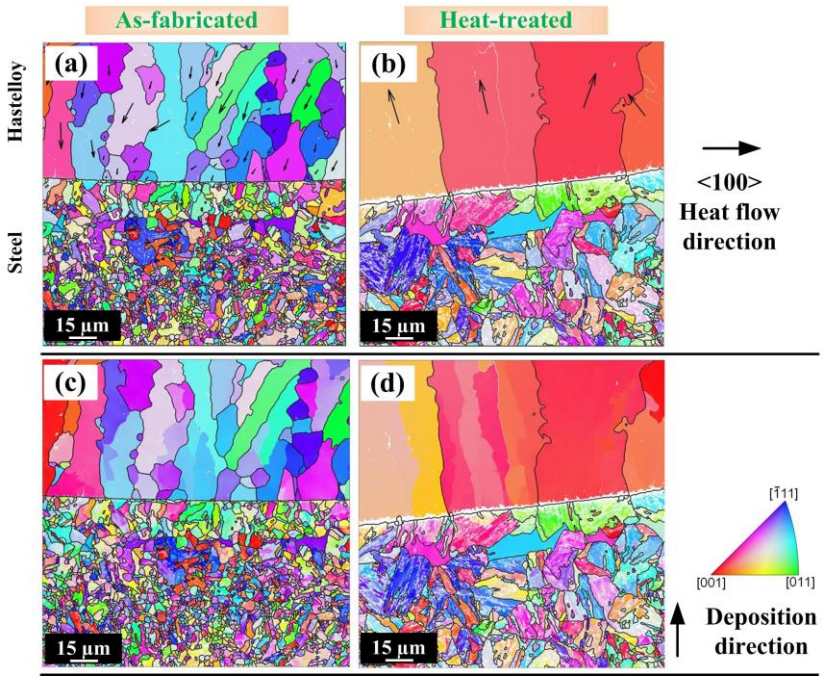

Fig. 8.5 Inverse pole figure (IPF) maps of two specimens: (a) - (b) present the heat flow indicated by arrows, and (c) - (d) show the IPF from the deposition direction.

Figure 8.6 displays misorientation-angle distribution of selected locations under two studied conditions. Low-angle grain boundaries (LAGBs) (2° < LAGB < 15°) and high-angle grain boundaries (HAGBs) (HAGB > 15°) are depicted as black and red lines,

respectively. Grain boundaries of both specimens are mostly composed of HAGBs and LAGBs. The HAGBs ratio is in a range of 87.7% ~ 97.6% for as-cladded and heat-treated states. It is well known that the presence of a large amount of HAGBs in the microstructure is often beneficial for suppressing crack propagation or turning cracks to another direction, which could significantly improve mechanical strength or toughness response to the material, thereby extending the usable life of structure under a combination of load and high temperature conditions [338]. Since grain growth is present in heat-treated specimens, LAGBs have an obvious reduction. This demonstrates an improvement in ductility and resistance to cracking.

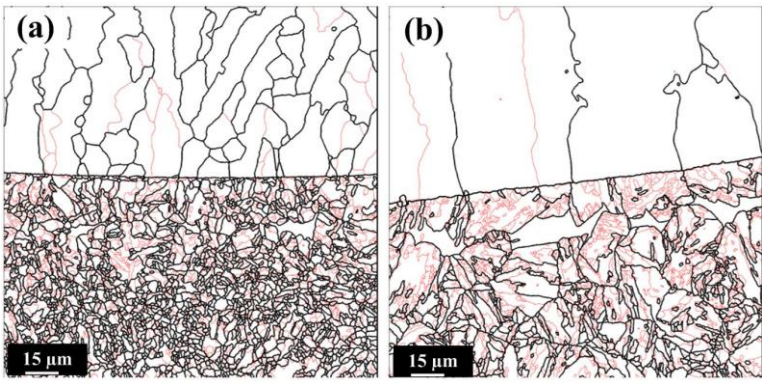

Fig. 8.6 Grain boundaries maps of (a) as-cladded and (b) heat-treated conditions, LAGBs (2° to 15°) in red, HAGBs (>15°) in black.

Figure 8.7 exhibits the detailed misorientation of two samples at as-cladded and HT conditions. Figs. 8.7a and 8.7b show Kernel Average Misorientation (KAM) images that could express local strain accumulation or dislocation slip in grains. From KAM map, the colour changes from blue to green and then to red, indicating that local KAM values increase successively. Higher KAM values could be found in the as-cladded state compared to heat-treated state. Figs. 8.7c and 8.7d further illustrate the local misorientation of two specimens, and the KAM values of most local misorientation are over 15, which indicates more plastic deformation or high defect density occurred. After

heat treatment, there is a significant change in the residual plastic strain (Fig. 8.7b), especially in substrate steel. Due to grain deformation, KAM values seem to be homogeneously distributed on both sides. For coating layers (Hastelloy C276), high KAM values occurred in inner grain boundaries, which demonstrates inner grains firstly deformed when heat process began. Dislocation activities at γ-Ni matrix also result in pronounced strain localization at the grain boundaries, as red areas (point) shown in Fig. 8.7a and 8.7b, where produced a number of new intermetallics. While, for P91 steel substrate, high KAM values appeared in the vicinity of the interface where undergone a large thermal gradient. It is evident that strain localization appeared during deposition, while it could be refined by heat treatment used in this study.

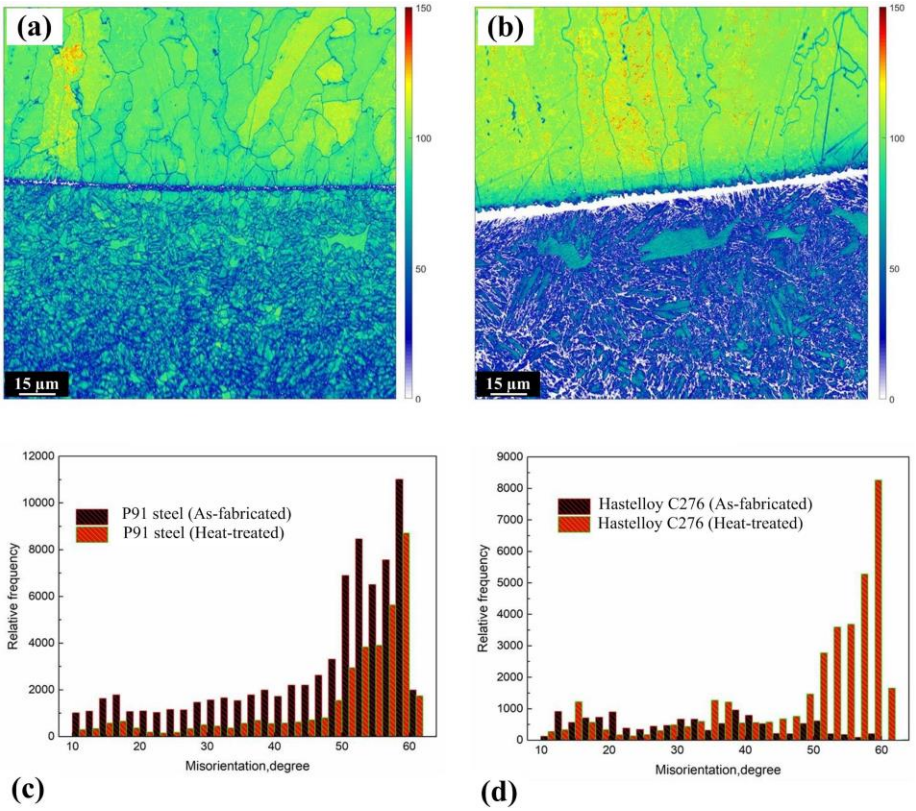

Fig. 8.7 KAM image for (a) as-cladded state and (b) heat-treated state, and misorientation-angle distribution histograms for (c) P91 steel substrate and (d) Hastelloy C276 coating.

8.3.3 Hardness distribution

Figure 8.8 shows a hardness map collected across the cladding to substrate. The hardness values are significantly determined by the microstructural evolution across the dissimilar materials. The high microhardness value appears in the CGHAZ due to the presence of untampered lath martensite and complete dissolution of carbides. After heat treatment, the overlay shows a decrease in average microhardness value from 250 HV to 220 HV, which is mainly attributed to the recovery and recrystallisation induced coarse grains (see Fig. 8.4). The hardness values in overall HAZ have an obvious reduction and became more homogenous compared to those without heat treatment (Fig. 8.8b), associated with the uniform microstructure. A similar observation has also been reported in previous research for hardness variation along the P91 HAZ in welded and post heat treatment [339]. The average hardness of P91 steel in the as-cladded state was measured at ~ 220 HV, while a slight 5% reduction was in heat-treated state. This is caused by further tempering of martensite (Fig. 8.1). Additionally, post-processing HT allowed microstructure homogenization and reprecipitation at CGHAZ, resulting in the reduction of the corresponding hardness. Here, it is mentioned that under the heat-treated condition used in this study, P91 steel has improved energy absorbing capacity, which could bring enhanced toughness to the material [324].

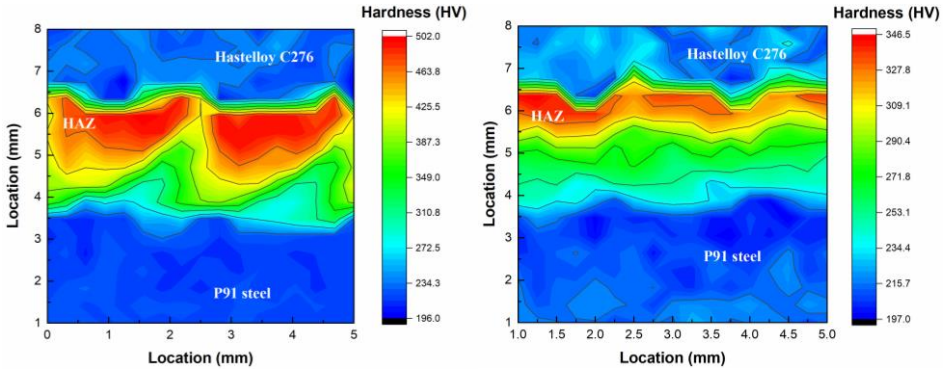

Fig. 8.8 Hardness mapping of studied specimens: (a) as-cladded state; (b) heat-treated state.

From the discussion above, it is well accepted that what this study prefers to display is the development of a new cladding structure for application in severe environments. It is believed that the analysis is beneficial to the study of Ni-steel bimetallic components. The experiments under high temperatures and corrosion environments will be continued in the near future.

8.4 Conclusion

A new dissimilar metal structure, where Hastelloy C276 was claded on low-alloyed creep resistance steel P91 using wire arc additive manufacturing, has been successfully achieved in this study. A systematic microstructural characterization of specimen at as-cladded and heat-treated conditions was performed. The findings include:

(1) The proposed steel-nickel-based alloy bimetallic structure exhibits a sound bonding with microstructure hierarchies where columnar dendrites and *P* phase formed in cladding layer, and equiaxed martensite and carbides precipitation generated in steel substrate. The HAZ at interfacial bonding regions performs different grain sizes, possibly due to the alternatively thermal cycles and solute elements diffusion between dissimilar materials.

(2) The post heat treatment brings a significant change to microstructure at both Hastelloy C276 and p91 steel, including promoted grain growth, modified grain orientation, and enhanced HAGBs, which are critical to the overall property improvement. In particular, HAGBs in cladding may provide conditions against cracks generation and propagation.

(3) The various expressions of the hardness in different locations with and without post heat treatment can be explained by the combined effects of the grain size,

crystallographic texture, grain boundaries as well as carbide distribution.

In sum, the study of material characterization of cladding Hastelloy C276 on P91steel enables a better understanding of steel-nickel-based alloy bimetallic components for structural application.

9 Conclusions and recommendations

This thesis provides an insightful understanding of WAAM fabricated Hastelloy C276 alloy by different working processes, in combination with an extensive investigation of microstructure and related mechanical properties under ambient and elevated temperatures. Involving the feasibility study and various in-situ and post processes, this work also extends the dissimilar metal fabrication in cladding Hastelloy C276 alloy on creep resistant P91 steel aiming to integrate a further cost reduction and optimise the properties of obtained structures. This chapter provides a summary of the work conducted in this thesis, as well as some recommendations for future research regarding the manufacturing of Hastelloy C276 alloy and property assessment.

9.1 General summary

Above all, the feasibility of varying process parameters to improve manufacture of Hastelloy C276 was studied by GT-WAAM, with an attempt to deposit material without visible defects. Microstructure and mechanical properties at ambinent and elevated temperatures have been extensively explored to provide a preliminary operation window for the WAAM processes.

Subsequently, various in-situ and post operations were performed to optimise the properties of the fabricated alloy. Stress relieving heat treatment (SRHT) and solid solution heat treatment (SSHT) were performed at 871 °C for 6 h and 1177 °C for 0.5 h to improve mechanical properties of GT-WAAM fabricated Hastelloy C276 alloy. The evolution of intermetallics and elemental distribution with different heat treatments were compared, particularly their effects on enhancing mechanical properties. Additionally, in-situ MAO, when combined with the GT-WAAM system, was used to

stir the molten pool in order to interrupt dendrite growth and subsequently create a refined microstructure in a preferential cost-effective manner. The effects on the related performance, including surface finish, microstructure and mechanical properties, were explored under different oscillation frequencies. Finally, it was demonstrated that properties could be further improved and controlled in a stable condition with less anisotropy through CMT-based WAAM with an application of active cooling and an effective interlayer temperature control. This was attributed to improved control of dendrite morphology, bulk texture, grain morphology and elemental distributions, all of which were studied in detail by various analytical technologies.

Considering the preferential operation window of Hastelloy C276 alloy by WAAM and the high cost of this alloy, the current work studied the dissimilar metal cladding of Hastelloy C276 on creep resistant P91 alloy to provide an application in a nuclear reactor with reduced cost. As-cladded and tempering treatment conditions were investigated and an aligned study of microstructure and hardness was conducted.

Given the extensive aforementioned studies, the outcomes or conclusions of the current thesis work, involving critical underlying issues in fabrication of Hastelloy C276 alloy by WAAM, are summarised as follows:

(1) From the study of GT-WAAM fabricated Hastelloy C276 alloy under as-deposited condition, the microstructure was inhomogeneously distributed, in which intermetallic *P* phase was found in the interdendritic areas due to solute element segregation. In addition, Ni_2Mo_4C carbides, as well as more subgrain boundaries were observed in the bottom areas, both being attributed to long-term thermal exposure. In comparison, the length and density of dislocations increased in the top areas with less thermal cycling. Additionally, relatively large-sized columnar grains

with epitaxial dendrites and strong fibre-type (200) crystallographic bulk texture were found in the γ-Ni matrix, which induced a well-distributed hardness from top to bottom areas, but anisotropy in tensile and preliminary creep properties.

(2) The hardness and tensile strength were increased by post heat treatments. It was found that with stress relieving heat treatment at 871 °C for 6 h, more *P* phase and newly formed intermetallic μ phase were found in the interdendritic areas and grain boundaries, which resulted in higher hardness and tensile strength at the expense of reduced ductility. After solid solution heat treatment at 1177 °C for 0.5 h, the *P* phase was partially dissolved and elemental distribution was highly refined, which contributed to enhanced strength and ductility with decreased anisotropy. Therefore, this latter heat treatment condition was highly recommended in this work.

(3) Incorporating MAO during the fabrication of Hastelloy C276 by GT-WAAM was shown to be an effective way to decrease arc density and increase solidification rate, through exploration at 5 Hz, 10 Hz and 20 Hz oscillation frequenccies. MAO enabled a refinement of macrostructure and incremental improvement of fabrication efficiency. Furthermore, with 5 Hz under current operation conditions, less Mo segregation and misoriented dendrites with a reduced DAS were found, leading to a slightly increased tensile strength and nano-hardness, reduced elastic modulus and increased resistance to plastic deformation. However, the bulk columnar grain size and *P* phase, produced no significant differences under three conditions.

(4) CMT-based WAAM processing provided a relatively lower heat input in comparison with GT-WAAM. By incorporating active cooling and interlayer temperature control in a zig-zag deposition path under three heat inputs of 276 J/mm, 368 J/mm and 553 J/mm, analogous mechanical properties were provided for the

fabricated alloys under the three heat inputs. However, lower heat input is more favourable for achieving slightly refined microstructure and decreased mechanical anisotropy. Associated with the lowest heat input of 276 J/mm, refined dendrite arm spacing (DAS), less Mo segregation, more low angle grain boundaries (LAGBs) and higher geometrically necessary dislocation (GND) densities characterised the matrix, compared to the higher heat inputs. Despite the variations of GND densities with heat inputs, there appeared to be no significant change in the average total dislocation density in the microstructure as suggested by the peak profile analysis of synchrotron X-ray diffraction data. This is potentially advantageous for lowering the solidification cracking susceptibility. Moreover, all as-fabricated alloys present a typical strong fibre-type (200) crystallographic bulk texture from neutron diffraction. Such texture was relatively weaker in the lowest heat input condition. The manipulated texture, in combination with refined dendrite arm spacing and reduced chemical segregation, is suggested to be responsible for the reduced mechanical anisotropy in the 276 J/mm heat input sample.

(5) A new dissimilar metal structure, where Hastelloy C276 was cladded on low-alloyed creep resistance steel P91 using WAAM, has been successfully achieved in this study. Sound bonding with microstructure hierarchies was obtained, where a columnar dendritic structure with *P* phase was formed on the side of Hastelloy C276, and equiaxed martensite and carbides precipitated on P91 side. The tempering treatment promoted grain growth, modified grain orientation, and enhanced HAGBs, which contribute to homogeneously distributed hardness and prohibition of the occurrence of cracking.

9.2 Recommendations for future work

WAAM processing of Hastelloy C276 alloy has been fairly well explored in this work, however, further research on AM of Ni-based Hastelloy C276 alloy is required, as is more research in order to make further use of its excellent properties applicable in a wide range of environments. Currently, standardisation of AM and post-processing of Ni-based alloys requires significant efforts from both academic and industrial communities. Development of international standards is essential to further guide fabrication methods and production quality for practical applications.

Next, an enhanced understanding of processing - microstructure - property relationships for Ni-based Hastelloy C276 alloy is required to achieve desired quality and functionalities of the produced components. Current research tends to be on small-sized samples, which limits the reliability of scale-up for practical applications. Based on the authors' previous work, product dimension and geometry can highly affect a material's performance. Hence, investment in scale-up of WAAM fabrication research is required. Additionally, the research has focused on wire and arc-based AM, however, exploration of laser and electron beam-based processes, with their high deposition accuracy has had relatively less study.

Before considering any potential AM processes, its adaptability can be investigated by thermodynamic and kinetic simulations and calculations, which are capable of providing useful insights into understanding AM segregation, solidification dendrite structure, texture, diffusion and precipitation. Via simulation, it is possible to further understand microstructure and manipulate texture induced by AM processes to control microstructures and properties.

Amelioration processes employed for quality optimisation require more detailed

investigations. As residual stress and distortion are critical challenges in AM, more work should be done for their quantification and control. The coupling of different energy fields in Ni-based alloys by AM is quite limited, and multi-energy field hybrids may be a way to improve deposition efficiency, except for the magnetic arc oscillation performed in this research. The others, such as wire arc in combination with ultrasonic and the use of oscillating laser-arc hybrid source, can be applied during the fabrication of Hastelloy C276 alloy for the capability of achieving improved surface accuracy, refined grains, and decreased porosity and anisotropies in tensile strengths.

Finally, as the Hastelloy C276 alloy was designed for the application of corrosion resistance and high temperature resistance, the properties of corrosion resistance under various corrosion environments should be studied. Moreover, current work covered creep resistance under 700 °C at 165 MPa of GT-WAAM fabricated Hastelloy C276 alloy. However, microstructure, stability, and mechanical performance under elevated temperatures require more thorough investigation, and benchmarking against traditionally processed materials.

References

[1] J.C. Lippold, S.D. Kiser, J.N. DuPont, Welding metallurgy and weldability of nickel-base alloys, John Wiley & Sons2011.

[2] O. Marenych, A. Kostryzhev, C. Shen, Z. Pan, H. Li, S. van Duin, Precipitation Strengthening in Ni–Cu Alloys Fabricated Using Wire Arc Additive Manufacturing Technology, Metals 9(1) (2019) 105.

[3] T. Bormann, R. Schumacher, B. Müller, M. Mertmann, M. de Wild, Tailoring selective laser melting process parameters for NiTi implants, Journal of Materials Engineering and Performance 21(12) (2012) 2519-2524.

[4] D. Bhattacharyya, J. Davis, M. Drew, R.P. Harrison, L. Edwards, Characterization of complex carbide–silicide precipitates in a Ni–Cr–Mo–Fe–Si alloy modified by welding, Materials Characterization 105 (2015) 118-128.

[5] S. Roy, R. Kumar, Anurag, A. Panda, R.K. Das, A Brief Review on Machining of Inconel 718, Materials Today: Proceedings 5(9, Part 3) (2018) 18664-18673.

[6] D.S. Watring, K.C. Carter, D. Crouse, B. Raeymaekers, A.D. Spear, Mechanisms driving high-cycle fatigue life of as-built Inconel 718 processed by laser powder bed fusion, Materials Science and Engineering: A 761 (2019) 137993.

[7] H. Attar, S. Ehtemam-Haghighi, N. Soro, D. Kent, M.S. Dargusch, Additive manufacturing of low-cost porous titanium-based composites for biomedical applications: Advantages, challenges and opinion for future development, Journal of Alloys and Compounds 827 (2020) 154263.

[8] D. Ding, Z. Pan, D. Cuiuri, H. Li, Wire-feed additive manufacturing of metal components: technologies, developments and future interests, The International Journal of Advanced Manufacturing Technology 81(1-4) (2015) 465-481.

[9] C.R. Cunningham, J.M. Flynn, A. Shokrani, V. Dhokia, S.T. Newman, Invited review article: Strategies and processes for high quality wire arc additive manufacturing, Additive Manufacturing 22 (2018) 672-686.

[10] R.K. Ananda-Kumar, W. Moscoso-Kingsley, G. Jacob, A. Donmez, V. Madhavan, Machining behavior of additively manufactured and cast-wrought nickel-based superalloy (IN 625), Procedia Manufacturing 26 (2018) 595-606.

[11] B. Wu, Z. Pan, D. Ding, D. Cuiuri, H. Li, Effects of heat accumulation on microstructure and mechanical properties of Ti6Al4V alloy deposited by wire arc additive manufacturing, Additive Manufacturing 23 (2018) 151-160.

[12] N.J. Harrison, I. Todd, K. Mumtaz, Reduction of micro-cracking in nickel superalloys processed by Selective Laser Melting: A fundamental alloy design approach, Acta Materialia 94 (2015) 59-68.

[13] A.N.M. Tanvir, M.R.U. Ahsan, C. Ji, W. Hawkins, B. Bates, D.B. Kim, Heat treatment effects on Inconel 625 components fabricated by wire+ arc additive manufacturing (WAAM)—part 1: microstructural characterization, The International Journal of Advanced Manufacturing Technology 103(9) (2019) 3785-3798.

[14] L. Zhou, A. Mehta, B. McWilliams, K. Cho, Y. Sohn, Microstructure, precipitates and mechanical properties of powder bed fused inconel 718 before and after heat treatment, Journal of Materials Science & Technology 35(6) (2019) 1153-1164.

[15] X. Xu, S. Ganguly, J. Ding, C.E. Seow, S. Williams, Enhancing mechanical properties of wire + arc additively manufactured INCONEL 718 superalloy through in-process thermomechanical processing, Materials & Design 160 (2018) 1042-1051.

[16] M.-Y. Shen, X.-J. Tian, D. Liu, H.-B. Tang, X. Cheng, Microstructure and fracture behavior of TiC particles reinforced Inconel 625 composites prepared by laser additive manufacturing, Journal of Alloys and Compounds 734 (2018) 188-195.

[17] S.W. Williams, F. Martina, A.C. Addison, J. Ding, G. Pardal, P. Colegrove, Wire+ arc additive manufacturing, Materials Science and Technology 32(7) (2016) 641-647.

[18] Q. Zhang, R. Tang, K. Yin, X. Luo, L. Zhang, Corrosion behavior of Hastelloy C-276 in supercritical water, Corrosion Science 51(9) (2009) 2092-2097.

[19] M. Dhananchezian, Study the machinability characteristics of Nicked based Hastelloy C-276 under cryogenic cooling, Measurement 136 (2019) 694-702.

[20] D. Chai, G. Ma, S. Zhou, Z. Jin, D. Wu, Cavitation erosion behavior of Hastelloy™ C-276 weld by laser welding, Wear 420-421 (2019) 226-234.

[21] M. Manikandan, P.R. Hari, G. Vishnu, M. Arivarasu, K.D. Ramkumar, N. Arivazhagan, M.N. Rao, G.M. Reddy, Investigation of Microstructure and Mechanical Properties of Super Alloy C-276 by Continuous Nd: YAG Laser Welding, Procedia Materials Science 5 (2014) 2233-2241.

[22] A.R. Kannan, S.M. Kumar, N.P. Kumar, N.S. Shanmugam, A. Vishnu, Y.J.M.L. Palguna, Process-microstructural features for tailoring fatigue strength of Wire Arc Additive Manufactured Functionally Graded Material of SS904L and Hastelloy C-276, (2020) 127968.

[23] J.R. Davis, Nickel, cobalt, and their alloys, ASM international2000.

[24] S.J. Rosenberg, Nickel and its alloys, US Department of Commerce, National Bureau of Standards1968.

[25] T.E. Abioye, D.G. McCartney, A.T. Clare, Laser cladding of Inconel 625 wire for corrosion protection, Journal of Materials Processing Technology 217 (2015) 232-240.

[26] J.N. DuPont, J.C. Lippold, S.D. Kiser, Welding metallurgy and weldability of nickel-base alloys, Hoboken, NJ: John Wiley & Sons. xiv, 2009.

[27] R.C. Reed, The superalloys: fundamentals and applications, Cambridge university press2008.

[28] R.W. Revie, Corrosion and corrosion control: an introduction to corrosion science and engineering, John Wiley & Sons2008.

[29] R.M. Carranza, M.A. Rodríguez, R.B. Rebak, Effect of Fluoride Ions on Crevice Corrosion and Passive Behavior of Alloy 22 in Hot Chloride Solutions, Corrosion 63(5) (2007) 480-490.

[30] G. Smith, S.J.S. Patel, The role of niobium in wrought precipitation-hardened nickel-base alloys, 718 (2005) 625-706.

[31] W. Wang, L. Jiang, C. Li, B. Leng, X.-X. Ye, R. Liu, S. Chen, K. Yu, Z. Li, X. Zhou, Effects of post-weld heat treatment on microstructure and mechanical properties of Hastelloy N superalloy welds, Materials Today Communications 19 (2019) 230-237.

[32] R.E. Gehlbach, H.E. McCoy, Phase instability in Hastelloy N, Seven Springs Pennsylvania, pp. 346-366.

[33] D. Wu, G. Ma, Y. Guo, D. Guo, Study of weld morphology on thin Hastelloy C-276 sheet of Study weld morphology on thin Hastelloy C-276 sheet of pulsed laser welding pulsed laser welding, Physics Procedia 5 (2010) 99-105.

[34] I. Gunes, Y. Kayali, Investigation of mechanical properties of borided Nickel 201 alloy, Materials & Design 53 (2014) 577-580.

[35] Z.R. Khayat, T.A. Palmer, Impact of iron composition on the properties of an additively manufactured solid solution strengthened nickel base alloy, Materials Science and Engineering: A 718 (2018) 123-134.

[36] C.V. Mikler, V. Chaudhary, T. Borkar, V. Soni, D. Choudhuri, R.V. Ramanujan, R. Banerjee, Laser additive processing of Ni-Fe-V and Ni-Fe-Mo Permalloys: Microstructure and magnetic properties, Materials Letters 192 (2017) 9-11.

[37] D. Van, G.P. Dinda, J. Park, J. Mazumder, S.H. Lee, Enhancing hardness of Inconel 718 deposits using the aging effects of cold metal transfer-based additive manufacturing, Materials Science and Engineering: A 776 (2020) 139005.

[38] K. Georgilas, R.H.U. Khan, M.E. Kartal, The influence of pulsed laser powder bed fusion process parameters on Inconel 718 material properties, Materials Science and Engineering: A 769 (2020) 138527.

[39] Y. Gao, D. Zhang, M. Cao, R. Chen, Z. Feng, R. Poprawe, J.H. Schleifenbaum, S. Ziegler, Effect of δ phase on high temperature mechanical performances of Inconel 718 fabricated with SLM process, Materials Science and Engineering: A 767 (2019) 138327.

[40] J.-P. Choi, G.-H. Shin, S. Yang, D.-Y. Yang, J.-S. Lee, M. Brochu, J.-H. Yu, Densification and microstructural investigation of Inconel 718 parts fabricated by selective laser melting, Powder Technology 310 (2017) 60-66.

[41] G.H. Cao, T.Y. Sun, C.H. Wang, X. Li, M. Liu, Z.X. Zhang, P.F. Hu, A.M. Russell, R. Schneider, D. Gerthsen, Z.J. Zhou, C.P. Li, G.F. Chen, Investigations of γ′, γ″ and δ precipitates in heat-treated Inconel 718 alloy fabricated by selective laser melting, Materials Characterization 136 (2018) 398-406.

[42] H.K. Kohl, K. Peng, Thermal stability of the superalloys Inconel 625 and Nimonic 86, Journal of Nuclear Materials 101(3) (1981) 243-250.

[43] G.P. Dinda, A.K. Dasgupta, J. Mazumder, Laser aided direct metal deposition of Inconel 625 superalloy: Microstructural evolution and thermal stability, Materials Science and Engineering: A 509(1) (2009) 98-104.

[44] C. Hong, D. Gu, D. Dai, M. Alkhayat, W. Urban, P. Yuan, S. Cao, A. Gasser, A. Weisheit, I. Kelbassa, M. Zhong, R. Poprawe, Laser additive manufacturing of ultrafine TiC particle reinforced Inconel 625 based composite parts: Tailored microstructures

and enhanced performance, Materials Science and Engineering: A 635 (2015) 118-128.

[45] R.P. Gangloff, H.M. Ha, J.T. Burns, J.R.J.M. Scully, M.T. A, Measurement and modeling of hydrogen environment-assisted cracking in Monel K-500, Metallurgical and Materials Transactions A 45(9) (2014) 3814-3834.

[46] B.C. Rincon Troconis, Z.D. Harris, H. Ha, J.T. Burns, J.R. Scully, The effect of heat-to-heat variations in metallurgy and hydrogen-metal interactions on the hydrogen embrittlement of Monel K-500, Materials Science and Engineering: A 703 (2017) 533-550.

[47] Z.D. Harris, J.T. Burns, The effect of isothermal heat treatment on hydrogen environment-assisted cracking susceptibility in Monel K-500, Materials Science and Engineering: A 764 (2019) 138249.

[48] Q. Han, Y. Gu, R. Setchi, F. Lacan, R. Johnston, S.L. Evans, S. Yang, Additive manufacturing of high-strength crack-free Ni-based Hastelloy X superalloy, Additive Manufacturing 30 (2019) 100919.

[49] T. Sakthivel, K. Laha, M. Nandagopal, K.S. Chandravathi, P. Parameswaran, S. Panneer Selvi, M.D. Mathew, S.K. Mannan, Effect of temperature and strain rate on serrated flow behaviour of Hastelloy X, Materials Science and Engineering: A 534 (2012) 580-587.

[50] M. Aghaie-Khafri, N. Golarzi, Forming behavior and workability of Hastelloy X superalloy during hot deformation, Materials Science and Engineering: A 486(1-2) (2008) 641-647.

[51] J.C. Zhao, M. Larsen, V. Ravikumar, Phase precipitation and time–temperature-transformation diagram of Hastelloy X, Materials Science and Engineering: A 293(1) (2000) 112-119.

[52] L.d.S. Ferreira, K. Graf, A.J.M.R. Scheid, Microstructure and properties of nickel-based C276 alloy coatings by PTA on AISI 316L and API 5L X70 steel substrates, Materials Research 18(1) (2015) 212-221.

[53] H. International, Corrosion-resistant Alloys, 2015. https://haynesintl.com/alloys/alloy-portfolio_#Corrosion-resistant-Alloys. 2020).

[54] N.R. Jaladurgam, A.K. Kanjarla, Hot deformation characteristics and microstructure evolution of Hastelloy C-276, Materials Science and Engineering: A 712

(2018) 240-254.

[55] C. Zhang, L. Zhang, W. Shen, M. Li, S.J.J.o.M.E. Gu, Performance, Characterization of hot deformation behavior of Hastelloy C-276 using constitutive equation and processing map, Journal of Materials Engineering and Performance 24(1) (2015) 149-157.

[56] T. Kvackaj, J. Zrnik, V. Vrchovinsky, P.J.H.T.M. Wangyao, Processes, Controlled rolling of Hastelloy-N, Materials and Processes 21(6) (2002) 351-360.

[57] H. INTERNATIONAL, Alloy Portfolio, 2015. http://www.haynesintl.com/alloys/alloy-portfolio_. (Accessed 23/03 2020).

[58] P. Panjan, I. Urankar, B. Navinšek, M. Terčelj, R. Turk, M. Čekada, V. Leskovšek, Improvement of hot forging tools with duplex treatment, Surface and Coatings Technology 151-152 (2002) 505-509.

[59] T. Kim, J. Jang, W. Ryu, J. Hong, A. Mitchell, Influence of precipitation and grain size on the hot ductility of alloy C-276 ESR ingots, High Temperature Materials and Processes 20(2) (2001) 143-154.

[60] T. Abe, H. Sasahara, Dissimilar metal deposition with a stainless steel and nickel-based alloy using wire and arc-based additive manufacturing, Precision Engineering 45 (2016) 387-395.

[61] K. Kadirgama, K.A. Abou-El-Hossein, M.M. Noor, K.V. Sharma, B. Mohammad, Tool life and wear mechanism when machining Hastelloy C-22HS, Wear 270(3) (2011) 258-268.

[62] D.A. Coroni, S.M.J.P.E. Croitoru, Prediction of cutting forces at 2D titanium machining, Procedia Engineering 69 (2014) 81-89.

[63] K. Xu, B. Zou, C. Huang, Y. Yao, H. Zhou, Z.J.C.J.o.M.E. Liu, Machinability of Hastelloy C-276 using Hot-pressed sintered Ti (C 7 N 3)-based cermet cutting tools, Chinese Journal of Mechanical Engineering 28(3) (2015) 599-606.

[64] R. Maurya, R. Kumar Porwal, EDM of Hastelloy – An overview, Materials Today: Proceedings (2019) 311-315.

[65] J. Kesavan, V. Senthilkumar, S. Dinesh, Experimental and numerical investigations on machining of Hastelloy C276 under cryogenic condition, Materials

Today: Proceedings (2019) 2441-2444.

[66] R. Choudhary, H. Garg, M. Prasad, D. Kumar, Effect of Cryogenic Treatment of Tool Electrode on the Machining Performance and Surface Finish during Electrical Discharge Machining of Hastelloy C-4, Materials Today: Proceedings 4(2, Part A) (2017) 1158-1166.

[67] Y.-L. Chen, S.-M. Zhu, S.-J. Lee, J.C. Wang, The technology combined electrochemical mechanical polishing, Journal of Materials Processing Technology 140(1) (2003) 203-205.

[68] D.M. Bowden, W.H. Peter, Near-net shape fabrication using low-cost titanium alloy powders, The Boeing Company, 2012.

[69] Y. He, J. Yang, H. Shen, L. Wang, Z. Gao, Brazing graphite to hastelloy N superalloy using pure-Au filler metal: Bonding mechanism and joint properties, Materials & Design 104 (2016) 1-9.

[70] M. Manikandan, N. Arivazhagan, M. Nageswara Rao, G.M. Reddy, Microstructure and mechanical properties of alloy C-276 weldments fabricated by continuous and pulsed current gas tungsten arc welding techniques, Journal of Manufacturing Processes 16(4) (2014) 563-572.

[71] U. Reisgen, J. Holk, S.J.M.u.W. Olschok, Electron beam welding of titanium aluminides, 40(11) (2009) 820-823.

[72] M. Ahmad, J.I. Akhter, M. Akhtar, M. Iqbal, E. Ahmed, M.A. Choudhry, Microstructure and hardness studies of the electron beam welded zone of Hastelloy C-276, Journal of Alloys and Compounds 390(1) (2005) 88-93.

[73] V. Dey, D.K. Pratihar, G.L. Datta, M. Jha, T. Saha, A.J.T.I.J.o.A.M.T. Bapat, Optimization and prediction of weldment profile in bead-on-plate welding of Al-1100 plates using electron beam, 48(5-8) (2010) 513-528.

[74] S. Wang, X.J.M. Wu, Design, Investigation on the microstructure and mechanical properties of Ti–6Al–4V alloy joints with electron beam welding, 36 (2012) 663-670.

[75] E. Akman, A. Demir, T. Canel, T. Sınmazçelik, Laser welding of Ti6Al4V titanium alloys, Journal of Materials Processing Technology 209(8) (2009) 3705-3713.

[76] E.R. Sharma, E.M. Kumar, D.A. Kamboj, Hastelloy C-276Weld Overlay

bySMAW Process, International Journal of Engineering Research and Applications 07(05) (2017) 86-91.

[77] Y. He, W. Zheng, J. Yang, D. Zhu, X. Yang, Y. Sun, Z. Gao, TEM study of microstructural characteristic and evaluation of mechanical performance for the hastelloy N/Ti/Hastelloy N superalloy joint brazed for diverse soaking time, Journal of Manufacturing Processes 35 (2018) 271-281.

[78] H. Ma, J. Chen, W. Cai, C. Shen, Y. Yao, Y. Jiang, The influence of operation parameters on stress of plate-fin structures in LNG heat exchanger, Journal of Natural Gas Science and Engineering 26 (2015) 216-228.

[79] W. Wang, C. Li, L. Jiang, X.-X. Ye, K. Yu, S. Chen, Z. Li, X. Zhou, Evolution of carbide precipitates in Hastelloy N joints during welding and post weld heat treatment, Materials Characterization 135 (2018) 311-316.

[80] K.S. Bal, J. Dutta Majumdar, A. Roy Choudhury, Study on uni-axial tensile strength properties of Ytterbium fiber laser welded Hastelloy C-276 sheet, Optics & Laser Technology 108 (2018) 392-403.

[81] L. Yuan, R. Hu, T.-b. Zhang, J.-s. Li, X.-q. Zhang, Oxidation behavior of Hastelloy C-2000 superalloy at 800 °C and 1000 °C, Transactions of Nonferrous Metals Society of China 25(1) (2015) 354-362.

[82] K.S. Bal, J. Dutta Majumdar, A. Roy Choudhury, Investigation into the intergranular corrosion behaviour of electron beam welded Hastelloy C-276 sheet using laser displacement sensor, Measurement 144 (2019) 345-365.

[83] K.K. Mehta, P. Mukhopadhyay, R.K. Mandal, A.K. Singh, Microstructure, Texture and Mechanical Properties Anisotropy of Ni-16Cr and Ni-16Cr-16Mo Solid Solution Alloys in Hot Rolled and Annealed Condition, Materials Today: Proceedings 2(4) (2015) 1127-1135.

[84] E.W. Huang, B. Clausen, Y. Wang, H. Choo, P.K. Liaw, M.L. Benson, L.M. Pike, D.L. Klarstrom, A neutron-diffraction study of the low-cycle fatigue behavior of HASTELLOY® C-22HSTM alloy, International Journal of Fatigue 29(9) (2007) 1812-1819.

[85] J.N. DuPont, J.C. Lippold, S.D. Kiser, Welding metallurgy and weldability of nickel-base alloys. , John Wiley & Sons, 2009.

[86] S. Mahadevan, S. Nalawade, J.B. Singh, A. Verma, B. Paul, K.J.S. Ramaswamy, Evolution of δ phase microstructure in alloy 718, Superalloy 718 and Derivatives 718 (2010) 737-750.

[87] K.S. Bal, J. Dutta Majumdar, A. Roy Choudhury, Effect of post-weld heat treatment on the tensile strength of laser beam welded Hastelloy C-276 sheets at different heat inputs, Journal of Manufacturing Processes 37 (2019) 578-594.

[88] R.B. Leonard, Thermal Stability of Hastelloy Alloy C-276, Corrsosion 25(5) (1969) 222-232.

[89] M.J. Cieslak, T.J. Headley, A.D. Romig, The welding metallurgy of HASTELLOY alloys C-4, C-22, and C-276, Metallurgical Transactions A 17(11) (1986) 2035-2047.

[90] K. Devendranath Ramkumar, A. Narenthiran, A. Konjenti, P.N. Pravin, T.C. Kanish, Effect of low energy laser shock peening on the mechanical integrity of Hastelloy C-276 welds, Journal of Materials Processing Technology 274 (2019) 116296.

[91] H.M. Tawancy, R.B. Herchenroeder, A.I.J.J. Asphahani, High-performance Ni-Cr-Mo-W alloys, Physical & Mechanical Metallurgy 35(6) (1983) 37-43.

[92] L. Yuan, R. Hu, T. Zhang, Y. Han, X. Xue, J.J.J.o.M.E. Li, Performance, Precipitation Behavior of σ-FeCr Phases in Hastelloy C-2000 Superalloy Under Plastic Deformation and Aging Treatment, Journal of Materials Engineering and Performance 24(2) (2015) 565-571.

[93] J. Cieslak, J. Tobola, S.M. Dubiel, Study of phase stability in the σ-FeCr system, Intermetallics 24 (2012) 84-88.

[94] P.E.A. Turchi, L. Kaufman, Z.-K. Liu, Modeling of Ni–Cr–Mo based alloys: Part I—phase stability, Calphad 30(1) (2006) 70-87.

[95] Y. Shi, Y. Liu, X. Wang, Y. Zhou, J. Ma, S. Zhang, Corrosion Study on Ni-based Alloy in Acidic Environment, IOP Conference Series: Materials Science and Engineering, IOP Publishing, 2019, p. 012008.

[96] T. Hong, M. Nagumo, The effect of SO42− concentration in NaCl solution on the early stages of pitting corrosion of type 430 stainless steel, Corrosion Science 39(5) (1997) 961-967.

[97] E. Ruedl, Phase transformations in the alloy hastelloy B, Materials Research Bulletin 10(12) (1975) 1267-1272.

[98] W. Cao, S. Xia, Q. Bai, W. Zhang, B. Zhou, Z. Li, L. Jiang, Effects of initial microstructure on the grain boundary network during grain boundary engineering in Hastelloy N alloy, Journal of Alloys and Compounds 704 (2017) 724-733.

[99] R. Gehlbach, Phase instability in Hastelloy N.

[100] Y. He, J. Yang, C. Qin, S. Chen, Z.J.J.o.A. Gao, Compounds, Characterization of the Ni–Mo–Cr superalloy subjected to simulated heat-affected zone thermal cycle treatment, 643 (2015) 7-16.

[101] J. Li, S.L. Shrestha, Y. Long, L. Zhijun, Z.J.M. Xintai, Design, The formation of eutectic phases and hot cracks in one Ni–Mo–Cr superalloy, 93 (2016) 324-333.

[102] K. Yu, Z. Jiang, B. Leng, C. Li, S. Chen, W. Tao, X. Zhou, Z. Li, Effects of post-weld heat treatment on microstructure and mechanical properties of laser welds in GH3535 superalloy, Optics & Laser Technology 81 (2016) 18-25.

[103] S. Chen, X.-X. Ye, K. Yu, C. Li, Z. Li, Z. Li, X. Zhou, Microstructure and mechanical properties of UNS N10003 alloy welded joints, Materials Science and Engineering: A 682 (2017) 168-177.

[104] J.D. Verhoeven, Fundamentals of physical metallurgy, Wiley New York1975.

[105] J.P. Shingledecker, N.D. Evans, G.M. Pharr, Influences of composition and grain size on creep–rupture behavior of Inconel® alloy 740, Materials Science and Engineering: A 578 (2013) 277-286.

[106] R.W. Kozar, A. Suzuki, W.W. Milligan, J.J. Schirra, M.F. Savage, T.M. Pollock, Strengthening Mechanisms in Polycrystalline Multimodal Nickel-Base Superalloys, Metallurgical and Materials Transactions A 40(7) (2009) 1588-1603.

[107] V. Randle, Twinning-related grain boundary engineering, Acta Materialia 52(14) (2004) 4067-4081.

[108] J. Akhter, M. Shaikh, M. Ahmad, M. Iqbal, K. Shoaib, W. Ahmad, Effect of aging on the hardness and impact properties of Hastelloy C-276, Journal of Materials Science Letters 20(4) (2001) 333-335.

[109] C.R. Brooks, Y.M. Wang, Tensile properties and fractography of aged hastelloy

B2 (550–850°C for up to 1200 H), Materials Characterization 25(2) (1990) 185-197.

[110] V. Shabashov, I. Brodova, A. Mukoseev, V. Sagaradze, A.J.J.o.P.C.M. Litvinov, Deformation-induced phase transformations in the Al–Fe system under intensive plastic deformation, 19(38) (2007) 386222.

[111] Y. Yang, T. Zhang, Y. Shao, G. Meng, F. Wang, Effect of hydrostatic pressure on the corrosion behaviour of Ni–Cr–Mo–V high strength steel, Corrosion Science 52(8) (2010) 2697-2706.

[112] Y. Luo, Q. Zhang, W. Jiang, Y. Zhang, M. Hao, S.-T. Tu, The microstructure, mechanical properties and fracture behavior of hastelloy C276-BNi2 brazed joint, Materials & Design 115 (2017) 458-466.

[113] S. Chen, D.K.L. Tsang, L. Jiang, K. Yu, C. Li, Z. Li, Z. Li, X. Zhou, J. Yang, Microstructure and local strains in GH3535 alloy heat affected zone and their influence on the mechanical properties, Materials Science and Engineering: A 699 (2017) 48-54.

[114] X.P. Mao, Q. Guo, S.Y. Zhang, S.Y. Hu, D.G. Lu, H. Xu, Creep properties and damage study of Ni-based alloy C276 at high temperature, Trans Tech Publ, pp. 1143-1148.

[115] X.P. Mao, Q. Guo, S.Y. Zhang, S.Y. Hu, D.G. Lu, H. Xu, Creep properties and damage study of Ni-based alloy C276 at high temperature, Advanced Materials Research, Trans Tech Publ, 2011, pp. 1143-1148.

[116] F. Kawashima, T. Igari, Y. Miyoshi, Y. Kamito, M.J.N.e. Tanihira, design, High temperature strength and inelastic behavior of plate–fin structures for HTGR, 237(6) (2007) 591-599.

[117] Y. Jiang, W. Guo, X.J.I.j.o.f. Shao, On the study of the effects of notch shape on the creep damage under cyclic loading, 29(5) (2007) 836-842.

[118] G. Chen, G.Z. Wang, F.Z. Xuan, S.T. Tu, Mismatch effect in creep properties on creep crack growth behavior in welded joints, Materials & Design 63 (2014) 600-608.

[119] Y. Luo, W. Jiang, W. Zhang, Y.C. Zhang, W. Woo, S.T. Tu, Notch effect on creep damage for Hastelloy C276-BNi2 brazing joint, Materials & Design 84 (2015) 212-222.

[120] X. Tang, S. Wang, D. Xu, Y. Gong, J. Zhang, Y.J.I. Wang, E.C. Research,

Corrosion behavior of Ni-based alloys in supercritical water containing high concentrations of salt and oxygen, 52(51) (2013) 18241-18250.

[121] M.A. Rodríguez, R.M. Carranza, R.B.J.M. Rebak, M.T. A, Influence of halide ions and alloy microstructure on the passive and localized corrosion behavior of alloy 22, 36(5) (2005) 1179-1185.

[122] S. Tuzi, H. Lai, K. Göransson, M. Thuvander, K.J.J.o.N.M. Stiller, Corrosion of pre-oxidized nickel alloy X-750 in simulated BWR environment, 486 (2017) 350-360.

[123] H. Zhu, R. Holmes, T. Hanley, J. Davis, K. Short, L. Edwards, High-temperature corrosion of helium ion-irradiated Ni-based alloy in fluoride molten salt, Corrosion Science 91 (2015) 1-6.

[124] L.C. Olson, J.W. Ambrosek, K. Sridharan, M.H. Anderson, T.R.J.J.o.F.C. Allen, Materials corrosion in molten LiF–NaF–KF salt, 130(1) (2009) 67-73.

[125] F.F. Han, B.M. Zhou, H.F. Huang, B. Leng, Y.L. Lu, Z.J. Li, X.T. Zhou, Effect of long-term thermal exposure on the hot ductility behavior of GH3535 alloy, Materials Science and Engineering: A 673 (2016) 299-306.

[126] X.-X. Ye, H. Ai, Z. Guo, H. Huang, L. Jiang, J. Wang, Z. Li, X. Zhou, The high-temperature corrosion of Hastelloy N alloy (UNS N10003) in molten fluoride salts analysed by STXM, XAS, XRD, SEM, EPMA, TEM/EDS, Corrosion Science 106 (2016) 249-259.

[127] J.-H. Park, L. Chen, K. Goretta, R. Koritala, U. Balachandran, Oxidation of hastelloy C276, AIP Conference Proceedings, AIP, 2002, pp. 495-502.

[128] J.C.L. Shoemaker, Special Alloys and Overmatching Welding Products Solve FGD Corrosion Problems.

[129] G. Ma, F. Niu, D. Wu, Y. Qu, Electrochemistry Corrosion Properties of Pulsed Laser Welding Hastelloy C-276, Physics Procedia 41 (2013) 31-37.

[130] C. Garcia, F. Martin, P. De Tiedra, Y. Blanco, M.J.C.S. Lopez, Pitting corrosion of welded joints of austenitic stainless steels studied by using an electrochemical minicell, 50(4) (2008) 1184-1194.

[131] G.E. Bean, D.B. Witkin, T.D. McLouth, D.N. Patel, R.J. Zaldivar, Effect of laser focus shift on surface quality and density of Inconel 718 parts produced via selective

laser melting, Additive Manufacturing 22 (2018) 207-215.

[132] K. Moussaoui, W. Rubio, M. Mousseigne, T. Sultan, F. Rezai, Effects of Selective Laser Melting additive manufacturing parameters of Inconel 718 on porosity, microstructure and mechanical properties, Materials Science and Engineering: A 735 (2018) 182-190.

[133] K. Solberg, J. Torgersen, F. Berto, Fatigue Behaviour of Additively Manufactured Inconel 718 Produced by Selective Laser Melting, Procedia Structural Integrity 13 (2018) 1762-1767.

[134] D. Herzog, V. Seyda, E. Wycisk, C. Emmelmann, Additive manufacturing of metals, Acta Materialia 117 (2016) 371-392.

[135] M. Bambach, I. Sizova, F. Silze, M. Schnick, Hot workability and microstructure evolution of the nickel-based superalloy Inconel 718 produced by laser metal deposition, Journal of Alloys and Compounds 740 (2018) 278-287.

[136] Z. Liu, X. Wang, H. Kim, Y. Zhou, W. Cong, H. Zhang, Investigations of Energy Density Effects on Forming Accuracy and Mechanical Properties of Inconel 718 Fabricated by LENS Process, Procedia Manufacturing 26 (2018) 731-739.

[137] Y. Zhai, D.A. Lados, E.J. Brown, G.N. Vigilante, Understanding the microstructure and mechanical properties of Ti-6Al-4V and Inconel 718 alloys manufactured by Laser Engineered Net Shaping, Additive Manufacturing 27 (2019) 334-344.

[138] D. Kotoban, A. Nazarov, I. Shishkovsky, Comparative study of selective laser melting and direct laser metal deposition of Ni3Al intermetallic alloy, Procedia IUTAM 23 (2017) 138-146.

[139] H. Helmer, A. Bauereiß, R.F. Singer, C. Körner, Grain structure evolution in Inconel 718 during selective electron beam melting, Materials Science and Engineering: A 668 (2016) 180-187.

[140] H.-J. Lee, H.-K. Kim, H.-U. Hong, B.-S. Lee, Influence of the focus offset on the defects, microstructure, and mechanical properties of an Inconel 718 superalloy fabricated by electron beam additive manufacturing, Journal of Alloys and Compounds 781 (2019) 842-856.

[141] D. Kotzem, T. Arold, T. Niendorf, F. Walther, Influence of specimen position on

the build platform on the mechanical properties of as-built direct aged electron beam melted Inconel 718 alloy, Materials Science and Engineering: A 772 (2020) 138785.

[142] F.A. List, R.R. Dehoff, L.E. Lowe, W.J. Sames, Properties of Inconel 625 mesh structures grown by electron beam additive manufacturing, Materials Science and Engineering: A 615 (2014) 191-197.

[143] P. Karimi, C. Schnur, E. Sadeghi, J. Andersson, Contour design to improve topographical and microstructural characteristics of Alloy 718 manufactured by electron beam-powder bed fusion technique, Additive Manufacturing 32 (2020) 101014.

[144] B. Wu, Z. Pan, D. Ding, D. Cuiuri, H. Li, J. Xu, J. Norrish, A review of the wire arc additive manufacturing of metals: properties, defects and quality improvement, Journal of Manufacturing Processes 35 (2018) 127-139.

[145] A. Shaji Karapuzha, D. Fraser, D. Schliephake, S. Dietrich, Y. Zhu, X. Wu, A. Huang, Microstructure, mechanical behaviour and strengthening mechanisms in Hastelloy X manufactured by electron beam and laser beam powder bed fusion, Journal of Alloys and Compounds 862 (2021).

[146] S. Zhang, J. Liu, X. Lin, Y. Huang, Y. Zhang, P. Guo, J. Li, W. Huang, Microstructure and anodic electrochemical behavior of additive manufactured Hastelloy X alloy via directed energy deposition, Additive Manufacturing 39 (2021).

[147] K. Yuan, W. Guo, P. Li, Y. Zhang, X. Li, X. Lin, Thermomechanical behavior of laser metal deposited Inconel 718 superalloy over a wide range of temperature and strain rate: Testing and constitutive modeling, Mechanics of Materials 135 (2019) 13-25.

[148] S. Goel, A. Sittiho, I. Charit, U. Klement, S. Joshi, Effect of post-treatments under hot isostatic pressure on microstructural characteristics of EBM-built Alloy 718, Additive Manufacturing 28 (2019) 727-737.

[149] C.E. Seow, H.E. Coules, G. Wu, R.H.U. Khan, X. Xu, S. Williams, Wire + Arc Additively Manufactured Inconel 718: Effect of post-deposition heat treatments on microstructure and tensile properties, Materials & Design 183 (2019) 108157.

[150] N. Nadammal, S. Cabeza, T. Mishurova, T. Thiede, A. Kromm, C. Seyfert, L. Farahbod, C. Haberland, J.A. Schneider, P.D. Portella, G. Bruno, Effect of hatch length

on the development of microstructure, texture and residual stresses in selective laser melted superalloy Inconel 718, Materials & Design 134 (2017) 139-150.

[151] J. Nguejio, F. Szmytka, S. Hallais, A. Tanguy, S. Nardone, M. Godino Martinez, Comparison of microstructure features and mechanical properties for additive manufactured and wrought nickel alloys 625, Materials Science and Engineering: A 764 (2019) 138214.

[152] Y. Yanqiu, W. Zhixun, Z. Yanchao, W. Jiapo, L. Zhenwei, Y. Zhufeng, Effect of crystallographic orientation on the corrosion resistance of Ni-based single crystal superalloys, Corrosion Science 170 (2020) 108643.

[153] O. Sanchez-Mata, X. Wang, J.A. Muñiz-Lerma, S.E. Atabay, M. Attarian Shandiz, M. Brochu, Dependence of mechanical properties on crystallographic orientation in nickel-based superalloy Hastelloy X fabricated by laser powder bed fusion, Journal of Alloys and Compounds 865 (2021).

[154] Z. Qiu, B. Wu, H. Zhu, Z. Wang, A. Hellier, Y. Ma, H. Li, O. Muransky, D. Wexler, Microstructure and mechanical properties of wire arc additively manufactured Hastelloy C276 alloy, Materials & Design (2020) 109007.

[155] B. Wu, Z. Pan, S. Li, D. Cuiuri, D. Ding, H. Li, The anisotropic corrosion behaviour of wire arc additive manufactured Ti-6Al-4V alloy in 3.5% NaCl solution, Corrosion Science 137 (2018) 176-183.

[156] X. Xu, J. Ding, S. Ganguly, S. Williams, Investigation of process factors affecting mechanical properties of INCONEL 718 superalloy in wire + arc additive manufacture process, Journal of Materials Processing Technology 265 (2019) 201-209.

[157] C. Zhong, A. Gasser, J. Kittel, K. Wissenbach, R. Poprawe, Improvement of material performance of Inconel 718 formed by high deposition-rate laser metal deposition, Materials & Design 98 (2016) 128-134.

[158] Y.L. Hu, Y.L. Li, S.Y. Zhang, X. Lin, Z.H. Wang, W.D. Huang, Effect of solution temperature on static recrystallization and ductility of Inconel 625 superalloy fabricated by directed energy deposition, Materials Science and Engineering: A 772 (2020) 138711.

[159] N. Ramenatte, A. Vernouillet, S. Mathieu, A. Vande Put, M. Vilasi, D. Monceau, A comparison of the high-temperature oxidation behaviour of conventional wrought

and laser beam melted Inconel 625, Corrosion Science 164 (2020) 108347.

[160] K. Wang, Y. Liu, Z. Sun, J. Lin, Y. Lv, B. Xu, Microstructural evolution and mechanical properties of Inconel 718 superalloy thin wall fabricated by pulsed plasma arc additive manufacturing, Journal of Alloys and Compounds 819 (2020) 152936.

[161] W. Yangfan, C. Xizhang, S. Chuanchu, Microstructure and mechanical properties of Inconel 625 fabricated by wire-arc additive manufacturing, Surface and Coatings Technology 374 (2019) 116-123.

[162] Z. Qiu, B. Wu, Z. Wang, D. Wexler, K. Carpenter, H. Zhu, O. Muránsky, J. Zhang, H. Li, Effects of post heat treatment on the microstructure and mechanical properties of wire arc additively manufactured Hastelloy C276 alloy, Materials Characterization 177 (2021) 111158.

[163] R.M. Kindermann, M.J. Roy, R. Morana, P.B. Prangnell, Process response of Inconel 718 to wire + arc additive manufacturing with cold metal transfer, Materials & Design 195 (2020).

[164] W.M. Tucho, P. Cuvillier, A. Sjolyst-Kverneland, V. Hansen, Microstructure and hardness studies of Inconel 718 manufactured by selective laser melting before and after solution heat treatment, Materials Science and Engineering: A 689 (2017) 220-232.

[165] D. Deng, J. Moverare, R.L. Peng, H. Söderberg, Microstructure and anisotropic mechanical properties of EBM manufactured Inconel 718 and effects of post heat treatments, Materials Science and Engineering: A 693 (2017) 151-163.

[166] T.G. Gallmeyer, S. Moorthy, B.B. Kappes, M.J. Mills, B. Amin-Ahmadi, A.P. Stebner, Knowledge of process-structure-property relationships to engineer better heat treatments for laser powder bed fusion additive manufactured Inconel 718, Additive Manufacturing 31 (2020) 100977.

[167] Y.-L. Kuo, S. Horikawa, K. Kakehi, The effect of interdendritic δ phase on the mechanical properties of Alloy 718 built up by additive manufacturing, Materials & Design 116 (2017) 411-418.

[168] M.R. Stoudt, E.A. Lass, D.S. Ng, M.E. Williams, F. Zhang, C.E. Campbell, G. Lindwall, L.E. Levine, The influence of annealing temperature and time on the formation of δ-phase in additively-manufactured Inconel 625, Metallurgical and Materials Transactions A 49(7) (2018) 3028-3037.

[169] S. Sui, H. Tan, J. Chen, C. Zhong, Z. Li, W. Fan, A. Gasser, W. Huang, The influence of Laves phases on the room temperature tensile properties of Inconel 718 fabricated by powder feeding laser additive manufacturing, Acta Materialia 164 (2019) 413-427.

[170] F. Xu, Y. Lv, Y. Liu, F. Shu, P. He, B. Xu, Microstructural Evolution and Mechanical Properties of Inconel 625 Alloy during Pulsed Plasma Arc Deposition Process, Journal of Materials Science & Technology 29(5) (2013) 480-488.

[171] G. Ravi, N. Murugan, R. Arulmani, Microstructure and mechanical properties of Inconel-625 slab component fabricated by wire arc additive manufacturing, Materials Science and Technology 36(16) (2020) 1785-1795.

[172] K.A. Small, M.L. Taheri, Role of Processing in Microstructural Evolution in Inconel 625: A Comparison of Three Additive Manufacturing Techniques, Metallurgical and Materials Transactions A (2021) 1-10.

[173] M. Dinovitzer, X. Chen, J. Laliberte, X. Huang, H. Frei, Effect of wire and arc additive manufacturing (WAAM) process parameters on bead geometry and microstructure, Additive Manufacturing 26 (2019) 138-146.

[174] D. Tomus, Y. Tian, P.A. Rometsch, M. Heilmaier, X. Wu, Influence of post heat treatments on anisotropy of mechanical behaviour and microstructure of Hastelloy-X parts produced by selective laser melting, Materials Science and Engineering: A 667 (2016) 42-53.

[175] M.L. Montero-Sistiaga, Z. Liu, L. Bautmans, S. Nardone, G. Ji, J.-P. Kruth, J. Van Humbeeck, K. Vanmeensel, Effect of temperature on the microstructure and tensile properties of micro-crack free hastelloy X produced by selective laser melting, Additive Manufacturing 31 (2020) 100995.

[176] D. Kong, X. Ni, C. Dong, L. Zhang, J. Yao, C. Man, L. Wang, K. Xiao, X. Li, Anisotropic response in mechanical and corrosion properties of hastelloy X fabricated by selective laser melting, Construction and Building Materials 221 (2019) 720-729.

[177] G. Marchese, S. Parizia, M. Rashidi, A. Saboori, D. Manfredi, D. Ugues, M. Lombardi, E. Hryha, S. Biamino, The role of texturing and microstructure evolution on the tensile behavior of heat-treated Inconel 625 produced via laser powder bed fusion, Materials Science and Engineering: A 769 (2020) 138500.

[178] Z. Qiu, B. Wu, H. Zhu, Z. Wang, A. Hellier, Y. Ma, H. Li, O. Muransky, D. Wexler, Microstructure and mechanical properties of wire arc additively manufactured Hastelloy C276 alloy, Materials & Design 195 (2020) 109007.

[179] E. Hosseini, V.A. Popovich, A review of mechanical properties of additively manufactured Inconel 718, Additive Manufacturing 30 (2019).

[180] G. Marchese, M. Lorusso, S. Parizia, E. Bassini, J.-W. Lee, F. Calignano, D. Manfredi, M. Terner, H.-U. Hong, D. Ugues, M. Lombardi, S. Biamino, Influence of heat treatments on microstructure evolution and mechanical properties of Inconel 625 processed by laser powder bed fusion, Materials Science and Engineering: A 729 (2018) 64-75.

[181] C. Li, R. White, X.Y. Fang, M. Weaver, Y.B. Guo, Microstructure evolution characteristics of Inconel 625 alloy from selective laser melting to heat treatment, Materials Science and Engineering: A 705 (2017) 20-31.

[182] M.M. Kirka, D.A. Greeley, C. Hawkins, R.R. Dehoff, Effect of anisotropy and texture on the low cycle fatigue behavior of Inconel 718 processed via electron beam melting, International Journal of Fatigue 105 (2017) 235-243.

[183] M.M. Kirka, F. Medina, R. Dehoff, A. Okello, Mechanical behavior of post-processed Inconel 718 manufactured through the electron beam melting process, Materials Science and Engineering: A 680 (2017) 338-346.

[184] M. Salarian, H. Asgari, M. Vlasea, Pore space characteristics and corresponding effect on tensile properties of Inconel 625 fabricated via laser powder bed fusion, Materials Science and Engineering: A 769 (2020) 138525.

[185] J.H. Yi, J.W. Kang, T.J. Wang, X. Wang, Y.Y. Hu, T. Feng, Y.L. Feng, P.Y. Wu, Effect of laser energy density on the microstructure, mechanical properties, and deformation of Inconel 718 samples fabricated by selective laser melting, Journal of Alloys and Compounds 786 (2019) 481-488.

[186] E. Chlebus, K. Gruber, B. Kuźnicka, J. Kurzac, T. Kurzynowski, Effect of heat treatment on the microstructure and mechanical properties of Inconel 718 processed by selective laser melting, Materials Science and Engineering: A 639 (2015) 647-655.

[187] H. Qi, M. Azer, A. Ritter, Studies of standard heat treatment effects on microstructure and mechanical properties of laser net shape manufactured Inconel 718,

Metallurgical and Materials Transactions A 40(10) (2009) 2410-2422.

[188] A. Strondl, M. Palm, J. Gnauk, G. Frommeyer, Microstructure and mechanical properties of nickel based superalloy IN718 produced by rapid prototyping with electron beam melting (EBM), Materials Science and Technology 27(5) (2011) 876-883.

[189] M. Rombouts, G. Maes, M. Mertens, W. Hendrix, Laser metal deposition of Inconel 625: Microstructure and mechanical properties, Journal of Laser Applications 24(5) (2012) 052007.

[190] L.E. Murr, E. Martinez, S.M. Gaytan, D.A. Ramirez, B.I. Machado, P.W. Shindo, J.L. Martinez, F. Medina, J. Wooten, D. Ciscel, Microstructural architecture, microstructures, and mechanical properties for a nickel-base superalloy fabricated by electron beam melting, Metallurgical and Materials Transactions A 42(11) (2011) 3491-3508.

[191] Y. Wang, X. Chen, Q. Shen, C. Su, Y. Zhang, S. Jayalakshmi, R.A. Singh, Effect of magnetic Field on the microstructure and mechanical properties of inconel 625 superalloy fabricated by wire arc additive manufacturing, Journal of Manufacturing Processes 64 (2021) 10-19.

[192] A.N.M. Tanvir, M.R.U. Ahsan, G. Seo, J.-d. Kim, C. Ji, B. Bates, Y. Lee, D.B. Kim, Heat treatment effects on Inconel 625 components fabricated by wire + arc additively manufacturing (WAAM)—part 2: mechanical properties, The International Journal of Advanced Manufacturing Technology 110(7-8) (2020) 1709-1721.

[193] R. Ghiaasiaan, M. Muhammad, P.R. Gradl, S. Shao, N. Shamsaei, Superior tensile properties of Hastelloy X enabled by additive manufacturing, Materials Research Letters 9(7) (2021) 308-314.

[194] H. Wang, L. Chen, B. Dovgyy, W. Xu, A. Sha, X. Li, H. Tang, Y. Liu, H. Wu, M.-S. Pham, Micro-cracking, microstructure and mechanical properties of Hastelloy-X alloy printed by laser powder bed fusion: As-built, annealed and hot-isostatic pressed, Additive Manufacturing 39 (2021).

[195] Q. Han, R. Mertens, M.L. Montero-Sistiaga, S. Yang, R. Setchi, K. Vanmeensel, B. Van Hooreweder, S.L. Evans, H. Fan, Laser powder bed fusion of Hastelloy X: Effects of hot isostatic pressing and the hot cracking mechanism, Materials Science and

Engineering: A 732 (2018) 228-239.

[196] B. Guo, Y. Zhang, F. He, J. Ma, J. Li, Z. Wang, J. Wang, J. Feng, W. Wang, L. Gao, Origins of the mechanical property heterogeneity in a hybrid additive manufactured Hastelloy X, Materials Science and Engineering: A 823 (2021).

[197] K.-T. Son, T.Q. Phan, L.E. Levine, K.-S. Kim, K.-A. Lee, M. Ahlfors, M.E. Kassner, The creep and fracture properties of additively manufactured inconel 625, Materialia 15 (2021) 101021.

[198] Y.-L. Kuo, A. Kamigaichi, K. Kakehi, Characterization of Ni-Based Superalloy Built by Selective Laser Melting and Electron Beam Melting, Metallurgical and Materials Transactions A 49(9) (2018) 3831-3837.

[199] M. Pröbstle, S. Neumeier, J. Hopfenmüller, L.P. Freund, T. Niendorf, D. Schwarze, M. Göken, Superior creep strength of a nickel-based superalloy produced by selective laser melting, Materials Science and Engineering: A 674 (2016) 299-307.

[200] S.-Y. Im, S.-Y. Jun, J.-W. Lee, J.-H. Lee, B.-S. Lee, H.-J. Lee, H.-U. Hong, Unidirectional columnar microstructure and its effect on the enhanced creep resistance of selective electron beam melted Inconel 718, Journal of Alloys and Compounds 817 (2020) 153320.

[201] F. Brenne, A. Taube, M. Pröbstle, S. Neumeier, D. Schwarze, M. Schaper, T. Niendorf, Microstructural design of Ni-base alloys for high-temperature applications: impact of heat treatment on microstructure and mechanical properties after selective laser melting, Progress in Additive Manufacturing 1(3-4) (2016) 141-151.

[202] Z. Zhao, P. Zhang, S. Li, J. Zhang, W. Shi, C. Zhang, Y. Li, J. Yan, F. Yang, C. Zhang, Fatigue-creep behaviors of Ni–Fe based superalloy under various testing conditions, Journal of Materials Research and Technology 15 (2021) 4694-4701.

[203] G.-Q. Wang, M.-S. Chen, H.-B. Li, Y.C. Lin, W.-D. Zeng, Y.-Y. Ma, Methods and mechanisms for uniformly refining deformed mixed and coarse grains inside a solution-treated Ni-based superalloy by two-stage heat treatment, Journal of Materials Science & Technology 77 (2021) 47-57.

[204] H. Yuan, W.C. Liu, Effect of the δ phase on the hot deformation behavior of Inconel 718, Materials Science and Engineering: A 408(1) (2005) 281-289.

[205] D.-G. He, Y.C. Lin, L.-H. Wang, Microstructural variations and kinetic behaviors

during metadynamic recrystallization in a nickel base superalloy with pre-precipitated δ phase, Materials & Design 165 (2019) 107584.

[206] K.T. Son, M.E. Kassner, K.A. Lee, The Creep Behavior of Additively Manufactured Inconel 625, Advanced Engineering Materials 22(1) (2019).

[207] K.-T. Son, T.Q. Phan, L.E. Levine, K.-S. Kim, K.-A. Lee, M. Ahlfors, M.E. Kassner, The creep and fracture properties of additively manufactured inconel 625, Materialia 15 (2021).

[208] Z. Qiu, B. Dong, B. Wu, Z. Wang, K. Carpenter, T. Wu, J. Zhang, D. Wexler, H. Zhu, H. Li, Tailoring the surface finish, dendritic microstructure and mechanical properties of wire arc additively manufactured Hastelloy C276 alloy by magnetic arc oscillation, Additive Manufacturing (2021) 102397.

[209] S. Liu, Y.C. Shin, Additive manufacturing of Ti6Al4V alloy: A review, Materials & Design 164 (2019) 107552.

[210] S. Goel, M. Neikter, J. Capek, E. Polatidis, M.H. Colliander, S. Joshi, R. Pederson, Residual stress determination by neutron diffraction in powder bed fusion-built Alloy 718: Influence of process parameters and post-treatment, Materials & Design 195 (2020) 109045.

[211] Z. Wang, E. Denlinger, P. Michaleris, A.D. Stoica, D. Ma, A.M. Beese, Residual stress mapping in Inconel 625 fabricated through additive manufacturing: Method for neutron diffraction measurements to validate thermomechanical model predictions, Materials & Design 113 (2017) 169-177.

[212] K. Yuan, W. Guo, P. Li, J. Wang, Y. Su, X. Lin, Y. Li, Influence of process parameters and heat treatments on the microstructures and dynamic mechanical behaviors of Inconel 718 superalloy manufactured by laser metal deposition, Materials Science and Engineering: A 721 (2018) 215-225.

[213] D.A. Lesyk, S. Martinez, B.N. Mordyuk, V.V. Dzhemelinskyi, A. Lamikiz, G.I. Prokopenko, Post-processing of the Inconel 718 alloy parts fabricated by selective laser melting: Effects of mechanical surface treatments on surface topography, porosity, hardness and residual stress, Surface and Coatings Technology 381 (2020) 125136.

[214] D.M. Bond, M.A. Zikry, Effects of electron beam manufacturing induced defects on fracture in Inconel 718, Additive Manufacturing 32 (2020) 101059.

[215] P. Kumar, J. Farah, J. Akram, C. Teng, J. Ginn, M. Misra, Influence of laser processing parameters on porosity in Inconel 718 during additive manufacturing, The International Journal of Advanced Manufacturing Technology 103(1) (2019) 1497-1507.

[216] J. Cui, L. Yuan, P. Commins, F. He, J. Wang, Z. Pan, WAAM process for metal block structure parts based on mixed heat input, The International Journal of Advanced Manufacturing Technology 113(1) (2021) 503-521.

[217] C.E. Seow, J. Zhang, H.E. Coules, G. Wu, C. Jones, J. Ding, S. Williams, Effect of crack-like defects on the fracture behaviour of Wire + Arc Additively Manufactured nickel-base Alloy 718, Additive Manufacturing 36 (2020).

[218] H. Zhao, G. Zhang, Z. Yin, L. Wu, A 3D dynamic analysis of thermal behavior during single-pass multi-layer weld-based rapid prototyping, Journal of Materials Processing Technology 211(3) (2011) 488-495.

[219] S. Cao, D. Gu, Q. Shi, Relation of microstructure, microhardness and underlying thermodynamics in molten pools of laser melting deposition processed TiC/Inconel 625 composites, Journal of Alloys and Compounds 692 (2017) 758-769.

[220] J.F. Wang, Q.J. Sun, H. Wang, J.P. Liu, J.C. Feng, Effect of location on microstructure and mechanical properties of additive layer manufactured Inconel 625 using gas tungsten arc welding, Materials Science and Engineering: A 676 (2016) 395-405.

[221] K.D. Ramkumar, A. Narenthiran, A. Konjenti, P.N. Pravin, T. Kanish, Effect of low energy laser shock peening on the mechanical integrity of Hastelloy C-276 welds, Journal of materials processing technology 274 (2019) 116296.

[222] K.S. Bal, J. Dutta Majumdar, A. Roy Choudhury, Study of intergranular corrosion mechanism of fiber laser welded 3-mm-thick Hastelloy C-276 sheet, Corrosion Science 157 (2019) 406-419.

[223] C. Zhang, L. Zhang, Y. Cui, Q. Feng, C. Cheng, Effects of high-temperature aging on precipitation and corrosion behavior of a Ni-Cr-Mo-based hastelloy C276 superalloy, Journal of Materials Engineering and Performance (2020) 1-9.

[224] A.R. Kannan, S.M. Kumar, N.P. Kumar, N.S. Shanmugam, A.S. Vishnu, Y. Palguna, Process-microstructural features for tailoring fatigue strength of wire arc

additive manufactured functionally graded material of SS904L and Hastelloy C-276, Materials Letters 274 (2020) 127968.

[225] S. Sundaresan, G.D.J. Ram, Use of magnetic arc oscillation for grain refinement of gas tungsten arc welds inα–βtitanium alloys, Science and Technology of Welding and Joining 4(3) (2013) 151-160.

[226] C.A. Schneider, W.S. Rasband, K.W. Eliceiri, NIH Image to ImageJ: 25 years of image analysis, Nature Methods 9(7) (2012) 671-675.

[227] A.A. Coelho, TOPAS, Graphics based profile and structure analysis software, Version 3.0, Bruker AXS, Inc. Madison, USA (2008).

[228] U. Garbe, New pole figure calculation software: 2DiffCalc, Journal of Applied Crystallography 42(4) (2009) 730-733.

[229] S.K. Dinda, W. Kockelmann, G.G. Roy, P. Srirangam, Neutron diffraction bulk texture study with impact property correlation of electron beam welded dissimilar Fe-7% Al alloy to steel joints, The International Journal of Advanced Manufacturing Technology 108(5) (2020) 1499-1508.

[230] H. Zhu, Y. Ma, T. Wei, H. Li, R. Aughterson, G.J.A.M. Lumpkin, The formation and Kr-ion irradiation behaviour of new microstructural features in additively manufactured titanium aluminium alloy, 29 (2019) 100766.

[231] X. Cai, B. Dong, X. Yin, S. Lin, C. Fan, C.J.A.M. Yang, Wire arc additive manufacturing of titanium aluminide alloys using two-wire TOP-TIG welding: processing, microstructures, and mechanical properties, (2020) 101344.

[232] T. Nagase, T. Hori, M. Todai, S.-H. Sun, T. Nakano, Additive manufacturing of dense components in beta-titanium alloys with crystallographic texture from a mixture of pure metallic element powders, Materials & Design 173 (2019) 107771.

[233] K.S. Bal, J. Dutta Majumdar, A. Roy Choudhury, Optimization of Melt Zone Area for Electron Beam Welded Hastelloy C-276 Sheet and Study of Corrosion Resistance of the Optimized Melt Zone in 3.5 wt% NaCl Aqueous Solution, Arabian Journal for Science and Engineering 44(2) (2019) 1617-1630.

[234] S. Rosenthal, S. Platt, R. Hölker-Jäger, S. Gies, S. Kleszczynski, A.E. Tekkaya, G. Witt, Forming properties of additively manufactured monolithic Hastelloy X sheets, Materials Science and Engineering: A 753 (2019) 300-316.

[235] R. Esmaeilizadeh, U. Ali, A. Keshavarzkermani, Y. Mahmoodkhani, E. Marzbanrad, E. Toyserkani, On the effect of spatter particles distribution on the quality of Hastelloy X parts made by laser powder-bed fusion additive manufacturing, Journal of Manufacturing Processes 37 (2019) 11-20.

[236] F. Wang, Mechanical property study on rapid additive layer manufacture Hastelloy® X alloy by selective laser melting technology, The International Journal of Advanced Manufacturing Technology 58(5) (2012) 545-551.

[237] J.P. Oliveira, A.D. LaLonde, J. Ma, Processing parameters in laser powder bed fusion metal additive manufacturing, Materials & Design 193 (2020) 108762.

[238] H. Chae, E.W. Huang, J. Jain, H. Wang, W. Woo, S.-W. Chen, S. Harjo, T. Kawasaki, S.Y. Lee, Plastic anisotropy and deformation-induced phase transformation of additive manufactured stainless steel, Materials Science and Engineering: A 762 (2019) 138065.

[239] K. Ohsasa, T. Narita, T. Shinmura, Numerical modeling of the transient liquid phase bonding process of Ni using Ni-B-Cr ternary filler metal, Journal of Phase Equilibria 20(3) (1999) 199.

[240] X.Y. Fang, H.Q. Li, M. Wang, C. Li, Y.B. Guo, Characterization of texture and grain boundary character distributions of selective laser melted Inconel 625 alloy, Materials Characterization 143 (2018) 182-190.

[241] L. Thivillon, P. Bertrand, B. Laget, I. Smurov, Potential of direct metal deposition technology for manufacturing thick functionally graded coatings and parts for reactors components, Journal of Nuclear Materials 385(2) (2009) 236-241.

[242] Y. Wang, J. Shi, Y. Liu, Competitive grain growth and dendrite morphology evolution in selective laser melting of Inconel 718 superalloy, Journal of Crystal Growth 521 (2019) 15-29.

[243] A.N.M. Tanvir, M.R. Ahsan, C. Ji, W. Hawkins, B. Bates, D.B. Kim, Heat treatment effects on Inconel 625 components fabricated by wire + arc additive manufacturing (WAAM)—part 1: microstructural characterization, 2019.

[244] T. Rodrigues, V. Duarte, D. Tomás, J. Ávila, J.D. Escobar, E. Rossinyol, N. Schell, T. Santos, J.P. Oliveira, In-situ strengthening of a high strength low alloy steel during Wire and Arc Additive Manufacturing (WAAM), Additive Manufacturing

(2020) 101200.

[245] Z. Zeng, B. Cong, J. Oliveira, W. Ke, N. Schell, B. Peng, Z. Qi, F. Ge, W. Zhang, S.J.A.M. Ao, Wire and arc additive manufacturing of a Ni-rich NiTi shape memory alloy: Microstructure and mechanical properties, 32 (2020) 101051.

[246] G. Ma, D. Wu, D. Guo, Segregation Characteristics of Pulsed Laser Butt Welding of Hastelloy C-276, Metallurgical and Materials Transactions A 42(13) (2011) 3853-3857.

[247] M. Leary, M. Mazur, H. Williams, E. Yang, A. Alghamdi, B. Lozanovski, X. Zhang, D. Shidid, L. Farahbod-Sternahl, G. Witt, I. Kelbassa, P. Choong, M. Qian, M. Brandt, Inconel 625 lattice structures manufactured by selective laser melting (SLM): Mechanical properties, deformation and failure modes, Materials & Design 157 (2018) 179-199.

[248] P.A. Colegrove, J. Donoghue, F. Martina, J. Gu, P. Prangnell, J. Hönnige, Application of bulk deformation methods for microstructural and material property improvement and residual stress and distortion control in additively manufactured components, Scripta Materialia 135 (2017) 111-118.

[249] B. Wu, Z. Pan, D. Ding, D. Cuiuri, H. Li, Z. Fei, The effects of forced interpass cooling on the material properties of wire arc additively manufactured Ti6Al4V alloy, Journal of Materials Processing Technology 258 (2018) 97-105.

[250] J. Sarma, R. Kumar, A.K. Sahoo, A. Panda, Enhancement of material properties of titanium alloys through heat treatment process: A brief review, Materials Today: Proceedings (2019).

[251] M.G. Fontana, Corrosion engineering, Tata McGraw-Hill Education2005.

[252] M.J. Donachie, S.J. Donachie, Superalloys: a technical guide, ASM international2002.

[253] H. McCoy, D. Canonico, Preirradiation and Postirradiation Mechanical Properties of Hastelloy N Welds, (1969) 20-23.

[254] J. Yang, Y. He, C. Qin, W. Zhao, S. Chen, Z. Gao, Microstructure evolution in a Ni–Mo–Cr superalloy subjected to simulated heat-affected zone thermal cycle with high peak temperature, Materials & Design 86 (2015) 230-236.

[255] O.D. Underwood, J.D. Madison, G.B. Thompson, Emergence and Progression of Abnormal Grain Growth in Minimally Strained Nickel-200, Metals 7(9) (2017).

[256] S. Dymek, M. Dollar, M. Farooqi, Optimization of mechanical properties of a Ni–Mo–Cr alloy by structural modifications induced by changes in heat treatment, Materials Science and Engineering: A 319-321 (2001) 284-289.

[257] K. Zhao, M. YH, H. ZQ, μ phase in a nickel base directionally solidified alloy, Materials transactions 46(1) (2005) 54-58.

[258] H.M. Tawancy, On the Precipitation of Intermetallic Compounds in Selected Solid-Solution-Strengthened Ni-Base Alloys and Their Effects on Mechanical Properties, Metallography, Microstructure, and Analysis 6(3) (2017) 200-215.

[259] J.A. Gonzalez, J. Mireles, S.W. Stafford, M.A. Perez, C.A. Terrazas, R.B. Wicker, Characterization of Inconel 625 fabricated using powder-bed-based additive manufacturing technologies, Journal of Materials Processing Technology 264 (2019) 200-210.

[260] H. Xiao, S. Li, X. Han, J. Mazumder, L. Song, Laves phase control of Inconel 718 alloy using quasi-continuous-wave laser additive manufacturing, Materials & Design 122 (2017) 330-339.

[261] T. Liu, J.S. Dong, L. Wang, Z.J. Li, X.T. Zhou, L.H. Lou, J. Zhang, Effect of Long-term Thermal Exposure on Microstructure and Stress Rupture Properties of GH3535 Superalloy, Journal of Materials Science & Technology 31(3) (2015) 269-279.

[262] Y.R. Zheng, D.T. Zhang, Color metallographic investigation of superalloys and steels, National Defense Technology Press, Beijing (1999).

[263] M. Simonetti, P. Caron, Role and behaviour of μ phase during deformation of a nickel-based single crystal superalloy, Materials Science and Engineering: A 254(1-2) (1998) 1-12.

[264] M. Hashim, K.E. Sarath Raghavendra Babu, M. Duraiselvam, H. Natu, Improvement of wear resistance of Hastelloy C-276 through laser surface melting, Materials & Design 46 (2013) 546-551.

[265] M.M. Attallah, R. Jennings, X. Wang, L.N. Carter, Additive manufacturing of Ni-based superalloys: The outstanding issues, MRS Bulletin 41(10) (2016) 758-764.

[266] D.R. Corradi, A.Q. Bracarense, B. Wu, D. Cuiuri, Z. Pan, H. Li, Effect of Magnetic Arc Oscillation on the geometry of single-pass multi-layer walls and the process stability in wire and arc additive manufacturing, Journal of Materials Processing Technology 283 (2020).

[267] X. Zhou, Q. Tian, Y. Du, Y. Zhang, X. Bai, Y. Zhang, H. Zhang, C. Zhang, Y. Yuan, Investigation of the effect of torch tilt and external magnetic field on arc during overlapping deposition of wire arc additive manufacturing, Rapid Prototyping Journal (2020).

[268] A.A. Tzavaras, H.J.J. Brody, Electromagnetic stirring and continuous casting—Achievements, problems, and goals, 36(3) (1984) 31-37.

[269] N. Anbarasan, N. Narein, S. Jerome, Influence of Mechanical Arc Oscillation on the Microstructural and Mechanical Properties of Inconel 718 Welds, Transactions of the Indian Institute of Metals 72(6) (2019) 1541-1544.

[270] S. Sundaresan, G.D.J. Ram, Use of magnetic arc oscillation for grain refinement of gas tungsten arc welds in α–β titanium alloys, Science and Technology of Welding and Joining 4(3) (1999) 151-160.

[271] M. Gong, Y. Meng, S. Zhang, Y. Zhang, X. Zeng, M. Gao, Laser-arc hybrid additive manufacturing of stainless steel with beam oscillation, Additive Manufacturing 33 (2020).

[272] G.J. Ram, R. Murugesan, Sundaresan, Fusion zone grain refinement in aluminum alloy welds through magnetic arc oscillation and its effect on tensile behavior, Journal of materials engineering performance 8(5) (1999) 513-520.

[273] G.J. Ram, R. Murugesan, S.J.J.o.m.e. Sundaresan, performance, Fusion zone grain refinement in aluminum alloy welds through magnetic arc oscillation and its effect on tensile behavior, 8(5) (1999) 513-520.

[274] C. Yang, Q. Xu, B. Liu, Primary dendrite spacing selection during directional solidification of multicomponent nickel-based superalloy: multiphase-field study, Journal of materials science 53(13) (2018) 9755-9770.

[275] Y. Shi, Q. Xu, R. Chen, B. Liu, Q. Wu, H. Yang, A microstructure-strength calculation model for predicting tensile strength of AlSi7Mg alloy castings, Proceedings of the 2nd World Congress on Integrated Computational Materials

Engineering (ICME), Springer, 2013, pp. 109-115.

[276] X. Yu, Y.C. Lim, R. Smith, S.S. Babu, D.F. Farson, J.C. Lippold, S. McCracken, Reducing hot cracking tendency of dissimilar weld overlay by magnetic arc oscillation, Materials Science and Technology 30(8) (2014) 930-937.

[277] C.T. Rueden, J. Schindelin, M.C. Hiner, B.E. DeZonia, A.E. Walter, E.T. Arena, K.W. Eliceiri, ImageJ2: ImageJ for the next generation of scientific image data, BMC bioinformatics 18(1) (2017) 1-26.

[278] W. Ou, T. Mukherjee, G.L. Knapp, Y. Wei, T. DebRoy, Fusion zone geometries, cooling rates and solidification parameters during wire arc additive manufacturing, International Journal of Heat and Mass Transfer 127 (2018) 1084-1094.

[279] J. Xiong, Y. Li, R. Li, Z. Yin, Influences of process parameters on surface roughness of multi-layer single-pass thin-walled parts in GMAW-based additive manufacturing, Journal of Materials Processing Technology 252 (2018) 128-136.

[280] V.T. Le, D.S. Mai, Q.H. Hoang, Effects of cooling conditions on the shape, microstructures, and material properties of SS308L thin walls built by wire arc additive manufacturing, Materials Letters 280 (2020).

[281] G. Yang, J. Ma, B.E. Carlson, H.-P. Wang, M.M. Atabaki, R. Kovacevic, Decreasing the surface roughness of aluminum alloy welds fabricated by a dual beam laser, Materials & Design 127 (2017) 287-296.

[282] T. Yamamoto, K. Takeda, T. Toh, J. Tanaka, Distribution of heat flux transported by a magnetically driven arc, Thin Solid Films

515(9) (2007) 4228-4233.

[283] B. Wu, D. Ding, Z. Pan, D. Cuiuri, H. Li, J. Han, Z. Fei, Effects of heat accumulation on the arc characteristics and metal transfer behavior in Wire Arc Additive Manufacturing of Ti6Al4V, Journal of Materials Processing Technology 250 (2017) 304-312.

[284] Z. Qiu, B. Wu, H. Zhu, Z. Wang, A. Hellier, Y. Ma, H. Li, O. Muransky, D.J.M. Wexler, Design, Microstructure and mechanical properties of wire arc additively manufactured Hastelloy C276 alloy, (2020) 109007.

[285] N.S. Biradar, R. Raman, Grain Refinement in Al-Mg-Si Alloy TIG Welds Using

Transverse Mechanical Arc Oscillation, Journal of Materials Engineering and Performance 21(11) (2012) 2495-2502.

[286] G.M. Reddy, A.A. Gokhale, K.P. Rao, Weld microstructure refinement in a 1441 grade aluminium-lithium alloy, Journal of Materials Science 32(15) (1997) 4117-4126.

[287] S. Kou, D. Sun, Fluid flow and weld penetration in stationary arc welds, Metallurgical Transactions A 16(1) (1985) 203-213.

[288] M. Becker, J.A. Dantzig, M. Kolbe, S.T. Wiese, F. Kargl, Dendrite orientation transition in AlGe alloys, Acta Materialia 165 (2019) 666-677.

[289] E. Vandersluis, C. Ravindran, Comparison of measurement methods for secondary dendrite arm spacing, Metallography, Microstructure, and Analysis 6(1) (2017) 89-94.

[290] M.V. Canté, C. Brito, J.E. Spinelli, A. Garcia, Interrelation of cell spacing, intermetallic compounds and hardness on a directionally solidified Al–1.0Fe–1.0Ni alloy, Materials & Design 51 (2013) 342-346.

[291] L. Liu, J. Zhang, C. Ai, Nickel-Based Superalloys, Reference Module in Materials Science and Materials Engineering, Elsevier2020.

[292] S. Ehtemam-Haghighi, G. Cao, L.-C. Zhang, Nanoindentation study of mechanical properties of Ti based alloys with Fe and Ta additions, Journal of Alloys and Compounds 692 (2017) 892-897.

[293] A. Hynowska, E. Pellicer, J. Fornell, S. González, N. Van Steenberge, S. Suriñach, A. Gebert, M. Calin, J. Eckert, M.D.J.M.S. Baró, E. C, Nanostructured β-phase Ti–31.0 Fe–9.0 Sn and sub-μm structured Ti–39.3 Nb–13.3 Zr–10.7 Ta alloys for biomedical applications: Microstructure benefits on the mechanical and corrosion performances, 32(8) (2012) 2418-2425.

[294] J. Fornell, N. Van Steenberge, A. Varea, E. Rossinyol, E. Pellicer, S. Suriñach, M.D. Baró, J. Sort, Enhanced mechanical properties and in vitro corrosion behavior of amorphous and devitrified Ti40Zr10Cu38Pd12 metallic glass, Journal of the Mechanical Behavior of Biomedical Materials 4(8) (2011) 1709-1717.

[295] J. Xu, G. dong Wang, X. Lu, L. Liu, P. Munroe, Z.-H.J.C.I. Xie, Mechanical and corrosion-resistant properties of Ti–Nb–Si–N nanocomposite films prepared by a double glow discharge plasma technique, 40(6) (2014) 8621-8630.

[296] E. Pellicer, S. Pané, K. Sivaraman, O. Ergeneman, S. Suriñach, M. Baró, B.J. Nelson, J.J.M.C. Sort, Physics, Effects of the anion in glycine-containing electrolytes on the mechanical properties of electrodeposited Co–Ni films, 130(3) (2011) 1380-1386.

[297] S. Zhang, Nanostructured thin films and coatings: mechanical properties, CRC Press2010.

[298] A.V. Sergueeva, V.V. Stolyarov, R.Z. Valiev, A.K.J.S.M. Mukherjee, Advanced mechanical properties of pure titanium with ultrafine grained structure, 45(7) (2001) 747-752.

[299] P. Zhang, S. Li, Z.J.M.S. Zhang, E. A, General relationship between strength and hardness, 529 (2011) 62-73.

[300] J. Campbell, Castings, Elsevier2003.

[301] L. Zhu, Z.F. Xu, P. Liu, Y.F. Gu, Effect of processing parameters on microstructure of laser solid forming Inconel 718 superalloy, Optics & Laser Technology 98 (2018) 409-415.

[302] C. Brito, G. Reinhart, H. Nguyen-Thi, N. Mangelinck-Noël, N. Cheung, J.E. Spinelli, A. Garcia, High cooling rate cells, dendrites, microstructural spacings and microhardness in a directionally solidified Al–Mg–Si alloy, Journal of Alloys and Compounds 636 (2015) 145-149.

[303] B. Wu, Z. Qiu, B. Dong, D. Wexler, Z. Pan, K. Carpenter, D.R. Corradi, H. Li, Effects of synchronized magnetic arc oscillation on microstructure, texture, grain boundary and mechanical properties of wire arc additively manufactured Ti6Al4V alloy, Additive Manufacturing 54 (2022) 102723.

[304] A.N.M. Tanvir, M.R.U. Ahsan, C. Ji, W. Hawkins, B. Bates, D.B. Kim, Heat treatment effects on Inconel 625 components fabricated by wire + arc additive manufacturing (WAAM)—part 1: microstructural characterization, The International Journal of Advanced Manufacturing Technology 103(9-12) (2019) 3785-3798.

[305] D. Ma, A.D. Stoica, Z. Wang, A.M. Beese, Crystallographic texture in an additively manufactured nickel-base superalloy, Materials Science and Engineering: A 684 (2017) 47-53.

[306] C. Zhang, Z. Qiu, H. Zhu, Z. Wang, O. Muránsky, M. Ionescu, Z. Pan, J. Xi, H.

Li, On the Effect of Heat Input and Interpass Temperature on the Performance of Inconel 625 Alloy Deposited Using Wire Arc Additive Manufacturing–Cold Metal Transfer Process, Metals 12(1) (2022).

[307] H.L. Wei, J. Mazumder, T. DebRoy, Evolution of solidification texture during additive manufacturing, Scientific reports 5(1) (2015) 1-7.

[308] G.P. Dinda, A.K. Dasgupta, J. Mazumder, Texture control during laser deposition of nickel-based superalloy, Scripta Materialia 67(5) (2012) 503-506.

[309] H.L. Wei, J. Mazumder, T. DebRoy, Evolution of solidification texture during additive manufacturing, Sci Rep 5 (2015) 16446.

[310] W. Wang, P.D. Lee, M. McLean, A model of solidification microstructures in nickel-based superalloys: predicting primary dendrite spacing selection, Acta Materialia 51(10) (2003) 2971-2987.

[311] N. Raghavan, S. Simunovic, R. Dehoff, A. Plotkowski, J. Turner, M. Kirka, S. Babu, Localized melt-scan strategy for site specific control of grain size and primary dendrite arm spacing in electron beam additive manufacturing, Acta Materialia 140 (2017) 375-387.

[312] W. Li, J. Liu, Y. Zhou, S. Li, S. Wen, Q. Wei, C. Yan, Y. Shi, Effect of laser scanning speed on a Ti-45Al-2Cr-5Nb alloy processed by selective laser melting: Microstructure, phase and mechanical properties, Journal of Alloys and Compounds 688 (2016) 626-636.

[313] Y. Chen, M. Xu, T. Zhang, J. Xie, K. Wei, S. Wang, L. Yin, P. He, Grain refinement and mechanical properties improvement of Inconel 625 alloy fabricated by ultrasonic-assisted wire and arc additive manufacturing, Journal of Alloys and Compounds 910 (2022) 164957.

[314] T. Ungár, Strain broadening caused by dislocations, Trans Tech Publ, pp. 151-157.

[315] T. Ungár, J. Gubicza, P. Hanák, I. Alexandrov, Densities and character of dislocations and size-distribution of subgrains in deformed metals by X-ray diffraction profile analysis, Materials Science and Engineering: A 319 (2001) 274-278.

[316] T. Ungár, I. Dragomir, Á. Révész, A. Borbély, The contrast factors of dislocations in cubic crystals: the dislocation model of strain anisotropy in practice, Journal of

applied crystallography 32(5) (1999) 992-1002.

[317] K.R. Grimes RW, Edwards L., Greater tolerance for nuclear materials, Nat Mater. 7(9) (2008) 683-685.

[318] D. Raabe, C.C. Tasan, E.A. Olivetti, Strategies for improving the sustainability of structural metals, Nature 575(7781) (2019) 64-74.

[319] B. Wu, Z. Qiu, Z. Pan, K. Carpenter, T. Wang, D. Ding, S.V. Duin, H. Li, Enhanced interface strength in steel-nickel bimetallic component fabricated using wire arc additive manufacturing with interweaving deposition strategy, Journal of Materials Science & Technology 52 (2020) 226-234.

[320] C. Zhang, L. Zhang, W. Shen, Q. Xu, Y. Cui, The processing map and microstructure evolution of Ni-Cr-Mo-based C276 superalloy during hot compression, Journal of Alloys and Compounds 728 (2017) 1269-1278.

[321] X.-y. Zhang, J. Zhong, S.-l. Guo, J. Zhao, Control of deformation and annealing process to produce incoherent Σ3 boundaries in Hastelloy C-276 alloy, Nuclear Materials and Energy 27 (2021) 100944.

[322] J.H. Weber, M.K. Banerjee, Nickel and Nickel Alloys: An Overview☆, Reference Module in Materials Science and Materials Engineering, Elsevier2019.

[323] C. Pandey, M.M. Mahapatra, P. Kumar, N. Saini, Comparative study of autogenous tungsten inert gas welding and tungsten arc welding with filler wire for dissimilar P91 and P92 steel weld joint, Materials Science and Engineering: A 712 (2018) 720-737.

[324] C. Pandey, A. Giri, M.M. Mahapatra, Evolution of phases in P91 steel in various heat treatment conditions and their effect on microstructure stability and mechanical properties, Materials Science and Engineering: A 664 (2016) 58-74.

[325] A. Grybėnas, V. Makarevičius, A. Baltušnikas, I. Lukošiūtė, R. Kriūkienė, Correlation between structural changes of M23C6 carbide and mechanical behaviour of P91 steel after thermal aging, Materials Science and Engineering: A 696 (2017) 453-460.

[326] S. Sridar, M.A. Klecka, W. Xiong, Interfacial characteristics of P91 steel - Inconel 740H bimetallic structure fabricated using wire-arc additive manufacturing, Journal of Materials Processing Technology 300 (2022) 117396.

[327] R. Hielscher, H. Schaeben, A novel pole figure inversion method: specification of the MTEX algorithm, Journal of Applied Crystallography 41(6) (2008) 1024-1037.

[328] S. Kumar, S. Sirohi, R.S. Vidyarthy, A. Gupta, C. Pandey, Role of the Ni-based filler composition on microstructure and mechanical behavior of the dissimilar welded joint of P22 and P91 steel, International Journal of Pressure Vessels and Piping 193 (2021) 104473.

[329] N.G. Peng, B. Ahmad, M.R. Muhamad, M. Ahadlin, Phase Transformation of P91 Steels upon Cooling after Short Term Overheating above Ac1 and Ac3 Temperature, Advanced Materials Research, Trans Tech Publ, 2013, pp. 1756-1765.

[330] R.W. Messler Jr, Principles of welding: processes, physics, chemistry, and metallurgy, John Wiley & Sons2008.

[331] P. Mayr, H. Cerjak, The impact of welding on the creep properties of advanced 9–12% Cr steels, Transactions of the Indian Institute of Metals 63(2) (2010) 131-136.

[332] A. Rajesh Kannan, S. Mohan Kumar, N. Pravin Kumar, N. Siva Shanmugam, A.S. Vishnu, Y. Palguna, Process-microstructural features for tailoring fatigue strength of wire arc additive manufactured functionally graded material of SS904L and Hastelloy C-276, Materials Letters 274 (2020) 127968.

[333] X. Cheng, Z. Du, S. Chu, J. Wu, J. Dong, H. Wang, Z. Ma, The effect of subsequent heating treatment on the microstructure and mechanical properties of additive manufactured Hastelloy X alloy, Materials Characterization 186 (2022) 111799.

[334] A. Renuka Balakrishna, R.D. James, A solution to the permalloy problem—A micromagnetic analysis with magnetostriction, Applied Physics Letters 118(21) (2021) 212404.

[335] X. Zhang, H. Xu, Z. Li, A. Dong, D. Du, L. Lei, G. Zhang, D. Wang, G. Zhu, B. Sun, Effect of the scanning strategy on microstructure and mechanical anisotropy of Hastelloy X superalloy produced by Laser Powder Bed Fusion, Materials Characterization 173 (2021) 110951.

[336] A. Aliyu, K. Sai Jyotheender, C. Srivastava, Texture and grain boundary engineering in nickel coating with tungsten addition and its effect on the coating corrosion behavior, Surface and Coatings Technology 412 (2021) 127079.

[337] N. D'Souza, M.G. Ardakani, A. Wagner, B.A. Shollock, M. McLean, Morphological aspects of competitive grain growth during directional solidification of a nickel-base superalloy, CMSX4, Journal of Materials Science 37(3) (2002) 481-487.

[338] S. Kim, S. Lee, B.S. Lee, Effects of grain size on fracture toughness in transition temperature region of Mn–Mo–Ni low-alloy steels, Materials Science and Engineering: A 359(1-2) (2003) 198-209.

[339] C. Pandey, M.M. Mahapatra, P. Kumar, A. Giri, Microstructure characterization and charpy toughness of P91 weldment for as-welded, post-weld heat treatment and normalizing & tempering heat treatment, Metals and Materials International 23(5) (2017) 900-914.